

Non-newtonian fluids and droplets in microchannels

Huang, Yi

2016

Huang, Y. (2016). Non-newtonian fluids and droplets in microchannels. Doctoral thesis, Nanyang Technological University, Singapore.

<https://hdl.handle.net/10356/68919>

<https://doi.org/10.32657/10356/68919>

Non-Newtonian Fluids and Droplets in Microchannels



Huang Yi

School of Mechanical and Aerospace Engineering

A thesis submitted to the Nanyang Technological University
in partial fulfilment of the requirement for the degree of

Doctor of Philosophy

2015

Abstract

With the development of microfluidics, electro-osmotic (EO) driven flow has gained intense research interest as a result of its unique flow profile and the corresponding benefits in its application in the transportation of sensitive samples. Challenges occur when the EO driven mechanism encounters complex rheology and vital questions such as “Can the zeta potential still be assumed to be constant when dealing with fluids with complex rheology?”, “Does the shear thinning effect enhances electro-osmotic driven flow?” need to be answered. Experiments were conducted via using current monitoring and microscopy fluorescent methods, and an analytical model was developed by coupling a generalized Smoluchowski approach with the power-law constitutive model. The zeta potential was calculated. The shear thinning effect is also addressed via experimental data and theoretical calculations.

The mathematical model for the two immiscible layers of electro-osmotic driven flow in the parallel microchannel was proposed. One layer is a conducting non-Newtonian power-law fluid driven by electro-osmotic force. The other layer is a non-conducting Newtonian layer driven by interface shear. The effects of Debye-Hueckel parameter κh_1 , interfacial zeta potential ψ_1 , the Newtonian viscosity μ_2 , the non-Newtonian fluid consistency coefficient m & flow behavior index n were discussed. The complex flow behavior, namely fluid consistency coefficient and flow behavior index, play important roles in the velocity distributions. The shear thinning effect is also analyzed. The results show that the shear thinning fluid is not only ideal for direct electro-osmotic driving but also for hybrid driving.

A flow-focusing geometry in a microfluidic device was studied for the formation of uniform droplets and we qualitatively illustrated aspects of controlling the droplet

size and breakup regimes when an active electric field is applied. The control of droplet size was demonstrated with applied electric fields by changing the voltage and frequency. Various droplet breakup regimes including squeezing, dripping, unstable breakup and jetting induced under different electric field parameters were observed. It is shown that the droplet size decreases with an increase in voltage. Similar decreasing of the droplet size is also found with the increase of electric field frequency, especially when the frequency is less than 2 kHz. In addition, the experimental results show the droplet size is much more in uniform at a lower frequency than that at a higher frequency.

Flow focusing microchannels with three orifice sizes and the non-contact type of electrodes were designed and fabricated for investigations of non-Newtonian droplet formation under the influence of applied AC electric fields. Non-Newtonian fluids that have similar rheological behavior of bio samples were adopted for droplet formation. Flow conditions of experiments, microchannel geometries, and AC electric field parameters have been implemented systematically. The influences of these variables were analyzed. Among them, the non-Newtonian droplet formation was highlighted and addressed. The dependency of the flow condition and electric field on the non-Newtonian droplet formation dynamics was presented and analyzed. The flow field of the non-Newtonian droplet formation was measured and analyzed quantitatively via a high speed μ PIV system. Different droplet formation regimes and the impact of AC electric field were considered when the measurements were conducted. Flow fields and the related vorticity distributions were used for flow characterization.

A particle free method for flow field visualization was proposed and achieved by analyzing liquid crystal polarization. The proposed concept is implemented by

imaging liquid crystal flow under microfluidic environment using a polarization based optical interferometric configuration. Fringe patterns give good presentation of flow characterizations for different nozzle/diffuser microchannel designs. The obtained results demonstrate that the flow shear and flow recirculation under various conditions can be evaluated in terms of interferometric fringe patterns. It is envisaged that the proposed methodology can make a potential impact in flow field visualization studies and related analysis.

A novel method for the investigation of the dynamics of droplet formation was proposed by liquid crystal polarization as the traditionally adopted μ PIV method had its vulnerability in interfacial and filament measurement. The interfacial dynamics of the droplet and the filament were observed and the associated flow characteristics were analyzed. In addition to the formation dynamics, the control of liquid crystal droplet generated in flow focusing microchannel was achieved by hydrodynamic alteration and implementation of AC electric field. The exponential decrease in liquid crystal droplet size in terms of capillary number was found. Micro level (μm) of droplet size adjustment was obtained in the presence of AC electric field in a microfluidic environment.

Acknowledgements

During my study at Nanyang Technological University, I received helps from a lot of professors, staffs and friends. It is an honor to conduct my Ph.D research with them and I would like to show my sincere gratitude to them.

Firstly and foremost, it is with immense gratitude that I acknowledge the support and help of my supervisor Associate Professor Wong Teck Neng. With the excellent and patient guidance of Prof. Wong, would I be able to carry out the research work.

I would like to appreciate the help from Associate Professor Murukeshan Vadakke Matham and Dr. Jong-Leng Liow. Their in-depth knowledge and invaluable advices are of great importance to this study.

I am indebted to my wife Yao Saijin for her unconditional support for my Ph.D research. Without her encouragement, I would not have enough strength to start my Ph.D research at Nanyang Technology University.

I would like to show my deepest gratitude to Mr. Yuan Kee Hock for the valuable assistance on my experiments.

I greatly appreciate my fellow research students and staffs, Dr. Li Haiwang, Dr. Che Zhizhao, Dr. Zhu Guiping, Dr. He Bin, Dr. Xu Bin, Dr. Cheung Yin Nee, Mr. Luong Trung Dung, Dr. Shinoj Vengalathunadakal K., Dr. Wang Yanling, Dr. Zhao Cunlu, Dr. Tan Say Hwa, Mr. Yan Zhibin, Mr. Yao Xin, Mr. Feng Huicheng, Ms. Zhong Xin, Mr. Zhao Yugang, Mr. Ding Zijing, and other friends in the Thermal and Fluid Research Laboratory for sharing their knowledge and skills.

I also would like to acknowledge the Research Scholarship offered by Nanyang Technology University.

Last but not least, I wish to thank my family for their understanding and support.

Contents

Abstract	I
Acknowledgements	IV
Contents	VII
List of Symbols	XI
List of Figures.....	XVI
List of Tables	XXVIII
Chapter 1 Introduction.....	1
1.1 Background and motivation.....	1
1.2 Objectives and scopes	3
Chapter 2 Literature Review	5
2.1. Electric double layer	5
2.2. Electro-kinetic phenomena	7
2.2.1 Measurement of electro-osmotic velocity.....	7
2.2.2 Zeta potential	9
2.3. Electro-osmotic based applications	11
2.3.1 Electro-osmotic pump.....	11
2.3.2 Control of the fluid-fluid interface.....	13
2.4. Fluids properties of non-Newtonian fluids	14
2.4.1. Time-independent non-Newtonian fluid.....	15
2.4.2. Shear thinning fluid	15
2.4.3. Shear thickening fluid	17
2.5. Electro-osmotic in non-Newtonian fluids.....	18
2.5.1 Theoretical approach.....	18
2.5.2 Numerical investigation.....	20
2.5.3 Experimental investigation on non-Newtonian fluids	22
2.6. Droplet microfluidics	23
2.6.1 Droplet formation	23
2.6.2 Non-Newtonian droplet formation.....	30
2.7. Liquid crystals based optofluidic	33
2.7.1 Thermotropic liquid crystal	33
2.7.2 Surface anchoring conditions.....	35
2.7.3 Liquid crystal optics.....	38
2.7.4 Applications of LC in microfluidics	42
2.8. Fabrications of microchannels	44
2.9. Summary	45

Chapter 3 Experimental and Theoretical Investigations of Non-Newtonian Electroosmotic Driven Flow in Rectangular Microchannels.....	47
3.1 Introduction	47
3.2 Experimental setup	49
3.2.1 Data acquisition system	49
3.2.2 Fluid sample preparation	49
3.2.3 Current monitoring method and microchannel.....	50
3.3 Results and discussion	52
3.3.1 Non-Newtonian EO driving velocity via current monitoring method....	52
3.3.2 Microscopy fluorescence study of the non-Newtonian electro-osmotic driven flow.....	53
3.3.3 Zeta potential for non-Newtonian fluids	54
3.3.4 Effect of shear thinning behavior on EO flow.....	60
3.4 Summary.....	62
Chapter 4 Two Immiscible Layers of Electro-osmotic Driven Flow with a Layer of Conducting non-Newtonian Fluid⁺	65
4.1 Introduction	65
4.2 Mathematical model	66
4.2.1 Electric potential distribution in the conducting layer	67
4.2.2 Governing equations for the non-Newtonian layer	68
4.2.3 Governing equation and power-law model.....	69
4.2.4 Governing equation for Newtonian layer	71
4.3 Results and discussion	72
4.3.1 Effect of κh_1	73
4.3.2 Effect of zeta potentials ψ_w ψ_i	76
4.3.3 Effect of the Newtonian layer viscosity μ_2 and the non-Newtonian layer fluid consistency coefficient m	79
4.3.4 Effect of flow behavior index n	81
4.4 Summary.....	85
Chapter 5 An Electric Field Activated Droplet Formation in Flow-focusing Device	87
5.1 Introduction	87
5.2 Experimental.....	88
5.2.1 Experimental System.....	88
5.2.2 Flow Focusing Device.....	90
5.2.3 External Electric Field.....	90
5.2.4 Experimental Measurement.....	91
5.3 Results and Discussion	92

5.3.1	Droplet Breakup Regimes.....	92
5.3.2	Droplet Size Varying with Electric Field	95
5.3.3	Droplet Size Distribution.....	98
5.4	Summary	98
Chapter 6 AC Electric Field Tuned Non-Newtonian Droplet Formation in Flow Focusing Microchannels.....		101
6.1	Introduction.....	101
6.2	Experimental setup	103
6.2.1	General setup	103
6.2.2	Microchannel	104
6.2.3	Materials	106
6.2.4	Fluidic and electric system setup	106
6.3	Results and discussion	107
6.3.1	Droplet breakup dynamics of the non-Newtonian fluid	108
6.3.2	Electric field tuned non-Newtonian droplet sizes.....	110
6.3.3	Flow dynamics coupled electric field effect upon non-Newtonian droplet formation.....	113
6.3.4	Effects of Orifice sizes on non-Newtonian droplet formation.....	118
6.3.5	Effective capacitance electric model for AC electric field assisted non-Newtonian droplet formation.....	120
6.3.6	High speed μ PIV measurement on non-Newtonian droplet formation dynamics	125
6.4	Summary	133
Chapter 7 Particle Free Optical Imaging of Flow Field by Liquid Crystal Polarization.....		135
7.1	Introduction.....	135
7.2	Materials and method.....	137
7.2.1	Optical setup	138
7.2.2	Fluidic setup.....	138
7.2.3	Materials	138
7.2.4	Microchannel	139
7.3	Results and discussion	140
7.3.1	Flow field induced fringe patterns in 15° opening angle microchannel	140
7.3.2	Fringe density for different opening angles under various flow rates .	144
7.3.3	Flow recirculation patterns of 5CB liquid crystal for diffuser and nozzle directions.....	146
7.3.4	Topological defects represented by Erikson number.....	149
7.4	Summary	150

Chapter 8 Investigations of Interfacial Dynamics of Droplet Production via Particle Free Flow Visualization Method.....	151
8.1 Introduction	151
8.2 Method and materials	152
8.2.1 Optical setup	153
8.2.2 Microchannel	154
8.2.3 Fluidic setup	156
8.2.4 Fluids	156
8.2.5 Electric setup	156
8.3 Results and discussion	157
8.3.1 Interfacial dynamics of LC droplet formation.....	157
8.3.2 Droplet formation and filament dynamics.....	160
8.3.3 LC droplet formation tuned by AC electric field	163
8.4 Summary.....	166
Chapter 9 Conclusions and Future work	169
9.1 Conclusions	169
9.2 Future work	171
Appendix A.....	173
A.1 Plots of droplet diameter as a function of applied voltage at various frequencies.....	173
A.2 Plots of droplet diameter as a function of frequency at various applied voltages.....	178
A.3 Plots of droplet diameter as a function of capillary number at various applied voltages	181
A.4 Plots of droplet diameter as a function of capillary number at various frequencies.....	183
A.5 Plots of droplet diameter as a function of capillary number for different orifice widths.....	185
Appendix B.....	186
Publications Arising from this Thesis.....	189
References	190

computer and the input and output experimental data and images can be collected simultaneously.

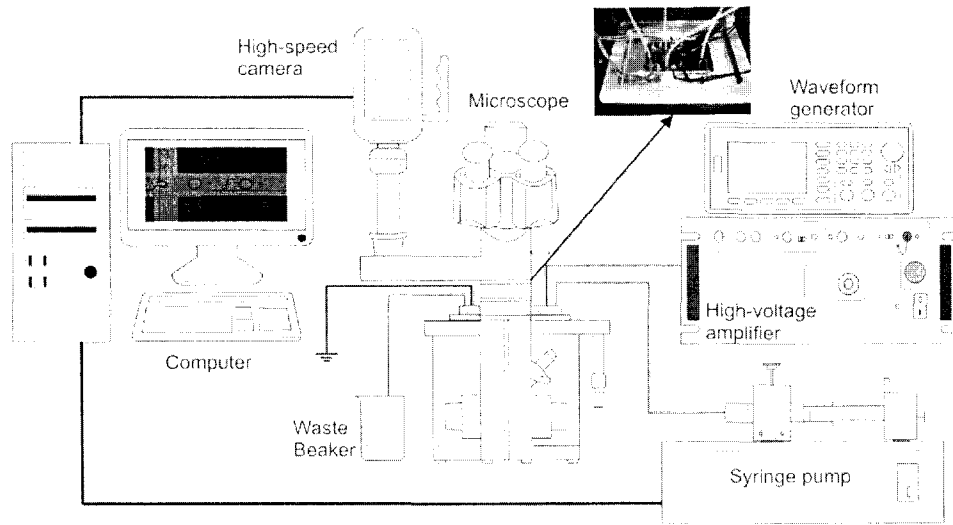


Figure 5.1 Schematic diagram of experimental setup. The apparatus fundamentally consisted of six parts: (1) Syringe pump system, (2) High-voltage generator system, (3) Flow focusing device (chip), (4) Microscope system, (5) High-speed camera, and (6) Data collection system.

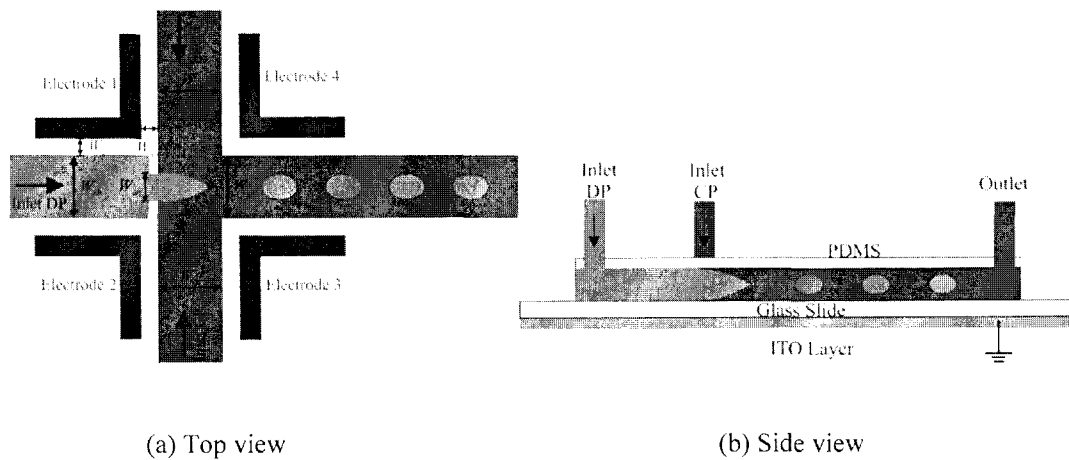


Figure 5.2 Schematic diagram of the flow-focusing geometry implemented in a microfluidic device. DP, CP here denote dispersed phase and continuous phase, respectively. The main channel width W_{ch} = 100 μm ; the height of microchannel is 35 μm . W_{ga} = 50 μm . Three sizes of orifices W_{or} = 25, 75 and 100 μm were designed.

List of Symbols

c_1, c_2	Solution concentrations [mol/L]
C_{PDMS}	Capacitance of the PDMS layer [pF]
C_{Glass}	Capacitance of the ITO glass slice [pF]
D	Diameter of the droplet
E_0	Electrical field charged on the non-Newtonian layer [V/m]
e_0	Fundamental electric charge [C]
F_x	Electro-osmotic induced body force [N]
f	Frequency of the applied AC electric field [Hz]
h	Height of the microchannel [μm]
h_1	Height of the non-Newtonian layer [μm]
h_2	Height of the Newtonian layer [μm]
K	Elastic constant of the liquid crystal [N]
$L_{channel}$	The length of the channel [μm]
m	Fluid consistency coefficient [$\text{Pa}\cdot\text{s}^n$]
n	Flow behavior index
n_0	Ionic concentration in the bulk solution
∇P	Pressure gradient [Pa/m]
P_1	Downstream pressure [Pa]
P_0	The upstream pressure [Pa]

Q_{DP}	Flow rate of the dispersed phase
Q_{CP}	Flow rate of the continuous phase
R_{Fluid}	Electrical resistance caused by the presence of the fluid [M Ω]
r_p	Radius of the particle [μm]
T	Absolute temperature [K]
$\overline{u_s}$	Dimensionless EO driven velocity
u_s, V_s	Generalized Smoluchowski velocity [m/s]
U	Peak to Peak voltage of the applied AC electric field [V]
\overline{U}_{Fluid}	Dimensionless voltage experienced by the dispersed phase
W_{ch}	The width of flow focusing main microchannels [μm]
W_d	The channel width of the disperse phase
W_c	The channel width of the continuous phase
W_{ga}	The gap between the electrode and channel wall [μm]
W_{or}	The width of the orifice in the microchannels [μm]
w_z	Vorticity distribution over the droplet
X_{CPMS}	Electrical resistance of the capacitance system
z_v	Valency of the ion
λ_b, λ_s	Bulk conductivity and surface conductivity

Greek Symbols

γ_{ave}	The average shear in the bulk fluid [s^{-1}]
ρ_e	The overall charge density [C/m^3]
ν_E	The mobility of the particle
ϵ_0	The electric permittivity of vacuum [F/m]
ϵ_r	The relative electric permittivity
μ	The fluid dynamic viscosity [$Pa \cdot s$]
κ	The Debye- Hueckel parameter [m^{-1}]
ψ	Zeta potential [mV]
ψ_W	Wall boundary zeta potential [mV]
ψ_I	Interface boundary zeta potential [mV]
κ_b	Boltzmann constant
τ_{μ_1}	Viscous shear stress for the non-Newtonian layer [Pa]
τ_{μ_2}	Viscous shear stress for the Newtonian layer [Pa]
τ_e	Electro-shear stress [Pa]
μ_0	Zero shear viscosity [$Pa \cdot s$]
μ_∞	Infinite-shear-rate viscosity [$Pa \cdot s$]
μ_1	Non-Newtonian layer viscosity [$Pa \cdot s$]
μ_2	Newtonian layer viscosity [$Pa \cdot s$]
σ	Surface tension [mN/m]

χ	Dimensional fringe density
χ^*	Dimensionless fringe density

Subscripts

Ref	Reference quantity
1	Conducting non-Newtonian layer
11,12,13	Sub-regions in conducting non-Newtonian layer
2	Non-conducting Newtonian layer
w	Wall
I	Interface
max	The maximum value
DP	Dispersed phase
CP	Continuous phase

List of Figures

Figure 2.1 Schematic diagram of ion distribution near the contact surface [12]	6
Figure 2.2 Schematic diagram of the EDL structure [14]	6
Figure 2.3 Indirect EDL measurement method [29].....	8
Figure 2.4 Schematic diagram of a μ PIV setup. [30].....	9
Figure 2.5 Non-dimensional electrical potential profile in one quarter of a rectangular microchannel (geometric ratio of height to width=2/3, non-dimensional electrokinetic diameter $K=24.7$) [18]	10
Figure 2.6 Working principle of AC EO pump [50]	12
Figure 2.7 Working principle of hybrid EO pump [54]	13
Figure 2.8 Fluid-fluid interface controlled by the combined effect of pressure and electro-osmotic driven method: (a) no electric field; (b) under -0.8 kV; (c) normalized concentration distribution of the fluorescent dye across the channel width under different applied voltages.[59]	14
Figure 2.9 Experimental results of flow switching [61].....	14
Figure 2.10 Schematic diagram for the time-independent fluid [62]	15
Figure 2.11 Shear thinning fluid properties [62]	16
Figure 2.12 Shear thickening fluid properties [68]	18
Figure 2.13 Schematic diagram for a single layer EO driven power-law fluid [72] ..	19

Figure 2.14 Schematic illustration of rough microchannel with complex-wavy surface.[82]	21
Figure 2.15 Microchannel with height of 30 μm and length of 210 μm . [84].....	21
Figure 2.16 A T junction for generation of droplets.....	23
Figure 2.17 Schematic diagram for flow focusing geometry	25
Figure 2.18 Four regimes of droplet formation. (a) squeezing, (b) thread forming, (c) dripping and (d) jetting.[108].....	26
Figure 2.19 Droplet formation under applied electric field. Corn oil and glycerine flow rates are 0.27 $\mu\text{L/s}$ and 0.75 $\mu\text{L/s}$, respectively.[95].....	26
Figure 2.20 Electric field controlled droplet formation. (A) microchannel setup, (B), (C), (D), (E) shows the droplet formation under the voltage of 0 V, 400 V, 600 V, 800 V, respectively. (F) Droplet size as a function of voltage. [112].....	27
Figure 2.21 Temperature controlled droplet formation in flow focusing microchannel. [114]	28
Figure 2.22 Droplet formation with (a) heater off and (b) heater on. [114]	28
Figure 2.23 Magnetic field controlled droplet formation in microchannels. [101] ...	29
Figure 2.24 The dependency of droplet size to magnetic flux in flow focusing configuration. [101]	29
Figure 2.25 (a)-(d) Pre-stretch region, (e)-(j) exponential self-thinning region of non-Newtonian droplet formation in a T junction microchannel. The interval between each image is 2.5 ms. [115]	30

Figure 2.26 Filament thickness versus time for both Newtonian and non-Newtonian fluid. The flow rate ratio is kept at 10, 30 and 60.[117]	31
Figure 2.27 Filament thickness versus time as a function of molecular weight of the non-Newtonian fluids. Three flow rate ratio, 10, 30, and 60 are considered. [118] ..	32
Figure 2.28 Representative diagram of calamitic and discotic liquid crystal micro structure [119]	33
Figure 2.29 Molecular alignment at different mesophase of liquid crystal [119]	34
Figure 2.30 Liquid crystal of 5CB [119]	34
Figure 2.31 Schematic diagram of the director \vec{n} and order parameter S [119]	35
Figure 2.32 Four types of surface anchoring conditions of nematic LC: (a) uniform planar anchoring, (b) homeotropic anchoring, (c) degenerate anchoring and (d) tilted anchoring [121, 122]	36
Figure 2.33 Two parameters describing the anchoring condition: azimuthal anchoring angle φ and zenithal anchoring angle θ [119]	36
Figure 2.34 (a), (b) show polarizing optical microscope observation of the degenerate planar anchoring in rectangular microchannel. The double head arrow indicates the orientation direction of the polarizer and analyzer. (c) demonstrates the image of fluorescence confocal polarizing microscope via laser polarization along the channel length as shown the double head arrow. [121, 126]	37
Figure 2.35 (a) (b) POM observation of LC uniform planar anchoring in a rectangular microchannel. (c) FCPM results of LC orientation in the azimuthal plane.	

(d) Normalized fluorescence for different LC anchoring: uniform planar (UP), degenerate planar (DP), and homeotropic (H) anchoring. [122]	38
Figure 2.36 Schematic diagram of uniformly oriented LC molecule in between optical polarizer and analyser. [127].....	39
Figure 2.37 Schematic diagram of transmission of white light across polarizer and analyzer. (a) LC orientated parallel to analyzer, (b) LC orientated arbitrarily but not parallel to analyzer.....	41
Figure 2.38 Schematic diagram of orthocopy and conoscopy imaging a liquid crystal sample. [127]	41
Figure 2.39 Schematic diagram for uniaxial and biaxial material via conoscopy setup. [127].....	42
Figure 2.40 LCs-aqueous interface in the presence of phospholipids (a) without phospholipids (b) after 20 minutes (c) after 2 hours [130].....	43
Figure 2.41 Optical images and cartoon representation of LC droplets [131].....	43
Figure 2.42 Schematic procedure of PDMS by soft-lithography fabrication [136] ..	44
Figure 3.1 Representative diagram for experimental setup	49
Figure 3.2 Schematic diagrams for the current monitoring method	50
Figure 3.3 Electric current evolution with time. Results were obtained by filling reservoir 1 and microchannel with 0.1% PEO aqueous solution whose concentration of sodium chloride is 0.7×10^{-3} M, while filling reservoir 2 with the same PEO solution with a sodium chloride concentration of 1.0×10^{-3} M.....	52

Figure 3.4 Average EO driven velocity versus applied electric field strength. Four different PEO concentrations (by weight), 0.1%, 0.3%, 0.5%, 0.7%, are measured.	53
Figure 3.5 Fluorescent images of EO driven flow with a non-Newtonian fluid	54
Figure 3.6 Rheological behavior of PEO aqueous solutions. Four different PEO concentrations were tested, 0.1%, 0.3%, 0.5%, 0.7% (by weight).....	55
Figure 3.7 Zeta potential values of PEO aqueous solutions under different electric field strength.....	59
Figure 3.8 Comparison between theoretical approach and experimental results	60
Figure 3.9 Shear thinning effect on non-Newtonian EO driven flow.	61
Figure 4.1 Schematic diagram of two immiscible layers electro-osmotic driven flow model	66
Figure 4.2 Comparisons of the analytical solution between the two-fluid flow model and the single-fluid model [72] for a larger value κh_1	75
Figure 4.3 Comparisons of the analytical solution between the two-fluid flow model and the single-fluid model [72] for a smaller value κh_1	76
Figure 4.4 Dimensionless velocity distribution for different values of wall zeta potential ψ_w . $\kappa h_1=400$, $E = 1000$ V/m.....	77
Figure 4.5 Dimensionless velocity distributions vary with the interface zeta potential. ($\kappa h_1=400$, $E=1000$ V/m and $\psi_w=-40$ mV)	78

Figure 4.6 Dimensionless velocity distributions for different values of Newtonian layer viscosity μ_2 . ($\kappa h_1=400$, $\psi_I=-20$ mV, $m = 0.001$ Pa·sⁿ and $n =0.5$) 79

Figure 4.7 Dimensionless velocity distributions affected by the non-Newtonian fluid consistency coefficient m . ($\psi_w=-40$ mV, $\psi_I=-20$ mV, $\kappa h_1=400$, $\mu_2 = 0.001$ Pa·s and $n=0.5$). 80

Figure 4.8 Dimensionless velocity distributions for different values of the flow behavior index n . ($\kappa h_1=10$, $E=1000$ V/m and $\psi_I=\psi_w=-40$ mV)..... 81

Figure 4.9 Variation of the maximum velocity with the fluid index n for different values of κh_1 .($E=1000$ V/m , $\psi_I=\psi_w=-40$ mV, $m = 0.001$ Pa·sⁿ and $n =0.5$) 82

Figure 4.10 Dimensionless non-Newtonian Layer volume flow rate versus the flow behavior index n . ($\psi_w=-40$ mV, $\psi_I=-20$ mV, $m = 0.001$ Pa·sⁿ and $\mu_2 = 0.001$ Pa·s) 84

Figure 4.11 Dimensionless Newtonian Layer volume flow rate versus the flow behavior index n . ($\psi_w=-40$ mV, $\psi_I=-20$ mV, $m = 0.001$ Pa·sⁿ and $\mu_2 = 0.001$ Pa·s) 85

Figure 5.1 Schematic diagram of experimental setup. The apparatus fundamentally consisted of six parts: (1) Syringe pump system, (2) High-voltage generator system, (3) Flow focusing device (chip), (4) Microscope system, (5) High-speed camera, and (6) Data collection system. 89

Figure 5.2 Schematic diagram of the flow-focusing geometry implemented in a microfluidic device. DP, CP here denote dispersed phase and continuous phase,

respectively. The main channel width $W_{ch} = 100 \mu\text{m}$; the height of microchannel is $35 \mu\text{m}$. $W_{ga} = 50 \mu\text{m}$. Three sizes of orifices $W_{or} = 25, 75$ and $100 \mu\text{m}$ were designed. .89

Figure 5.3 Droplet breakup regimes at different applied voltages and frequencies. $Q_{DP}/Q_{CP} = 200/400 \mu\text{l/hr}$. $Ca = 0.05$, $W_{or} = 100 \mu\text{m}$, $W_{ch} = 100 \mu\text{m}$92

Figure 5.4 Different droplet breakup regimes in flow-focusing device, here $Q_{DP}/Q_{CP} = 200/400 \mu\text{l/hr}$ and the orifice width $W_{or} = 100 \mu\text{m}$. (I) Dripping, (II) Unstable breakup and (III) Jetting. The dripping regime can be further classified based on the generated satellite droplets.94

Figure 5.5 Effect of applied voltage on droplet size at a fixed frequency $f = 2 \text{ kHz}$, $W_{or} = 100 \mu\text{m}$95

Figure 5.6 Effect of applied electric field frequency on droplet size at a fixed voltage $U = 750 \text{ V}$, $W_{or} = 100 \mu\text{m}$96

Figure 5.7 Influence of applied voltage at different frequencies on droplet size. $Q_{DP}/Q_{CP} = 200/400 \mu\text{l/hr}$, $W_{or} = 100 \mu\text{m}$. $Ca = 0.05$96

Figure 5.8 Droplet size distribution with different electric field parameters. $Q_{DP}/Q_{CP} = 200/400 \mu\text{l/hr}$, $W_{or} = 100 \mu\text{m}$. The above and below “-” here are the maximum and minimum value of the droplet diameter, respectively. The upper quartile is the 75th percentile, the lower quartile is the 25th percentile, and the median is the 50th percentile. The blank box is the mean droplet diameter.98

Figure 6.1 Experimental setup for electric tuned non-Newtonian droplet formation103

Figure 6.2 Schematic diagram of the microchannel104

Figure 6.3 Lay out of the flow focusing microchannel with non-contact type of electrode. DP, CP denote dispersed phase and continuous phase respectively. 105

Figure 6.4 Non-Newtonian droplet formation processes under different electric fields. Flow rates are $Q_{DP} : Q_{CP} = 10:40 \mu\text{L/hr}$, Orifice size $W_{or} = 100 \mu\text{m}$ 108

Figure 6.5 Filament thickness versus time. $Q_{DP} : Q_{CP} = 20:40 \mu\text{L/hr}$ 109

Figure 6.6 Non-Newtonian droplet diameters versus applied voltages. AC frequency is fixed at 5 KHz. Four groups of flow rate ratios are adopted. $Q_{DP} = 10 \mu\text{L/hr}$ 111

Figure 6.7 Droplet diameter dependence of AC frequency under various flow rate ratios. 113

Figure 6.8 Non-Newtonian droplet diameter varies as the function of Ca under different applied voltages with a fixed AC frequency of 5 KHz. $Q_{DP} = 10 \mu\text{L/hr}$ 115

Figure 6.9 Non-Newtonian droplet diameter dependency on Ca under different AC frequencies with fixed voltage of (a) 250 V and (b) 1 KV respectively. $Q_{DP} = 10 \mu\text{L/hr}$ 116

Figure 6.10 Merging of droplets in jetting regime. $Q_{DP} : Q_{CP} = 20:160 \mu\text{L/hr}$, applied electric field: 750 V, 5 KHz. 118

Figure 6.11 Non-Newtonian droplet formations for different orifice sizes. (a) $W_{or} = 100 \mu\text{m}$, (b) $W_{or} = 75 \mu\text{m}$, (c) $W_{or} = 25 \mu\text{m}$. $Q_{DP} : Q_{CP} = 10:80 \mu\text{L/hr}$, electric field is applied at the voltage of 500 V, frequency of 5 KHz. 118

Figure 6.12 Non-Newtonian droplet diameter dependency of the orifice size in terms of Ca . $Q_{DP} = 10 \mu\text{L/hr}$ 119

Figure 6.13 Effective capacitance model of the microchannel	120
Figure 6.14 (a) Comparison between the capacitance model and experimental data (25 μm orifice). $Q_{DP} : Q_{CP}$ is in $\mu\text{L/hr}$	123
Figure 6.15 (b) Comparison between the capacitance model and experimental data (75 μm orifice).....	123
Figure 6.16 (c) Comparison between the capacitance model and experimental data (100 μm orifice).....	124
Figure 6.17 Fluorescent imaging of non-Newtonian droplet formation via high speed μPIV . $W_{or} = 25 \mu\text{m}$. The scale bar indicates 25 μm . $Q_{DP} : Q_{CP} = 10:20 \mu\text{L/hr}$	126
Figure 6.18 Flow field of the non-Newtonian droplet formation in the squeezing regime ($Q_{DP} : Q_{CP} = 10:20 \mu\text{L/hr}$, no electric field applied).....	127
Figure 6.19 Vorticity of the dispersed phase during the droplet formation process in the squeezing regime ($Q_{DP} : Q_{CP} = 10:20 \mu\text{L/hr}$, no electric field applied).....	128
Figure 6.20 Flow field of the non-Newtonian droplet formation in dripping regime ($Q_{DP} : Q_{CP} = 10:80 \mu\text{L/hr}$, no electric field applied).....	129
Figure 6.21 Vorticity of the dispersed phase during the droplet formation process in the dripping regime ($Q_{DP} : Q_{CP} = 10:80 \mu\text{L/hr}$, no electric field applied)	130
Figure 6.22 Flow field of the non-Newtonian droplet formation in the dripping regime with AC electric field ($Q_{DP} : Q_{CP} = 10:80 \mu\text{L/hr}$, $V = 1 \text{ KV}$, $f = 1 \text{ KHz}$)	131

Figure 6.23 Vorticity distribution of the dispersed phase during non-Newtonian droplet formation with AC electric field in the dripping regime ($Q_{DP} : Q_{CP} = 10:80$ $\mu\text{L/hr}$, $V = 1$ KV, $f = 1$ KHz)	132
Figure 7.1 Experimental setup for visualizing single phase liquid crystal flow in nozzle-diffuser microchannels	137
Figure 7.2 Representative diagram of the microchannel.	139
Figure 7.3 Fringe patterns of 15° opening angle microchannel along diffuser and nozzle directions.	141
Figure 7.4 Fringe pattern characteristics along both diffuser and nozzle directions	143
Figure 7.5 Variation in fringe density as function of flow rates for opening angles	144
Figure 7.6 Variation in central fringe density as function of flow rate for various opening angles with flow along and against diffuser direction	145
Figure 7.7 Variation in central fringe density as function of flow rate for different opening angles with flow along and against nozzle direction	146
Figure 7.8 Flow recirculation fringe pattern for different opening angles	146
Figure 7.9 Variation of flow recirculation central positions in diffuser direction with flow rates for different opening angles	147
Figure 7.10 Variation of flow recirculation central positions along nozzle direction with flow rates for 15° opening angle	148
Figure 7.11 Critical Er number for different opening angles.....	149

Figure 8.1 Schematic diagram of the microchannel on liquid crystal droplet generation with AC electric field	152
Figure 8.2 Schematic diagram of the flow focusing microchannel.....	154
Figure 8.3 Layout and dimensions of the flow focusing microchannel with non-contact type of electrodes. DP, CP denotes the dispersed phase and continuous phase respectively.....	155
Figure 8.4 Time evolutions of the LC droplet formation	157
Figure 8.5 The time evolution of the LC droplet formation at higher flow rates.....	159
Figure 8.6 Dimensionless fringe density of the LC droplet versus dimensionless time.	160
Figure 8.7 Dimensionless fringe density of the droplet as the function of capillary number.....	161
Figure 8.8 Filament evolution for $Q_{DP} : Q_{CP} = 2.5:10 \mu\text{L/h}$	162
Figure 8.9 Dimensionless fringe number of the filament versus the dimensionless time	163
Figure 8.10 The LC droplet diameter as the function of Ca	164
Figure 8.11 Fringe patterns of the LC droplet with diverse electric fields. Applied voltage=500 V (p-p).	165
Figure 8.12 The dependency of the LC droplet diameter on the frequency of the AC electric field. The applied voltage=500 V (p-p).	166

List of Tables

Table 3.1 Fluid coefficient m and flow behavior index n for PEO aqueous solutions
.....56

Chapter 1 Introduction

1.1 Background and motivation

Microfluidics has attracted much attention due to its rapid development and promising applications in fields of bio-engineering, chemical industry [1-6]. Microfluidics can significantly lower cost as it requires small sample volume at the order of 100 nL. With the development of microfluidics, the concept of lab-on-a-chip was proposed. It integrates the sample preparation, transportation and analysis into a single chip. Micro-electromechanical systems (MEMS) technologies prompted micro scale system including the microfluidic systems, such as the complex microchannels for lab-on-a-chip experiments. The bio based applications typically involve transportation of the DNA samples and usually involve only minimal samples and short time scales, for which microfluidics are ideal.

The electro-osmotic driven method has various advantages as compared to the traditional pressure gradient driven method. The flow profile of the electro-osmotic driven method shows a plug flow, rather than the traditional parabolic flow. This indicates a lower shear rate in bulk flow, which causes less influence to the molecular structures within bio samples, such as the long-chained DNA molecules. Recently, the research on two or multi fluids electro-osmotic driven flow has gained enormous achievements. Interfacial control of the two fluids was reported to be controlled by the electro-osmotic method. The interfacial control forms the foundation for applications of sorting, separation and mixing [7-9]. However, most of the research carried out target the simple Newtonian flow, which exhibits a different flow behavior from that of bio samples, as most of the biological samples

are non-Newtonian fluids. The two or multi fluids electro-osmotic driven flow with a non-Newtonian fluid has to expand application to the biological fields.

Microfluidic droplet deals with the formation and the manipulation of discrete droplets in microfluidic environment. The impact of microfluidic droplets has been increasing as the properties, such as the fast generation rate and monodispersity with associated approaches for droplet sorting, splitting and merging making it suitable for biochemical processes like fast chemical reaction tests, bio genetic transportation and drug delivery. The fundamental concept of the droplet microfluidic, droplet formation, attracts our attention. Fast response droplet formation and the precise control of droplet sizes can be achieved via electric field applied in flow focusing microchannels where contamination can be avoided by non-contact electrodes. Much research has been carried out to investigate the dynamics responses of Newtonian fluids in the process of the droplet formation. However fluids in the aforementioned applications, such as DNA sample are the one with complex rheological behavior owing to the presence of long DNA chain structure, explaining the increase in attention of droplet formation process of non-Newtonian fluids in microfluidics.

Liquid crystals (LCs) are a group of non-Newtonian fluids whose orientations can be tuned via various stimuli. The optical pattern varies with the external pressure gradient such that LCs show distinct patterns under different flow conditions, making perfect conditions for optofluidic research [10, 11]. The flow confinement of LCs provided by microfluidics is flow visualization due to the refined control of flow conditions. The coupling of flow fields with molecular reorientations at micro scale to achieve a novel method for flow visualization has yet to be studied.

1.2 Objectives and scopes

Investigations on flow of non-Newtonian fluids in microchannels form the foundation of applications. The objective of the present study is to study the electro-osmotic driven flow of non-Newtonian fluids theoretically and experimentally, to investigate the droplet formation of both Newtonian and non-Newtonian fluids under an applied AC electric field and to develop a novel method for flow visualization in microfluidic environments.

The scope of the current study includes:

- (1) To study a single layered non-Newtonian fluid driven by the electro-osmosis in a rectangular microchannel theoretically and experimentally. To develop a two fluids model driven by electro-osmosis involving one layer of conducting non-Newtonian fluid and the other layer of non-conducting Newtonian fluid.
- (2) To investigate the dynamics of droplet formation under an applied electric field for both Newtonian fluids and non-Newtonian fluids in flow focusing microchannels. To understand the strategy of precise control of droplet size via varying the electrical parameters. To deepen the understanding of non-Newtonian filament break up process with the presence of AC electric fields.
- (3) To develop a novel flow visualization method based on the birefringence property of liquid crystals and the dynamic response of the liquid crystals' molecules to flow fields. Both single fluid flow in nozzle/diffuser microchannels and two fluids flow in flow focusing microchannels are to be visualized and analyzed.

Chapter 2 Literature Review

This chapter reviews the related literatures. The first part covers the fundamental aspects of electric double layer, electro-kinetic phenomena in microchannels. The following part covers electro-osmotic flow in non-Newtonian fluid. In the third part of this chapter, droplet formation including non-Newtonian droplet formation is present. Lastly, liquid crystal based optofluidic is reviewed.

2.1. Electric double layer

The concept of electric double layer (EDL) was first proposed by stern in 1924, by combining two models: the Helmholtz and the Gouy-Chapman models [12, 13]. Among Helmholtz was the first researcher found out the charged electrodes repels the co-ions and attract the counter-ions in the electrolyte solutions while Louis Georges Gouy (in 1910) and David Leonard Chapman (in 1913) found out that the charge distribution is a function of distance away from the metal plate. The EDL is formed due to the surface ion attraction. Ion charge appears on the surface of the substance when it is contacted with one polar medium due to the ionization, ion adsorption and ion dissolution (Figure 2.1). Influenced by the surface charge density, the ion with opposite charge will be attracted near the surface and the ion with same charge will be repelled away from the surface. Thus, the ion distribution changes near the surface. Far from the surface, the neutral ion distribution applies. As shown in Figure 2.2, the electric double layer (EDL) is mainly composed of the stern layer and the diffuse layer. The stern layer is a very thin layer (0.5nm) where the ions are strongly bounded by attraction force with no mobility. While the in the diffuse layer, the attraction force is not strong enough to bound the ions. The ions in this layer obtain the mobility and spread out due to the thermal energy. The thickness usually

varies from several to hundreds of nanometers resulting from the ionic concentration, PH value, surface properties as well as the fluid properties.

The zeta potential ψ is defined as the electric potential at the shear plane, which is an assumed plane between the stern layer and the diffuse layer. The fluid between the wall and the shear plane remains stationary (as shown Figure 2.1 and Figure 2.2).

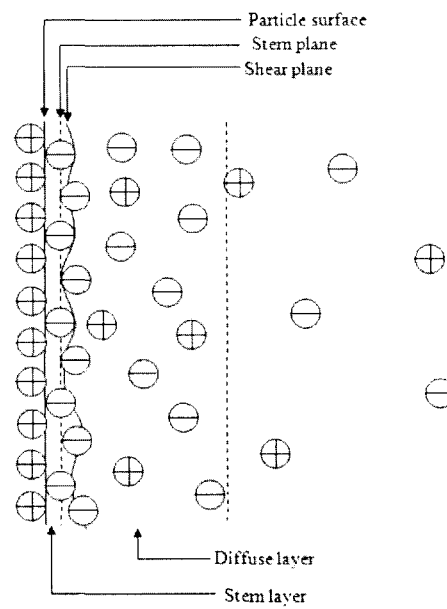


Figure 2.1 Schematic diagram of ion distribution near the contact surface [12]

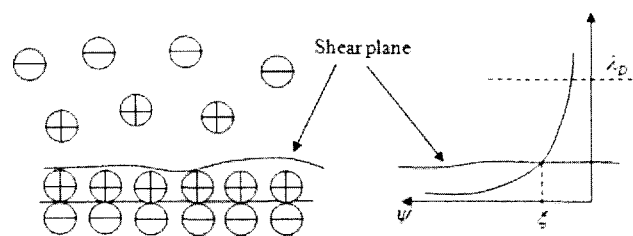


Figure 2.2 Schematic diagram of the EDL structure [14]

Under the influence of the EDL, the overall charge density ρ_e within the diffuse layer is not zero. When an electric field is applied along the surface, the ions in the diffuse layer move and hence drag the bulk fluid to flow. Since the diffuse layer is

thin, a plug-shape velocity profile is generated. The flow generated by the applied electric field and the EDL is called the electro-osmotic driven flow.

2.2. Electro-kinetic phenomena

Electro-osmosis is one of the four types of electro-kinetic phenomena. The four types are electrophoresis, electro-osmotic, streaming potential and sedimentation potential [12]. Electrophoresis and sedimentation potential describe the particle behavior immersed in quiescence fluid while electro-osmotic and streaming potential describe the motion that the flow of a fluid pass by a stationary charged surface. They can be divided into two groups depending on whether an external electric field is needed. For electrophoresis and electro-osmotic an external electric field is applied to drive the particle or fluid. While for sedimentation and streaming potential, an electric field is generated due to the movement of the charged particle or the fluid with non-zero electric density.

2.2.1 Measurement of electro-osmotic velocity

Various methods have been proposed to measure the electro-osmotic velocity [12, 15, 16]. Theoretical predictions of the electro-osmotic velocity in microchannel have been studied [12, 17-19]. Various channel shapes were presented, such as the slit channel [20], rectangular channel [18, 21], cylindrical channel [22, 23], irregular channel [24], and arbitrary shaped channel [25]. Experimental methods can be classified into two types: the indirect and direct method.

One of the indirect methods is the current monitoring method as shown in Figure 2.3 [26-29]. It utilizes two solution with the same electrolyte and different ionic concentrations, c_1, c_2 ($c_2 > c_1$). Reservoir 1 and the microchannel are initially filled

with a lower concentration c_1 and reservoir 2 is filled with a higher concentration c_2 . After an external electric field is applied along the microchannel, the solution of high concentration c_2 from reservoir 2 displaces the solution of low concentration c_1 cause the flow towards the reservoir 1. By monitoring the change of electric current in the microchannel, the displacement time t_{\max} can be measured, hence the average electro-osmotic velocity can be determined by $u = (L_{\text{channel}} / t_{\max})$ where L_{channel} is the length of the microchannel.

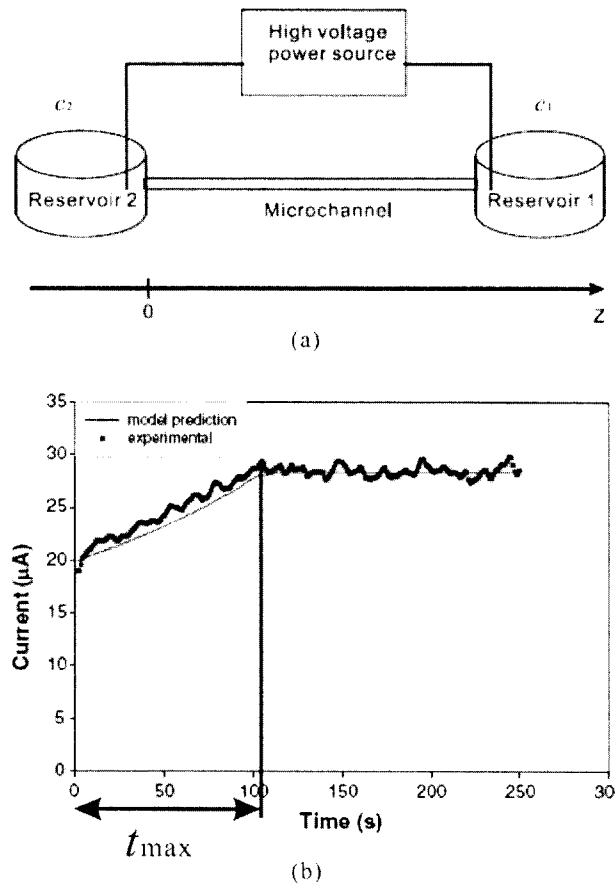


Figure 2.3 Indirect EDL measurement method [29]

The direct method uses fluorescent dye for flow field visualization. The position of the dye can be captured at specific time. By comparing the dye positions at different times, the whole velocity field can be visualized. The best known direct

measurement method is the Micro-scale Particle Image Velocimetry (μ PIV) technology as shown in Figure 2.4 [30].

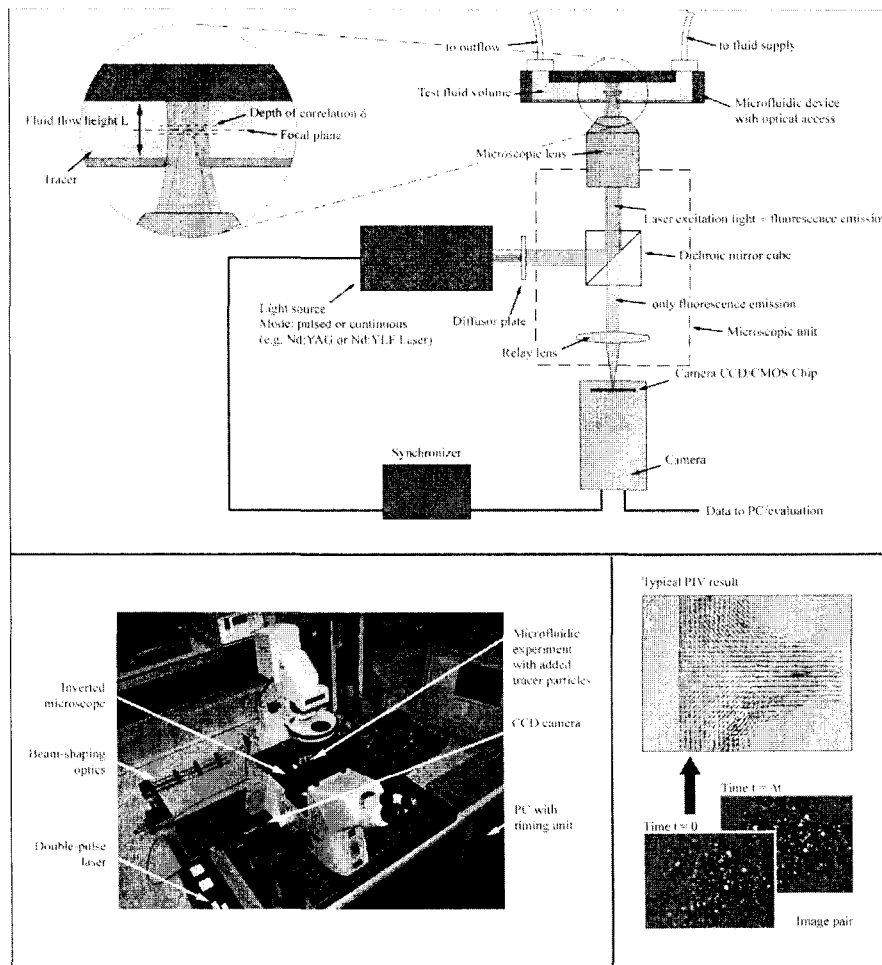


Figure 2.4 Schematic diagram of a μ PIV setup. [30]

2.2.2 Zeta potential

The zeta potential is an important parameter to characterize the electro-kinetics effect. The electric potential distributions including the characteristics of zeta potential have been studied extensively. Yang *et al.* (Figure 2.5) [18, 21] studied the forced liquid convection in rectangular microchannels with electro-kinetic effects. The electrical potential distribution is obtained by solving the Poisson-Boltzmann equation both analytically and numerically. The electric potential distribution in the overlapped EDL region, which cannot be described by the classic Poisson-Boltzmann equation,

was investigated by Qu *et al.* [31]. A new governing equation was derived, the result indicates a lower electrical potential than that calculated by the classic theory.

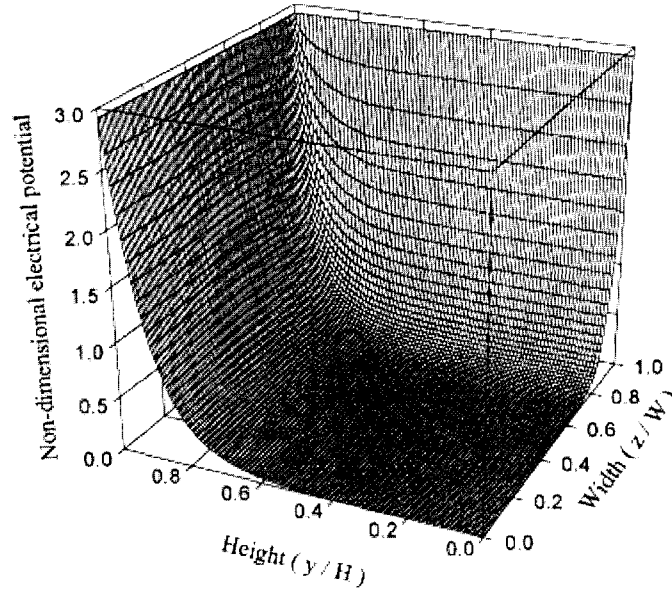


Figure 2.5 Non-dimensional electrical potential profile in one quarter of a rectangular microchannel (geometric ratio of height to width=2/3, non-dimensional electro-kinetic diameter $K=24.7$) [18]

The value of zeta potential holds the significant impact [32] on applications such as electro-osmotic driven flow [33, 34], electrophoresis related particle moving [35], membrane characteristics [36, 37] and biomedical polymer features. The indirect measurement method provides the relation between the electric field, zeta potential and flow or particle velocity. Three electro-kinetics phenomena, electrophoresis, streaming potential and electro-osmotic, can be utilized to measure the zeta potential [32].

Electrophoresis can be used to determine the zeta potential as the particle moves under an external electric field [28]. The zeta potential of the interface can be evaluated by the Smoluchowski equation: $\nu_E = 4\pi\epsilon_0\epsilon_r \frac{\psi}{6\pi\mu} (1 + \kappa r_p)$, where ν_E is the mobility of the particle, ϵ_0 , ϵ_r are the electric permittivity of vacuum and the relative

electric permittivity, μ is the fluid viscosity, κ is the Debye-Hückel parameter [38], r_p is the radius of the particle and ψ is the zeta potential [12].

Similarly, in streaming potential, the relation between pressure gradient and the induced electric field is: $\frac{E_s}{\nabla P} = \frac{\varepsilon_0 \varepsilon_r \psi}{\mu (\lambda_b + 2\lambda_s / h)}$, where E_s is the streaming potential, ∇P is the pressure gradient, $\varepsilon_0, \varepsilon_r$ are the electric permittivity of vacuum and the relative electric permittivity respectively, μ is the fluid viscosity, ψ is the zeta potential, λ_b and λ_s are the bulk conductivity and surface conductivity, h is the height of the microchannel. The disadvantages lie in the issues of measuring the surface, bulk conductivity and the streaming potential [39-42].

Electro-osmotic driven velocity in a microchannel can be used to calculate the zeta potential using $u_E = \frac{\psi \varepsilon_0 \varepsilon_r}{\mu} E$ [32]. Once u_E velocity is measured, the zeta potential can be calculated. Among the three measurement techniques, electro-osmotic is easier to implement [43].

2.3. Electro-osmotic based applications

2.3.1 Electro-osmotic pump

The electro-osmotic (EO) pump utilizes the electro-osmotic force as the driven force [44-47]. The EO pump can be cataloged as: direct, indirect and hybrid type.

The direct EO pump can be divided into directing current (DC) and alternating current (AC). The direct DC EO pump gains its advantages mainly in velocity profile. As EDL is thin, the velocity profile is a plug like profile, no shear is experienced in most of the fluid, which is good in transporting fluids with large molecular weight,

long-chain biofluid (blood, DNA). Chen *et al.* [48] designed an EO pump using the monolithic silica with a stall pressure of 400 kPa. However, its disadvantages include: bubbles generated from the fluid and a relatively high electric field which is required to drive the flow [49]. The AC EO pump can be used to drive the fluid due to the asymmetrical electrodes (Figure 2.6) [50]. The AC EO pump can be operated at a lower voltage, usually smaller than 10 V [51, 52].

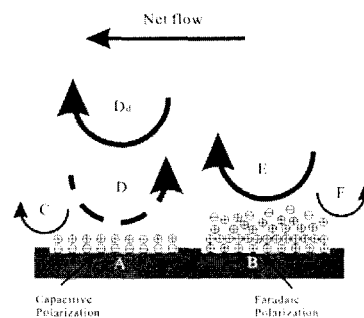


Figure 2.6 Working principle of AC EO pump [50]

In indirect EO pump, the electrodes are separated by some barriers from the conducting buffer. When the indirect EO pump operates, the ions can pass the barriers from surface of the electrodes to bulk fluids, but the fluids cannot pass through the barriers [45].

The idea of the hybrid EO pump is to use a conducting fluid to drive another non-conducting fluid (Figure 2.7). The conducting fluid is to be driven by the direct EO pump mechanism and the non-conducting fluid is to be dragged by the interface shear [53, 54]. Gao *et al.* [55] presented both numerical and mathematical models to describe a two-fluid electroosmotic pump technique.

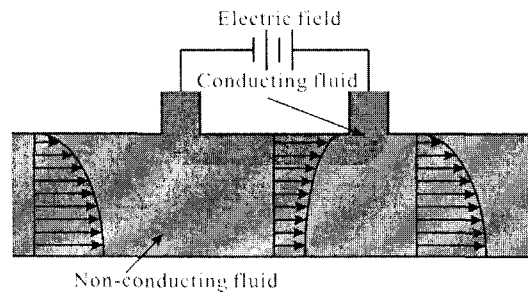


Figure 2.7 Working principle of hybrid EO pump [54]

2.3.2 Control of the fluid-fluid interface

The electro-osmotic based interface control for two or multi immiscible fluids has been investigated extensively [55-58]. Wang *et al.* [29, 59] showed that the location of the interface can be controlled by the combined effect of pressure and electro-osmotic driven method (Figure 2.8).

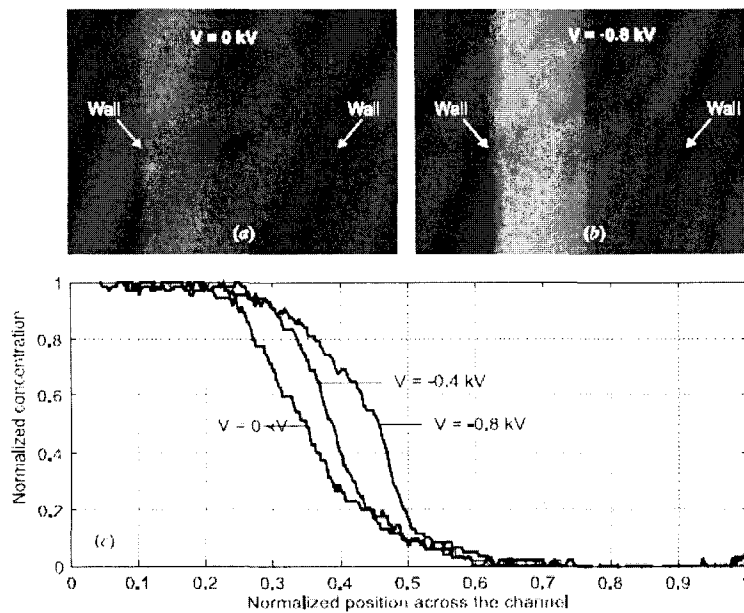


Figure 2.8 Fluid-fluid interface controlled by the combined effect of pressure and electro-osmotic driven method: (a) no electric field; (b) under -0.8 kV; (c) normalized concentration distribution of the fluorescent dye across the channel width under different applied voltages.[59]

Flow switching is an extension of the control of fluid-fluid interface: as the interface can be located precisely, the fluid sample can be guided into the desired outlets. A simple analytical model, flow-rate-ratio method was proposed to evaluate the switching performance [60]. Figure 2.9 shows the experimental results of flow switching.

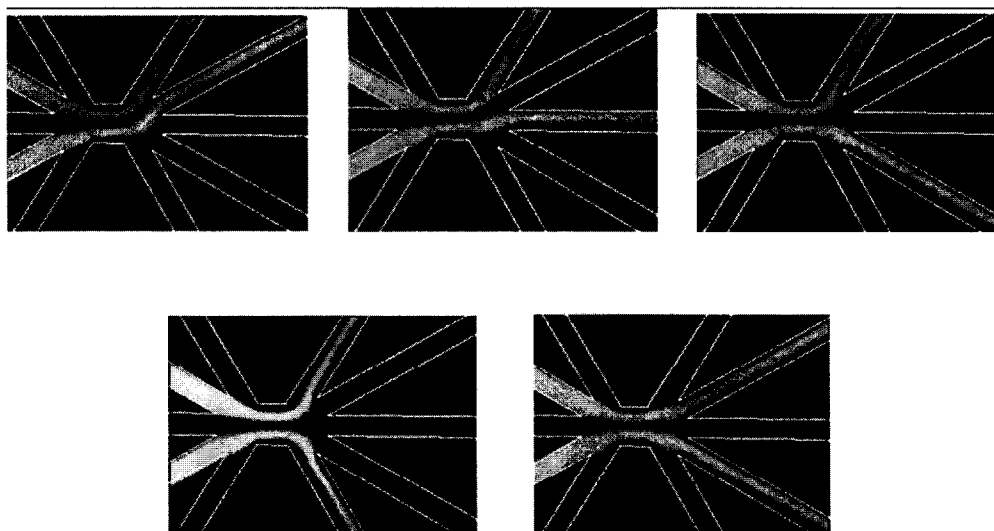


Figure 2.9 Experimental results of flow switching [61]

2.4. Fluids properties of non-Newtonian fluids

Generally the non-Newtonian fluid can be classified as:

1. Time independent non-Newtonian fluids. The shear stress is independent of the history of the shear rate but depends only on the current value of shear rate (the pressure and temperature are certain).
2. Time dependent non-Newtonian fluids. The shear stress does not only depend on the current value of the shear rate, but also the shear rate variation history.

3. Visco-elastic non-Newtonian fluids. Unlike the ideal Newtonian fluid, the visco-elastic obtains partial viscous of the ideal fluid and partial elastic of solid, which allows the fluid to partially recover from deformation.

This report focus on the time-independent fluid.

2.4.1. Time-independent non-Newtonian fluid

Figure 2.10, shows an overview of basic relationship between shear rate and shear stress for fluids subjected for shear deformation.

The time-independent fluid can further classified as: shear thickening (Dilatant), shear thinning (Pseudo plastic), Bingham plastic, Yield pseudo plastic.

For non-Newtonian fluids, the relationship between shear rate and shear stress is not linear. A shear rate dependent viscosity is presented, termed as the apparent viscosity.

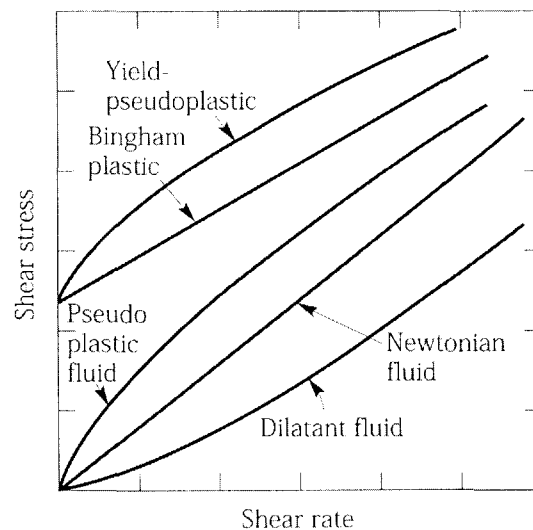


Figure 2.10 Schematic diagram for the time-independent fluid [62]

2.4.2. Shear thinning fluid

Most common type of time-independent non-Newtonian fluid is a shear thinning fluid whose apparent viscosity decreases with the increase of the shear rate, as shown

in Figure 2.11. The apparent viscosity at very low and high shear rate are known as the zero shear viscosity μ_0 and infinite shear rate viscosity μ_∞ . From μ_0 to μ_∞ , the shear stress-shear rate generally follows a linear relation. It's difficult to measure the infinite shear viscosity μ_∞ . For example, the polymer solution which contains long chains of molecular will face the degradation problem under high shear rate.

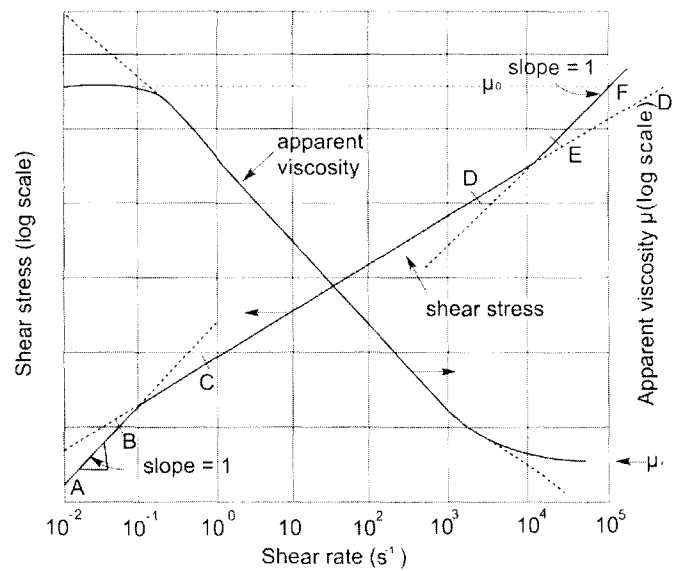


Figure 2.11 Shear thinning fluid properties [62]

There is no unique model that can describe the behavior from the low shear rate (10^{-2} s^{-1}) to high range (10^5 s^{-1}) perfectly. Therefore, there are several mathematical models presenting the shear stress and shear rate relation within limited scope.[63-67]

The power law or Ostwald de Waele model [63-65]

The power law model is particularly popular because of the number of exact solution which can be obtained from this model. It can be written:

$$\mu = m |\dot{\gamma}_{yx}|^{n-1} \quad (2.1)$$

$$\tau_{yx} = \mu \dot{\gamma}_{yx} \quad (2.2)$$

For $n < 1$, it describes the shear thinning fluid;

$n=1$, it represents the Newtonian fluid;

$n>1$, it shows the shear thickening fluid.

It is a two-parameter constitutive law, where m and n are fluid consistency coefficient and flow behavior index respectively. The model cannot describe the zero shear viscosity μ_0 and the infinite viscosity μ_∞ . It also means the model is not validated among all the shear rate range.

The Carreau viscosity model [66, 67]

This model considers the zero and infinite shear viscosity , μ_0 , μ_∞ respectively.

$$\frac{\mu - \mu_\infty}{\mu_0 - \mu_\infty} = \{1 + (\lambda \dot{\gamma}_{yx})^2\}^{(n-1)/2} \quad (2.3)$$

This model expands the limitation of usage by incorporating μ_0 and μ_∞ , which also makes the model more complicated.

2.4.3. Shear thickening fluid

The apparent viscosity increases with shear rate increase. Although the shear thickening fluid is not as widespread as the shear thinning fluid, some typical examples were found when dealing with high solid fluids (Figure 2.12).

The power law model is also capable of describing the shear thickening behavior.

When $n > 1$, Eq (2.1) and (2.2) represent the shear thickening property.

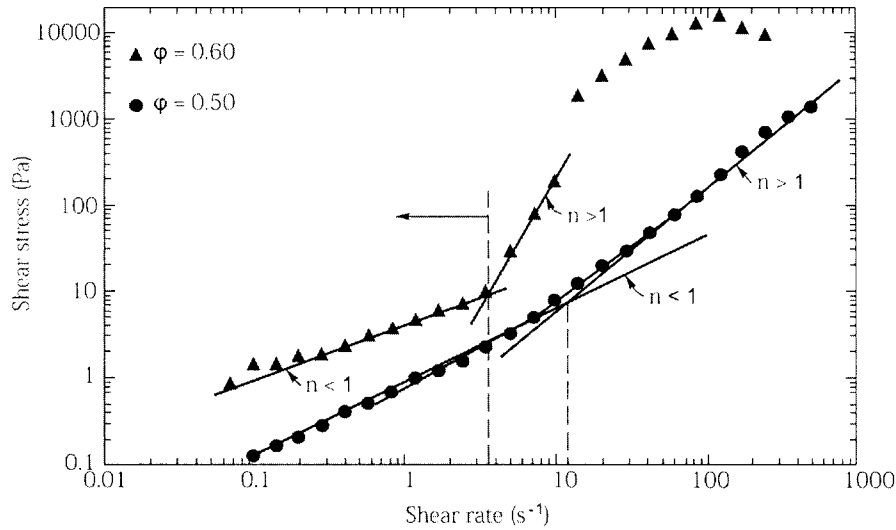


Figure 2.12 Shear thickening fluid properties [68]

2.5. Electro-osmotic in non-Newtonian fluids

2.5.1 Theoretical approach

Non-Newtonian fluids are known for its complex fluid behavior. Most of the electro-osmotic (EO) related research bears one common condition, that the fluid is a simple Newtonian fluid. Limited work has been carried out on non-Newtonian fluid. Currently, theoretical research of non-Newtonian fluids on microsystem for biotechnology mainly concentrates on polymer solution, with which the bio-sample behaviors similarly [69, 70]. Das and Chakraborty [71] firstly derived a analytical model for electro-osmosis of non-Newtonian fluids in parallel plate. By utilizing the Poisson-Boltzmann equation, momentum and energy equations, the velocity profile and temperature distribution are obtained for the power law non-Newtonian fluid. Zhao and Yang [72, 73] derived an exact solution for a single layer EO driven flow of power law non-Newtonian fluids with a symmetrical EDL condition in a slit microchannel (Figure 2.13). The flow behavior index n and the Debye-Hueckel parameter κ were investigated. The mathematical model was furthered expanded by

indicating the Gouy-Chapman solution to the Poisson-Boltzmann equation and applying the Carreau fluid constitutive model [74]. The non-linear ordinary equation was solved numerically and a more general model is obtained. The results showed that the Carreau fluid model performs well. Vasu and De [75] expanded the single layer power law fluid model by solving the EDL potential distribution at a higher zeta potential, upon which the Debye Hueckel linear approximation is no longer valid. The possibility of using pseudoplastic fluid to achieve higher flow rate was presented.

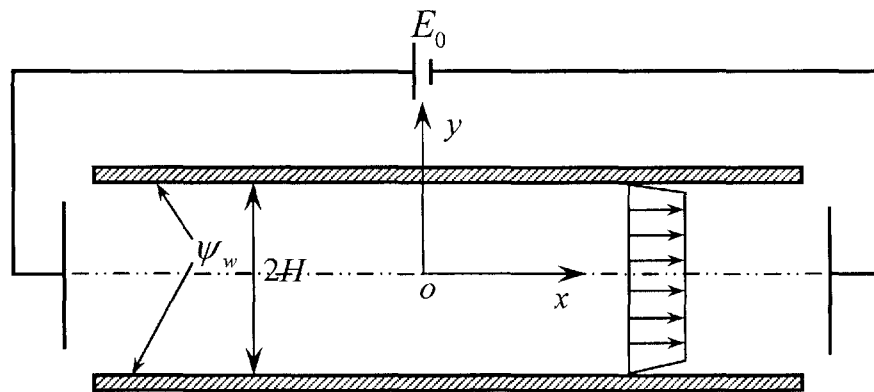


Figure 2.13 Schematic diagram for a single layer EO driven power-law fluid [72]

Berli and Olivares developed a analytical model to simulate the EO flow of non-Newtonian fluids through slit and cylinder microchannel [69, 70]. Calculation are based on constitutive models of the fluid viscosity and take into account the wall depletion effects of the polymer solution. The output pressure and EO pumping energy efficient were also exploited [76]. Khair *et al.* [77] proposed a analytical model to calculate the coupling effect of the electrophoretics and rheology. The charged colloidal particles are immersed in the shear rate dependent viscosity non-Newtonian fluids. The model presents the general results of particles influenced by the coupling effects. Li, *et al.* [78] derived a model for N layers of immiscible flow under the electro-osmotic and pressure gradient driven respectively. The N-layer

pressure driven power law fluid is considered and compared with that of the Newtonian fluid.

Besides those studies of inelastic non-Newtonian fluids, investigation on the viscoelastic non-Newtonian fluid can be found. Afonsoa, *et al.* [79] obtained analytical solutions for viscoelastic non-Newtonian fluid via incorporating the Debye–Hückel approximation, simplified Phan-Thien–Tanner model (sPTT) and the FENE-P model. Velocity distributions of the non-Newtonian fluid were presented under the combined effect of fluid rheology, electro-osmotic and pressure gradient.

Dhinakaran *et al.* [80] investigated the EO driven viscoelastic model in a slit microchannel via the Phan-Thien-Tanner model. The maximum electrical potential to be utilized to maintain the steady state flow is then proposed in the work.

2.5.2 Numerical investigation

Ahmed [81] studied forced convection heat transfer for non-Newtonian power law fluids in a rectangular duct with an external magnetic field. The solution is obtained via the finite difference method. Two different boundary conditions are considered: constant wall temperature and constant heat flux. Cho, *et al.* [82] numerically modelled the flow of electro-kinetically driven non-Newtonian fluid in rough microchannels with complex-wavy surface (Figure 2.14). The results show that the flow behavior index has significant impact on the flow characteristics such as the volume flow rate. The flow near the wall is more sensitive to the roughness than that in the center of the channel.

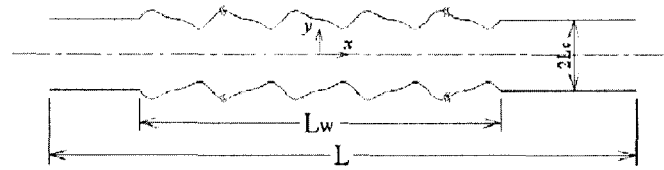


Figure 2.14 Schematic illustration of rough microchannel with complex-wavy surface.[82]

The electro-osmotic driven Carreau non-Newtonian fluid in a T junction was simulated by Craven, *et al.* [83]. The simulation was conducted via the finite element method. The Carreau fluid parameters were discussed. Hadigol *et.al* [84] studied the flow of biofluids within a microchannel (Figure 2.15). The biofluid is driven by the asymmetrical zeta potential. The finite volume method was adopted in the numerical investigation. The results show that the shear dependent viscosity has a great impact on the mixing efficiency.

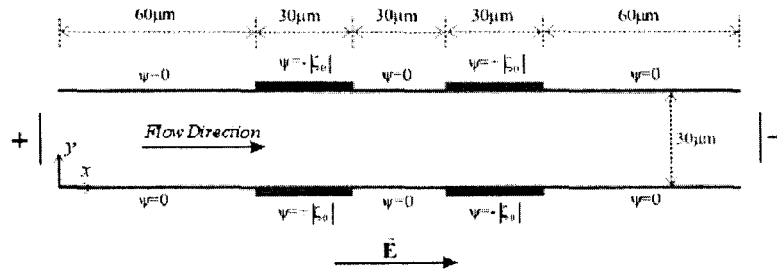


Figure 2.15 Microchannel with height of 30 μm and length of 210 μm . [84]

Wang and Ho [85] utilized a novel lattice Boltzmann method to investigate the shear-thinning non-Newtonian blood flows described by the power-law, Carreau–Yasuda and Casson rheology models. The results give a second order accuracy and provide a new numerical method for simulating the flow of complex fluids.

The numerical study of Carreau non-Newtonian behavior in a T junction was carried out by Zimmerman *et al.*[86]. A two-dimensional finite element model was developed to simulate the electro-kinetic flow. This research simplified the EDL

characteristics by rendering a slip velocity at the boundary. The flows near corners were investigated.

2.5.3 Experimental investigation on non-Newtonian fluids

Pipe and McKinley [87] studied the rheological behavior of non-Newtonian phenomena at micro-scale. The rheologist characteristics were measured and discussed in both shear and extensional flows. Other flows including capillary, stagnation and contraction were presented. Juang *et.al.* [88] conducted experiments on the electrokinetic-induced stagnation flow in a cross microchannel. Two dimensional elongation flow is observed. It is found that the DNA molecules and the residence time are greatly affected by the extend of DNA stretching. The simulation results match reasonably well with those in the experiments. Steinhaus *et al.* [89] tested the effects of the fluid elasticity and channel dimension. Different molecular weights of poly ethylene oxide solutions along with different geometry settings were investigated. Various time scales such as the Rayleigh time, viscocapillary Tomotika time and the polymer relaxation time were presented. Key dimensionless numbers including the elasticity number, elastocapillary number and Deborah number were investigated. The influences of the parameters of molecular weight, elastocapillary and Deborah number were observed in the experiments. Sousa *et.al.*[90] also performed the experiments on rectification effect of the viscoelastic. Two types of polymer solutions: polyacrylamide and polyethylene oxide with different molecular weights were adopted for experiments while the rectification effect is successfully observed for the non-Newtonian viscoelastic fluid.

Blood is one of the most important bio-fluids, and is fundamental in bio-medical research. Zeng and Zhao [91] investigated the measurement of blood sample

rheological features under different flow conditions. Their major focus was the electrical behavior of blood samples and the measurement was obtained by utilizing the electrical impedance spectroscopy, through which the blood viscosity can be obtained. This approach is potentially capable of healthy monitoring, providing an easy method for blood sample testing.

2.6. Droplet microfluidics

2.6.1 Droplet formation

In application of droplet microfluidics, the fundamental process is the formation of various droplets such as droplets with high monodispersity, size of sub micro level, complex emulsion systems and high frequency generation [92-96]. The microchannel geometries utilized for droplet generation can be generally classified into two major types: cross microchannel also known as T junction and flow focusing microchannel [97-99]. The generation procedure can also be labelled as passive or active method.

Droplets generated by T junction microchannel

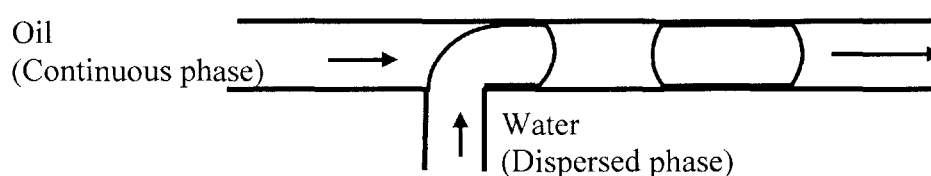
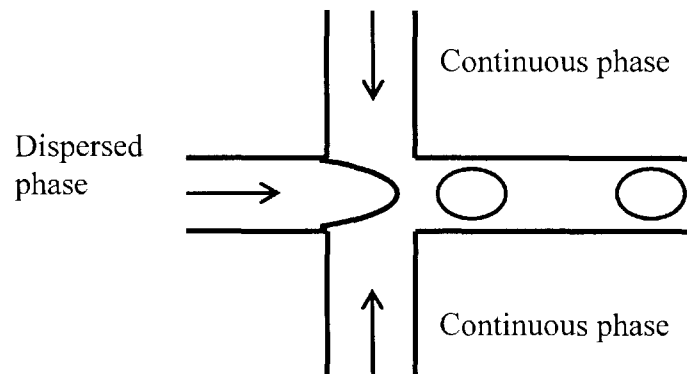


Figure 2.16 A T junction for generation of droplets

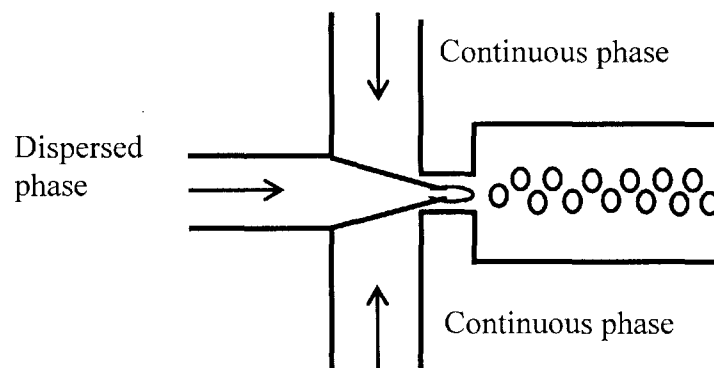
As shown in Figure 2.16, two immiscible phases, continuous phase (CP) and dispersed phase (DP) are introduced separately into a microchannel. The continuous phase is introduced through the main channel while the dispersed phase is introduced through the side channel. The competition between interfacial tension and viscous stress results in three regimes of droplet formation: squeezing, dripping and jetting

[94, 98, 100-102]. The size of the droplet produced depends on the flow rates of CP and DP, viscosity of CP which influences the shear stress, interfacial tension and channel geometries. Capillary number (Ca) is an important factor influencing the process of droplet formation. Ca characterizes the effect between viscous force and surface tension. Squeezing and dripping regimes were found by Menech [103]. Under low Ca where squeezing happens, the emerging droplet blocks the flow of the CP. The hydrodynamic pressure builds up on the upstream of the emerging droplet and pinches off eventually. Garstecki reported that the pressure gradient is the dominating factor in squeezing regime rather than the shear stress in the dripping regime [100].

Droplet formation in flow focusing microchannel



(a) Normal flow focusing geometry



(b) Flow focusing geometry with orifice

Figure 2.17 Schematic diagram for flow focusing geometry

Figure 2.17 shows the geometry for flow focusing geometry. The dispersed phase is introduced into the middle channel, while the continuous phase is introduced symmetrically from the side channels [104, 105]. The formation of monodispersed droplet generation has been reported [99, 105-107]. The flow focusing geometry with an orifice placed at a distance for the inlet is also proposed. Depending on the flow and geometrical parameters, the interaction of the fluids results in the breakup of the dispersed phase into droplet. The interplay of the viscous force and the interfacial tension results in the distinct formation regimes [108]. The research shows that the capillary number and Weber number are important parameters that can influence droplet formation process and droplet size [109, 110]. Capillary number of flow focusing junction with an orifice place at a distance from the inlet is given as:

$$Ca = \frac{\mu_c Q_c w_D}{2\sigma h \Delta z} \left[\frac{1}{w_{or}} - \frac{1}{2w_c} \right] \quad (2.4)$$

Where μ_c , Q_c , denotes the dynamic viscosity and the flow rate of continuous phase. w_D , w_c , and w_{or} are the width of dispersed phase, continuous phase and orifice respectively. σ , h shows the interfacial tension and the distance from the end of the inner microchannel to the entrance of the orifice. Δz is and the height of the microchannel [108].

Chapter 2 Literature Review

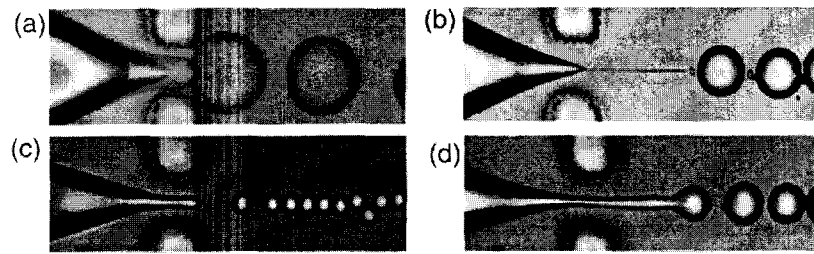


Figure 2.18 Four regimes of droplet formation. (a) squeezing, (b) thread forming, (c) dripping and (d) jetting.[108]

For a small value of Ca , droplets form in squeezing regime. The emerging interface of the dispersed phase fluid squeezes through the orifice and blocks the flow. The pressure drop of the continuous phase across the orifice squeezes the dispersed phase at the neck and causes the tip of the dispersed phase to break up. The regime shifts to dripping via increasing Ca . When Ca is large enough, the flow rate of the dispersed phase is insufficient for droplet formation and the dispersed phase is pushed downstream where the droplet is finally generated at the tip [111]. Hence in this regime, the neck is stabilized by the outer flow, causing it to elongate further downstream, away from the orifice.

Electric field controlled droplet formation

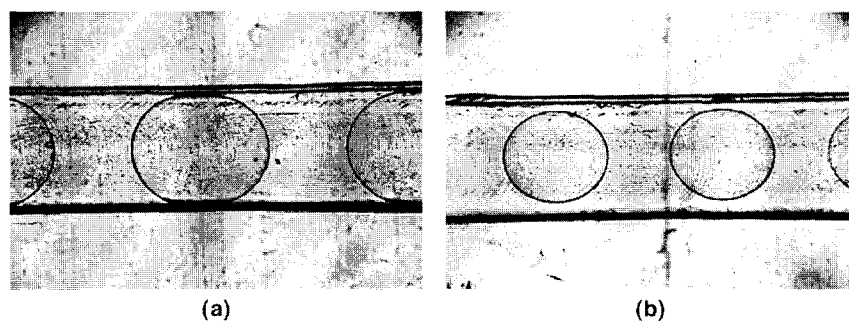


Figure 2.19 Droplet formation under applied electric field. Corn oil and glycerine flow rates are 0.27 $\mu\text{L/s}$ and 0.75 $\mu\text{L/s}$, respectively.[95]

Ozen, *et. al*, proposed the monodisperse droplet formation in square microchannels, where the electrohydrodynamic instability of the interface is used, as shown in

Figure 2.19. Droplet size can be adjusted via the flow rates applied and the electric field strength across the microchannel [95].

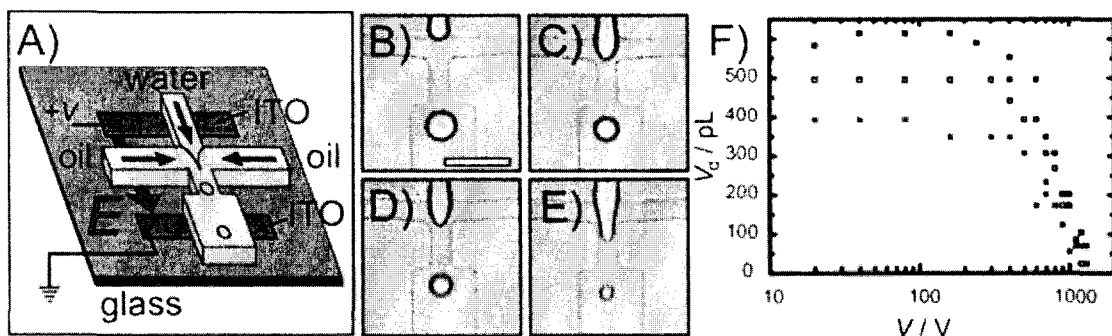


Figure 2.20 Electric field controlled droplet formation. (A) microchannel setup, (B), (C), (D), (E) shows the droplet formation under the voltage of 0 V, 400 V, 600 V, 800 V, respectively. (F) Droplet size as a function of voltage. [112]

Methods of adopting both contact and non-contact type of electrodes in flow focusing microchannel were reported in success of droplet formation control [112, 113]. Figure 2.20 shows the results of droplet control via DC electric field. The electrode was fabricated by patterned ITO coating on the glass plate. While the non-contact type of electrode in AC electrode adopted in droplet formation of flow focusing microchannel was also reported [113].

Temperature field controlled droplet formation

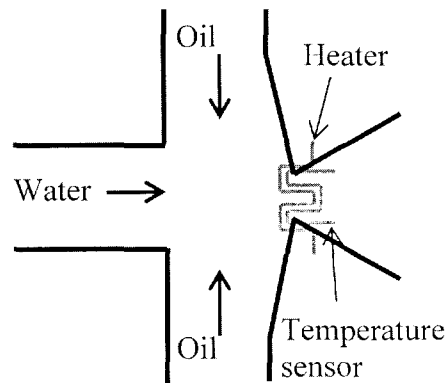


Figure 2.21 Temperature controlled droplet formation in flow focusing microchannel. [114]

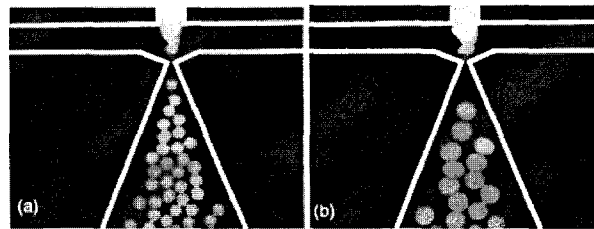


Figure 2.22 Droplet formation with (a) heater off and (b) heater on. [114]

The droplet formation controlled by temperature field was also reported [114]. Figure 2.21 depicts the microchannel setup. The design used a flow focusing microchannel imbedded with a microheater at the cross junction region. Figure 2.22 shows the results without and with temperature control respectively. The interfacial tension between the two fluids is directly related to local temperature. By varying the interfacial tension, the droplet size can be controlled.

Magnetic field controlled droplet formation

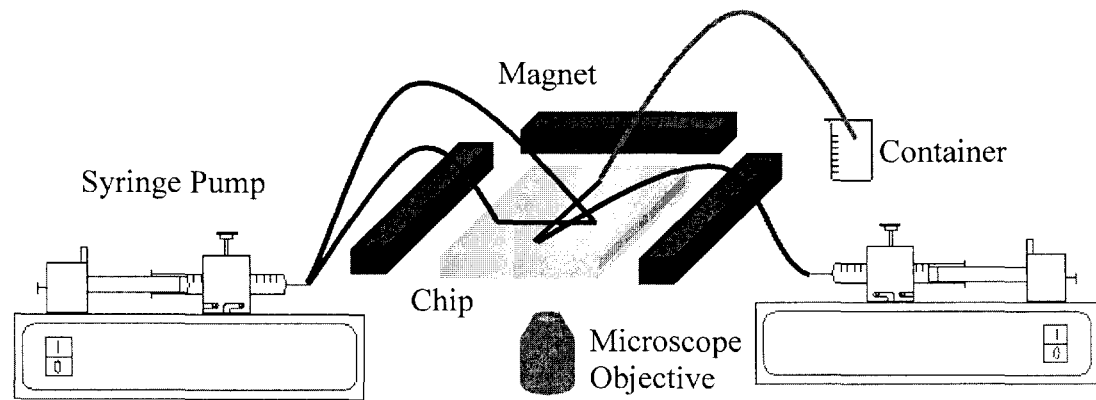


Figure 2.23 Magnetic field controlled droplet formation in microchannles. [101]

Tan *et al.* studied the dependency of magnetic polarity, flux strength and the orientation to ferrofluidic droplet production in both T-junction and flow focusing junction configurations [101]. The experimental setup is presented in Figure 2.23. As a result of the alignment of magnetic nanoparticles in the direction of magnetic field, this delays the necking process and the droplet formation. Droplet size increased with the increase of magnetic flux as shown in Figure 2.24.

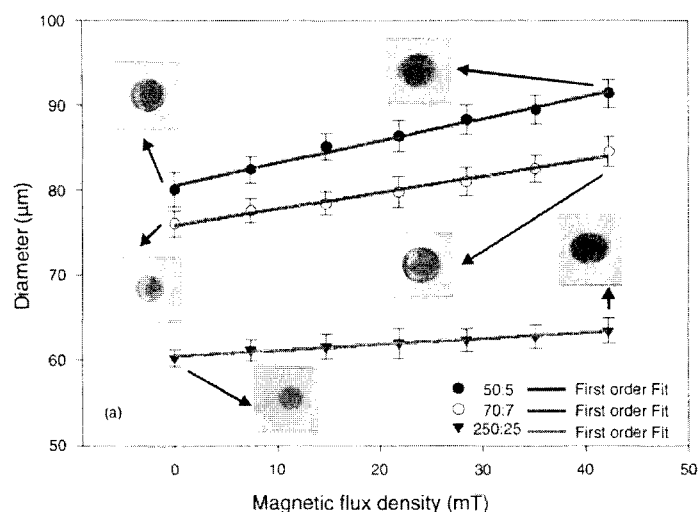


Figure 2.24 The dependency of droplet size to magnetic flux in flow focusing configuration. [101]

2.6.2 Non-Newtonian droplet formation

The breakup dynamics of non-Newtonian droplet formation in a T-junction microchannel has been investigated by Husny and Cooper White [115]. The appearance of thin filaments during the droplet production is caused by the elastic properties of the non-Newtonian fluid. The necking process is classified into two regions, the pre-stretch and exponential self-thinning region, as shown in Figure 2.25. In the pre-stretch region, the droplet is in the necking region and accelerated away from the cross junction, as a result of interfacial tension, viscous force and elastic force. In the self-thinning region, the filament does not experience further extension and necking is influenced by the interfacial tension and elastic force. Besides the two distinct regions, numerous tiny beads develop along the filament termed as beads on the string was observed. The migration and coalescence of these tiny is known as the iterative stretching. The splitting phenomena of PEO droplet (a type of non-Newtonian droplet) is observed by Christonpher and Anna at a lower capillary number [116].

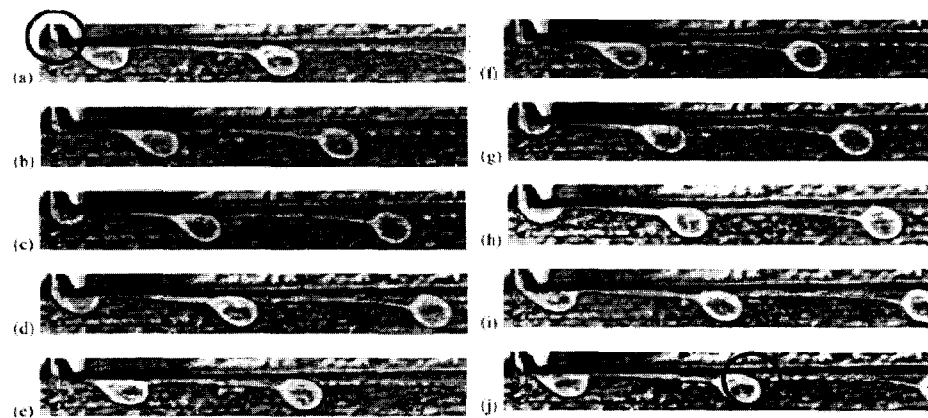


Figure 2.25 (a)-(d) Pre-stretch region, (e)-(j) exponential self-thinning region of non-Newtonian droplet formation in a T junction microchannel. The interval between each image is 2.5 ms. [115]

The dynamics of the filament length at break up and the break up time are a function of the polymer relaxation time and the flow rate. Generally larger molecular weight of the inherent microstructure and higher flow rate of the continuous phase leads to a longer filament length at breakup.

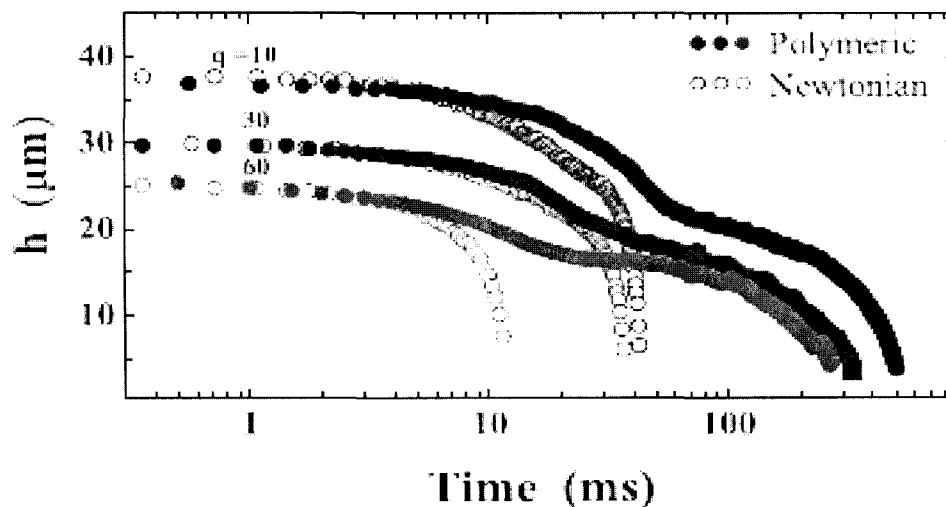


Figure 2.26 Filament thickness versus time for both Newtonian and non-Newtonian fluid. The flow rate ratio is kept at 10, 30 and 60.[117]

The filament thinning behaviour is illustrated in Figure 2.26. The initial stage of thinning is similar for both Newtonian and polymeric fluids. After the filament is stretched to a certain extent, the thinning rate of polymeric fluids is slower than that of the Newtonian as a result of the elasticity of the fluids [117]. Polymeric fluids with higher molecular weight exhibit a slower thinning rate of the filament due to higher elastic stress (Figure 2.27) [118].

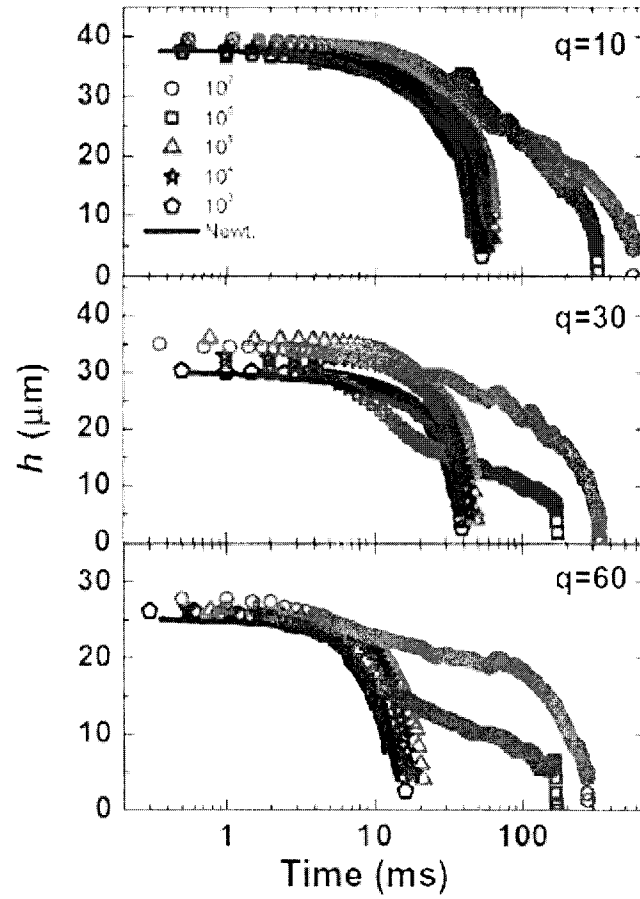


Figure 2.27 Filament thickness versus time as a function of molecular weight of the non-Newtonian fluids. Three flow rate ratio, 10, 30, and 60 are considered. [118]

2.7. Liquid crystals based optofluidic

Liquid crystals (LCs) are a group of materials as it can exhibit intermediate state between solid crystalline and isotropic fluid phase. LCs have the ordering properties of solids but they flow like liquids.

LCs can generally be classified into two major types, lyotropic and thermotropic, depending on their composition. Lyotropic LCs consist surfactant which has the polar and non-polar parts. The phase behavior of lyotropic LCs are influenced by both the chemical concentration and temperature of solvent. On the other hand, thermotropic LCs are widely used. In this report, thermotropic LCs are adopted in the experiment.

2.7.1 Thermotropic liquid crystal

Thermotropic LCs can be further divided into two types: calamitics (rod-like) and discotics (disc-like), as shown in Figure 2.28.

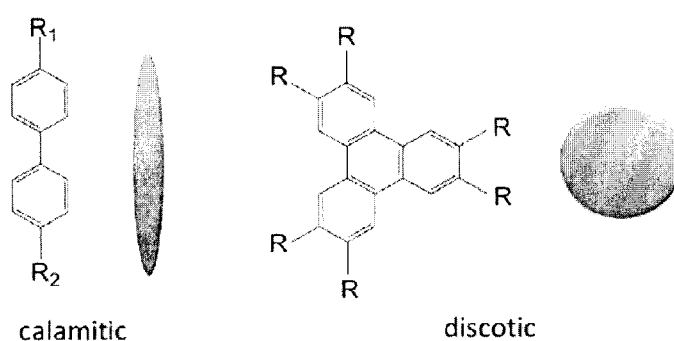


Figure 2.28 Representative diagram of calamitic and discotic liquid crystal micro structure [119]

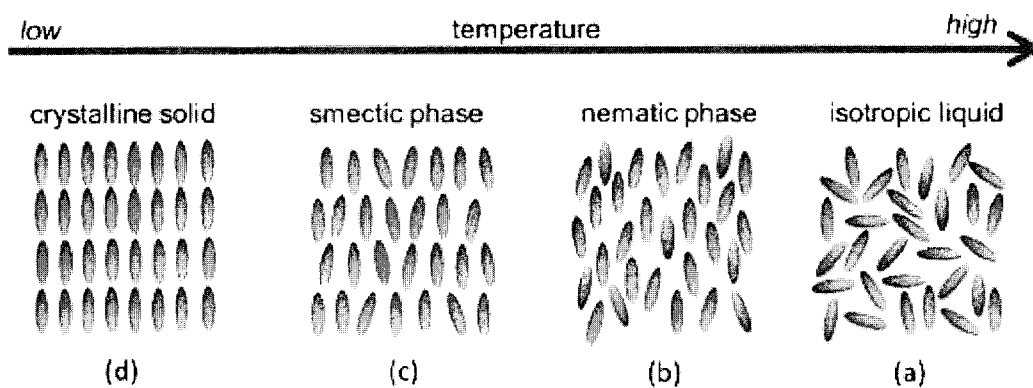


Figure 2.29 Molecular alignment at different mesophase of liquid crystal [119]

Figure 2.29 shows the molecular arrangement with the axis denotes the direction of increasing temperature. At the temperature of melting point, LCs are crystal solid. Above the melting point, the compounds exist a smetic or nematic phase. In the smetic phase, besides the long-range molecular orientation, there is also a one-dimensional positional order. In the nematic phase, LCs are characterised by possessing the molecular orientation only. At high temperature, the molecules will be oriented arbitrarily forming an isotropic liquid.

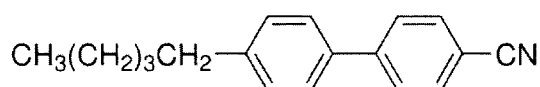


Figure 2.30 Liquid crystal of 5CB [119]

The molecular structure of 4-Cyano-4'-pentylbiphenyl (5CB) is shown in Figure 2.30. 5CB is widely adopted as it remains nematic phase under room temperature. 5CB is a type of nematic liquid crystal (NCL) called calamitics which has a rod-like molecular structure [120].

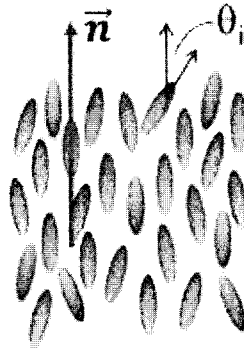


Figure 2.31 Schematic diagram of the director \vec{n} and order parameter S [119]

There are two important parameters in the liquid crystal, director \vec{n} and order parameter S . The director \vec{n} is a unit director that demonstrates the overall molecular orientation (Figure 2.31). The definition of S is listed in Eq (2.5).

$$S = 0.5 \langle 3 \cos^2 \theta_i - 1 \rangle \quad (2.5)$$

Where θ_i is the angle between the long axis of the molecular and the director \vec{n} , symbol $\langle \rangle$ denotes the overall average value. $S=1$ implies that the LC is in perfect crystal phase while value 0 indicates a isotropic phase. Typical value of S is in the range of 0.3 to 0.8. This value will decrease with increasing temperature [119].

2.7.2 Surface anchoring conditions

The spatial symmetry is influenced by the presence of surface boundaries so as the LC molecular orientations. The interaction between LC and surface plays an important role in determining LC dynamics. Therefore the surface properties known as the surface anchoring conditions are important.

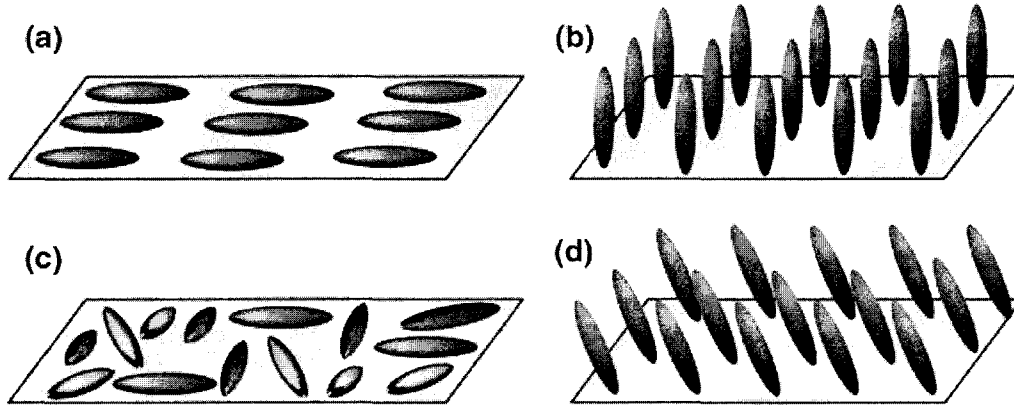


Figure 2.32 Four types of surface anchoring conditions of nematic LC: (a) uniform planar anchoring, (b) homeotropic anchoring, (c) degenerate anchoring and (d) tilted anchoring [121, 122]

Figure 2.32 demonstrates four types of LC surface anchoring conditions: uniform planar, homeotropic, degenerate and tilted anchoring. In uniform planar anchoring that the surface director is oriented parallel to the surface, for homeotropic anchoring it is oriented an ideal perpendicular to the surface. Degenerate anchoring is similar to the uniform planar anchoring, surface director anchors parallel to the surface plan but in a random arrangement. The tilted anchoring presents a tilted angle between the axis of the molecule and the surface. The anchoring condition is primarily determined by the surface property. Various methods were proposed to modify the surface anchoring condition for the microfluidics prevailing PDMS channel. Mechanical treatment and chemical coating are the two major types [123, 124].

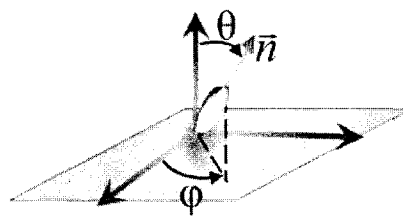


Figure 2.33 Two parameters describing the anchoring condition: azimuthal anchoring angle φ and zenithal anchoring angle θ [119]

The energy due to the free distortion of the LC can be expressed by Eq (2.6) [125].

$$F_s = 0.5[W_{\theta_0} \sin^2(\theta - \theta_0) + W_{\varphi_0} \sin^2(\varphi - \varphi_0)] \quad (2.6)$$

Where φ_0 and θ_0 are the referenced azimuthal and zenithal anchoring angles respectively. W_{φ_0} defines the azimuthal potential (the maximum energy required to distort the director from φ_0). Similarly W_{θ_0} denotes the polar potential which is the maximum energy to deviate the director from θ_0 (Figure 2.33). The surface anchoring energy ranges from $10^{-6} \sim 10^{-4} \text{ J/m}^2$.

Sengupta *et al.* [121] reported that after the plasma treatment process, the freshly prepared PDMS microchannel would become degenerated planar due to the reduction of the wetting angle of 5CB on the confining surfaces. The investigation was carried out using polarizing optical microscope (POM) and fluorescence confocal polarizing microscope (FCPM).

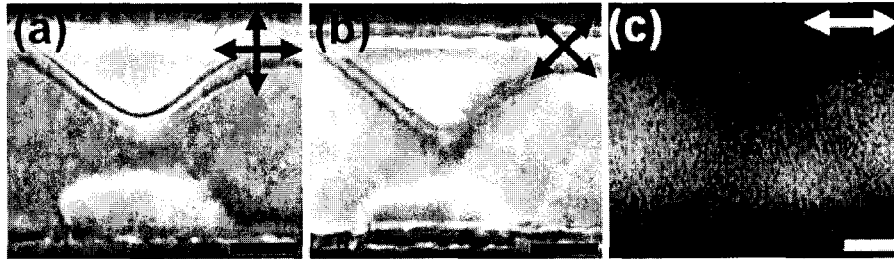


Figure 2.34 (a), (b) show polarizing optical microscope observation of the degenerate planar anchoring in rectangular microchannel. The double head arrow indicates the orientation direction of the polarizer and analyzer. (c) demonstrates the image of fluorescence confocal polarizing microscope via laser polarization along the channel length as shown the double head arrow. [121, 126]

Figure 2.34 presents the POM and FCPM observation of the LC degenerate planar anchoring. The birefringent domain was illustrated via randomly oriented 5CB (Figure 2.34 (a), (b)). The non-homogeneously distributed fluorescence intensity obtained from FCPM observation further confirmed the degenerate planar anchoring.

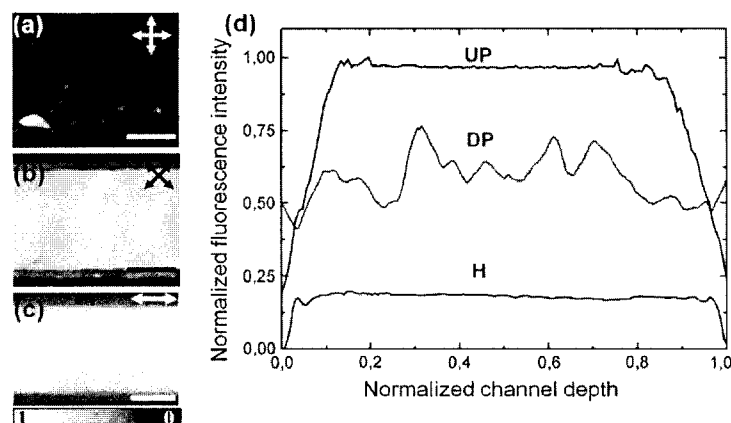


Figure 2.35 (a) (b) POM observation of LC uniform planar anchoring in a rectangular microchannel. (c) FCPM results of LC orientation in the azimuthal plane. (d) Normalized fluorescence for different LC anchoring: uniform planar (UP), degenerate planar (DP), and homeotropic (H) anchoring. [122]

Figure 2.35 demonstrates results of LC uniform planar (UP) anchoring in rectangular microchannels via both the POM and FCPM method. Uniform planar anchoring can be achieved via photo-alignment method where the Para-fluoro polyvinyl cinnamate (PVCN-F) coated microchannel wall is exposed to the polarized UV light. Figure 2.35 (a) shows a dark POM micrograph when one of the polarizers parallel to the resultant liquid crystals director orientation. Figure 2.35 (b) shows the bright POM micrograph when the director is 45° to the polarizers. Furthermore, the uniformly high fluorescence signal confirms the orientation of liquid crystal which is along the laser polarization (Figure 2.35 (c)). By performing FCPM imaging along the cross-section (yz plane), the fluorescence intensity distribution along the channel depth was established. This was used to measure the spatial homogeneity of equilibrium orientation within the functionalized microchannels. Results show that UP has the highest light intensity while homeotropic shows the lowest.

2.7.3 Liquid crystal optics

Due to the birefringence property of LC and its inherent molecular structure, the orientation cannot be observed via normal microscopy. Specialized optics are

required to reveal the molecular orientation of LC. There are the polarization microscopy and conoscopy microscopy .

Optical characteristics of liquid crystal

The optical anisotropy in nematic LC is shown by the two distinct refractive indices, along the optical axis n_{\parallel} and the perpendicular to the optical axis n_{\perp} . The optically positive and negative phase of LC are determined by the sign of value $\Delta n = n_{\parallel} - n_{\perp}$. Generally, LC of smectic and nematic phase are optically positive $\Delta n > 0$. When an incoming light beam is transmitted within a birefringent material, it splits into two components: the ordinary ray with the ordinary refractive index n_o and the extraordinary ray with refractive index n_e . The refractive indices can be derived from the two principle refraction indices, n_{\parallel} and n_{\perp} .

$$n_o = n_{\perp} \quad (2.7)$$

$$n_e = \frac{n_{\parallel} n_{\perp}}{(n_{\parallel}^2 \cos^2 \Phi + n_{\perp}^2 \sin^2 \Phi)^{0.5}} \quad (2.8)$$

Where Φ is the angle between the optic axis and the direction of light propagation, as shown in Figure 2.36.

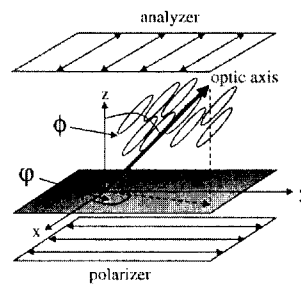


Figure 2.36 Schematic diagram of uniformly oriented LC molecule in between optical polarizer and analyser. [127]

A phase difference δ is generated between the ordinary ray and extraordinary ray,

$$\delta = (2\pi / \lambda)(n_e - n_o)d \quad (2.9)$$

Where λ is the vacuum wave length of propagating beam, d is the thickness of the optical cell.

Polarization optical microscopy

Polarization optical microscopy (POM) is used to reveal the molecular orientation of LCs (Figure 2.37). White light first passes through a polarizer so that the light transmitted is linearly polarized. The polarization direction can be adjusted via turning the axis of the polarizer. This light then passes through a LC sample cell and an analyser. The analyzer is also a polarizer, whose axis can be parallel, perpendicular or at any intermediate angle relative to the initial polarizer. In POM, crossed-polarized state is applied when both the polarizer and analyzer axis are mutually perpendicular.

Normal samples without the ability of changing the orientation of light are placed in between the polarizer and analyser. This allows no light to pass through the analyzer. The LC, which is capable of altering the light's orientation allows light to pass through the analyzer as shown in Figure 2.37 (b). Hence, bright image appears when a component of elliptical polarized light passes through the analyzer (Figure 2.37 (b)). Dark image appears when optical axis of the liquid crystal aligns parallel to analyzer (Figure 2.37 (a)).

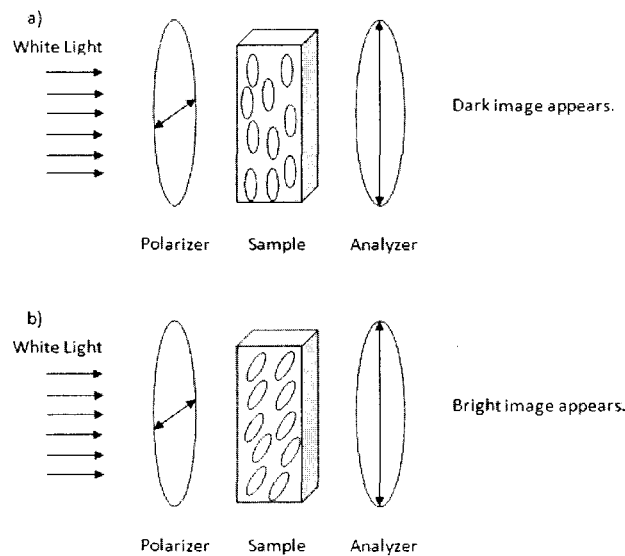


Figure 2.37 Schematic diagram of transmission of white light across polarizer and analyzer. (a) LC orientated parallel to analyzer, (b) LC orientated arbitrarily but not parallel to analyzer.

Conoscopy microscopy

Conoscopy is an optical interferometric technique which is used in investigation of birefringence samples. For a standard polarizing optical microscope, conoscopy can be achieved by the insertion of a Bertrand lens between the analyzer and the ocular. The working mechanisms of a standard orthoscopy and conoscopy are shown in Figure 2.38.

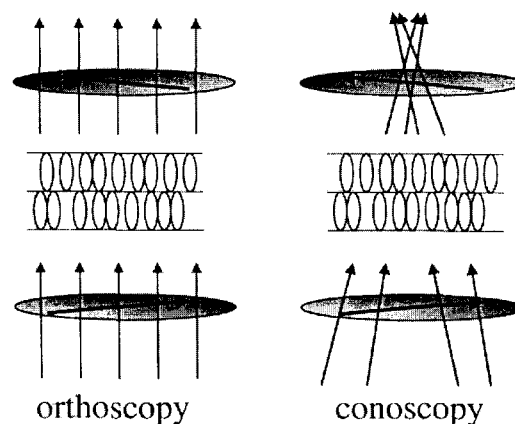


Figure 2.38 Schematic diagram of orthoscopy and conoscopy imaging a liquid crystal sample. [127]

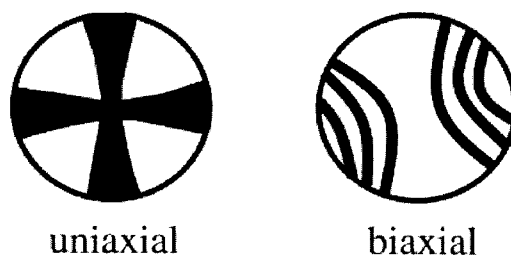


Figure 2.39 Schematic diagram for uniaxial and biaxial material via conoscopy setup. [127]

Figure 2.39 shows the detection of the axiality via using a conoscopy setup. A typical cross pattern is obtained for the uniaxial material. The arm of the cross is called isogyres which is parallel to the polarizers. The other type of interference pattern obtained is biaxial. The two arms of interference pattern on the two sides with different widths can be observed.

2.7.4 Applications of LC in microfluidics

LCs has been incorporated into polarization microscopes by many researchers at larger scale [128, 129]. Fast response speed of LCs-based components provides more structural details. Owing to the fascinating properties, the LCs-based analysis has great potential for developing rapid, simple and label-free detection.

LCs-aqueous interfaces

The effect of phospholipids at the LCs-aqueous interface was studied for analysing LCs molecular re-orientation. The interface of LCs with an aqueous medium induces a planar alignment (Figure 2.40 (a)) and the addition of lipids induces a change in this orientation (Figure 2.40 (b,c)). Figure 2.40 demonstrates a schematic of the reorientation with respect to time [130]. This approach provides a method to monitor the enzymatic action using a phospholipid decorated liquid crystal surface.

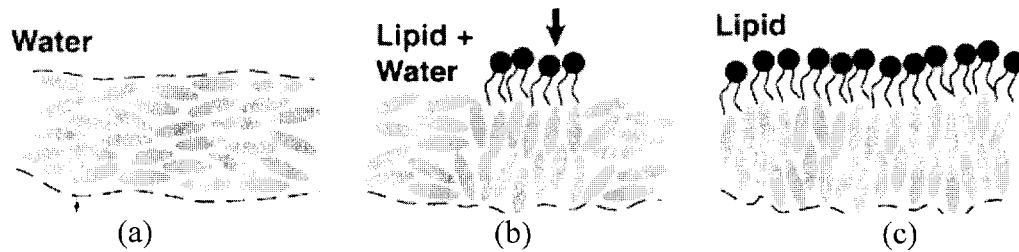
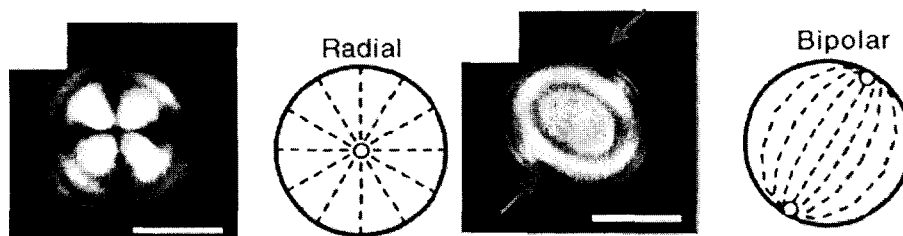


Figure 2.40 LCs-aqueous interface in the presence of phospholipids (a) without phospholipids (b) after 20 minutes (c) after 2 hours [130].

LCs-Droplet

Instead of forming a planar LCs-aqueous interface, LCs can be emulsified to form LCs droplets. LCs droplets have recently emerged as a unique optical probe for detection of biological and chemical species. An interesting observation of using LCs droplets to detect endotoxin from *E.coli* [131] was reported. Before exposure to endotoxin, LCs possess a bipolar configuration Figure 2.41(a)), with two point defects at two poles of the droplets. After exposure to endotoxin, it was observed that the ordering of the LCs change to a radial configuration, with a defect located at the center of the droplet (Figure 2.41 (b)). This response provided an approach of screening biological and chemical species based on LCs' structural characteristics.



(a) : Before exposure to endotoxin (b) After exposure to endotoxin

Figure 2.41 Optical images and cartoon representation of LC droplets [131]

2.8. Fabrications of microchannels

The rapid development of fabrication technology provides the microfluidics with various possibilities. Among the fabrication methods, silicon has been used and attracted extensive attention. The well-developed semiconductor technology and chromatography method makes the silicon based fabrication dominant. Nguyen [132] provided the brief silicon fabrication procedure and Lee [133] specifically focuses on the electrokinetic micromixer based on silicon. The silicon based technology offers the ways that the surface properties can be modified to prompt the micromixing. Dreyfus [134] and Thorsen [135] also studied multi-phase flow within the silicon based microchannels. It is a well-developed method comparatively, nonetheless, its application are limited as a result of the drawbacks. For instances, the procedure is complex and expensive, difficulty occurs in assembling and most of all it cannot be adopted in biological applications. Poly-dimethylsiloxane (PDMS) and soft-lithography are adopted commonly in microfluidics quite often recently. It is more accessible to researchers than the conventional methods.

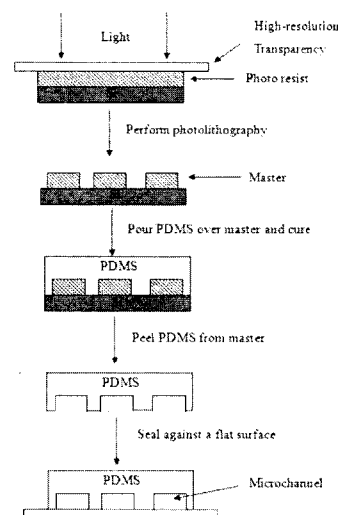


Figure 2.42 Schematic procedure of PDMS by soft-lithography fabrication [136]

Figure 2.42 describes the PDMS fabrication method via soft-lithography. The pre-lithography material in the liquid form is filled in the master. Cured PDMS layer can be peeled off the master without damaging it. The master can be fabricated by various methods, among which the commonly utilized are standard microelectronics and photolithography. For photolithography, the microstructures are designed by CAD software and then the patterns will be printed in transparencies. The lateral resolution is 25 μm when operates at 5080 dpi and it can achieve 8 μm operating at 20000 dpi. The patterned transparencies are taken as photomasks in UV lithography procedure, during which the patterns are transferred into the SU-8 resist mask.[136]

The research group in Harvard University [137] was the first group utilized the PDMS in microfluidics applications. Ichikawa [138] and Kim [139] also used the PDMS method for fabrication of rectangular microchannels. Sato [140] conducted the microfluidics experiments in a T-shaped channel using the PDMS method for fabrication.

2.9. Summary

Literature review show that most of EO related research conducted bears one common condition that the fluid is a simple Newtonian fluid. However, most of the bio samples are fluid with complex rheological behavior. Limited work has been carried out on non-Newtonian fluids.

Droplet based microfluidics have shown great potentials in biomedical applications. Up to now, very limited work has been reported on the droplet generation in the non-Newtonian fluids. The coupling of electric field and hydrodynamics on droplet formation in the non-Newtonian fluid is yet explored.

Large amount of the reported work has been carried out to study the behavior of isotropic fluid or isotropic-droplet-based microfluidics. The study of complex anisotropic LCs flow is limited. Although, recently experimental investigations of LCs in microchannels have been initiated, most of the existing literature focuses on the flow of nematic LCs within very wide channels – or slits, as relevant in display application. The LCs' flow behavior is still unexplored in modern microfluidics. The coupling of flow field with molecular reorientation at microscale is yet to be studied.

Chapter 3 Experimental and Theoretical Investigations of Non-Newtonian Electroosmotic Driven Flow in Rectangular Microchannels

3.1 Introduction

Electro-osmotic (EO) driven flow has gained intense focus in microfluidics due its inherent benefits [55, 56, 141, 142]. The distinguishing phenomenon is that an EO driven flow shows a plug flow profile rather than the traditional parabolic one, and thus has great potentials in fluid transportation [57, 58]. The plug flow profile will reduce the shear induced stress as there is little velocity gradient in the bulk flow, and is thus a niche area for sensitive sample transportation [17, 141, 143]. Fluid samples such as bio samples (blood and DNA) are known to be highly sensitively to shear stresses and may degrade under a high level of shear [53, 74, 144, 145]. Unfortunately, the most commonly adopted transportation method, that is the hydrodynamic driven method, shows a parabolic profile leading to a relatively high shear stress in the bulk flow. The EO driven method can overcome this drawback.

Measurement methods, such as current monitoring and micro-PIV, were introduced and utilized to determine velocity field of EO driven flow [26, 29, 30, 43, 59, 139]. These theoretical predictions have been proven to accurately model the experimental measurements. It showed that the zeta potential ψ is a property related parameter representing the attraction strength to ions at the wall boundary or interfaces for a low-concentrated-ion solution.

However, most of the EO related research conducted bears one common condition in that the fluid is a simple Newtonian fluid. Conversely most of the bio-samples are

fluids with complex rheological behavior termed as non-Newtonian fluids [62, 76, 146]. Limited work has been carried out on non-Newtonian fluids [74, 82, 84, 142, 145, 147]. The challenge lies in the coupling of EO driven mechanism and the complex rheological behavior. Currently, some analytical models have been proposed for both single and two phase parallel plane flow, in which the power-law and the Carreau model were chosen for simulating fluid behavior [69, 70, 75, 78, 79, 145]. However, the models lacked solid support from experiments and questions arise when dealing with a double layer whose range is of the same order as the microstructures of the non-Newtonian fluid. Will the micro structures influence the physics of the double layer? Is the Smoluchowski approach still valid for a non-Newtonian fluid?

To answer these questions, we systematically measured the average EO driven velocity of one type of non-Newtonian fluid, poly ethylene oxide (PEO) aqueous solution, via varying the PEO concentration and applied electric field. Aqueous solutions of PEO behave similarly to that of bio samples [148-150]. Comparisons between the experimental results with a analytical model were made. To this end, the shear thinning effect upon EO driven flow was analyzed.

3.2 Experimental setup

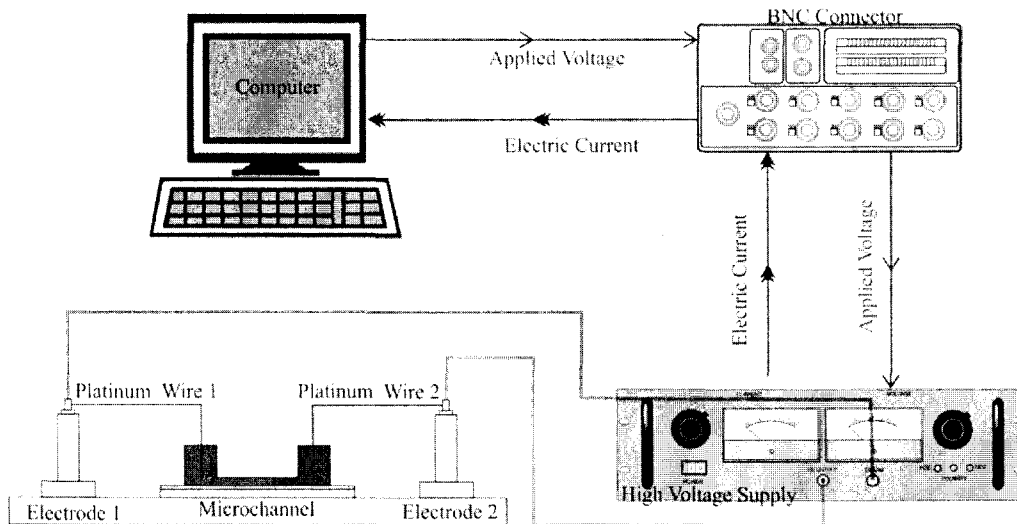


Figure 3.1 Representative diagram for experimental setup

Figure 3.1 shows the general experimental setup for current monitoring method [29]. The system consist of one high voltage supply, one set of signal acquiring system, one microchannel and one computer used to control the applied electric field and record the current value.

3.2.1 Data acquisition system

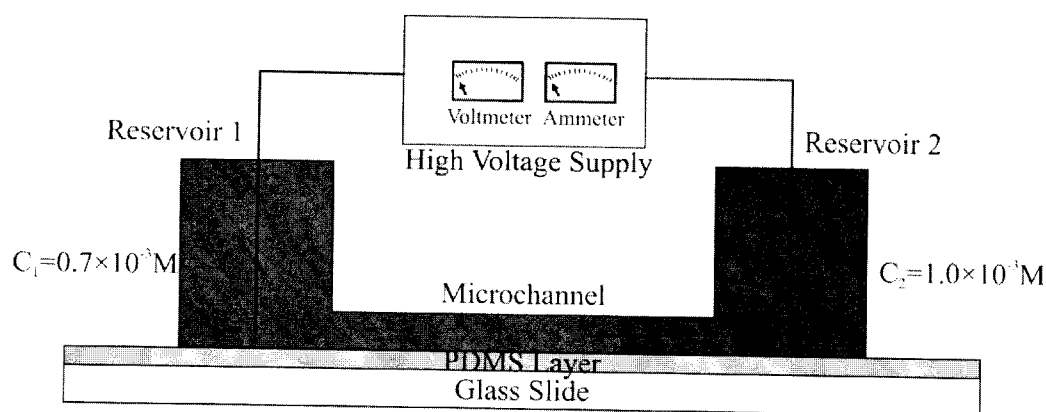
The data acquisition system consists of an acquisition card (National instrument PCI-6052E), BNC connector (NI BNC-2110) and one custom program written in LabVIEW. This system allows direct control of applied voltage (electric field strength) via sending signals to the high voltage supply (CZE 1000R) as well as automatically receiving and recording current values from the supply.

3.2.2 Fluid sample preparation

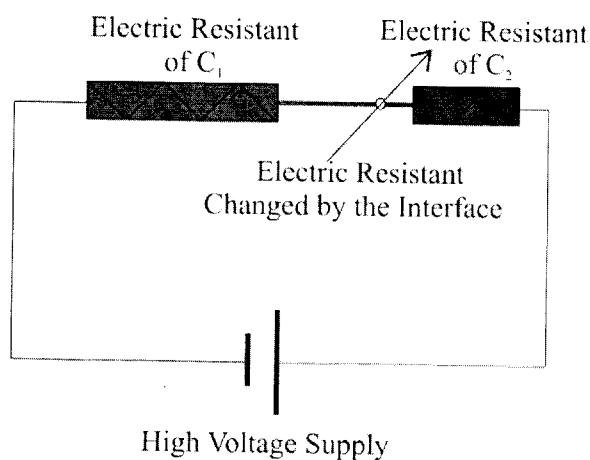
The fluid sample used in this experiment is poly ethylene oxide (PEO) aqueous solution, produced by stir-mixing PEO powder of molecular weight 4M (Sigma Aldrich) for 24 hours at room temperature [144, 146]. Two different types of water

samples, DI water (Mili-Q grade II) mixed with sodium chloride (Sigma Aldrich) at concentrations of $1 \times 10^{-3} \text{M}$ and $0.7 \times 10^{-3} \text{M}$ respectively, were prepared for each specific concentration of PEO aqueous solution. The sodium chloride added is to vary the ion concentrations so that the current will vary under a constant applied electric field. Four different PEO concentrations, 0.1%, 0.3%, 0.5%, 0.7% (by weight), were prepared for the experiment, with $1 \times 10^{-3} \text{M}$ and $0.7 \times 10^{-3} \text{M}$ of sodium chloride.

3.2.3 Current monitoring method and microchannel



(a) Layout of the current monitoring method



(b) Equivalent electric circuit of the current monitoring method

Figure 3.2 Schematic diagrams for the current monitoring method

Figure 3.2 shows the schematic diagram of the current monitoring method and the geometry of the microchannel. The current monitoring method utilizes electro-osmotic driven mechanisms by displacing electrolyte from reservoir 2 to reservoir 1 through an external electric field [29, 32, 43]. By monitoring the current change, the electro-osmotic driven velocity can be obtained. As seen in Figure 3.2, the two reservoirs are filled with PEO solutions of different sodium chloride concentrations, 0.7×10^{-3} M (reservoir 1) and 1×10^{-3} M (reservoir 2) respectively. When a constant voltage is applied over the microchannel, the electric current through the microchannel varies during the displacement process, which can be seen by the variable electric resistant in Figure 3.2 (b). The data acquisition system recorded the current versus time for later analysis. Two platinum wires (Sigma Aldrich) were used to connect high voltage power supply and the reservoirs to avoid electro-chemical reactions.

The microchannel is made of one rectangular channel of size $300 \times 75 \times 30000$ micrometers (width \times height \times length) connected by two cylinder-shaped reservoir of size 10×5 mm at each end to store the fluid sample. The microchannel was fabricated by standard soft lithographic procedures followed by polydimethylsiloxane (PDMS, Dow Corning Sylgard 184) process and bonded via plasma bonding method with one side of the microscope glass spin coated with a thin layer of PDMS to ensure uniform surface conditions [137]. The wettability changes from hydrophobic to hydrophilic during the plasma bonding, but reverts back gradually within 1-2 hours depending on the humidity and temperature. After plasma bonding, the microchannel was baked in an oven for 2 hours at a temperature of 120°C to ensure a stable and hydrophobic surface property.

3.3 Results and discussion

3.3.1 Non-Newtonian EO driving velocity via current monitoring method

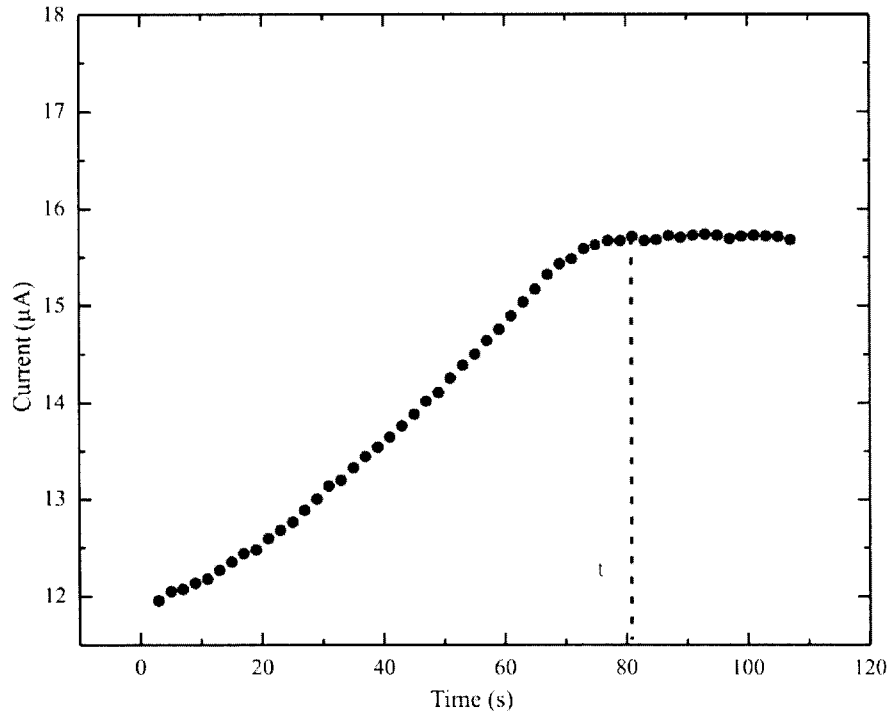


Figure 3.3 Electric current evolution with time. Results were obtained by filling reservoir 1 and microchannel with 0.1% PEO aqueous solution whose concentration of sodium chloride is 0.7×10^{-3} M, while filling reservoir 2 with the same PEO solution with a sodium chloride concentration of 1.0×10^{-3} M.

Figure 3.3 shows that the evolution of the electric current with time. Measurements were repeated for minimum 3 times to ensure repeatability. As the PEO with a higher concentration of sodium chloride (C_2) replaces the lower one (C_1), the electric resistance decreases resulting in the rising trend of electric current being observed when the electric field strength is kept constant during the measurement. The current will continue to rise until the microchannel is completely filled with C_2 . By tracking the time when the current stops changing, the average EO driven velocity on non-Newtonian fluid can be calculated.

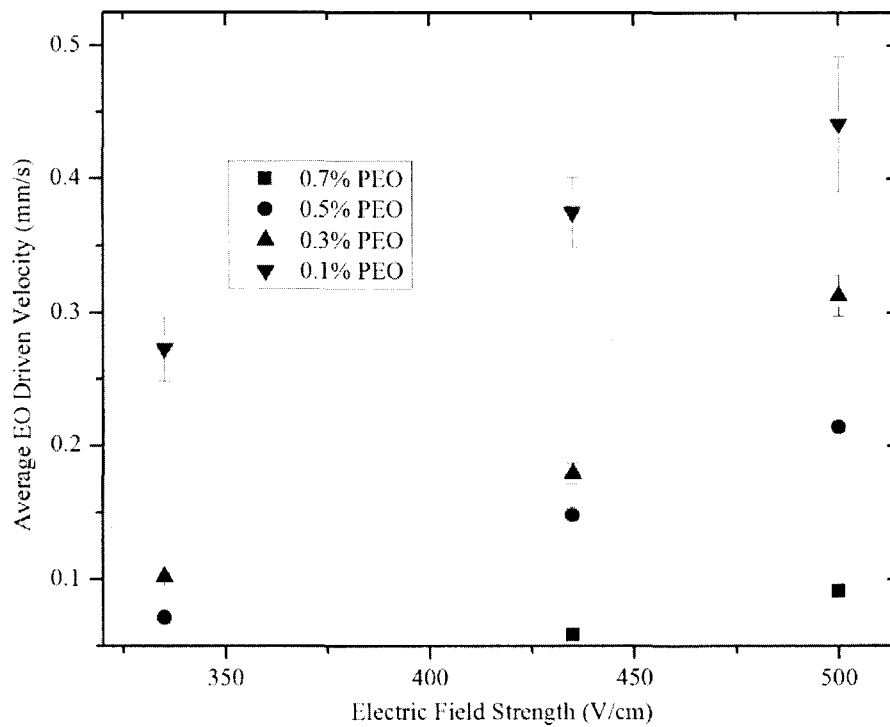


Figure 3.4 Average EO driven velocity versus applied electric field strength. Four different PEO concentrations (by weight), 0.1%, 0.3%, 0.5%, 0.7%, are measured.

The average EO driven velocity obtained after analyzing the current variation record is shown in Figure 3.4. The results show that the velocity increases with electric field strength but decreases with PEO concentration. An higher electric field will transfer more energy into the fluid, causing a higher flow speed, while a higher PEO concentration will increase the fluid viscosity significantly. When the PEO concentration increases to 0.7%, no EO induced flow occurs for a low electric field strength due to the high apparent viscosity.

3.3.2 Microscopy fluorescence study of the non-Newtonian electro-osmotic driven flow

Figure 3.4 shows the average velocity of the EO driven flow without indicating other details such as the flow profile [140]. It is well known that EO driven mechanism can create ‘plug-shape’ flow profiles. To resolve the flow profile of non-Newtonian fluid

driven by EO force (EOF), we conducted microscopy fluorescence imaging experiment to capture the flow profile. The general setup is shown in Figure 3.1. The microchannel was placed under an inverted fluorescent microscope (Leica DM ILM) for observation. Concentration of 0.2 mM fluorescent dye (Rhodamin B, Sigma Aldrich) was added in fluid C₂ (see Figure 3.2) to create a fluorescent trace. Images were recorded with a Phantom V611 video camera at the frame rate of 50 fps.

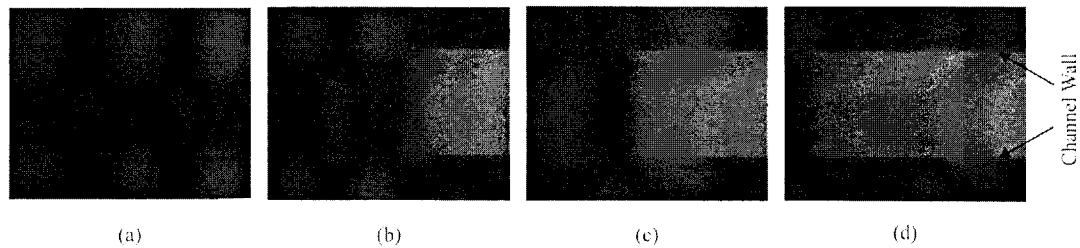


Figure 3.5 Fluorescent images of EO driven flow with a non-Newtonian fluid

Figure 3.5 represents the non-Newtonian fluid flow through the microchannel under EO driving. The fluid with Rhodamin B lights up while the fluid without dye appears black. The light intensity boundary reveals the profile of the flow field. Results in Figure 3.5 shows sharp ‘plug’ shape flow profile.

3.3.3 Zeta potential for non-Newtonian fluids

The zeta potential is one of the critical parameters used to study the EO flow and it has been assumed to be a constant for Newtonian fluid. So far, a constant zeta potential has been widely accepted when dealing with non-Newtonian problems without solid evidence from experiments. We will couple the Smoluchowski approach and the power-law model to determine the zeta potential for the non-Newtonian EO flow given the EO driven velocity as shown in Figure 3.4.

Rheology measurement

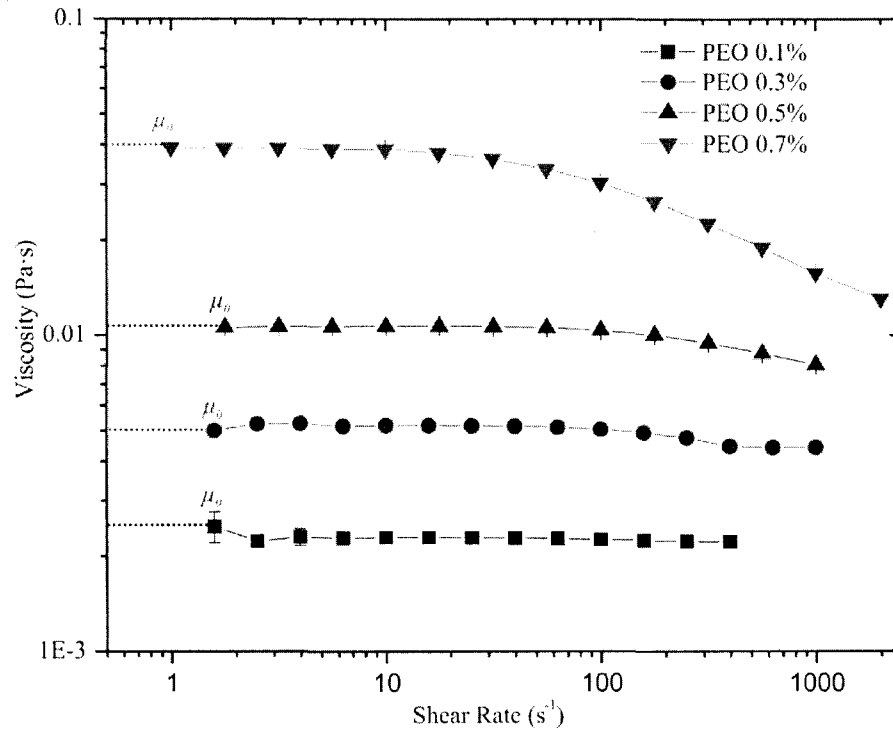


Figure 3.6 Rheological behavior of PEO aqueous solutions. Four different PEO concentrations were tested, 0.1%, 0.3%, 0.5%, 0.7% (by weight).

Figure 3.6 displays the viscosity against shear rate measured on a TA Instruments Discovery Hybrid Rheometer (DHR-2), that was pre-calibrated using a standard viscous oil. μ_0 denotes the zero shear viscosity. It is inferred that the shear thinning behavior becomes more pronounced with increasing PEO concentrations. The viscosity to shear rate behavior of the PEO aqueous solutions is necessary before calculation of the zeta potential and it can be described by the power-law model

$$\mu = m\gamma^{n-1} \quad (3.1)$$

Where μ is the fluid apparent viscosity, γ is the shear rate, m and n are fluid coefficient and flow behavior index respectively.

The power-law model is a two parameter constitutive law for fitting shear rate dependent viscosity behavior. The two parameters are derived from rheological measurements by Matlab curve fitting. The results are listed in Table 1.

Table 3.1 Fluid coefficient m and flow behavior index n for PEO aqueous solutions

PEO concentration (wt. %)	m	n
0.10%	0.0023	0.99
0.30%	0.0060	0.94
0.50%	0.0160	0.87
0.70%	0.0600	0.78

Table 3.1 shows that all the n values are smaller than 1 indicating a shear thinning behavior. A smaller n suggests a higher degree of shear thinning behavior. The n value decreases with increasing PEO concentration. The m value is the fluid viscosity for a shear rate of 1 s^{-1} .

Generalized Smoluchowski approach for non-Newtonian fluids

The simplified parallel flow model is considered in this chapter as the rectangular microchannel flow is too complex for theoretical analysis. The general trend of the parallel flow is the same with the rectangular microchannel flow since the thin electric double layer (EDL) condition determines the fully developed EO driven velocity which is independent of the microchannel shape.

We will address the ion distributions first, which leads to the EO force in the fluidic governing equation. Then, we will couple the EO force to the fluidic governing equation. Finally, we solve the equation with the appropriate boundary conditions.

The electric potential distribution follows the Poisson-Boltzmann equation:

$$\nabla^2 \psi = -\frac{\rho_e}{\epsilon} \quad (3.2)$$

where ψ is the electric potential in the solution, ρ_e is the electric charge density, and ε is the electric permittivity of the solution.

The electric charge density, ρ_e , follows the distribution stated below:

$$\rho_e = -2z_v e_0 n_0 \sinh\left(\frac{z_v e_0}{\kappa_b T}\right) \quad (3.3)$$

where n_0 is ionic concentration in the bulk solution, e_0 is the fundamental electric charge, z_v is the valence of the ion, ε is the electric permittivity of the solution, κ_b is the Boltzmann constant, and T is the absolute temperature.

Eq (3.3) can be linearized and simplified via the Debye-Hueckel approximation under the condition that zeta potential value is smaller than 50 mV. Therefore the electrical potential is expressed as:

$$\frac{d^2\psi}{dy^2} = \kappa^2 \psi \quad (3.4)$$

$$\kappa^2 = \frac{2z_v^2 e_0^2 n_0}{\varepsilon \kappa_b T} \quad (3.5)$$

where κ is the Debye-Hueckel parameter and κ^{-1} is normally considered the thickness of EDL.

The boundary conditions for the electric potential are:

Wall boundary zeta potential at $y = h$: $\psi = \psi_w$,

at $y = 0$: $\psi = \psi_w$.

The solution for the electric potential (Eq (3.4)) under the boundary conditions is:

$$\psi = \left[\frac{\sinh(\kappa y)}{\sinh(\kappa h)} + \frac{\sinh(\kappa h - \kappa y)}{\sinh(\kappa h)} \right] \psi_w. \quad (3.6)$$

The EO force created by the presence of ion under an electric field is

$$F_x = E_0 \rho_e = E_0 (-\varepsilon \nabla^2 \psi) = -E_0 \varepsilon \kappa^2 \left[\frac{\sinh(\kappa y)}{\sinh(\kappa h)} + \frac{\sinh(\kappa h - \kappa y)}{\sinh(\kappa h)} \right] \psi_w \quad (3.7)$$

where E_0 is the applied electric field strength.

The governing flow equation for a non-Newtonian fluid gives:

$$\frac{d}{dy} \left(m \left| \frac{du}{dy} \right|^{n-1} \frac{du}{dy} \right) = E_0 \varepsilon \kappa^2 \left[\frac{\sinh(\kappa y)}{\sinh(\kappa h)} + \frac{\sinh(\kappa h - \kappa y)}{\sinh(\kappa h)} \right] \psi_w \quad (3.8)$$

with the no slip boundary condition imposed for its solution, where $y = 0$ & $y = h$,
 $u = 0$.

As the solution is symmetrical only half of the microchannel needs to be considered for a solution. After substituting all the boundary conditions, the velocity distribution of the half microchannel, where $\frac{h}{2} < y < h$, can be express as:

$$u = \frac{1}{\kappa} \coth[\kappa h] {}_2F_1 \left[\frac{1}{2}, \frac{-1+n}{2n}, \frac{3}{2}, \cosh[\kappa h]^2 \right] \left(\frac{\varepsilon E_0 \kappa \psi_w \text{Sech}[h\kappa] \sinh[\kappa h]}{m} \right)^{\frac{1}{n}} \left(-\sinh[\kappa h]^2 \right)^{\frac{-1+n}{2n}} \\ - \frac{1}{\kappa} \coth[\kappa(2y-h)] {}_2F_1 \left[\frac{1}{2}, \frac{-1+n}{2n}, \frac{3}{2}, \cosh[\kappa(2y-h)]^2 \right] \\ \left(\frac{\varepsilon E_0 \kappa \psi_w \text{Sech}[h\kappa] \sinh[\kappa(2y-h)]}{m} \right)^{\frac{1}{n}} \left(-\sinh[\kappa(2y-h)]^2 \right)^{\frac{-1+n}{2n}} \quad (3.9)$$

Where ${}_2F_1[, , ,]$ denotes a four-parameter hypergeometric function.

Under the thin EDL condition which proves to be valid from our experiment, the EO velocity can achieve a fully developed non-Newtonian EO driven velocity termed as Generalized Smoluchowski velocity shown in Eq (3.10).

$$u_s = n \kappa^{\frac{1-n}{n}} \left(-\frac{\varepsilon \psi_w E_0}{m} \right)^{\frac{1}{n}} \quad (3.10)$$

The expression of the non-Newtonian zeta potential is obtained by rearranging Eq (3.10):

$$\psi_w = -\frac{m}{\varepsilon E_0} \kappa^{n-1} \left(\frac{u_s}{n}\right)^n \quad (3.11)$$

The zeta potential ψ_w is calculated by substituting the EO velocity u_s which is the average EO velocity shown in Figure 3.4, the electric field strength E_0 and the non-Newtonian rheological behavior parameters (m and n) into Eq (3.11). The final results are shown in Figure 3.7.

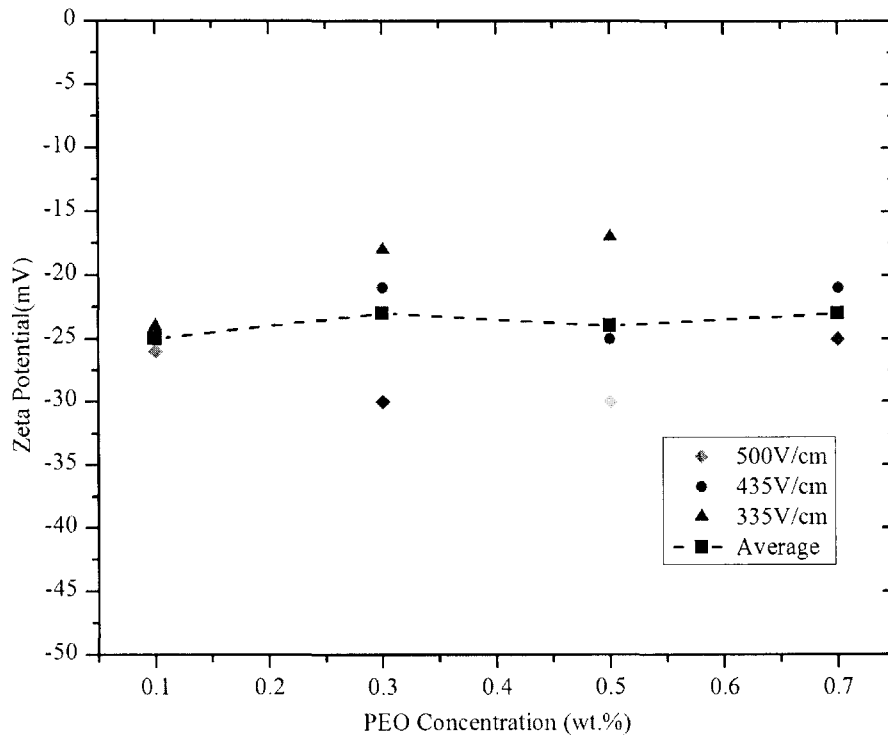


Figure 3.7 Zeta potential values of PEO aqueous solutions under different electric field strength.

Figure 3.7 gives zeta potentials of four PEO aqueous solutions, 0.1%, 0.3%, 0.5%, 0.7% under different electrical field strengths. The zeta potential as shown in Figure 3.7 indicates there is some fluctuation under different electric field strength. However, within experimental errors, the average value suggests a constant value. Substitute the constant zeta potential value into Eq (3.9) and compare it with that of the experimental results shown in Figure 3.4 to test if the constant zeta potential

assumption will give acceptable estimation of the non-Newtonian EO driven behavior.

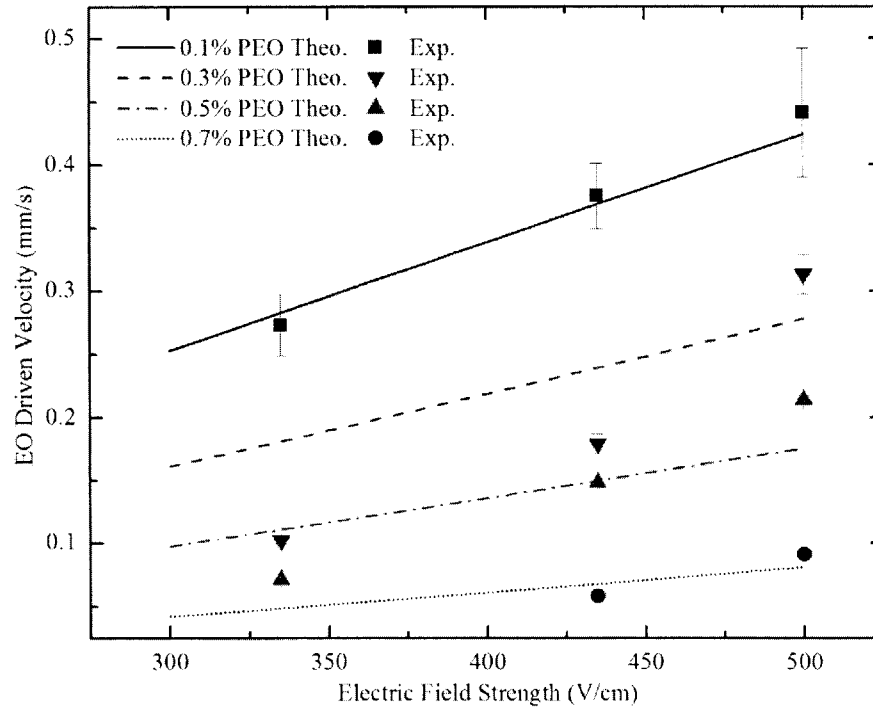


Figure 3.8 Comparison between theoretical approach and experimental results

Figure 3.8 is plotted to verify the constant zeta potential assumption when dealing with non-Newtonian EO driven flow. The results are within an acceptable error margin. The rising trend and the actual velocity can be predicted by using constant zeta potential assumption, which provides a convenient method for EO flow analysis as the complex rheology does not interfere with the inherent EO characteristics.

3.3.4 Effect of shear thinning behavior on EO flow

The theoretical analysis shows an improvement in the magnitude of the EO driven velocity caused by the shear thinning behavior. The shear thinning effect will be addressed both experimentally and theoretically as the average shear rate can be calculated by the model while the EO velocity is measured experimentally. The shear

rate is defined as the velocity gradient and the average shear is evaluated via the following formulation given the velocity distribution which is obtained from Eq (3.9).

$$\gamma_{ave} = \frac{\int_{h/2}^h \frac{\partial u}{\partial y} dy}{h/2} \quad (3.12)$$

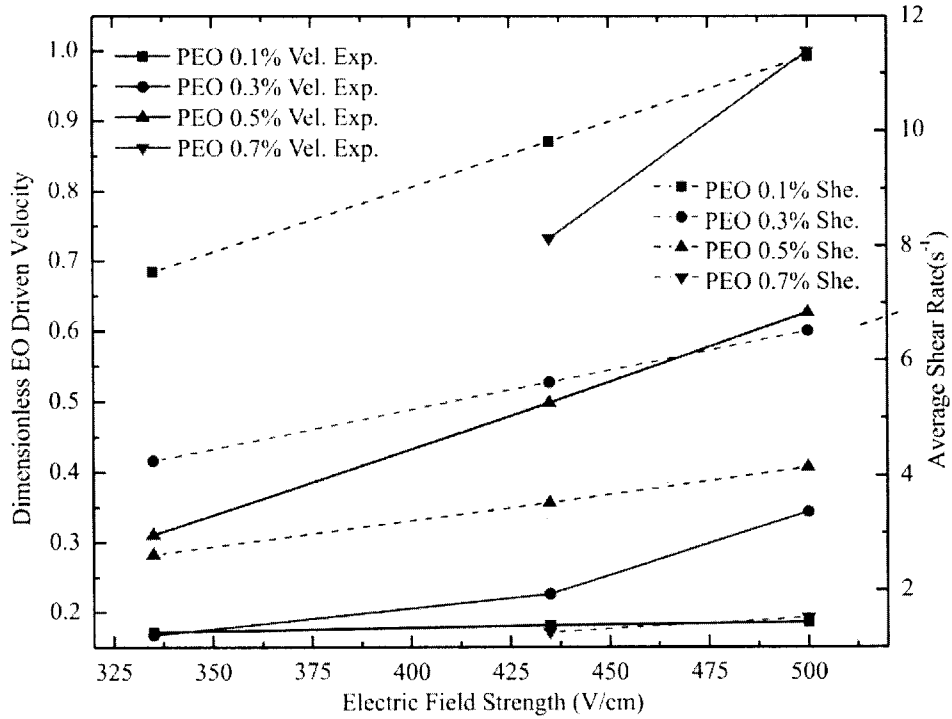


Figure 3.9 Shear thinning effect on non-Newtonian EO driven flow.

Figure 3.9 shows both the dimensionless EO driven velocity and the average shear rate versus the electric field strength. The average shear increases with increasing applied electric field strength due the fact that a stronger electric field stimulates the EO flow. It is inferred that flows with a smaller apparent viscosity and higher electric field can generate a larger average shear rate.

The dimensionless EO driven velocity is defined as:

$$\overline{u_s} = \frac{u_s \cdot \mu_0 / E_0}{u_s' \cdot \mu_0' / E_0'} \quad (3.13)$$

where u_s is the generalized Smoluchowski velocity, μ_0 is the zero shear viscosity of the specific PEO solution, and E_0 is the electric field strength. Eq (3.13) is made dimensionless by u_s' which denotes the velocity of 0.7% PEO solution flows under the electric field of 500 V/cm. μ_0' and E_0' stands for the zero shear viscosity of 0.7% PEO solution and the maximum electric field strength applied in the experiment. Therefore the definition takes both zero shear viscosity and electric field into account.

Figure 3.9 demonstrates the significant enhancing effect of shear thinning. It reveals that a stronger electric field can increase the shear rate leading to a more pronounced shear thinning effect. On the other hand, the PEO concentration is vital to the dimensionless EO velocity. As shown in Table 3.1, a PEO of concentration 0.7% provides the most significant shear thinning effect (smallest n value). The results prove that both the electric field and PEO concentration can promote EO driven effect due to the shear thinning rheological behavior.

3.4 Summary

EO driven flow has developed significantly, both theoretically and experimentally, in recent years. However challenges are still faced when dealing with EO driven flow of a non-Newtonian fluid due to its complex rheological behavior. Experimental and theoretical studies were conducted to tackle some of the challenges. The current monitoring method adopted as the major method in the experiment to measure the velocity of the non-Newtonian EO flow in a microchannel, is fabricated by soft lithography and standard PDMS procedures. The fluorescent microscopy imaging method was utilized to measure the flow profile. The results demonstrate that plug flow exist for a PEO solution at a moderate concentration. The zeta potential was calculated through coupling a generalized Smoluchowski approach and the power-

law constitutive model. The zeta potential values showed a slight variation with different PEO concentrations and the applied electric fields. However, as the variation were small, a constant zeta potential is suggested which was proven to be valid through the comparison between theoretical and experimental results. It can also be concluded that the for a shear thinning fluid, the EO driven flow can be enhanced as the shear fields setup by the flow itself reduce the apparent viscosity.

Chapter 4 Two Immiscible Layers of Electro-osmotic Driven

Flow with a Layer of Conducting non-Newtonian Fluid[†]

4.1 Introduction

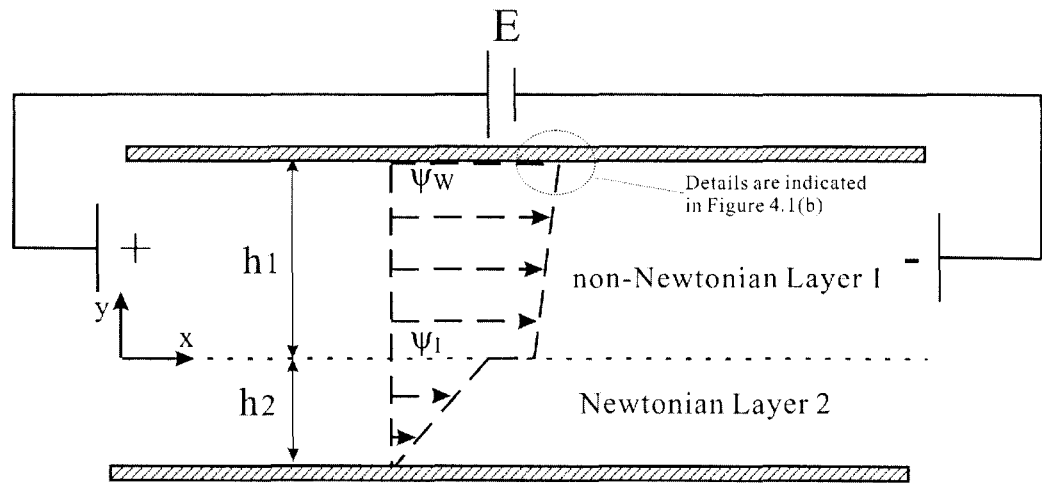
Electro-osmotic driven flow gets wide applications in microfluidics, among which the electro-osmotic (EO) pump utilizes the electro-osmotic force as the driven force. The drawback is that the non-conducting fluid cannot be driven by the electro-osmotic force directly. The idea of driving the non-conducting fluid by viscous shear stress of the conducting fluid is proposed (hybrid EO pump) [53]. Gao *et al.* [55, 56] and Li *et al.* [57, 58] conducted a study on two or multi layers immiscible fluids driven by electro-osmotic effect. Mathematical models were developed by solving the Poisson-Boltzmann and Navier-Stokes equations.

The non-Newtonian fluid based applications, such as DNA sample transportation, separation, mixing of lab-on-a-chip, are in high demand and received intense focus [144, 151, 152]. Due to the complexity of non-Newtonian behavior, theoretical investigations on the non-Newtonian electro-osmotic flow are limited. Currently, theoretical research mainly focus on polymer solutions, with which the bio-sample behavior similarly [70, 76, 77, 153].

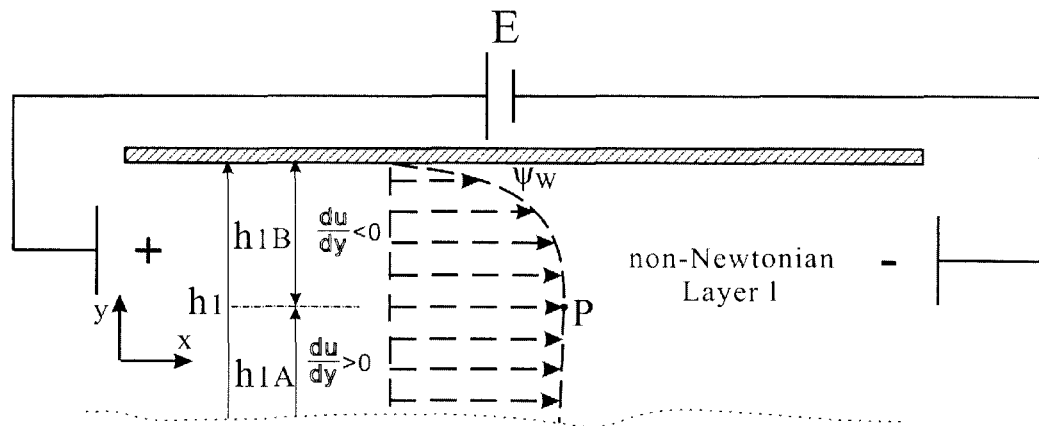
This chapter aims to develop analytical model for two immiscible layers of electro-osmotic driven flow in a parallel slit microchannel. One layer is a conducting non-Newtonian fluid driven by electro-osmotic force, the other layer is a non-conducting Newtonian fluid driven by interface shear. The constitutive equation of then non-Newtonian layer is described by power-law. The shear thinning effect which prompts the flow rate by reducing the shear rate dependent viscosity makes the shear thinning fluid ideal for hybrid EO pump.

4.2 Mathematical model

Figure 4.1 shows the model of the two immiscible layers flow between parallel plates. There are two physical layers, a non-Newtonian layer 1 and a Newtonian layer 2 represented by h_1 and h_2 , respectively (Figure 4.1 (a)).



(a) Two-fluid model over the whole channel



(b) Details in the non-Newtonian layer 1 near the wall boundary

Figure 4.1 Schematic diagram of two immiscible layers electro-osmotic driven flow model

The upper layer is a conducting non-Newtonian layer described by power-law model, driven by an applied external electric field. The lower layer is the non-conducting Newtonian layer driven by the interface viscous shear stress. To develop the

analytical model, the non-Newtonian layer h_1 is sub-divided into different regions as indicated in Figure 4.1 (b).

The heights of the non-Newtonian and Newtonian layers are h_1 and h_2 respectively.

The zeta potentials on the wall and the interface are ψ_w and ψ_I respectively.

4.2.1 Electric potential distribution in the conducting layer

The electric potential distribution only exists within the conducting non-Newtonian fluid and it follows the Poisson-Boltzmann equation:

$$\nabla^2 \psi = -\frac{\rho_e}{\varepsilon} \quad (4.1)$$

where: ψ is the electric potential in the solution, ρ_e is the electric charge density, ε is the electric permittivity of the solution.

The electric charge density can be expressed as:

$$\rho_e = -2z_v e_0 n_0 \sinh\left(\frac{z_v e_0}{\kappa_b T}\right) \quad (4.2)$$

where: n_0 is ionic concentration in the bulk solution, e_0 is the fundamental electric charge, z_v is the valence of the ion, ε is the electric permittivity of the solution, κ_b is the Boltzmann constant, T is the absolute temperature.

For the parallel plate model, the equation can be simplified as:

$$\frac{d^2 \psi}{dy^2} = \frac{2z_v e_0 n_0}{\varepsilon} \sinh\left(\frac{z_v e_0}{\kappa_b T}\right) \quad (4.3)$$

Eq (3) can be linearized by using the Debye-Hueckel approximation,

$\sinh\left(\frac{z_v e_0}{\kappa_b T}\right) = \frac{z_v e_0}{\kappa_b T}$. It physically means: $|z_v e_0 \psi| < \kappa_b T$. The linearized equation for the

electric potential distribution:

$$\frac{d^2\psi}{dy^2} = \kappa^2\psi \quad (4.4)$$

$$\kappa^2 = \frac{2z_v^2 e_0^2 n_0}{\varepsilon k_b T} \quad (4.5)$$

where κ is the Debye-Hueckel parameter and κ^{-1} is normally considered as the thickness of electric Debye layer(EDL).

Boundary conditions for the electric potential:

Wall boundary zeta potential at $y = h_1$: $\psi = \psi_w$

Interface boundary zeta potential at $y = 0$: $\psi = \psi_i$

The solution for the electric potential (Eq 4.4) under the boundary conditions is:

$$\psi = \frac{\sinh(\kappa y)}{\sinh(\kappa h_1)} \psi_w + \frac{\sinh(\kappa h_1 - \kappa y)}{\sinh(\kappa h_1)} \psi_i \quad (4.6)$$

4.2.2 Governing equations for the non-Newtonian layer

To evaluate the effect of electro-osmotic effect upon the non-Newtonian fluid, the model assumes that :

- (1) The non-Newtonian fluid is conducting and incompressible.
- (2) The properties of the non-Newtonian fluid are not influenced by local electric fields. While the local electric field may hold influence to the non-Newtonian fluid properties, but it is neglected in the model [141].
- (3) The liquid properties are independent of temperature. The Joule heating effects is neglected due to the low electric field strength and dilute electrolytes [154].

(4) The flow is fully developed and the no-slip boundary condition is applied.

Viscous flow stands and the convection term in the momentum equation is ignored due to low Reynolds number.

4.2.3 Governing equation and power-law model

The Cauchy momentum equation for an incompressible non-Newtonian liquid is given by:

$$\frac{d}{dy}(\mu_1 \frac{du_1}{dy}) - \tilde{N} P + F_x = 0 \quad (4.7)$$

The viscosity depends on shear rate and is described by the power-law model. We consider a non-Newtonian fluid whose viscosity depends only on the shear rate, namely shear thinning and shear thickening fluids.

A power-law rheology [62] which is the relationship between the viscosity and shear rate is given as follows:

$$\mu_1 = m \left| \frac{du_1}{dy} \right|^{n-1} \quad (4.8)$$

where m and n are fluid consistency coefficient and flow behavior index respectively.

For $0 < n < 1$, it indicates the shear thinning fluid;

$n > 1$, it indicates the shear thickening fluid;

$n = 1$, it represents the Newtonian fluid.

F_x represents the effect of body force due to the electro-osmotic force .

$$F_x = E_0 \rho_e = E_0 (-\varepsilon \nabla^2 \psi) = -E_0 \varepsilon \kappa^2 \psi \quad (4.9)$$

Substituting Eq (4.9) into equation (4.7), the momentum equation of the non-Newtonian layer gives:

$$\frac{d}{dy} \left(m \left| \frac{du_1}{dy} \right|^{n-1} \frac{du_1}{dy} \right) = E_0 \varepsilon \kappa^2 \psi \quad (4.10)$$

A typical electro-osmotic velocity profile is a plug flow [155]. To solve Equation (4.10), different regions should be discussed separately referring to the sign of the velocity gradient. As shown in Figure 4.1 (b), a turning point “P” exists where the sign of velocity gradient changes. The non-Newtonian layer h_1 is sub-divided into h_{1A} and h_{1B} accordingly.

In the region (h_{1A} , h_1) we have:

$$\mu_1 = m \left(-\frac{du_{1B}}{dy} \right)^{n-1} \quad (4.11)$$

The governing equation becomes:

$$\frac{d}{dy} \left(-m \left(-\frac{du_{1B}}{dy} \right)^n \right) = E_0 \varepsilon \kappa^2 \psi \quad (4.12)$$

Integrate twice gives:

$$u_{1B} = -\int_{h_{1A}}^y \left[\frac{E_0 \varepsilon \kappa}{m \sinh(\kappa h_1)} (\psi_l \cosh(\kappa h_1 - \kappa y) - \psi_w \cosh(\kappa y)) + c_1 \right]^{\frac{1}{n}} dy + c_3 \quad (4.13)$$

Similarly, in the region (0, h_{1A}) the governing equation becomes:

$$\frac{d}{dy} \left(m \left(\frac{du_{1A}}{dy} \right)^n \right) = E_0 \varepsilon \kappa^2 \psi \quad (4.14)$$

Hence,

$$u_{1A} = \int_0^y \left[\frac{E_0 \varepsilon \kappa}{m \sinh(\kappa h_1)} (\psi_w \cosh(\kappa y) - \psi_l \cosh(\kappa h_1 - \kappa y)) + c_2 \right]^{\frac{1}{n}} dy + c_4 \quad (4.15)$$

$c_1 \sim c_4$ are integration constants to be determined by boundary conditions.

At the location where the velocity gradient changes sign at point P (Figure 4.1 (b)) ($y = h_{1A}$), the velocity gradient equals zero and the matching condition is applied:

$$\left[\frac{E_0 \varepsilon \kappa}{m \sinh(\kappa h_1)} (\psi_w \cosh(\kappa y) - \psi_l \cosh(\kappa h_1 - \kappa y)) + c_2 \right]^{\frac{1}{n}} = 0 \quad (4.16)$$

$$\begin{aligned} & \int_0^y \left[\frac{E_0 \varepsilon \kappa}{m \sinh(\kappa h_1)} (\psi_w \cosh(\kappa y) - \psi_l \cosh(\kappa h_1 - \kappa y)) + c_2 \right]^{\frac{1}{n}} dy + c_4 \\ &= - \int_{h_1}^y \left[\frac{E_0 \varepsilon \kappa}{m \sinh(\kappa h_1)} (\psi_l \cosh(\kappa h_1 - \kappa y) - \psi_w \cosh(\kappa y)) + c_1 \right]^{\frac{1}{n}} dy + c_3 \end{aligned} \quad (4.17)$$

4.2.4 Governing equation for Newtonian layer

Similar assumptions with that of the non-Newtonian layer can be made.

The governing equation is:

$$\mu_2 \frac{d^2 u_2}{dy^2} = 0 \quad (4.18)$$

Hence, the velocity profile is:

$$u_2 = c_5 y + c_6 \quad (4.19)$$

c_5 and c_6 are integration constants to be determined by boundary conditions.

Boundary conditions

At the wall ($y = h_1$), no-slip boundary condition is applied:

$$- \int_{h_1}^y \left[\frac{E_0 \varepsilon \kappa}{m \sinh(\kappa h_1)} (\psi_l \cosh(\kappa h_1 - \kappa y) - \psi_w \cosh(\kappa y)) + c_1 \right]^{\frac{1}{n}} dy + c_3 = 0 \quad (4.20)$$

At the interface between the non-Newtonian and Newtonian ($y = 0$), due to the surface charge, shear stress is not continuous. The matching conditions are the continuities of velocity and the shear stress balance:

$$\int_0^y \left[\frac{E_0 \varepsilon \kappa}{m \sinh(\kappa h_1)} (\psi_w \cosh(\kappa y) - \psi_l \cosh(\kappa h_1 - \kappa y)) + c_2 \right]^{\frac{1}{n}} dy + c_4 = c_5 y + c_6 \quad (4.21)$$

$$\tau_{\mu_1} + \tau_e = \tau_{\mu_2} \quad (4.22)$$

where τ_{μ_1} is viscous shear stress for the non-Newtonian layer,

$$\tau_{\mu_1} = \mu_1 \frac{du_{1A}}{dy} = m \left| \frac{du_{1A}}{dy} \right|^{n-1} \frac{du_{1A}}{dy};$$

τ_e is the electro-shear stress caused by the presence of the electric charge at the

interface, $\tau_e = E(-\varepsilon) \frac{d\psi}{dy}$; and τ_{μ_2} is the viscous shear stress for the Newtonian layer,

$\tau_{\mu_2} = \mu_2 \frac{du_2}{dy}$. So the shear stress balance (Eq (4.22)) becomes:

$$\begin{aligned} & m \left[\frac{E_0 \varepsilon \kappa}{m \sinh(\kappa h_1)} (\psi_w \cosh(\kappa y) - \psi_i \cosh(\kappa h_1 - \kappa y)) + c_2 \right]^{\frac{1}{n}-1} \\ & \left[\frac{E_0 \varepsilon \kappa}{m \sinh(\kappa h_1)} (\psi_w \cosh(\kappa y) - \psi_i \cosh(\kappa h_1 - \kappa y)) + c_2 \right]^{\frac{1}{n}} \\ & + E(-\varepsilon) \frac{d \left[\frac{\sinh(\kappa y)}{\sinh(\kappa h_1)} \psi_w + \frac{\sinh(\kappa h_1 - \kappa y)}{\sinh(\kappa h_1)} \psi_i \right]}{dy} = \mu_2 \frac{du_2}{dy} \end{aligned} \quad (4.23)$$

For the Newtonian layer, at wall ($y = -h_2$), no-slip boundary is applied.

$$u_2 = 0 \quad (4.24)$$

4.3 Results and discussion

In section 4.2, the EDL distributions were derived in the conducting non-Newtonian layer and the velocity distributions for both the non-Newtonian layer and Newtonian layer were obtained. The non-Newtonian layer height $h_1 = 100 \mu\text{m}$ and the Newtonian layer height h_2 is $30 \mu\text{m}$.

The wall zeta potential ψ_w depends on the wall properties and fluid ionic properties.

In the analysis, we choose $\psi_w = -40\text{mv}$. The interface zeta potential ψ_i is determined by ionic properties of both fluids, PH value and the concentration of electrolyte. The interface zeta potential ψ_i is chosen as -40mV . The applied electrical field $E = 1000$

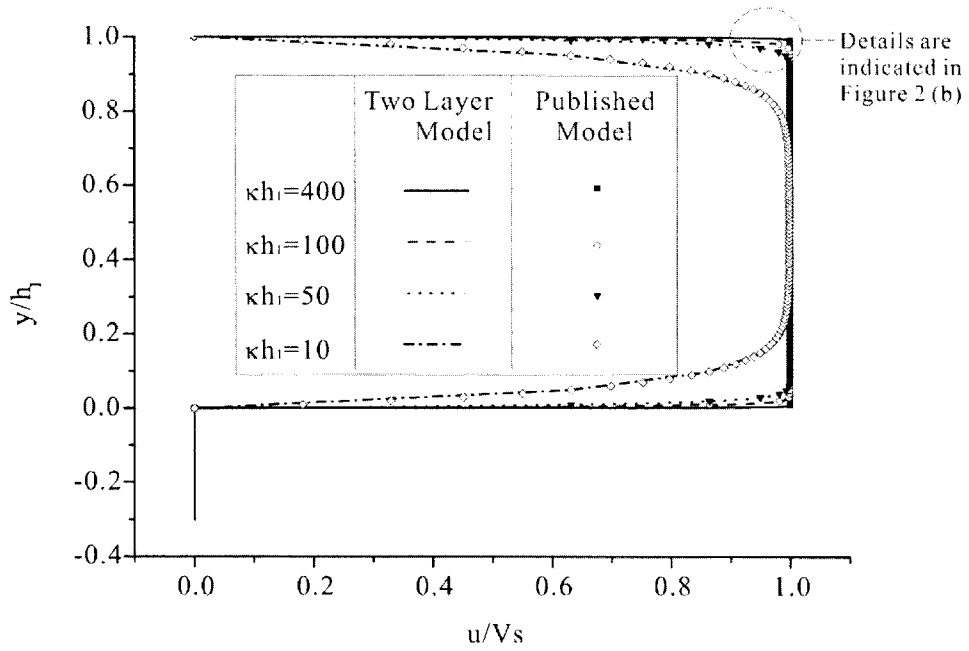
V/m, the electrical permittivity $\varepsilon = 7.08 \times 10^{-10}$ F/m, fluid consistency coefficient $m = 0.001$ Pa·sⁿ and fluid behavior index $n = 0.5$, Newtonian fluid viscosity $\mu_2 = 0.001$ Pa·s. The generalized Smoluchowski velocity V_s is chosen as reference velocity [72], $V_s = n\kappa^{\frac{1-n}{n}} \left(-\frac{\varepsilon\psi_w E}{m} \right)^{\frac{1}{n}}$.

4.3.1 Effect of κh_1

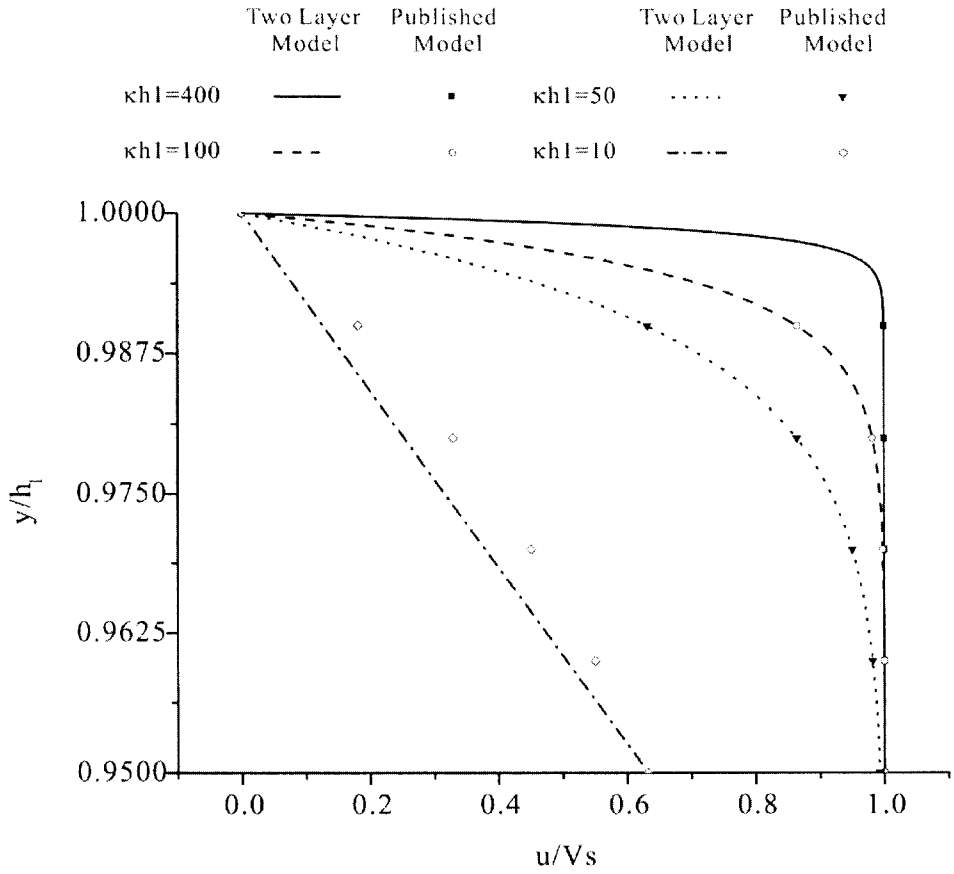
κh_1 means ratio of the non-Newtonian layer height over the EDL thickness. To better understand the effect of κh_1 , the results present in this part is calculated under symmetrical EDL condition, i.e. $\psi_w = \psi_l$. As shown in Figure 4.2 and Figure 4.3, to compare the proposed model with a single layer power law fluid [72, 73], μ_2 is chosen as 1000 Pa·s. The symmetrical EDL condition $\psi_l = \psi_w$ makes the Newtonian layer fluid resemble that of the wall. In that case the non-Newtonian layer flow resembles the single layer fluid EOF driven flow [72]. As shown in Figure 4.2 and Figure 4.3, the proposed two layer model matches well with the single layer model, which proves the validity of this model.

A larger value of κh_1 corresponds to a thinner EDL. When κh_1 is large, the electro-osmotic force will be confined near the wall and the interface, while the electro-osmotic effect takes negligible effect outside the thin EDL region. Under symmetrical zeta potential, it forms the plug-like shape. The velocity accelerates to its maximum value within the thin EDL region and maintains its maximum value until it reaches the interface, where velocity reduces sharply to zero. When $\kappa h_1 = 400$, the velocity profile represents a uniform profile in the non-Newtonian region. When $\kappa h_1 = 10$, the electro-osmotic force is not confined near the wall and interface.

Instead, it takes a large portion of the channel. Therefore, the profile is becoming more parabolic.



(a) Dimensionless velocity distributions of the whole channel under symmetric EDL condition



(b) Dimensionless velocity distributions near the wall boundary

Figure 4.2 Comparisons of the analytical solution between the two-fluid flow model and the single-fluid model [72] for a larger value κh_1 .

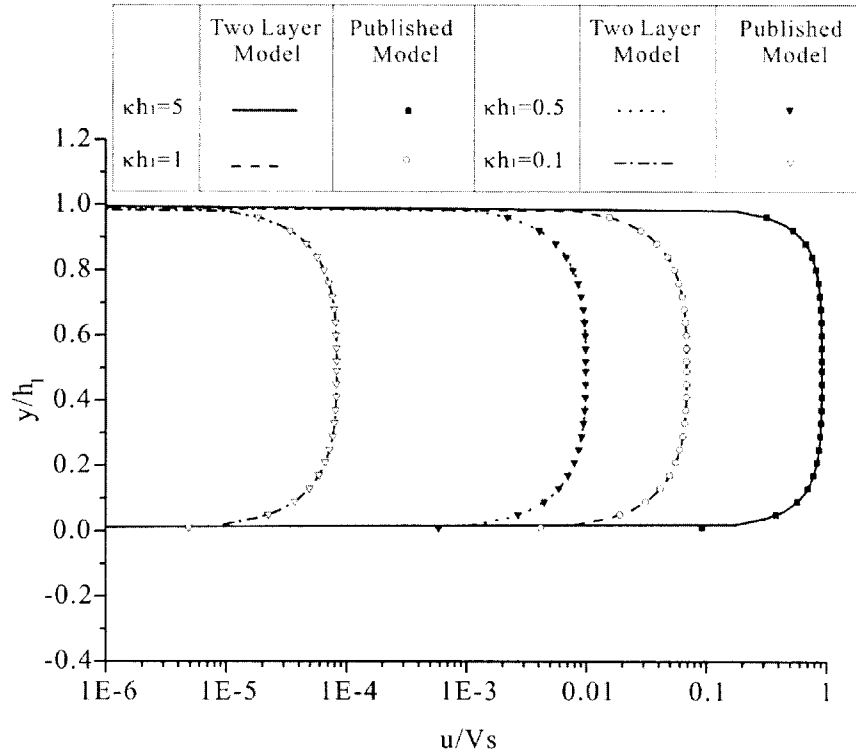


Figure 4.3 Comparisons of the analytical solution between the two-fluid flow model and the single-fluid model [72] for a smaller value κh_1 .

As the value of κh_1 continue to reduce from $\kappa h_1=5$ to $\kappa h_1=0.1$, the electro-osmotic force are distributed over the whole non-Newtonian layer. The maximum velocity cannot reach the generalized Smoluchowski velocity V_s and it becomes a parabolic-shape profile.

4.3.2 Effect of zeta potentials ψ_w & ψ_i

The zeta potential is related to both the material properties which form the boundary and the interface. As such, the unsymmetrical EDL condition is considered. The interface zeta potential will be set to zero to investigate the influence of wall zeta potential ψ_w .

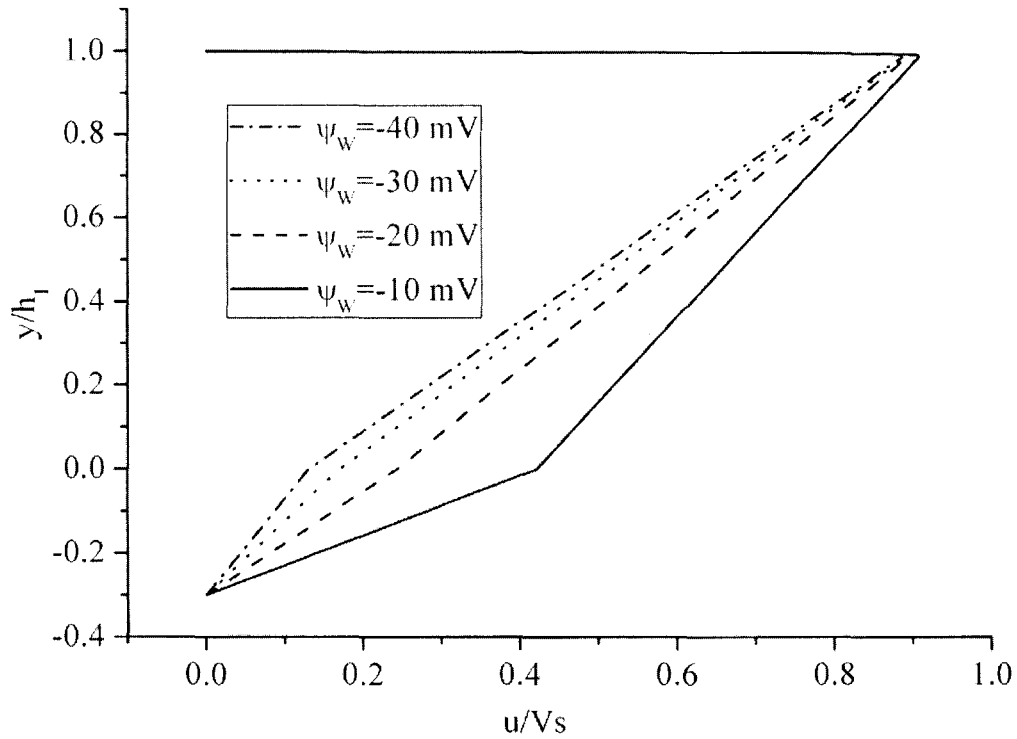


Figure 4.4 Dimensionless velocity distribution for different values of wall zeta potential $\psi_w \cdot \kappa h_1 = 400$, $E = 1000$ V/m

Figure 4.4 shows the dimensionless velocity profile at the symmetric line of the two fluids with the applied electric field $E = 1000$ V/m. As shown in Figure 4.4, the magnitude of wall zeta potential will determine the maximum speed hence the velocity gradient, which will influence the non-Newtonian fluid apparent viscosity. In shear thinning fluid, higher wall zeta potential leads to a higher velocity gradient hence a lower apparent viscosity. Results in Figure 4.4 show that when $\psi_w = -40$ mV, the velocity gradient is larger and the average apparent viscosity is smaller. When ψ_w changes from -40 mV to -10 mV, the results indicate a smaller velocity gradient and a larger apparent average viscosity.

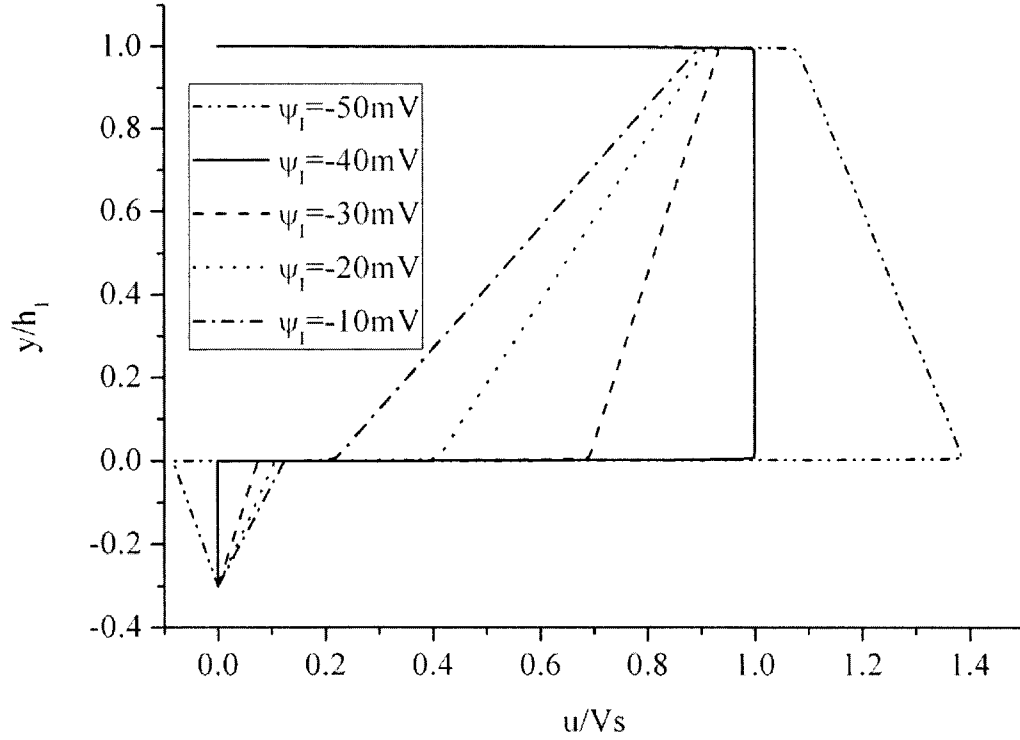


Figure 4.5 Dimensionless velocity distributions vary with the interface zeta potential. ($\kappa h_1 = 400$, $E = 1000$ V/m and $\psi_w = -40$ mV)

Figure 4.5 shows the influence of the interface zeta potential on the dimensionless velocity distribution. The flow conditions remain the same with that of Figure 4.4, except that a fixed wall zeta potential $\psi_w = -40$ mV and variable ψ_i are used. When $\psi_i = -50$ mV, which is larger than ψ_w , the velocity profile is different from those whose interfacial potentials are smaller than ψ_w . The velocity gradients in both the non-Newtonian and Newtonian layers are negative due to a large velocity jump near the interface. For the symmetrical EDL in the non-Newtonian layer, $\psi_i = \psi_w = -40$ mV, the Newtonian layer will have no obvious velocity. When $\psi_i \ll \psi_w$, fluid velocity change decreases near the interface. When ψ_i becomes smaller, the electro-osmotic effect is also reduced, leading to a smaller velocity jump at the interface. Hence, cause the velocity gradient of the Newtonian layer to be smaller.

4.3.3 Effect of the Newtonian layer viscosity μ_2 and the non-Newtonian layer fluid

consistency coefficient m

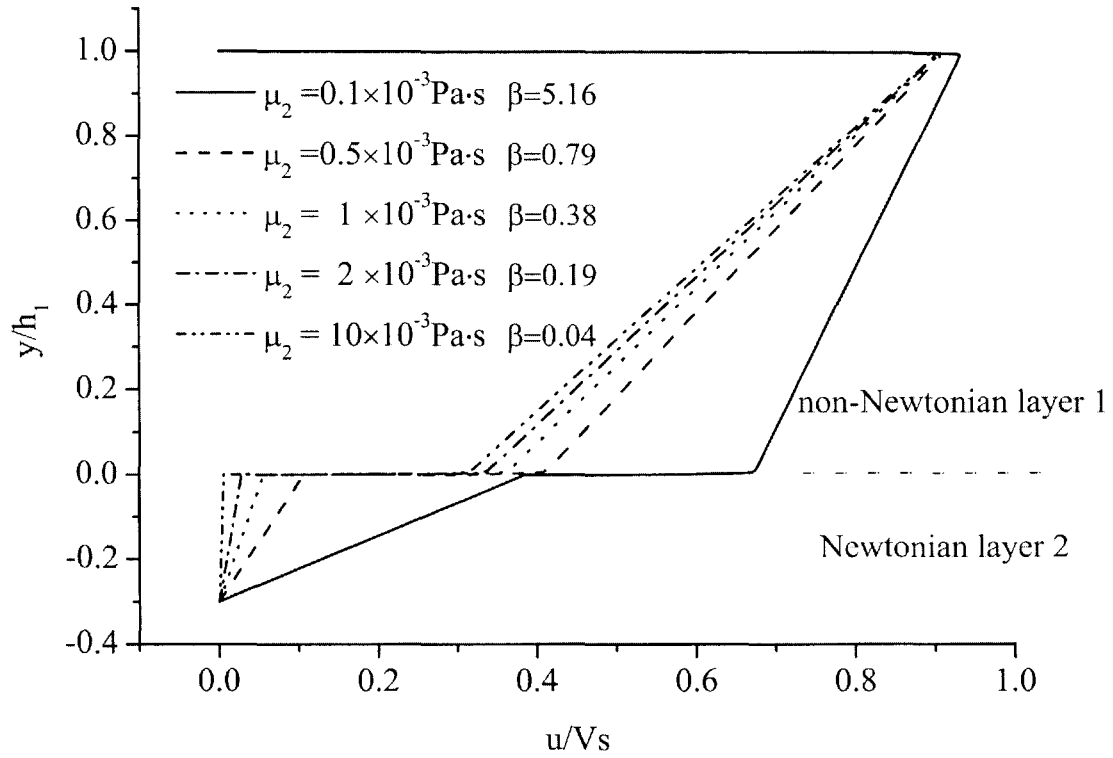


Figure 4.6 Dimensionless velocity distributions for different values of Newtonian layer viscosity μ_2 .

$$(\kappa h_1 = 400, \psi_f = -20 \text{ mV}, m = 0.001 \text{ Pa} \cdot \text{s}^n \text{ and } n = 0.5)$$

When μ_2 is small, the flow resistance of the layer 2 is also small. Hence layer 2 will be driven easily (Figure 4.6). A steeper velocity gradient of layer 2 is observed when the viscosity ratio is larger due to the higher flow resistance of layer 2. The viscosity of Newtonian layer 2 (μ_2) influences the Non-Newtonian layer in several ways. Firstly, the maximum speed of the non-Newtonian layer 1 is smaller when the Newtonian layer 1 is more viscous. Secondly, the velocity profile of the non-Newtonian layer 1 becomes steeper when it is beside a more viscous Newtonian layer 2, so that the no-slip boundary condition can be satisfied. In Figure 4.6 and Figure 4.7, β is defined as the viscosity ratio of non-Newtonian layer 1 over

Newtonian layer 2 ($\beta = \bar{\mu}_1 / \mu_2$), where $\bar{\mu}_1 = \int_{\text{layer 1}} m \left| \frac{du_1}{dy} \right|^{n-1} dy$. β is introduced to indicate the overall viscosity ratio between non-Newtonian layer 1 and Newtonian layer 2.

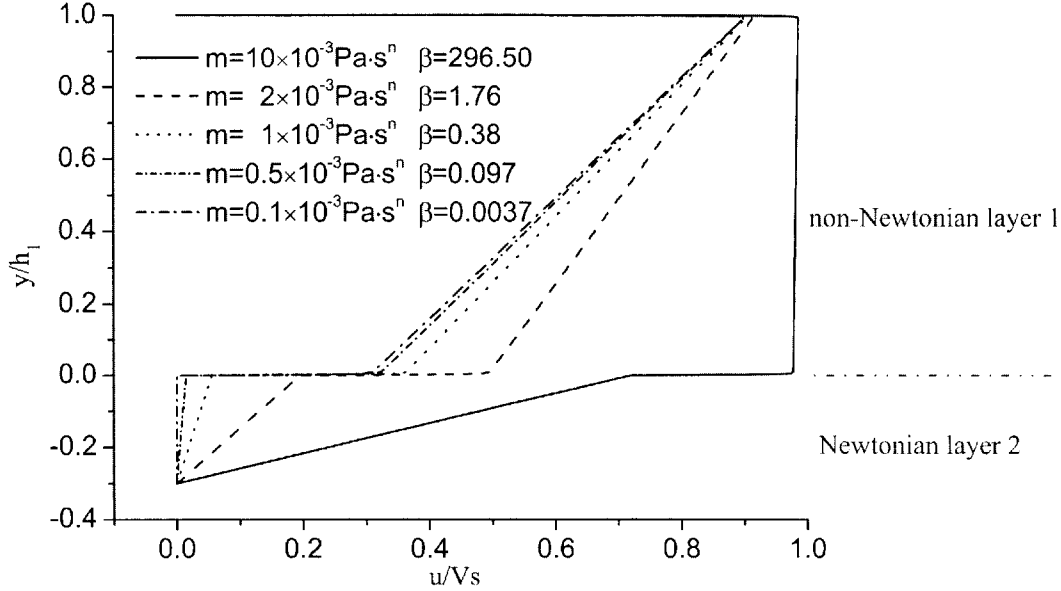


Figure 4.7 Dimensionless velocity distributions affected by the non-Newtonian fluid consistency coefficient m . ($\psi_w = -40$ mV, $\psi_l = -20$ mV, $\kappa h_1 = 400$, $\mu_2 = 0.001$ Pa·s and $n=0.5$).

The non-Newtonian layer fluid consistency coefficient m is one of the two parameters that describe the power-law of the non-Newtonian fluid behavior. The influence of the parameter m to the velocity profile is shown in Figure 4.7. When m is large ($m = 10 \times 10^{-3}$ Pa·sⁿ), the non-Newtonian velocity can reach the generalized Smoluchowski velocity V_s and the drag from the Newtonian layer will have limited influence upon the non-Newtonian layer. The velocity gradient in the non-Newtonian layer 1 is small while in Newtonian layer 2 is large. However, when m is smaller, the Newtonian layer 2 will take greater effects on the non-Newtonian layer 1. Figure 4.7 shows that when m is smaller, u_1 cannot reach the generalized Smoluchowski velocity V_s . When m is small ($m = 1 \times 10^{-4}$ Pa·sⁿ), the Newtonian layer velocity gradient decreases.

4.3.4 Effect of flow behavior index n

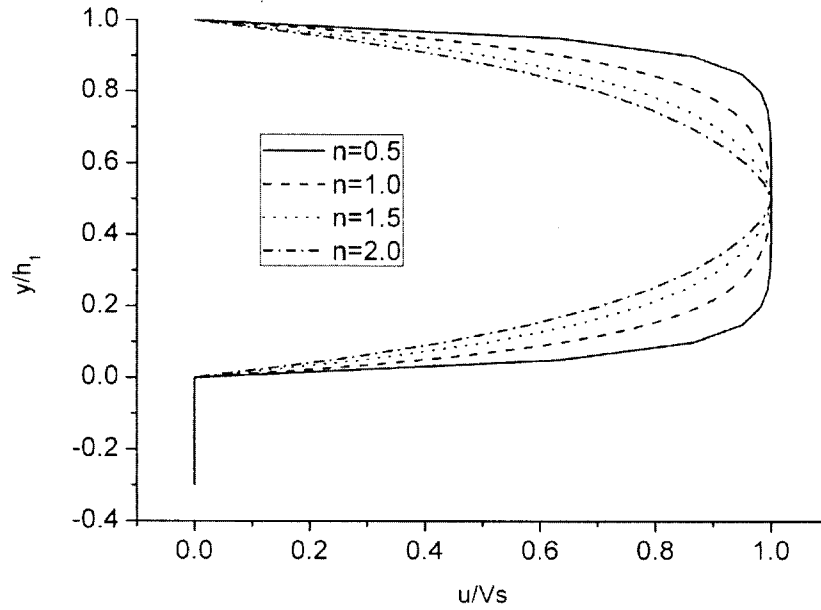


Figure 4.8 Dimensionless velocity distributions for different values of the flow behavior index n .

$$(\kappa h_1 = 10, E = 1000 \text{ V/m and } \psi_I = \psi_W = -40 \text{ mV})$$

Figure 4.8 shows the dimensionless velocity profile for different values of the flow behavior index of the non-Newtonian layer. In the analysis $m = 0.001 \text{ Pa}\cdot\text{s}^n$, $\mu_2 = 1000 \text{ Pa}\cdot\text{s}$. The flow behavior index n influences the shape of the velocity profile. As n decreases, the velocity profile becomes more plug-like. This is because that lower n will reduce the apparent viscosity. Considering the same shear rate, the higher value n will increase the apparent viscosity making the flow more parabolic. Note that the value of κh_1 is comparatively low and as such the effect of n is obvious. While under a high value of κh_1 , a thin EDL region, the effect of n on the velocity profile is limited. The flow behavior index takes great impact on the velocity profile only under a relatively thick EDL condition.

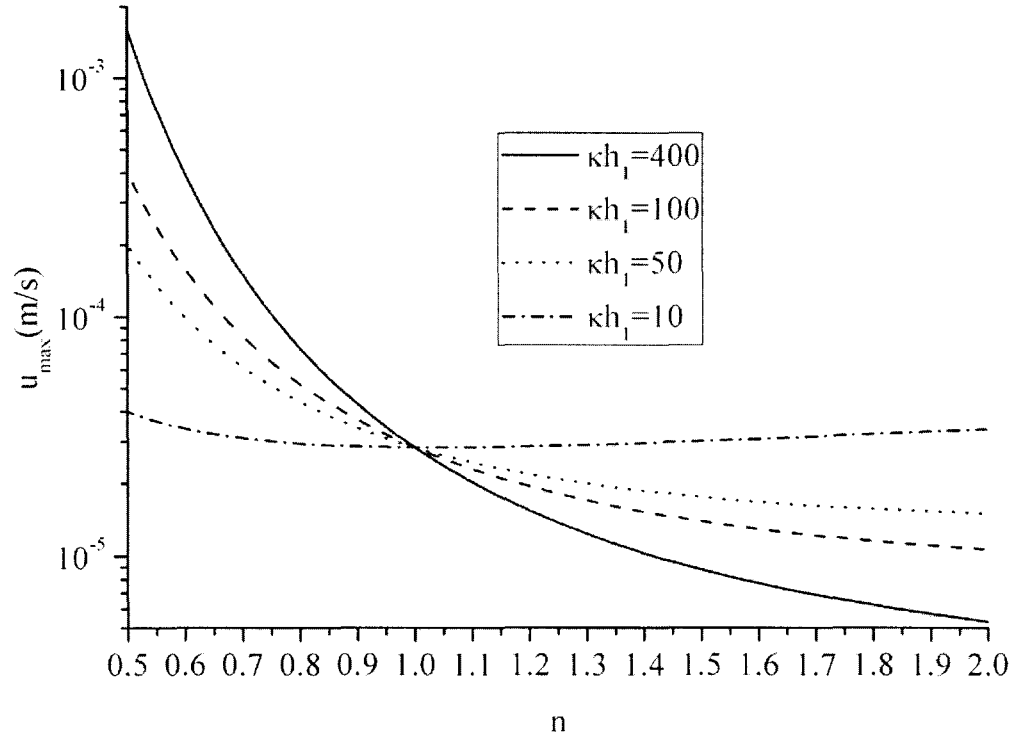


Figure 4.9 Variation of the maximum velocity with the fluid index n for different values of

$$\kappa h_1. (E=1000 \text{ V/m}, \psi_I = \psi_W = -40 \text{ mV}, m = 0.001 \text{ Pa} \cdot \text{s}^n \text{ and } n = 0.5)$$

Figure 4.9 shows the variation of the maximum velocity of the non-Newtonian layer 1 with flow behavior index n . The flow behavior index influences the maximum velocity. The maximum velocity varies from 10^{-3} to 10^{-6} m/s as n varies from 0.5 to 2.0 for $\kappa h_1 = 400$. The larger n contributes to an exponential increasing in the apparent viscosity which causes the reduction in the maximum velocity. This parameter has a significant impact on the maximum velocity. It is also indicated that smaller κh_1 will lead to a smaller value of maximum velocity for the shear thinning fluid ($n < 1$). On the other hand, higher value of κh_1 can generate high maximum velocity for shear thinning fluid. For shear thickening fluid, the influence is not significant.

One of the most important effects of driving by the non-Newtonian fluid is that the shear thinning effect. Generally, for power-law fluid: $\mu = m \left| \frac{du_1}{dy} \right|^{n-1}$, m and n are fluid consistency coefficient and flow behavior index respectively. For shear thinning fluid ($n < 1$), higher shear rate will lower the viscosity, therefore the flow rate will be enhanced.

The average flow rate for the non-Newtonian layer 1 is defined as:

$$\begin{aligned} Q_1 &= \int_{y \in (0, h_1)} u_1 dy \\ &= \int_{y \in (0, h_{1,A})} \left[\int_0^y \left[\frac{E_0 \varepsilon \kappa}{m \sinh(\kappa h_1)} (\psi_w \cosh(\kappa y) - \psi_l \cosh(\kappa h_1 - \kappa y)) + c_2 \right]^{\frac{1}{n}} dy + c_4 \right] dy \\ &\quad + \int_{y \in (h_{1,A}, h_1)} \left[- \int_{h_{1,A}}^y \left[\frac{E_0 \varepsilon \kappa}{m \sinh(\kappa h_1)} (\psi_l \cosh(\kappa h_1 - \kappa y) - \psi_w \cosh(\kappa y)) + c_1 \right]^{\frac{1}{n}} dy + c_3 \right] dy \end{aligned} \quad (4.25)$$

and the average flow rate for Newtonian layer 2 is expressed as:

$$\begin{aligned} Q_2 &= \int_{y \in (-h_2, 0)} u_2 dy \\ &= \int_{y \in (-h_2, 0)} [c_5 y + c_6] dy \end{aligned} \quad (4.26)$$

where $c_3 \sim c_6$ are parameters to be determined by boundary conditions.

Figure 4.10 shows the dimensionless volume flow rate of the non-Newtonian layer 1 versus the flow behavior index n . The non-Newtonian layer is driven by EOF. Q_1 is the volume flow rate of the non-Newtonian layer 1. Q_{1m} is the reference volume flow rate of the non-Newtonian layer 1. When $n=1$ and an electric strength $E=1.0 \times 10^3 \text{ V/m}$. The impact of n is significant and is clearly shown in Figure 4.10. For the shear thinning fluid ($n < 1$), the flow rate is significant higher. For shear thickening fluid ($n > 1$), the increase of flow rate is not as significant as that of the shear thinning fluid ($n < 1$).

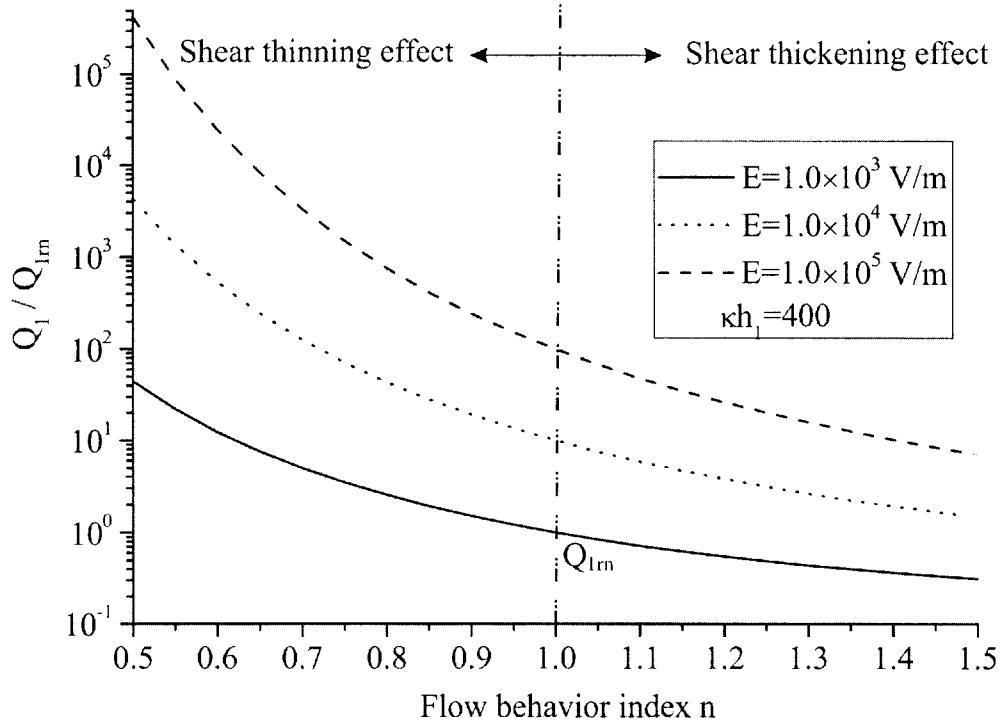


Figure 4.10 Dimensionless non-Newtonian Layer volume flow rate versus the flow behavior index n .

$$(\psi_w = -40 \text{ mV}, \psi_l = -20 \text{ mV}, m = 0.001 \text{ Pa}\cdot\text{s}^n \text{ and } \mu_2 = 0.001 \text{ Pa}\cdot\text{s})$$

One of the most promising applications for the two-layer model is to use the non-Newtonian EOF effect to drive the non-conducting fluid. Figure 4.11 presents the volume flow rate of the Newtonian layer 2, which is driven by the interface shear generated by the non-Newtonian layer 1. Q_2 is the volume flow rate of the Newtonian layer, Q_{2m} is the reference volume flow rate of the Newtonian layer when $n=1$ and electric strength $E = 1.0 \times 10^3 \text{ V/m}$.

The results (Figure 4.11) shows that the shear thinning effect improves the flow rate Q_2 . On the other hand, if the Newtonian layer is driven by shear thickening fluid, marginal increase in flow rate Q_2 is seen even though the electric field is increased by 2 orders. This shows that the shear thinning fluid is more effective on fluid driving.

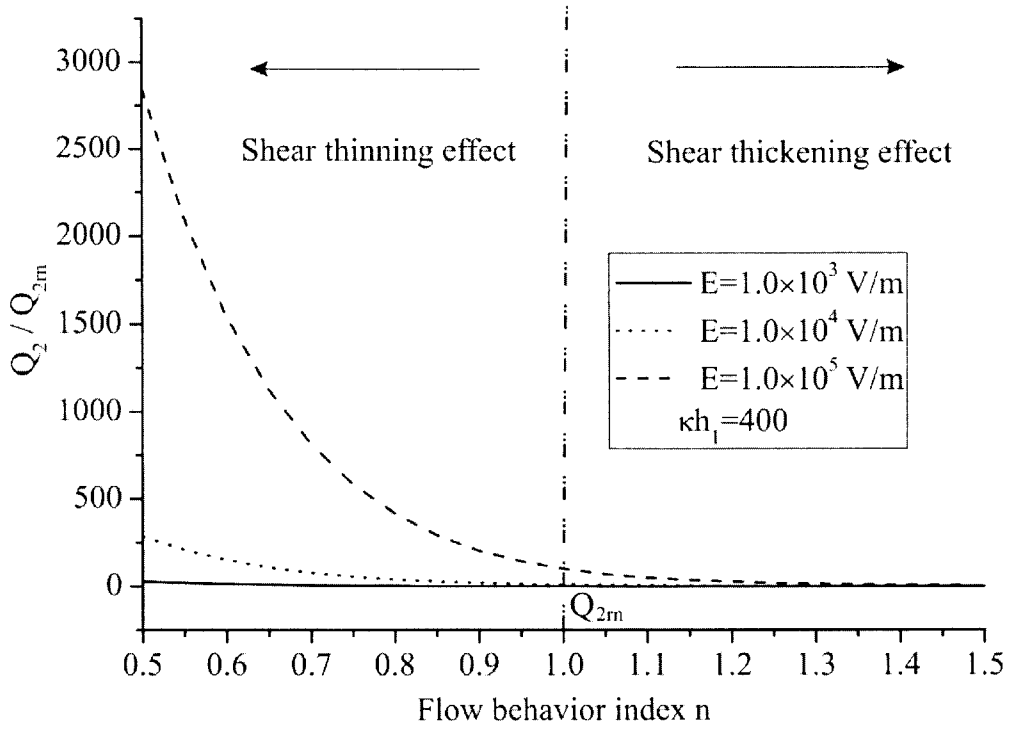


Figure 4.11 Dimensionless Newtonian Layer volume flow rate versus the flow behavior index n . (ψ_w

$$=-40 \text{ mV}, \psi_l=-20 \text{ mV}, m=0.001 \text{ Pa}\cdot\text{s}^n \text{ and } \mu_2=0.001 \text{ Pa}\cdot\text{s})$$

The results show that the shear thinning effect makes the driving of both layers more effectively. The increase in the flow rate is significant due to the reduction of the apparent viscosity.

4.4 Summary

The two immiscible layers electro-osmotic driven flow model with one layer of conducting non-Newtonian fluid was proposed. The non-conducting fluid is driven by the interface shear.

Both the m and n take great impact on the shape of the velocity profile and the volume flow rate. When flow index n reduces from 1 to 0.5, the flow rate increases by 40 times. The results show that the shear thinning effect improves the volume flow rate, which makes it ideal for both direct electro-osmotic driving and hybrid driving.

Chapter 5 An Electric Field Activated Droplet Formation in Flow-focusing Device

5.1 Introduction

Droplets formation of one liquid in the other immiscible liquid are useful in a wide range of applications, such as drug discovery, gene expression analysis, and high throughput assays [156, 157], especially when the droplet size can be accurately controlled on the micro- or nano-scale [156, 158]. Although there are still many fundamental problems which need to be resolved, it is clear that microfluidic technologies offer a promising new route for the generation of monodisperse droplets [159, 160], ranging from some micrometers to hundreds of micrometers [161].

The most common microchannel geometries for generating droplets are T-junction [162-165] and flow focusing devices [158, 166-170]. Both types of systems are capable of producing monodisperse droplets. The first microfluidic droplet generator was reported by Thorsen *et al.* [171] who used a T-junction geometry to generate water droplets in an organic oil. Similar microfluidic approaches have been described elsewhere [158, 166-170, 172].

The size of droplet in the microfluidic system is largely determined by the channel geometry, the properties of the liquids and the flow rates of the two liquids involved [104, 173-177]. Besides, several flow regimes, such as squeezing, dripping and jetting, are formed in different flow rates for a specific geometry, which have a great effect on the droplet size distributions. Therefore, a specific size of droplet is not easy to form in the microchannel and the timing of the droplet production cannot be controlled simultaneously. One potential means of overcoming these limitations is to use active droplet formation methods. When an electric field is applied to the liquids

by integrating electrodes into microchannel directly [178, 179] or with the use of ITO glass [180-182], it has a great potential to rapidly control the droplet formation.

The geometry and location of the external electrodes usually has a strong influence on the electric field distribution [183], making the droplet formation system sensitive to electric field. In addition, electrochemical effects represent a major limitation in the droplet formation devices when the electrodes are in direct contact with the liquid, such as flow instabilities, degradation of the electrodes, droplet size drastic change, satellites of droplet and bubble formation. A reliable method of non-contact electrodes to avoid electrochemical effects needs further investigation.

In this study, an external electric field was implemented in a flow-focusing device. The droplet size varying by changing the voltage and frequency of the electric field were investigated. In addition, the droplet regimes and the droplet size distribution under different external electric fields for a fixed flow rate of the liquids were also analyzed.

5.2 Experimental

5.2.1 Experimental System

The schematic diagram of the experimental setup is shown in Figure 5.1. The flow focusing device was connected to the syringe pump system (Centoni neMESYS) and a high voltage generator system which were used to control the flow rates and the applied electric field, respectively. Droplet formation behavior was observed under an inverted microscope (Lecia DM ILM) and recorded via a high-speed camera (Phantom V611, shutter speed up to 1/100 000 s). Moreover, the camera, high voltage generator system, and the syringe pump system are connected with a

computer and the input and output experimental data and images can be collected simultaneously.

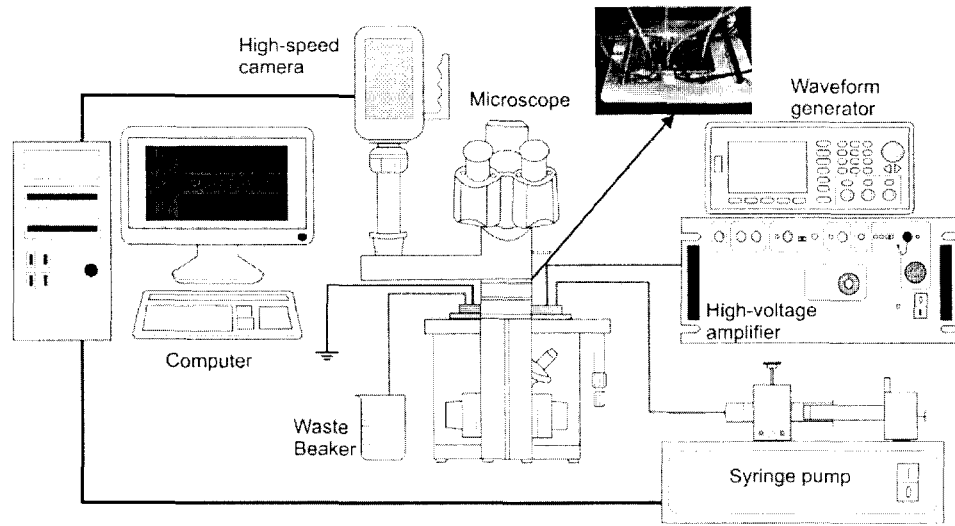


Figure 5.1 Schematic diagram of experimental setup. The apparatus fundamentally consisted of six parts: (1) Syringe pump system, (2) High-voltage generator system, (3) Flow focusing device (chip), (4) Microscope system, (5) High-speed camera, and (6) Data collection system.

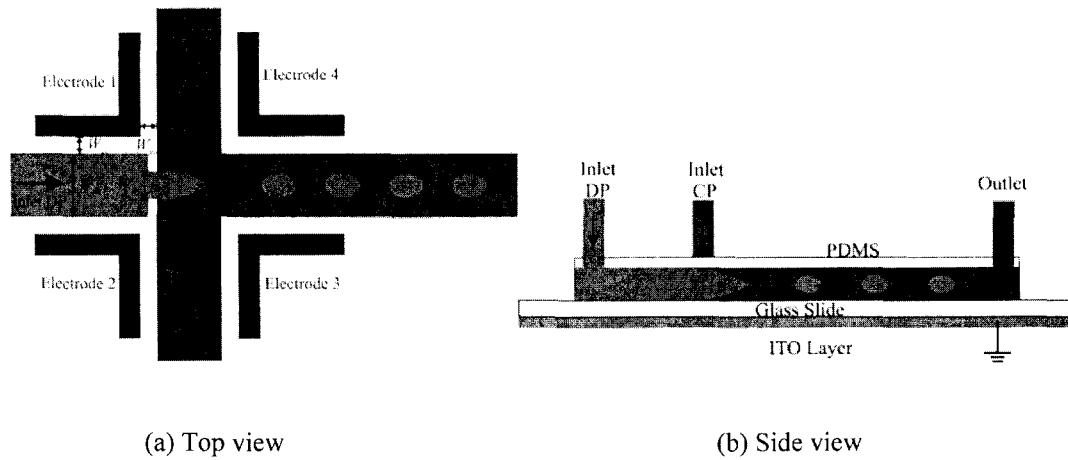


Figure 5.2 Schematic diagram of the flow-focusing geometry implemented in a microfluidic device. DP, CP here denote dispersed phase and continuous phase, respectively. The main channel width $W_{ch} = 100 \mu m$; the height of microchannel is $35 \mu m$. $W_{ga} = 50 \mu m$. Three sizes of orifices $W_{or} = 25, 75$ and $100 \mu m$ were designed.

5.2.2 Flow Focusing Device

Figure 5.2 shows the overall view of the flow-focusing geometry implemented in the experiment. The cross section of the channels was rectangular. Three channels of liquids converges into a main channel and flow downstream through a contraction. The dispersed phase flows in the center channel while the continuous phase flows in the two side channels. Droplet breakup and formation occurs once the viscous force overcome surface tension at the two-phase interface.

The flow-focusing chip under investigation was fabricated with a soft-lithography technique [184]. Polydimethylsiloxane (PDMS, Dow Corning Co. SYLGARD® 184) was used as the stamp resin to replicate the channel details from an SU-8 mold (SU-8 2075, Micro-Chem Co.) mold and the hardened PDMS with inlet and outlet holes was then bonded to an Indium Tin Oxide (ITO) glass (One side of the glass was coated with ITO to ensure its uniform conductive property) by oxygen plasma bonding.

5.2.3 External Electric Field

Four electrodes (see Figure 5.2 (a)) were patterned parallel to the channels by using the microsolidics technique [185]. The liquids and electrode channels were therefore within the same plane and positioned within a micron accuracy. Electrodes 1 and 2 were connected with high voltage and Electrodes 3 and 4 were grounded, which induce an electric field in the streaming direction. The electrodes are not in contact with the liquids to avoid electrochemical effects. The bottom of the ITO glass was grounded to prevent electrocoalescence downstream of the channel and ensure stable droplet formation.

Electric field was generated by the combination of Agilent 33500 B waveform generator and Trek 5/80 high voltage amplifier. The waveform generator generated one electric signal of specific voltage and frequency (sine wave is adopted), which was then amplified by the amplifier at the constant amplification factor of 1000 before it reached the microchannel. A two-channel oscilloscope (Tektronix TDS210) was attached to the amplifier to monitor the voltage and current to ensure experimental safety. The experiments were carried out by increasing the applied voltage ranges from 0 to 1 kV. The sinusoidal signal frequency changes in the range of 500 Hz to 10 kHz. In the following discussion, all voltages are peak to peak.

5.2.4 Experimental Measurement

DI water (Mili-Q grade II) was used as the dispersed phase and the continuous phase was the mineral oil (M5904, Sigma Aldrich) with 5 wt% of non-ionic surfactant (Span80, Sigma Aldrich), which was used to assist droplet formation and avoid droplet coalescence. The surfactant solution was prepared by mechanically mixing the two components for approximately 30 min and then filtering to eliminate aggregates and prevent clogging of the microchannel. Centoni neMESYS high precision syringe pump and gas tight microliter syringes (Hamilton Gastight 1002) were utilized to pump the DI water and mineral oil into the microchannel thus creating a confined flow condition. The liquids were introduced into the microchannel through flexible tubing and the flow rate can be controlled easily by using separate syringe pumps. In this study, the flow rate of the continuous phase liquid, Q_{CP} , was always greater than the flow rate of the dispersed phase liquid, Q_{DP} , to create a reasonable conic water tip [178]. Four different flow rate ratios are chosen, $Q_{DP}/Q_{CP} = 1/1, 1/2, 1/4$ and $1/8$ ($Q_{DP} = 50, 100, 200 \mu\text{l/hr}$), where Q_{CP} is the total flow

rate for both inlet streams. All of our experiments were conducted at room temperature and atmospheric pressure. Tests were repeated to ensure repeatability.

5.3 Results and Discussion

5.3.1 Droplet Breakup Regimes

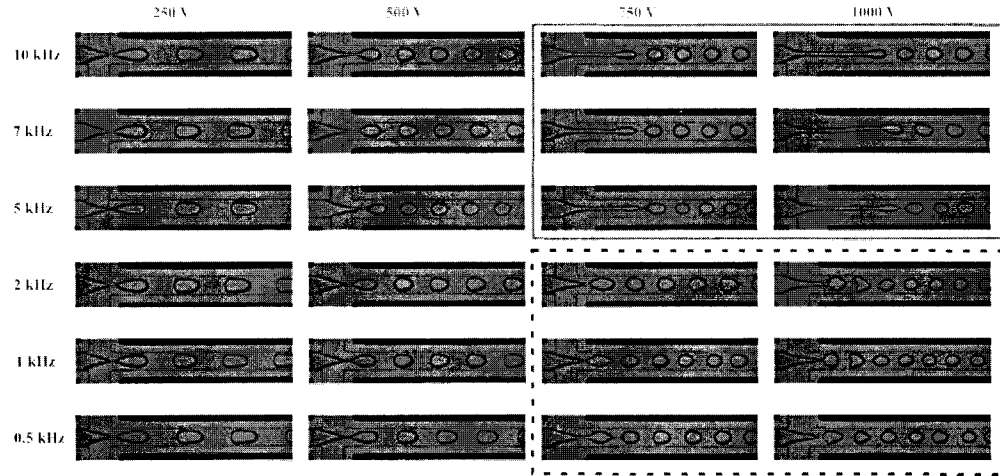


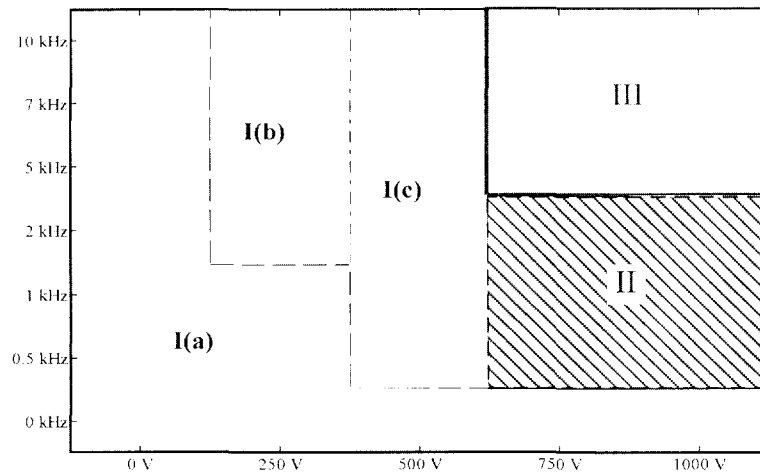
Figure 5.3 Droplet breakup regimes at different applied voltages and frequencies. $Q_{DP}/Q_{CP} = 200/400$ $\mu\text{l/hr}$. $Ca = 0.05$, $W_{or} = 100 \mu\text{m}$, $W_{ch} = 100 \mu\text{m}$.

In flow-focusing device, the droplet breakup regimes arise as the dispersed phase liquid flow rate increases, such as dripping, jetting and the squeezing, based on the change of the surface tension and viscous forces at the two-phase interface [158, 171, 182]. Interestingly, the size, shape, and frequency of the droplets can be tuned by varying the electric strength. A thorough understanding of the breakup regimes in the droplet generation is necessary to obtain high quality droplets. Several droplet breakup regimes in the main channel can be observed by changing the magnitudes of the applied voltages or frequencies at a fixed Q_{DP}/Q_{CP} of both the continuous phase and dispersed phase liquids were adopted (see Figure 5.3). Within each regime, the droplet size and frequency of breakup varies with the electric field parameters. The applied voltage varies from 0 V to 1000 V while the frequency ranges from 0 Hz to 10 kHz. The details of the droplet breakup regimes are represented in Figure 5.4. It

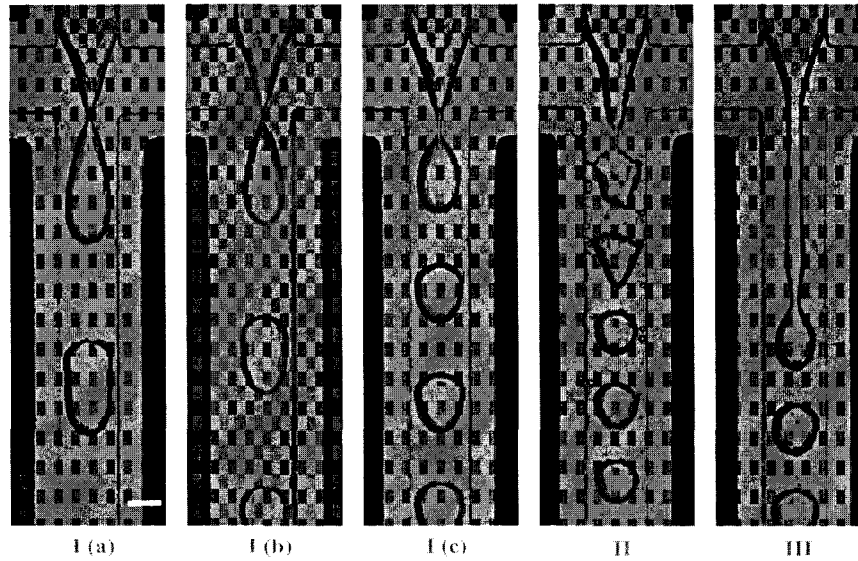
shows three droplet breakup regimes (**I**: dripping, here **(a)**, **(b)** and **(c)** are drippings with or without several visible satellite droplets; **II**: unstable breakup; **III**: jetting) at the cross-junction in the flow-focusing device. Figure 5.4 (b) shows the typical images of droplet breakup regimes in the main microfluidic geometries.

The dripping regime (**I**) is characterized by droplets that pinch off within one characteristic diameter of the flow focusing orifice, while the portion of the interface left behind after pinch off remains at a fixed location within the orifice [170]. The mechanism for droplet pinch off in the dripping regime is a mixture of electrohydrodynamics instabilities combined with viscous force and surface tension on the emerging droplet from the outer liquid, which stretches and thins the necked region behind the droplet. However, one or more satellite droplets are observed in a regular and reproducible manner in dripping regime. In **I(a)** regime, no satellite droplet is observed; In dripping **I(b)** regime, a few of satellite droplets accompany the large droplet and they are not absorbed by the large droplet; while in **I(c)** the satellite droplets generated at the breakup tip are absorbed into the large droplet in the downstream region.

At a higher applied voltage and frequency, a transition from dripping (**I**) to jetting (**III**) is observed. The localized electrohydrodynamic stress at the interface disrupts the balance of the viscous force and surface tension. In jetting regime, the dispersed phase finger extends beyond the exit of the orifice and resembles a long jet. The jet interface exhibits undulations that grow until discrete droplets pinch off. The resulting droplets in jetting regime are smaller than that in dripping regime, which is much different with the traditional transition by change the flow rate of the dispersed phase liquid.



(a) The influence of applied voltage and applied frequency on droplet, $Q_{DP}/Q_{CP} = 200/400 \mu\text{l/hr}$.



(b) Images of droplet breakup regimes. The scale bar is $50 \mu\text{m}$. **I(a)**: without electric field; **I(b)**: 250 V, 5 kHz; **I(c)**: 500 V, 1 kHz; **II**: 1000 V, 500 Hz; **III**: 1000 V, 10 kHz.

Figure 5.4 Different droplet breakup regimes in flow-focusing device, here $Q_{DP}/Q_{CP} = 200/400 \mu\text{l/hr}$ and the orifice width $W_{or} = 100 \mu\text{m}$. **(I)** Dripping, **(II)** Unstable breakup and **(III)** Jetting. The dripping regime can be further classified based on the generated satellite droplets.

Figure 5.4 also shows that an unstable breakup regime were observed with an increase in electric field strength. An unstable droplet is generated at the junction with many satellite droplets. This phenomenon is seldom observed in the traditional

flow-focusing device. The droplet production becomes unstable, leading to polydisperse droplets, and no stable jets are formed in this unstable breakup regime.

5.3.2 Droplet Size Varying with Electric Field

As mentioned above, electric field effects on droplet size and droplet breakup regimes. Here the droplet size denotes the average diameter of more than 100 droplets in each measurement. The ability to control the local flow field via changing the electric field makes it possible to control the deformation and breakup of every individual droplet.

Experiment was conducted via altering the applied voltage and frequency systematically considering different dispersed phase flow rates and the associated flow rate ratios. Figure 5.5 shows the droplet size as a function of applied voltage at a fixed frequency $f = 2$ kHz, which is much larger than the droplet production frequency (from 13 to 65.4). When the applied voltage increases from 0 to 1000 V, the droplet size decreases almost linearly as electrohydrodynamics stress promotes the interfacial instability.

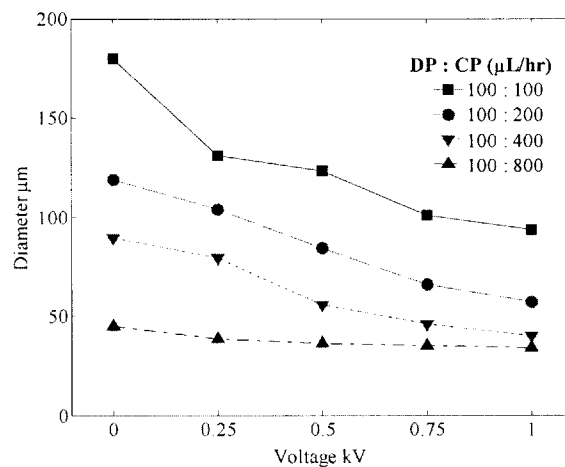


Figure 5.5 Effect of applied voltage on droplet size at a fixed frequency $f = 2$ kHz, $W_{or} = 100$ μm.

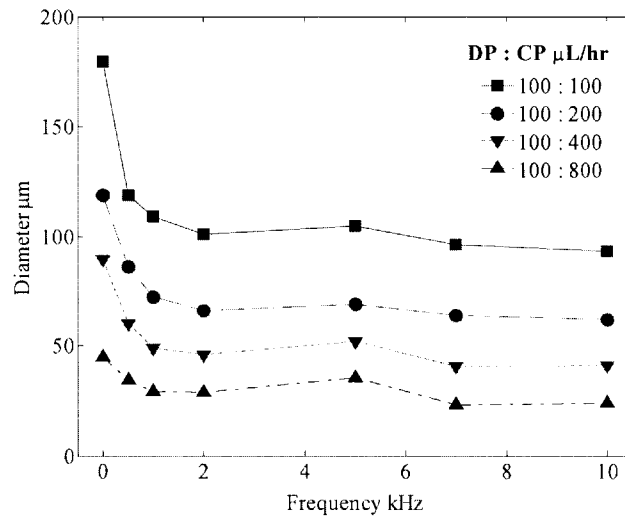


Figure 5.6 Effect of applied electric field frequency on droplet size at a fixed voltage $U = 750$ V, $W_{or} = 100$ μm .

Figure 5.6 shows the influence of applied frequency on the droplet size at a fixed electric voltage $U = 750$ V. The droplet size decrease dramatically when the electric frequency is increased from 0 to 2 kHz. Experimental results obtained at different applied frequencies show negligible difference in the measured droplet diameter when the applied frequency is more than 2 kHz.

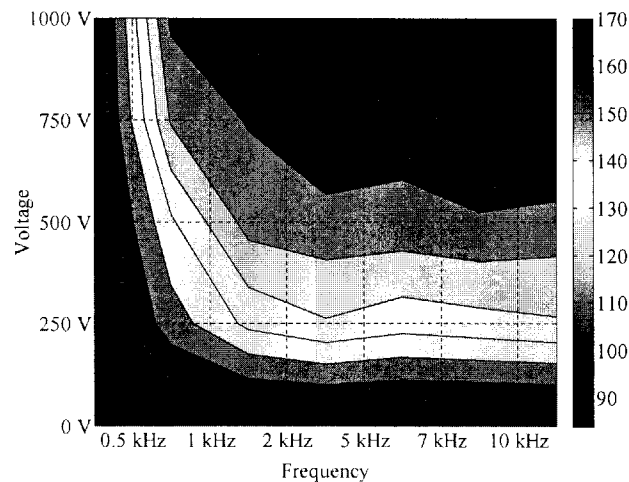


Figure 5.7 Influence of applied voltage at different frequencies on droplet size. $Q_{DP}/Q_{CP} = 200/400$ $\mu\text{L/hr}$, $W_{or} = 100$ μm . $Ca = 0.05$.

Figure 5.7 depicts the droplet size variation with different external electric parameters (voltage and frequency), ranging from 0 to 1000 V in voltage and 0 to 10 kHz in frequency. The droplet size decreases continuously with increasing electric strength. The dependence of the droplet size on applied voltage and frequency are summarized below. When an electric field is applied, the induced Maxwell stress is acting on the growing droplet.

Unlike in co-flowing and cross-flowing configurations, no simple model exists that can predict the droplet size as a function of control parameters in microfluidic flow-focusing, in which capillary pressure and viscous stresses are generally more significant than inertia [159, 186]. In microfluidic droplet formation, the capillary number Ca is the most important parameter characterizing the relative importance of viscous force and surface tension at the two-phase interface. The capillary number is defined in terms of the continuous phase flow field that acts to deform the droplet,

$$Ca = \frac{\mu_c W_d / 2}{\sigma} \frac{\Delta U}{W_c} = \frac{\mu_c Q_c W_{or}}{2\sigma h W_{ch}} \left[\frac{1}{W_{ch}} - \frac{1}{2W_{ch}} \right] = \frac{\mu_c Q_c W_{or}}{4\sigma h W_{ch}^2} \quad (5.1)$$

Where μ_c represents the viscosity of the continuous phase, $\sigma = 5 \text{ mN/m}$ is the surface tension of the continuous phase, W_d , W_c are the channel width of the dispersed phase and continuous phase respectively, ΔU stands for the velocity variation in the flow-focusing region where the droplet formation happens, Q_c describes the flow rate of continuous phase, W_{ch} , W_{or} and h denotes the channel width, orifice width and channel height, respectively, as shown in Figure 5.2. This definition is consistent with classic experiments examining the deformation and breakup of isolated droplets in linear flows [187].

5.3.3 Droplet Size Distribution

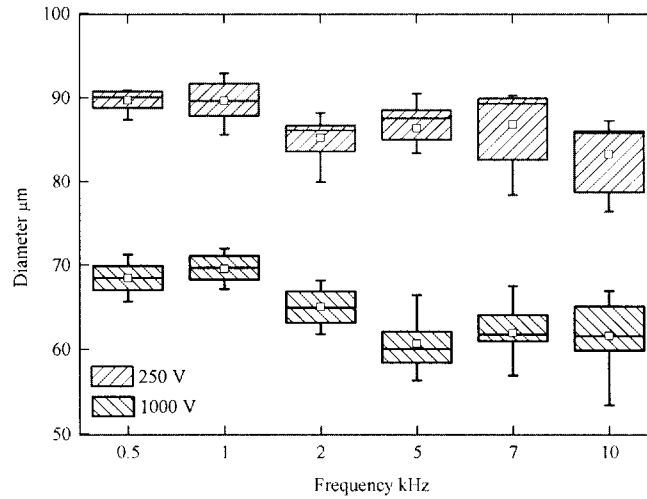


Figure 5.8 Droplet size distribution with different electric field parameters. $Q_{DP}/Q_{CP} = 200/400 \mu\text{l/hr}$, $W_{or} = 100 \mu\text{m}$. The above and below “-” here are the maximum and minimum value of the droplet diameter, respectively. The upper quartile is the 75th percentile, the lower quartile is the 25th percentile, and the median is the 50th percentile. The blank box is the mean droplet diameter.

The precise control of droplet size is one of the most important objectives in the droplet formation [158]. We also study the droplet size distribution effect under different external electric strength. More than 200 droplets are taken into account in each case to study the droplet size distribution. Figure 5.8 presents the droplet size distribution under the effect of the two different electric fields. Droplets are relatively uniform in size at low frequencies ($< 2 \text{ kHz}$). Hence low frequency is a better choice in the droplet generation when accurately droplet sizes are required.

5.4 Summary

Three droplet breakup regimes including dripping, unstable breakup and jetting were observed at the cross-junction in flow-focusing device by changing the magnitudes of the applied electric voltages or frequencies at fixed flow rates of both phase liquids. Within each regime, the droplet size and frequency of breakup also varies

with the electric field parameters. In addition, droplets in jetting regime are smaller than that in dripping regime when an electric field are applied, which is much different with the traditional transition by change the flow rate of the dispersed phase liquid.

The dependence of the droplet size on applied voltage and frequency are summarized, ranging from 0 to 1000 V in voltage and 0 to 10 kHz on frequency, respectively. As electrohydrodynamics stress promotes the interfacial instability, the droplet size shows an approximately linear decrease with the increasing of voltage and a dramatically decrease trend by half an order of magnitude with the increasing of electric frequency from 0 to 2 kHz.

The droplet size distribution under different voltages and frequencies were investigated. Droplets are relatively uniform in size at low frequency (< 2 kHz).

Chapter 6 AC Electric Field Tuned Non-Newtonian Droplet

Formation in Flow Focusing Microchannels

6.1 Introduction

In recent years, the emergence of microfluidics has gained intense research focus owing to its potentials in scientific research and industrial applications [99, 151, 188]. The impact of microfluidic droplets has been increasing as the properties such as the fast generation rate and monodispersity [92-94, 108, 189-192] with associated approaches for droplet sorting, splitting and merging [97, 193-195] making it suitable for biochemical processes such as fast chemical reaction test, bio genetic transportation and drug delivery [93, 144, 196].

Droplet formation is the fundamental process for droplets microfluidics, by which the monodispersity and formation rate are controlled. Microchannel geometries utilized in this process can be generally classified as T shaped junctions [94, 97, 107, 197] and flow focusing (co-flowing is essentially the same) [98, 104, 105, 190], both of which generate droplets via promoting interfacial instability. Flow focusing has a more complex geometry, which allows more flexibility in the control of droplet size and the formation frequency [108, 198, 199]. By tuning the flow parameters and orifice geometry, flow focusing is more reliable in size control and small droplets generation [99, 111]. The flow focusing concept was first proposed by Umbanwar and then revised by Anna to be the current adopted microchannel geometry [104, 108].

Much research effort has been carried out to study the droplet size control using the aforementioned two geometries, through external fields of various types as microfluidic is an interdisciplinary research field. Electric [95, 113], temperature

[200, 201], acoustic [189, 202], magnetic fields [111], etc. have been explored. As the response time for temperature is relatively long, instant control in fast formation is hardly achieved. Acoustic needs time for relaxation and magnetic field usually contaminates the flows due to the presence of the magnetic particle. Fast response droplet formation can be achieved via electric field applied in flow focusing microchannels where contamination can be avoided by non-contact electrodes [113]. Experimental results show that AC electric field induced Maxwell stress is capable of promoting interfacial instability and tuning the droplet size.

Most of the research carried out in microfluidics utilize Newtonian fluids with simple rheological behavior. However fluids in the aforementioned applications such as DNA sample are the one with complex rheological behavior owing to the presence of long DNA chain structure, which explains the rising attention on non-Newtonian fluids in microfluidics [145, 203, 204].

What is the dynamic response of non-Newtonian fluids under electric field given that the relaxation time is in mili or even micro seconds order [62]? Can the electric field fine-tune the droplet size? Questions as such attract our attention. In this chapter, we have systematically investigated the ac electric field tuned non-Newtonian droplet formation in flow focusing microchannels. Polymer aqueous solution with a long chain micro structure, which behaviors similarly to DNA samples in rheological perspective, was chosen for droplet formation characterization [66, 77, 142, 205]. Fluidic parameters such as capillary number (Ca), dispersed phase flow rate (Q_d); applied voltage (U) and frequency (f) were considered. Three types of flow focusing microchannels with different orifice sizes were fabricated for investigation of geometry induce interfacial instability on AC electric tuned non-Newtonian

droplet formation. Finally, the flow field of droplet formation was quantitatively measured via a high speed μ -PIV system. Characteristic flow field is shown and analyzed.

6.2 Experimental setup

6.2.1 General setup

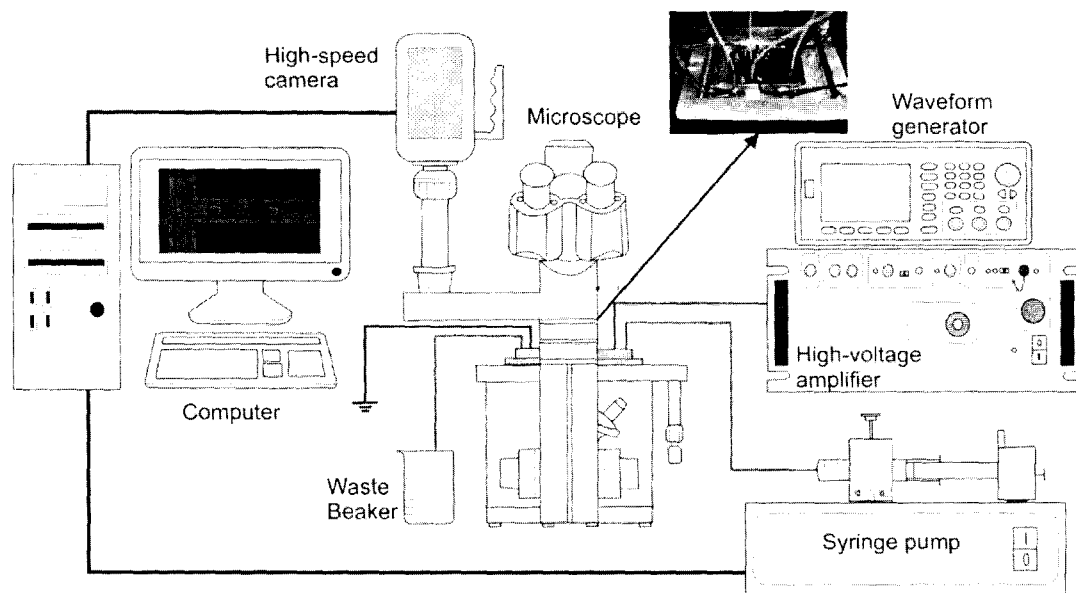


Figure 6.1 Experimental setup for electric tuned non-Newtonian droplet formation

Figure 6.1 shows the schematic diagram of the experimental setup. The microchannel is connected with the syringe pump, and a high voltage supply system, which is used to control the flow rate and applied electric field respectively. Fluidic behavior is observed through an inverted microscope (Lecia DM ILM) and recorded via a high speed camera (Phantom V611). The camera and the pump is connected to the computer and controlled by the software.

6.2.2 Microchannel

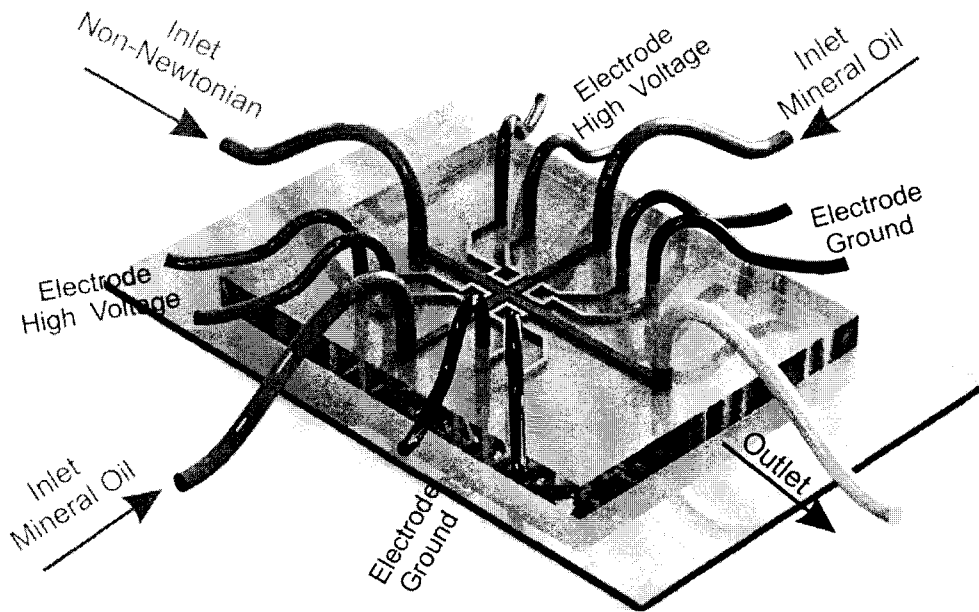


Figure 6.2 Schematic diagram of the microchannel

Figure 6.2 shows the overall view of the microchannel used in the experiment. The microchannel is connected with three inlets. One of the inlets is for aqueous non-Newtonian fluid and the other two are for mineral oil, forming the water in oil emulsion system. Four electrodes, as indicated in Figure 6.2 are fabricated for electric field implementation. Among them, two are connected to the high voltage and another two are grounded, completing the electric circuit.

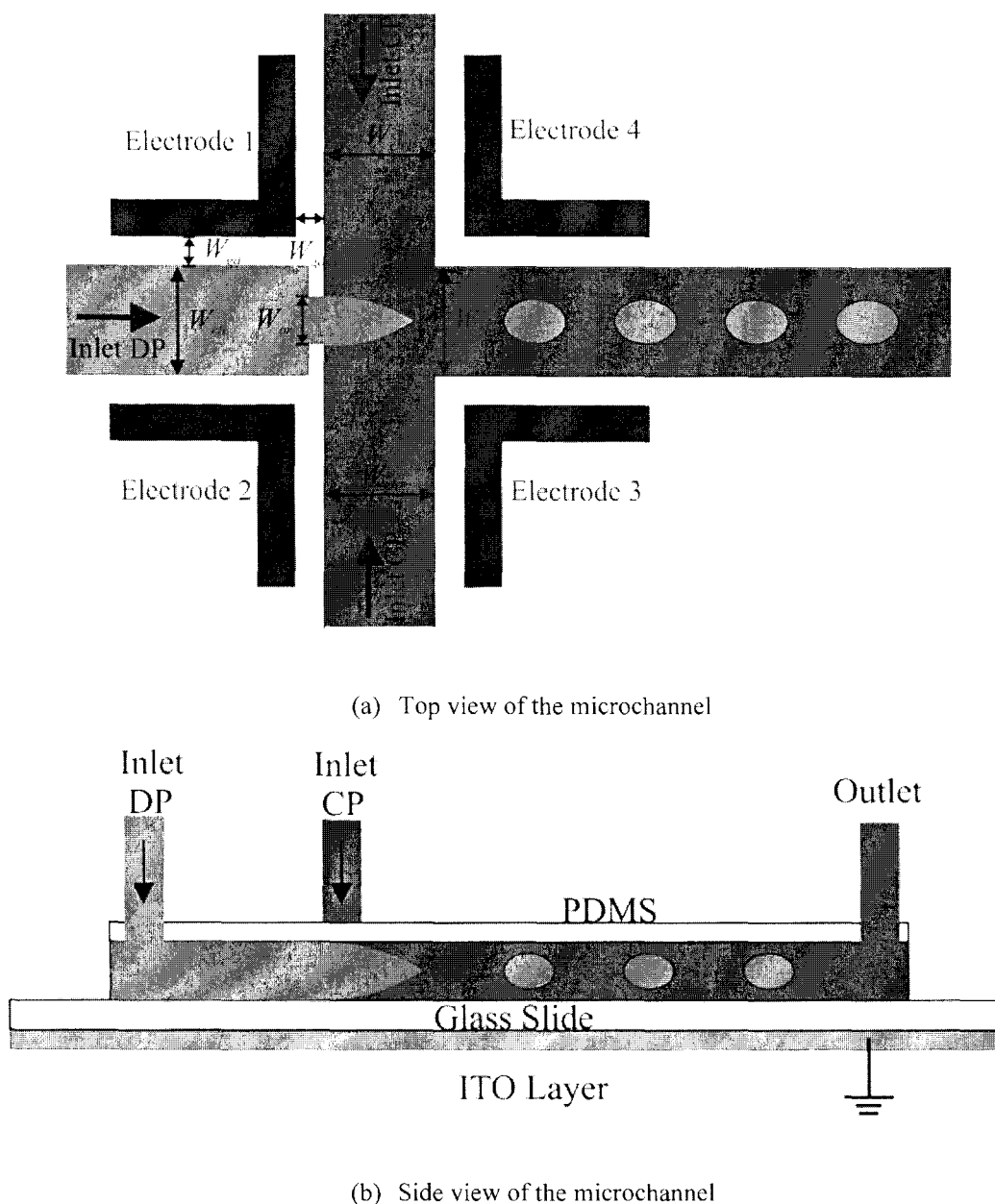


Figure 6.3 Lay out of the flow focusing microchannel with non-contact type of electrode. DP, CP denote dispersed phase and continuous phase respectively.

The flow focusing microchannel is fabricated by the standard soft lithographic procedure followed by polydimethylsiloxane (PDMS, Dow Corning Sylgard 184) process and plasma bonding with one slice of ITO microscope glass. One thin layer of Aquapel is coated on channel wall to ensure uniform hydrophobic surface property. The ITO is connected with ground to avoid floating voltage and ensure stable droplet formation (see Figure 6.3 (b)). As shown in Figure 6.3 (a), four

electrodes are designed and fabricated by melting indium alloy (Indium Corporation of America) into the electrode channel, which is then connected with the high voltage supply system via electric wires.

The main channel width is $W_{ch}=100\text{ }\mu\text{m}$, the height of microchannel controlled by spin coating is fabricated to be $h=35\text{ }\mu\text{m}$ and the gap between the electrode and channel wall, W_{ga} , is designed to be $50\text{ }\mu\text{m}$. Orifice is designed in the upstream rather than the traditional downstream for the consideration of enhancing the impact of electric field. Three different sizes of orifice $W_{or}=25, 75$ and $100\text{ }\mu\text{m}$ are considered in our experiments.

6.2.3 Materials

Fluid samples adopted in this experiment are water in oil emulsion system. The dispersed phase (DP) is poly ethylene oxide (PEO) aqueous solution at the constant ratio of 0.5% by weight, and the molecular weight is 4M (Sigma aldrich). The solution is prepared by stir-mixing PEO powder in to DI (Mili-Q grade II) water for 24 hours under room temperature [144, 146]. In the continuous phase (CP) light mineral oil (M5904, Sigma aldrich) is chosen, in which 5% wt. of surfactant (Span 80, Sigma aldrich) is added to assist droplet formation and avoid droplet coalescence.

6.2.4 Fluidic and electric system setup

Centoni neMESYS high precision syringe pump and gas tight microliter syringe (Hamilton Gastight 1002) are utilized to pump the non-Newtonian fluid and mineral oil into the microchannel to create a confined flow condition. PTFE micro tubing is chosen to connect syringe and microchannel in case of chemical corrosion.

Electric field is generated by the combination of Agilent 33500B waveform generator and Trek 5/80 high voltage amplifier. The waveform generator generates one electric signal of specific voltage and frequency (sine wave is adopted), which is then amplified by the amplifier at the constant amplification factor of 1000 before it reaches the microchannel. One two-channel oscilloscope (Tektronix TDS210) is attached to the amplifier to monitor the voltage and current to ensure experimental safety. The applied voltage ranges from 0 to 1 KV while the frequency varies from 500 to 7 KHz.

6.3 Results and discussion

The experiment was conducted systematically to investigate the influences of electric field and orifice sizes on the non-Newtonian droplet formation. Parameters such as flow rate ratio, flow rate of the dispersed phase, electric voltage, and electric frequency are discussed. The impact of the orifice size is also addressed. Generally, the flow rate ratios ($Q_{dp}:Q_{cp}$) of 1:2, 1:4, 1:8, 1:16 are adopted while three flow rates of dispersed phase (Q_{dp}) 5, 10, 20 $\mu\text{L/hr}$ are considered for each set of the flow rate ratios. Five different electric voltages, 0 V, 250 V, 500 V, 750 V, and 1 KV are applied to the microchannel. Five electric frequencies, 500 Hz, 1 KHz, 2 KHz, 5 KHz, and 7 KHz are varied for each specific flow conditions and voltage. Three types of microchannels with different orifice sizes, 25, 75, 100 μm are tested to investigate the impact of orifice sizes on droplet formation. For each specific experimental condition (Q_{dp} , flow rate ratio, voltage, frequency, orifice size), each experiment was performed three times to ensure the repeatability.

6.3.1 Droplet breakup dynamics of the non-Newtonian fluid

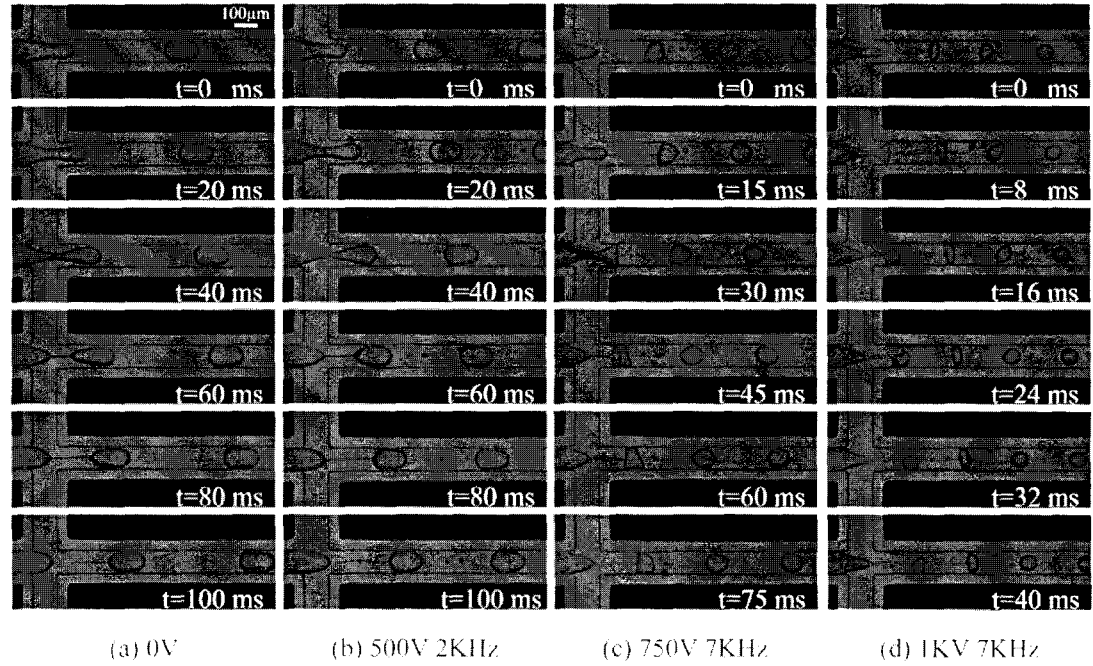


Figure 6.4 Non-Newtonian droplet formation processes under different electric fields. Flow rates are

$$Q_{DP} : Q_{CP} = 10:40 \text{ } \mu\text{L/hr, Orifice size } W_{or} = 100 \text{ } \mu\text{m.}$$

Figure 6.4 shows the dynamics of non-Newtonian droplet formation for flow rates of $Q_{DP} : Q_{CP} = 10:40 \text{ } \mu\text{L/hr}$ under different electric fields. Figure 6.4 (a) illustrates the formation dynamics without electric field (0 V). Two distinct regimes of droplet formation exist in non-Newtonian fluid, namely pre-stretch and self-thinning regimes [115]. The emerging droplet tends to form and flow away from the tip of the dispersed phase within pre-stretching regime as shown in Figure 6.4 (a) $t = 0 \sim 40 \text{ ms}$. After the droplet forms, one thread is generated due to viscoelastic property of the dispersed phase after which the self-thinning regime occurs. The self-thinning process of the thread caused by the elongation flow of the continuous phase is observed in Figure 6.4 (a) $t = 60 \sim 100 \text{ ms}$. Another phenomena which differs from the Newtonian fluid is the dynamics of satellite droplet formation. As inferred from Figure 6.4 (b), relatively bigger satellite droplets are formed due to coalescence of small droplets

formed by the self-thinning of the thread while there is no significant variation upon main droplet generation. Results presented in Figure 6.4 (c) & (d) demonstrate the influence of strong electric field on the droplet formation. Both of the results show a significant reduction in droplet size and an obvious increasing droplet formation frequency due to the electric field. It can be directly observed that stronger electric field leads to smaller and faster formation.

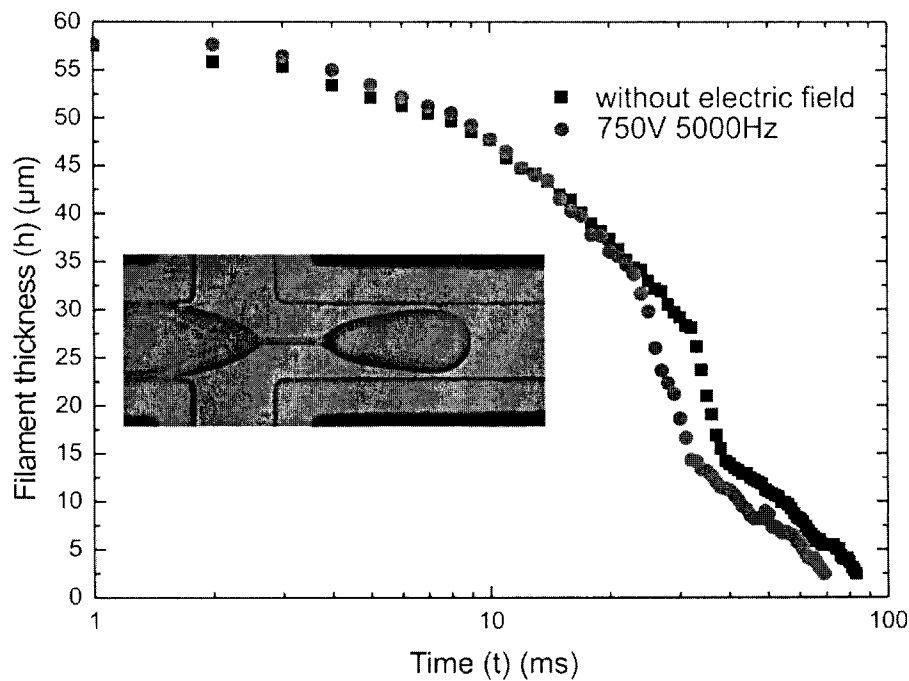


Figure 6.5 Filament thickness versus time. $Q_{DP} : Q_{CP} = 20:40 \mu\text{L/hr}$.

Figure 6.5 shows the dynamics of non-Newtonian filament thinning behaviour with and without an electric field. A similar trend is reported by Arratia *et al.* [117, 206] that the filament thickness exhibit obvious self-thinning behaviour, resulting in the longer breakup duration. The results depict a negligible effect of the electric field on the filament thickness during the initial stage as the continuous phase induced shearing force is the dominate force in reducing the initial filament thickness. Thereafter, the electric field helps to shorten the process after a critical time, causing

the filament thickness to drop significantly. It can be inferred that the Maxwell stress have a major influence on the filament breakup process.

During the self-thinning regime, the beads on string phenomenon can be observed before they finally break up into satellite droplets. Experiments show that uniform and miniature satellite droplets are formed at low electric field strength or without an electric field. Relatively larger satellite droplets are seen in the presence of high AC electric field due to the AC field induced instability. Therefore, formation of satellite droplet can be controlled via electric field.

6.3.2 Electric field tuned non-Newtonian droplet sizes

Influence of the AC field voltage

The experiment were conducted via altering the applied voltage and frequency systematically considering different Q_{DP} and the associated flow rate ratios. The applied voltage varies from 0V to 1000 V while the frequency ranges from 0 Hz to 7 KHz. The droplet dynamics is captured with an inverted microscope attached with the high speed camera (Phantom V611). Results are analyzed by a self-coded Matlab programme which is capable of droplet identifying, tracking and measuring.

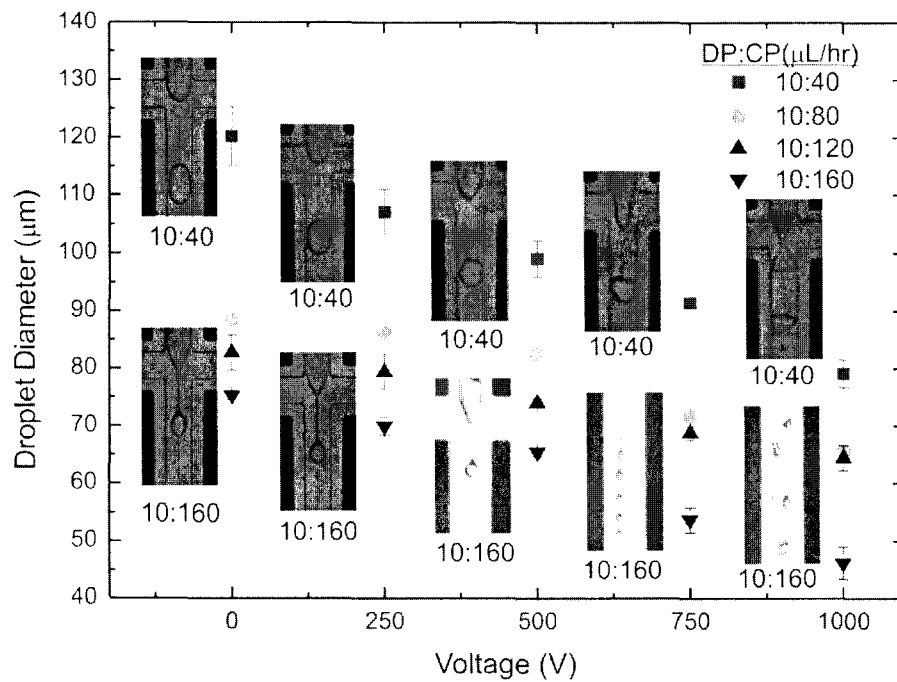


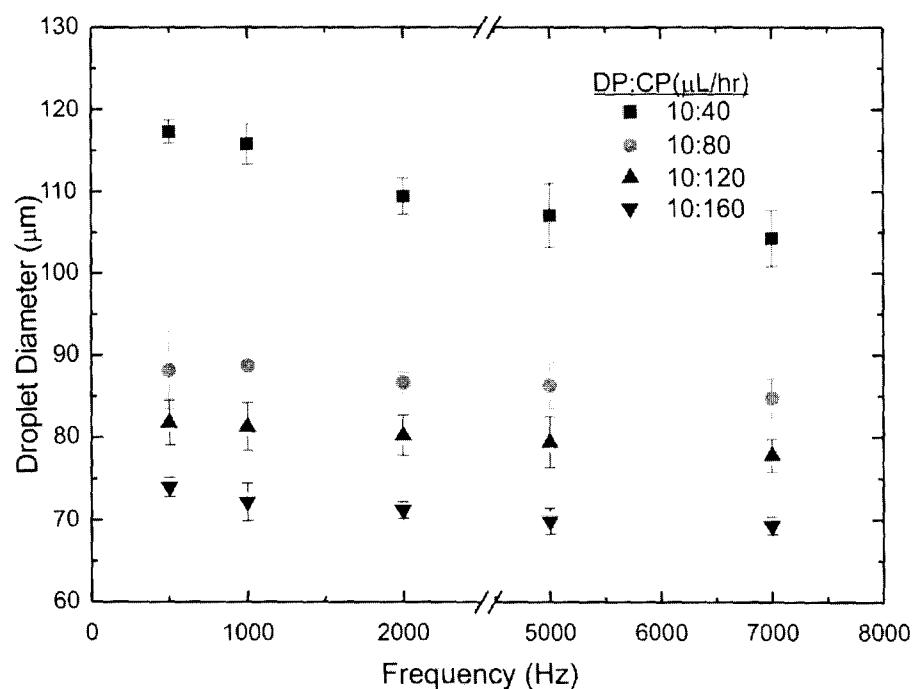
Figure 6.6 Non-Newtonian droplet diameters versus applied voltages. AC frequency is fixed at 5 KHz.

Four groups of flow rate ratios are adopted. $Q_{DP}=10 \mu\text{L/hr}$

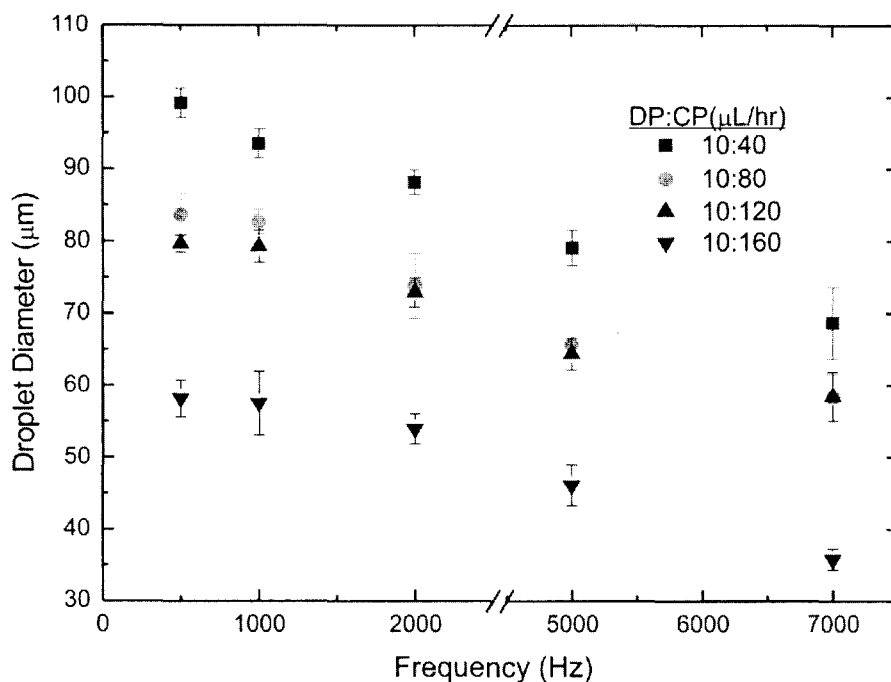
Figure 6.6 depicts the dynamics of non-Newtonian droplet formation under applied voltage. Four different flow rate ratios at the frequency of 5 KHz are plotted. Droplet formation is in the squeezing regime under the flow rate of $Q_{DP}:Q_{CP}=10:40$. The droplet diameter decreases with an increase in the voltage as Maxwell stress promotes the interfacial instability. The droplet formation mechanism changes from squeezing to dripping via increasing the flow rate ratio from 10:40 to 10:160. In addition, the filament length decreases when the applied voltage increases within squeezing and dripping regimes. The shifting from dripping to jetting occurs when the applied voltage is larger than 500V under the flow rate ratio of 10:160. There is a dramatic size drop when the formation happens in jetting regime. The appearance of jetting in flow focusing microchannel without electric field is due to the insufficiency of fluid from the dispersed phase, therefore causing the droplet to form in the downstream [111]. The AC field induced Maxwell stress prompts the fluid to move downstream,

forcing it to shift from dripping to jetting. After the formation, the presence of a higher applied electric field may tear the droplet apart, as shown in Figure 6.6. Hence, the formation become unstable and monodispersity will not be achieved as indicated by a large error bar at high voltages. Results on the influence of applied voltage on other frequencies and flow rates can be seen in Appendix A.

Influence of the AC field frequency



(a) Non-Newtonian droplet diameters at voltage of 250V



(b) Non-Newtonian droplet diameters at voltage of 1 kV

Figure 6.7 Droplet diameter dependence of AC frequency under various flow rate ratios.

Figure 6.7 (a) and (b) explains the influence of AC frequency on droplet diameter under different applied voltages. Results also show a decreasing trend with the increasing frequency. However the variation of the frequency is not significant when the applied voltage is low, as shown in Figure 6.7 (a). A higher frequency will dramatically increase the electric current and reduce the droplet size under the condition that the voltage is high. Supplementary results are presented in the Appendix for reference.

6.3.3 Flow dynamics coupled electric field effect upon non-Newtonian droplet formation

In this section, droplets sizes are compared with different flow conditions under specific applied voltage and frequency. Flow conditions are presented in terms of Q_{DP} and capillary number (Ca), as proposed by Anna, etc. [108]. The definition of Ca is:

$$Ca = \frac{\mu_c W_d / 2}{\sigma} \frac{\Delta U}{W_c} = \frac{\mu_c Q_{cp} W_{or}}{2\sigma h W_{ch}} \left[\frac{1}{W_{ch}} - \frac{1}{2W_{ch}} \right] = \frac{\mu_c Q_{cp} W_{or}}{4\sigma h W_{ch}^2} \quad (6.1)$$

Where μ_c represents the viscosity of the continuous phase, $\sigma=5$ mN/m is the surface tension of the continuous phase, W_d , W_c are the channel width of the dispersed phase and continuous phase respectively, ΔU stands for the velocity variation in the flow focusing region where the droplet formation happens, Q_{cp} describes the flow rate of continuous phase, W_{ch} , W_{or} & h denotes the channel width, orifice width and channel height respectively as shown in Figure 6.2.

Capillary number versus voltage

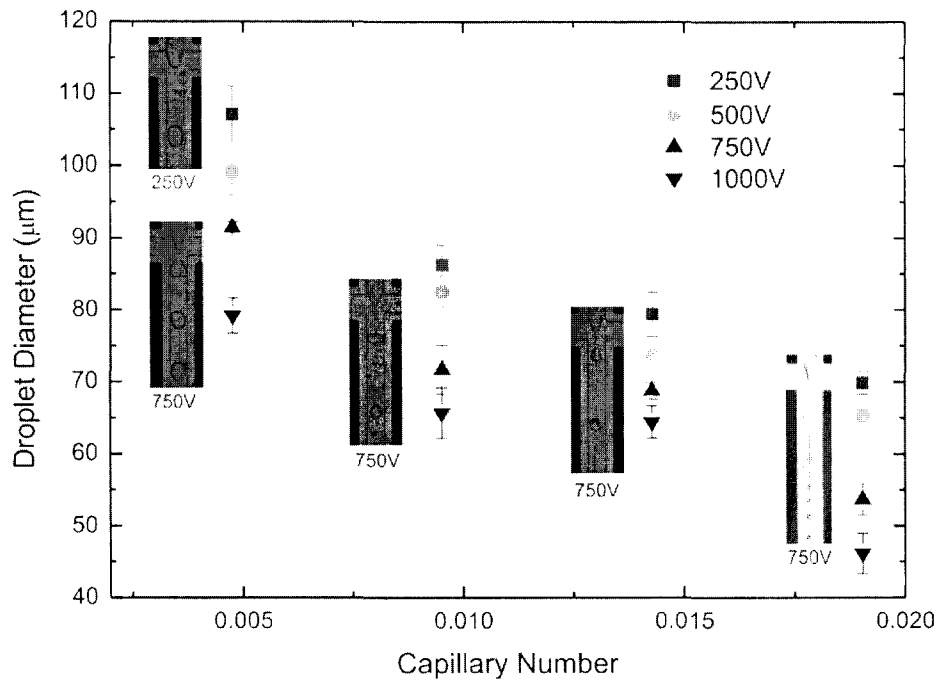
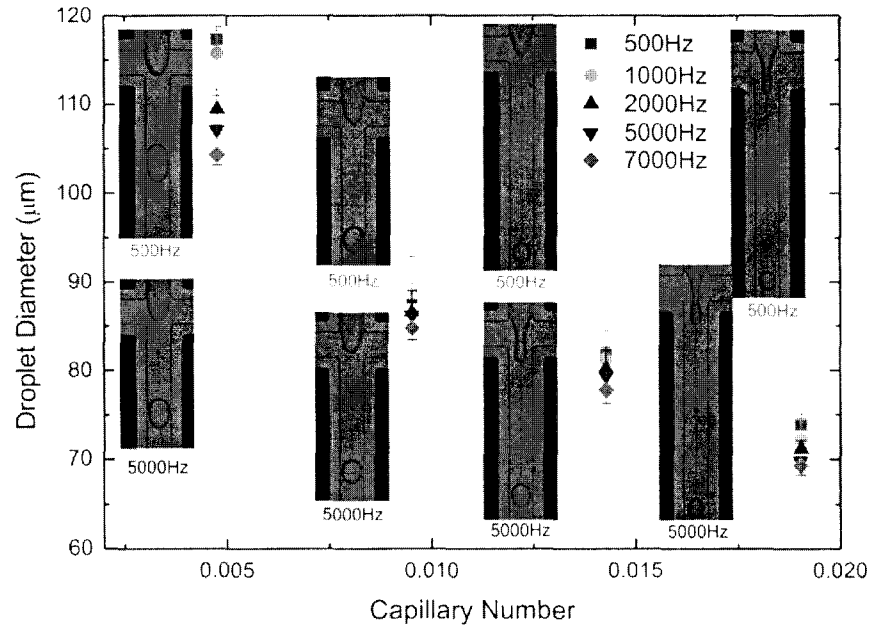


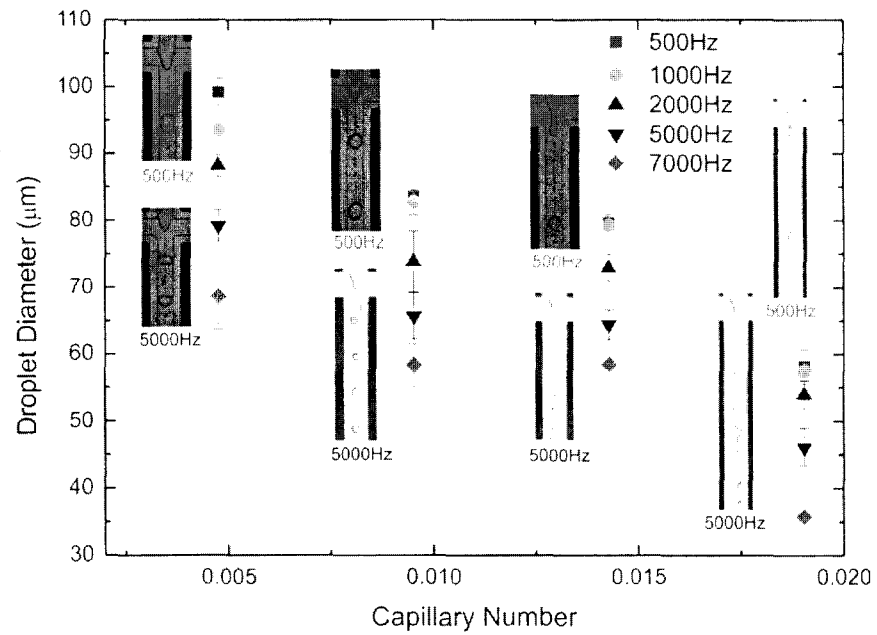
Figure 6.8 Non-Newtonian droplet diameter varies as the function of Ca under different applied voltages with a fixed AC frequency of 5 KHz. $Q_{DP}=10 \mu\text{L/hr}$.

Figure 6.8 shows the influence of Ca on droplet diameter at different voltages. The increasing Ca alters non-Newtonian droplet formation mechanisms from the squeezing to dripping and finally to jetting. A high electric field reduces the non-Newtonian droplet size and influences the regimes of droplet formation. It is observed that at $Ca=0.014$ the flow regime transits from dripping to jetting when the applied voltage is increased from 750 V to 1 KV. In the jetting regime, the jet length can be significantly enhanced via electric field and droplet merging becomes observable leading to the non-uniform droplet formation.

Capillary number versus frequency



(a) Non-Newtonian droplet formation at voltage of 250 V



(b) Non-Newtonian droplet formation at voltage of 1 KV

Figure 6.9 Non-Newtonian droplet diameter dependency on Ca under different AC frequencies with fixed voltage of (a) 250 V and (b) 1 KV respectively. $Q_{DP} = 10 \mu\text{L/hr}$.

Figure 6.9 (a) and (b) represent the dependency of non-Newtonian droplet diameter to Ca under different frequencies at fixed voltages of 250 V and 1 KV respectively.

Both (a) and (b) show the same tendency that droplet diameter decreases with increasing of the Ca or frequency. However, the influence of frequency is insignificant when the applied voltage is relatively low. As demonstrated in Figure 6.9 (a), the variation of the diameter with various frequencies is small at 250 V. However, the dynamics of satellite droplet formation differs when the frequency increases. As indicated in Figure 6.9 (a), the size of the satellite droplet shows a smooth decreasing trend, with the largest satellite droplet close to the droplet and the smallest near the formation region when the AC frequency is 500Hz. When the AC frequency increases to 5 KHz, the coalescence of satellite droplet becomes phenomenal, leading to the occurrence of large satellite droplet near the formation region. The transition of the flow regime is not observed at this stage. In Figure 6.9 (b), when the applied voltage is increased to 1000 V, droplet diameter shrinks rapidly with increasing the frequency. Moreover, the transition from dripping to jetting occurs when frequency equals to or higher than 5 KHz, indicating that higher frequency influence the regime for droplet formation. In addition, coalescence-induced non-uniformity also occurs in the jetting regime due to the high frequency of the electric field, as shown in Figure 6.10. The dynamics of the satellite droplets formation is strongly disturbed by the electric field induced Maxwell stress, thus irregular formation of satellite droplets are observed.

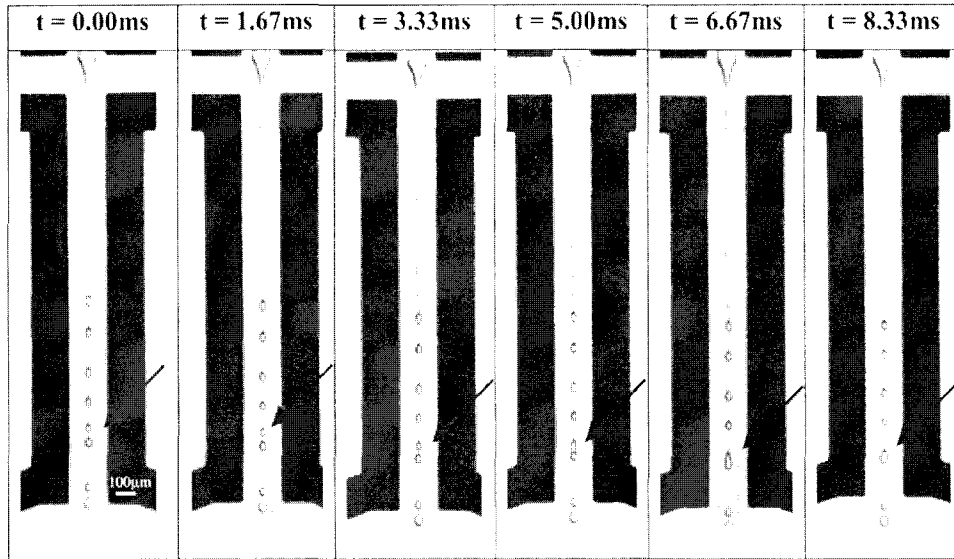


Figure 6.10 Merging of droplets in jetting regime. $Q_{DP} : Q_{CP} = 20:160 \mu\text{l/hr}$, applied electric field: 750 V, 5 KHz.

6.3.4 Effects of Orifice sizes on non-Newtonian droplet formation

The purpose of this section is to investigate the formation of droplets in flow focusing microchannels with three orifice sizes (25 μm , 75 μm , and 100 μm) at specified flow conditions and applied AC electric field.

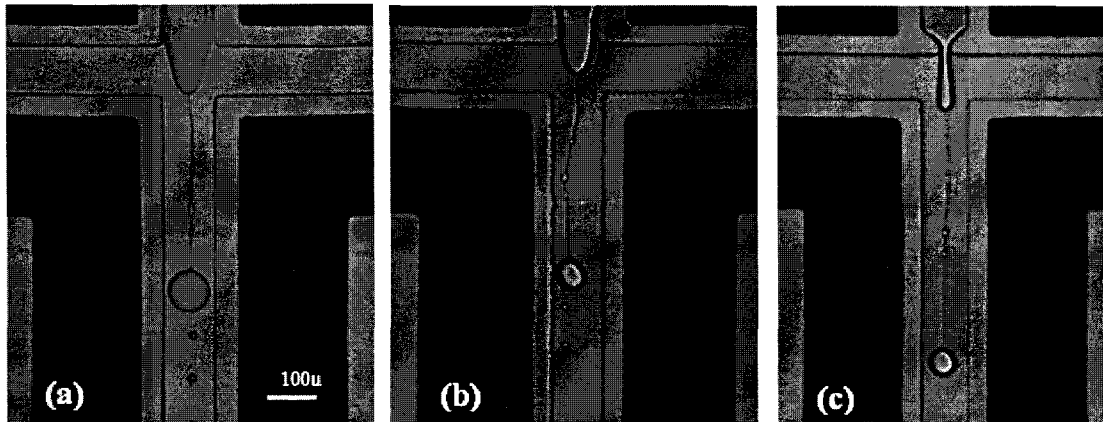


Figure 6.11 Non-Newtonian droplet formations for different orifice sizes. (a) $W_{or} = 100 \mu\text{m}$, (b) $W_{or} = 75 \mu\text{m}$, (c) $W_{or} = 25 \mu\text{m}$. $Q_{DP} : Q_{CP} = 10:80 \mu\text{L/hr}$, electric field is applied at the voltage of 500 V, frequency of 5 KHz.

Figure 6.11 shows the effect of orifice size on droplet formation, when the flow condition is $Q_{DP}:Q_{CP}=10:80$ $\mu\text{L/hr}$ and the applied voltage is 500 V, frequency is 5 KHz. As shown in Figure 6.11, the presence of orifice at the upstream directly limits the size of the necking region resulting in a smaller droplet generation. Therefore, under the same flow rates and electric field, smaller droplet can also generated by tuning the orifice size. We will also investigate the effect of orifice size in terms of Ca since it considers both the flow condition and geometry.

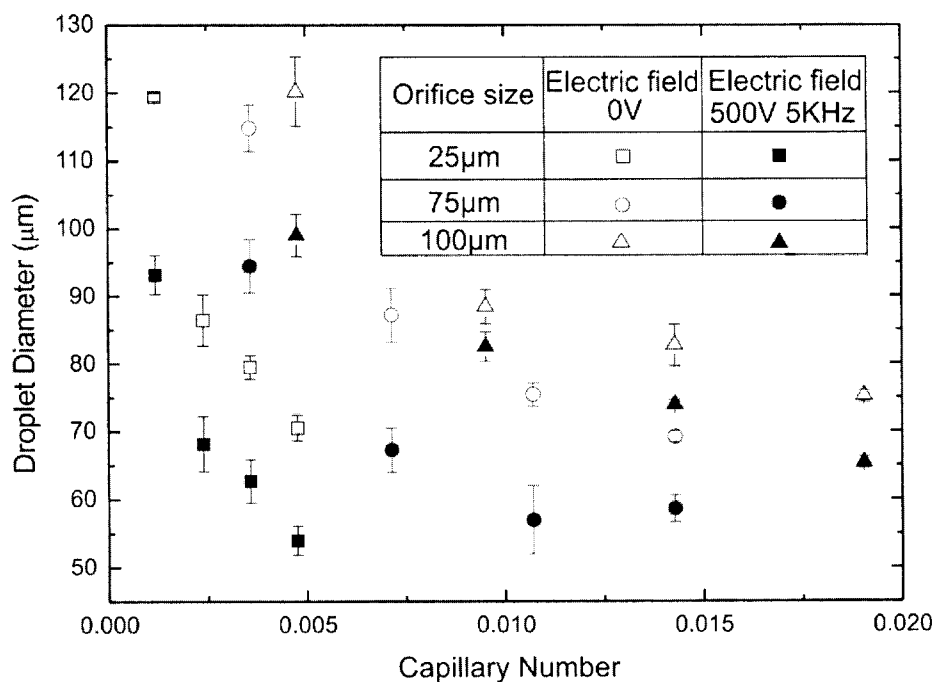


Figure 6.12 Non-Newtonian droplet diameter dependency of the orifice size in terms of Ca . $Q_{DP}=10$ $\mu\text{L/hr}$.

Figure 6.12 investigates the influence of the orifice size. Besides the electric field reducing the droplet sizes, we can see that orifice size has significant impact in the formation process. It provides an alternative approach for the control of droplet size. However, challenges can occur in the fabrication and experimental investigation due to the limitation of soft lithographic and the immense pressure gradient required to pump the fluid through the orifice.

6.3.5 Effective capacitance electric model for AC electric field assisted non-Newtonian droplet formation

The droplet diameter has been investigated for both T junction and flow focusing microchannels. Good scaling laws of droplet diameter for T junction have been proposed [94, 100], while only simply approximation can be seen in the literatures for flow focusing microchannel due to the complexity of droplet breakup process. In this section, we developed a “capacitance” model to describe the dependency of the flow condition and electric field on the non-Newtonian droplet formation.

The parameters that influence the droplet diameter are: (i) flow rates, (ii) the fluid properties (viscosity of the continuous and dispersed phase, and interfacial tension), (iii) microchannel geometry (microchannel dimensions and orifice size), and (iv) electric parameters (applied voltage, frequency, electrical conductivity and permittivity). We will address the diameter in terms of Ca and electric field parameters.

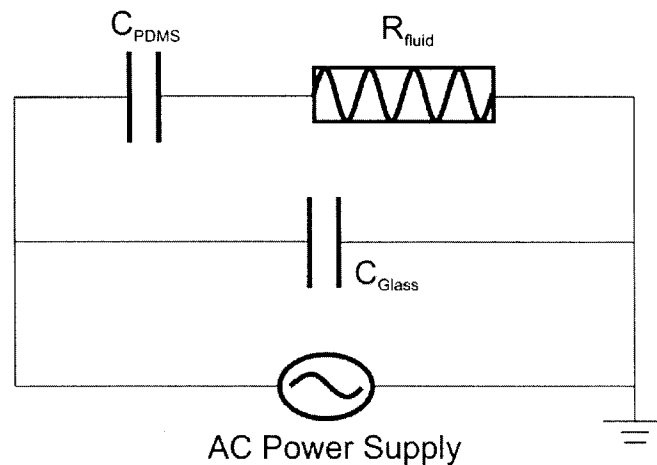


Figure 6.13 Effective capacitance model of the microchannel

Figure 6.13 shows a simplified electric circuit model of the flow focusing system. The model accounts for the electric field, which starts from the upstream electrode

(Figure 6.3 (a)) and terminates on the downstream electrodes. The electric network consists of the PDMS layer capacitance C_{PDMS} , the fluid resistance R_{Fluid} and the single side coated ITO glass capacitance C_{Glass} .

Results in Figure 6.9 show that droplet diameter and the regime of the droplet formation are strongly influenced by AC frequency. Since the dispersed fluid and the upstream electrode are separated by the PDMS layer capacitance, the voltage at the tip of the dispersed fluid can be different from the applied voltage [113].

In this section, the difference between the applied voltage U and the voltage at the tip of the dispersed fluid are modelled due to the frequency-dependent effective capacitance model as shown in Figure 6.13.

The capacitance and resistance can be estimated as:

$$R_{Fluid} = \frac{L}{\kappa A} \approx \frac{W_{ch}}{\kappa(W_{ch}h/4)} \approx 400 M\Omega \quad (6.2)$$

$$\begin{cases} C_{PDMS} = \frac{\epsilon_0 \epsilon_{rPDMS} L_{elec} h}{d} \approx 0.15 pF \\ X_{C_{PDMS}} = \frac{1}{2\pi f C_{PDMS}} \end{cases} \quad (6.3)$$

Eq (6.2) and Eq (6.3) shows the electrical resistance of the fluids and the capacitance respectively, where κ denotes the electric conductivity of the disperse phase, ϵ_0 , ϵ_{rPDMS} , L_{elec} , d represent the absolute electric permittivity, relative permittivity of PDMS, length of the electrode and the gap of the capacitor respectively. The value of the parameters are measured or determined via the literatures, thus we have $\kappa = 3.0 \mu S/cm$, $\epsilon_0 = 8.85 \times 10^{-12} F/m$, $\epsilon_{rPDMS} = 5$, $L_{elec} = 20 \text{ mm}$, $d = 200 \mu m$. f in Eq (6.3)

stands for the frequency of the AC electric field, which influences the electric resistance of the system capacitance $X_{C_{PDMS}}$.

$$\overline{U}_{Fluid} = \frac{U}{U_{\max}} \cdot \frac{1}{(1 + (\frac{X_{C_{PDMS}}}{R_{Flu}})^2)^{1/2}} \quad (6.4)$$

\overline{U}_{Fluid} is the dimensionless voltage experienced by the dispersed phase. U and U_{\max} refer to the applied voltage and the maximum voltage adopted in the experiment respectively.

On a log-log scale, the results of droplet formation without electric field show a good linear relation between the diameter and Ca . The fitted exponent corresponding to the experimental data follows the relation: $D \sim Ca^{-0.37}$, which is consistent with the reported result [108].

Considering both the hydrodynamic and electric effects, the droplet diameter can be expressed as Eq (6.5) from the frequency-dependent effective capacitance circuit.

$$\frac{D}{Ca^{-0.37}} = \alpha (\overline{U}_{Fluid})^\beta = \alpha \left[\frac{U}{U_{\max}} \cdot \frac{1}{(1 + (\frac{1}{2\pi f C_{PDMS}} \cdot \frac{1}{R_{Fluid}})^2)^{1/2}} \right]^\beta \quad (6.5)$$

Where α and β denote the coefficients of the scaling law.

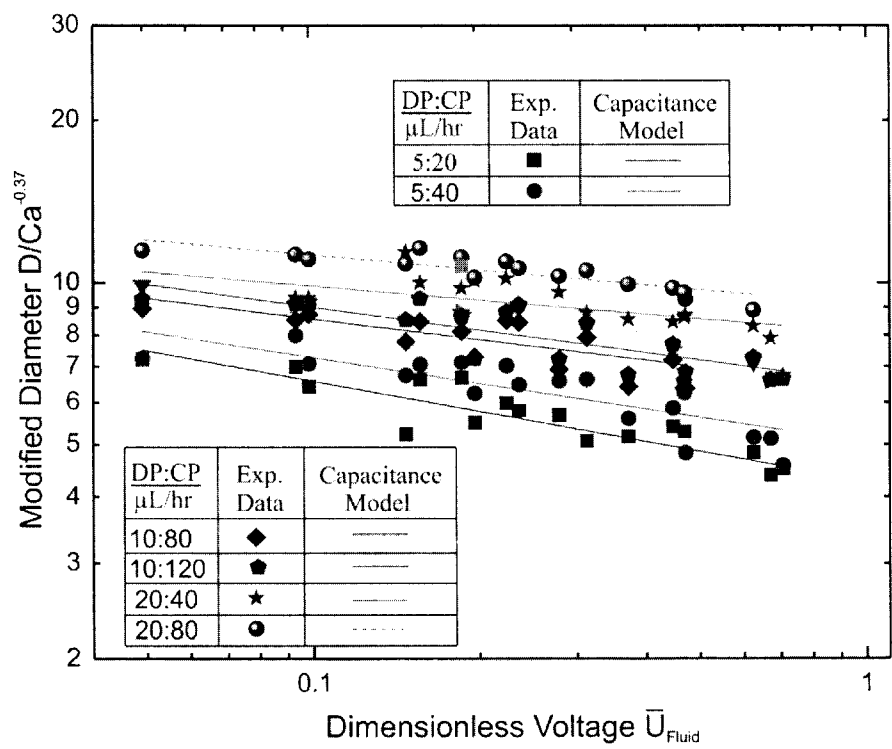


Figure 6.14 (a) Comparison between the capacitance model and experimental data (25 μm orifice).

$Q_{DP} : Q_{CP}$ is in $\mu\text{L/hr}$

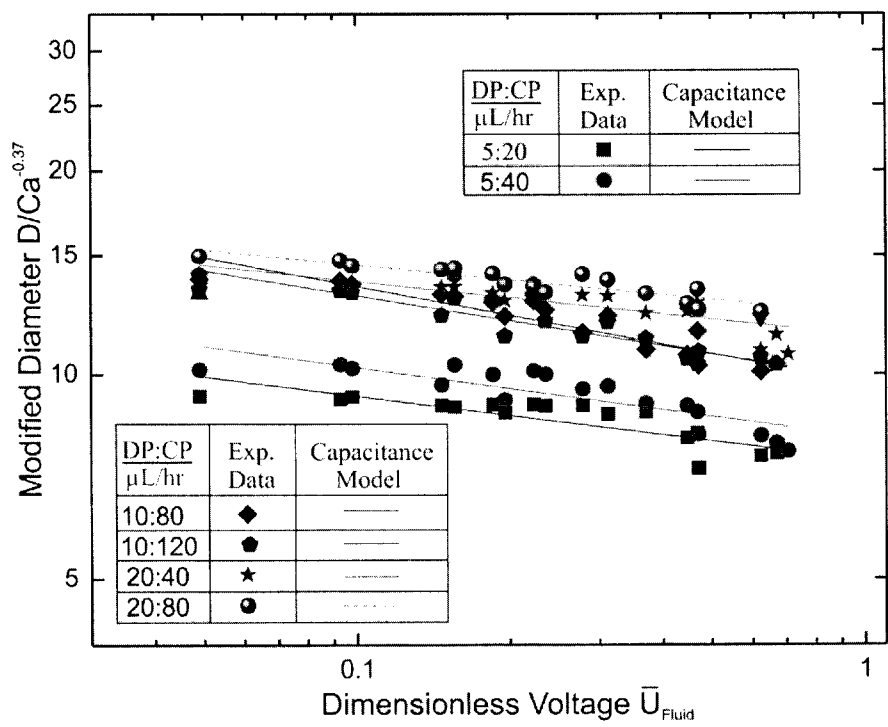


Figure 6.15 (b) Comparison between the capacitance model and experimental data (75 μm orifice).

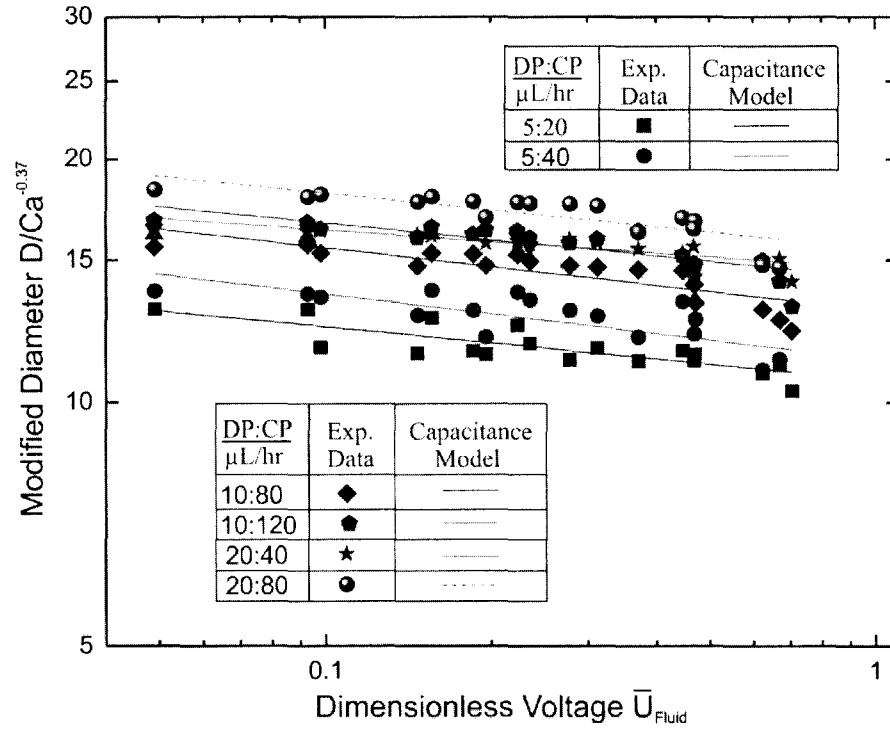


Figure 6.16 (c) Comparison between the capacitance model and experimental data (100 μm orifice).

Figure 6.14 shows comparison between the proposed model and the experimental data with different orifice sizes. There is a good agreement between the model and the experiment. It is worth mentioning that the experimental data utilized in Figure 6.14 excludes the jetting regime as the flow behavior is significantly differently when compared to that of the dripping regime. Eq (6.5) indicates that the dimensionless voltage \bar{U}_{Flu} can be used as a good approximation for the AC electric field when both the applied voltage and frequency are considered. β represents the influence of AC electric field. The value for β are $\beta_{25} = -0.115$ (25 μm orifice), $\beta_{75} = -0.104$ (75 μm orifice) and $\beta_{100} = -0.083$ (100 μm orifice). The variation trend of β indicates that smaller orifice size amplifies the influence of AC electric field. α is a coefficient that is highly influenced by Q_{DP} & Q_{CP} .

6.3.6 High speed μ PIV measurement on non-Newtonian droplet formation dynamics

Droplet formation in microchannels enjoys the benefit of high monodispersity and high frequency. The frequency, as high as the order of 1000 per second, makes the droplet formation a typical transient problem. The time scale for experimental observation usually stays at the millisecond or microsecond level. The observation and measurement of the droplet formation becomes a big challenge for experimental investigation and yet attracts intense research interest.

μ PIV has been a widely adopted approach for flow field visualization and results of various flow field in microfluidic have been reported [102, 202, 207-210]. This study reveals the detailed information on the formation dynamics by adopting a high speed μ PIV system. The formation process of the non-Newtonian droplet in flow focusing microchannels in different regimes is of our concern. The impact of electric field is also addressed in this section.

The high speed μ PIV utilized the Phantom high speed camera (Phantom V611) with 6200 fps at the full resolution of 1280×800. A plan objective of 40× (Leica) is adopted in the measurement. The dispersed phase is doped with 20% orange fluorescent particles (Life Technology, 1 μ m, 540/560 nm) by volume. The fluid sample is illuminated by one double cavity high speed pulse laser (Litron, 527 nm) whose working frequency ranges from 200 to 10 KHz.

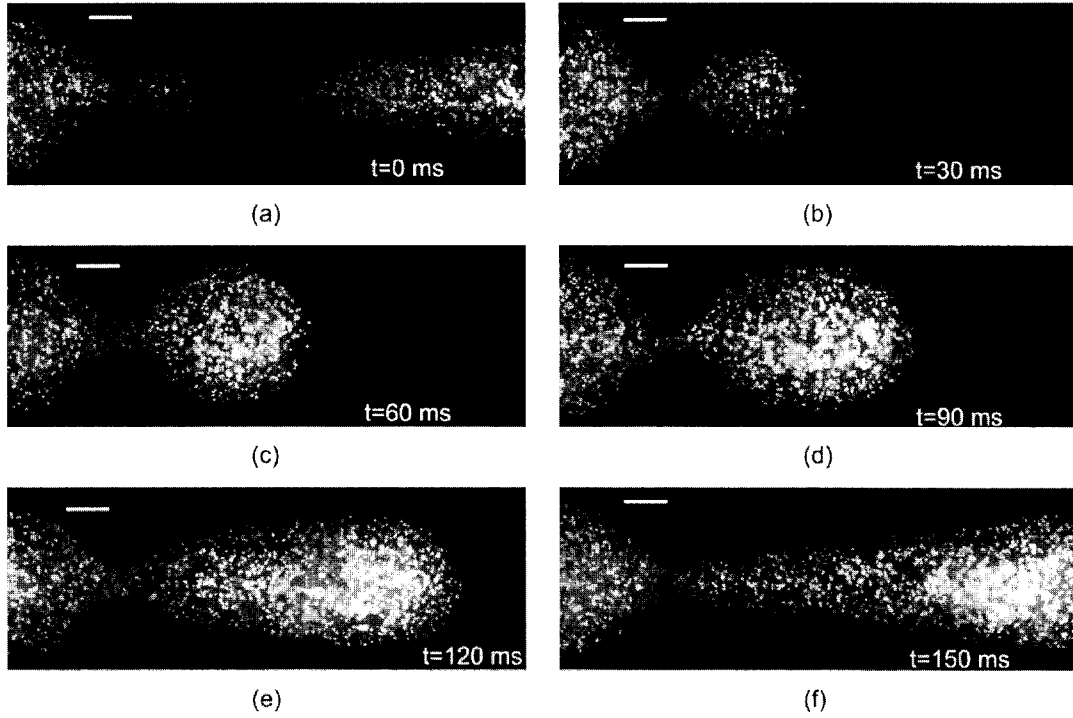


Figure 6.17 Fluorescent imaging of non-Newtonian droplet formation via high speed μ PIV. $W_{or} = 25$ μm . The scale bar indicates 25 μm . $Q_{DP} : Q_{CP} = 10:20$ $\mu\text{L/hr}$

Figure 6.17 shows the fluorescent image of the non-Newtonian droplet formation, which has to be processed in order to obtain the flow field. The imaging speed is controlled at 2000 frames per second considering the speed of the dispersed phase and the size of the integration window.

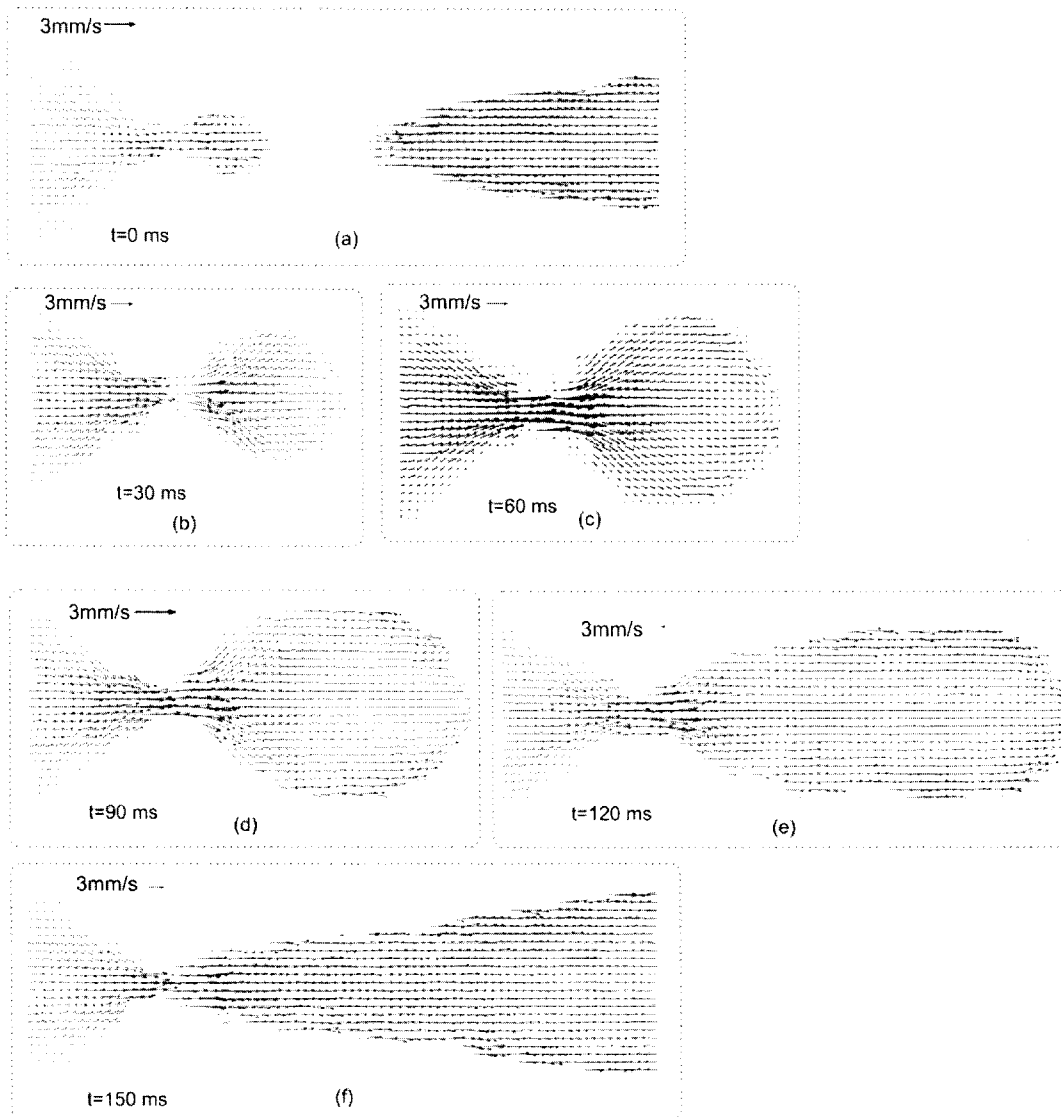


Figure 6.18 Flow field of the non-Newtonian droplet formation in the squeezing regime ($Q_{DP} : Q_{CP} = 10:20 \mu\text{L/hr}$, no electric field applied)

Figure 6.18 shows the flow field of the non-Newtonian droplet formation with reference to different formation stages in Figure 6.17. The vector form of the flow field is obtained by advance particle imaging correlation from the PIV processing software supplied by Dantech. The 50% window overlap and the 32 pixel based coherent filter is adopted during the processing. It can be seen that during the initial stage of formation (Figure 6.18 (a) ~ (d)), the maximum speed occurs in the necking region. The continuous phase induced stress creates flow recirculation. The next

coming stage (Figure 6.18 (e) & (f)) shows an accelerated flow field before it breaks up.

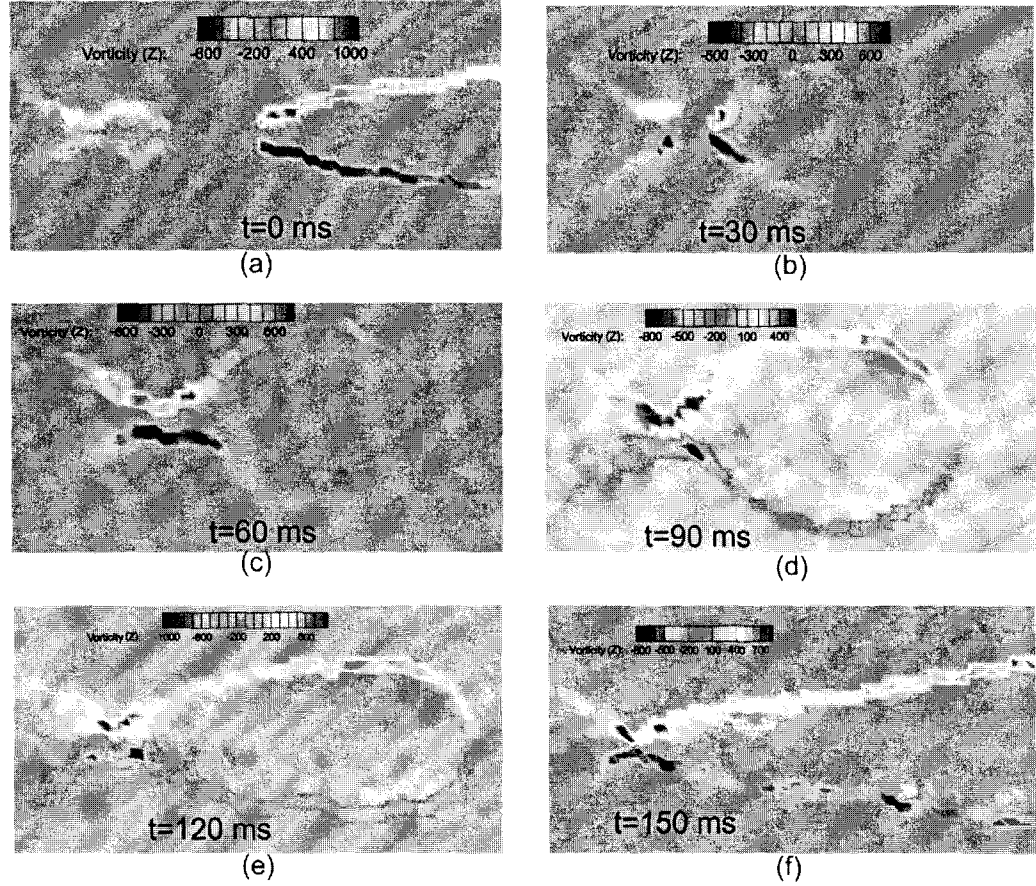


Figure 6.19 Vorticity of the dispersed phase during the droplet formation process in the squeezing regime ($Q_{DP} : Q_{CP} = 10:20 \mu\text{L/hr}$, no electric field applied)

Figure 6.19 is obtained via scalar processing with the flow field shown in Figure 6.16

The vorticity is defined as:

$$\vec{w} = \nabla \times \vec{V} = \left(\frac{\partial W}{\partial y} - \frac{\partial V}{\partial z} \right) \vec{i} + k \left(\frac{\partial U}{\partial z} - \frac{\partial W}{\partial x} \right) \vec{j} + \left(\frac{\partial V}{\partial x} - \frac{\partial U}{\partial y} \right) \vec{k} \quad (6.6)$$

For the 2D μPIV measurement, it can be simplified as:

$$w_z = \frac{\partial V}{\partial x} - \frac{\partial U}{\partial y} \quad (6.7)$$

Figure 6.19 (a)~(c) indicate that in the initial phase of droplet formation, the recirculation occurs in the necking region. When more fluid is accumulated, flow recirculation becomes observable in flow front of the droplet due to the shear stress acted at the interface, see Figures 17 (d) ~ (f).

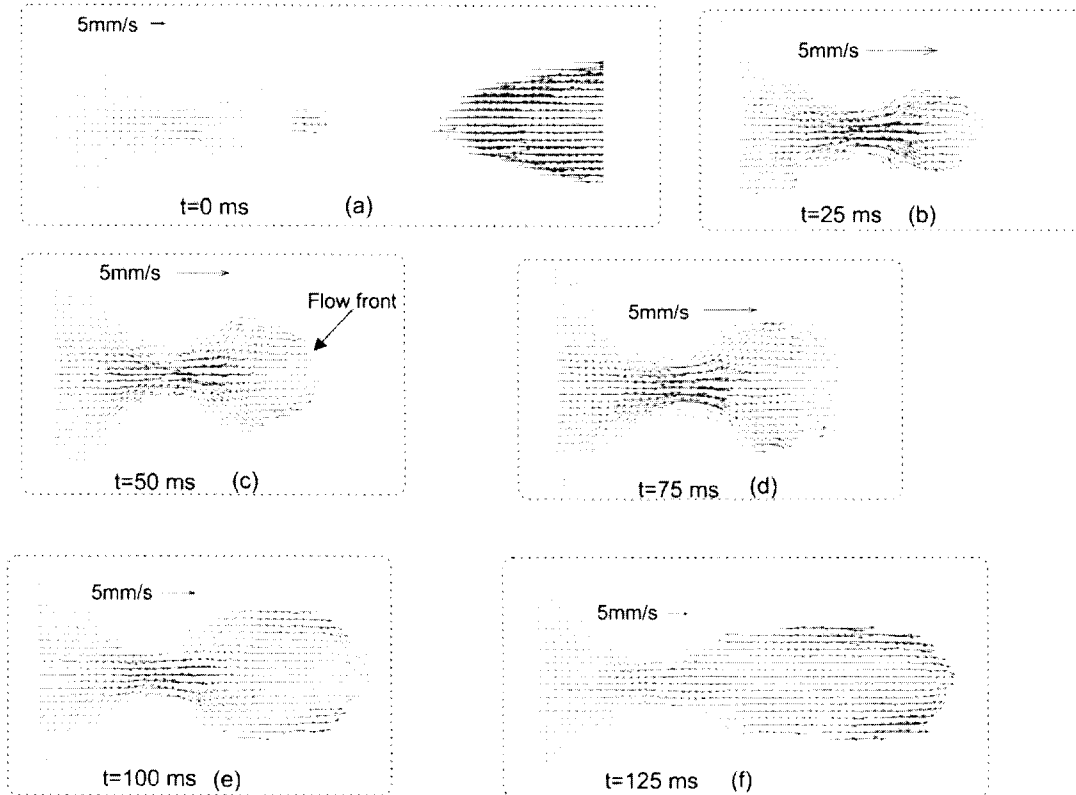


Figure 6.20 Flow field of the non-Newtonian droplet formation in dripping regime ($Q_{DP} : Q_{CP} = 10:80$ $\mu\text{L/hr}$, no electric field applied)

Figure 6.20 shows the velocity distribution of the non-Newtonian droplet in dripping regime. The overall speed is higher than that in the squeezing regime and the droplet size is smaller due to the larger shear stress generated by the continuous phase. Figure 6.20 (a)~(e) show similar distributions where the maximum speeds occurs near the necking region. The major difference between squeezing and dripping is indicated in Figure 6.18 (e) and Figure 6.20 (f). Droplet breakup in squeezing is dominated by the pressure gradient caused by the blockage of microchannel while it

is highly influenced by the elongated shear in dripping regime. Therefore the overall speed is much higher in the dripping regime and droplet shape is elongated into thin thread.

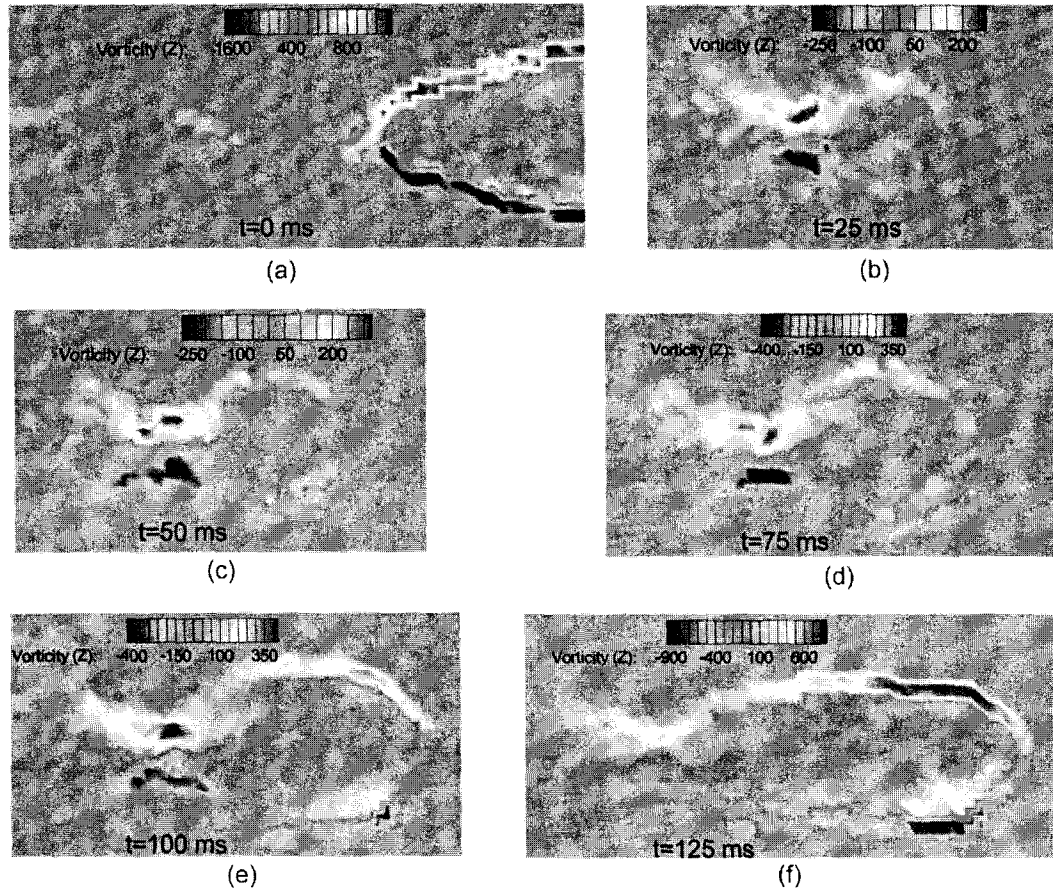


Figure 6.21 Vorticity of the dispersed phase during the droplet formation process in the dripping regime ($Q_{DP} : Q_{CP} = 10:80 \mu\text{L/hr}$, no electric field applied)

Figure 6.21 presents the corresponding vorticity distribution of droplet formation in the dripping regime. When the droplet begins to form (Figure 6.21 (a) ~ d)), the vorticity can be seen primarily in the necking region, similar to that in the squeezing regime. In the final stage of formation, the vorticity becomes obvious at the flow front of droplet. From Figure 6.21 (e) ~ (f), the vorticity at the flow front grows significant, caused by elongated shear of the dripping. Figure 6.21 (f) clearly

demonstrates two regions in both the upper and lower area at the flow front where both positive and negative vorticity is presented.

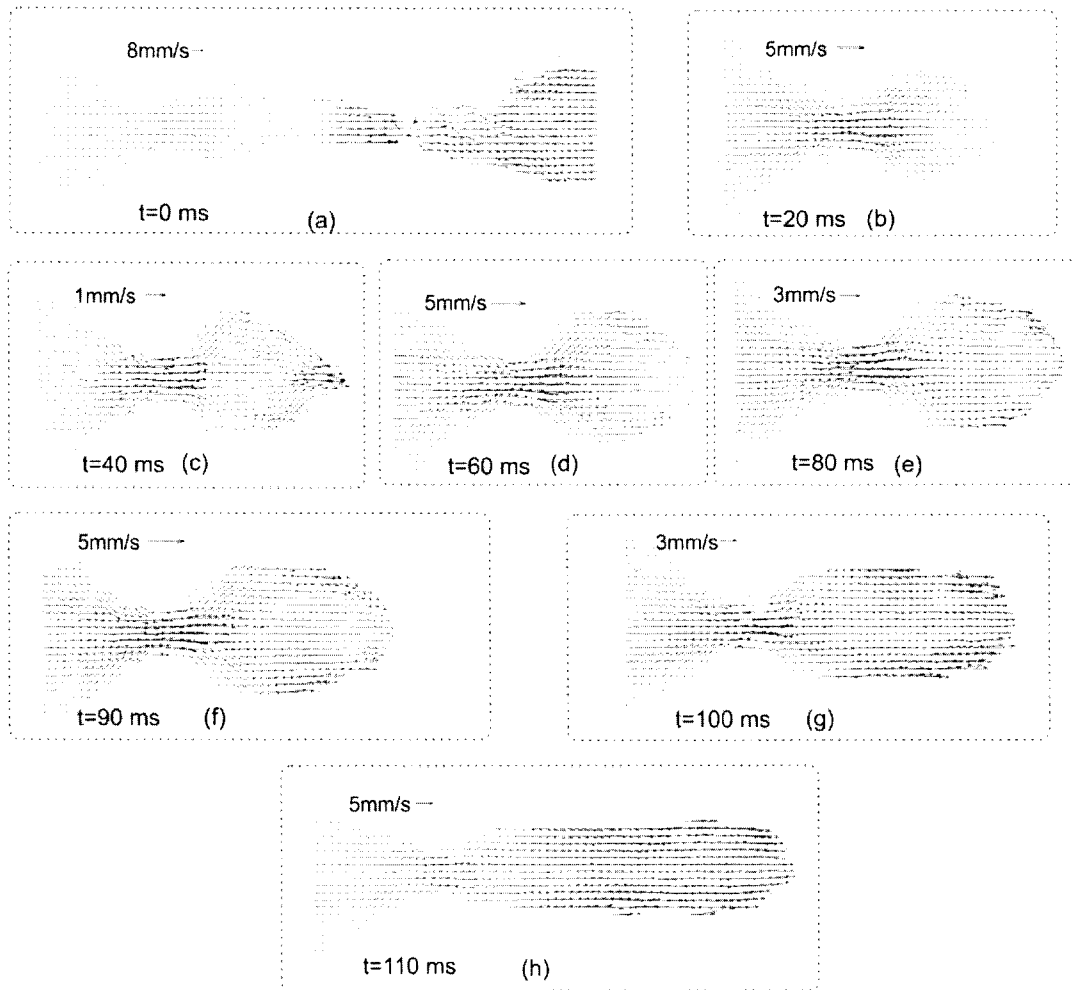


Figure 6.22 Flow field of the non-Newtonian droplet formation in the dripping regime with AC electric field ($Q_{DP} : Q_{CP} = 10:80 \mu\text{L/hr}$, $V = 1 \text{ KV}$, $f = 1 \text{ KHz}$)

Figure 6.22 illustrates the flow field of non-Newtonian droplet formation under the influence of AC electric field. When compared to the results without the application of electric field, the time required for the whole process is shortened. As seen in Figure 6.22 (f) ~ (h), the forming and breakup of the droplet are accelerated by the AC electric field. The non-Newtonian droplet is further deformed via the AC field so that a “flat” interface is observed.

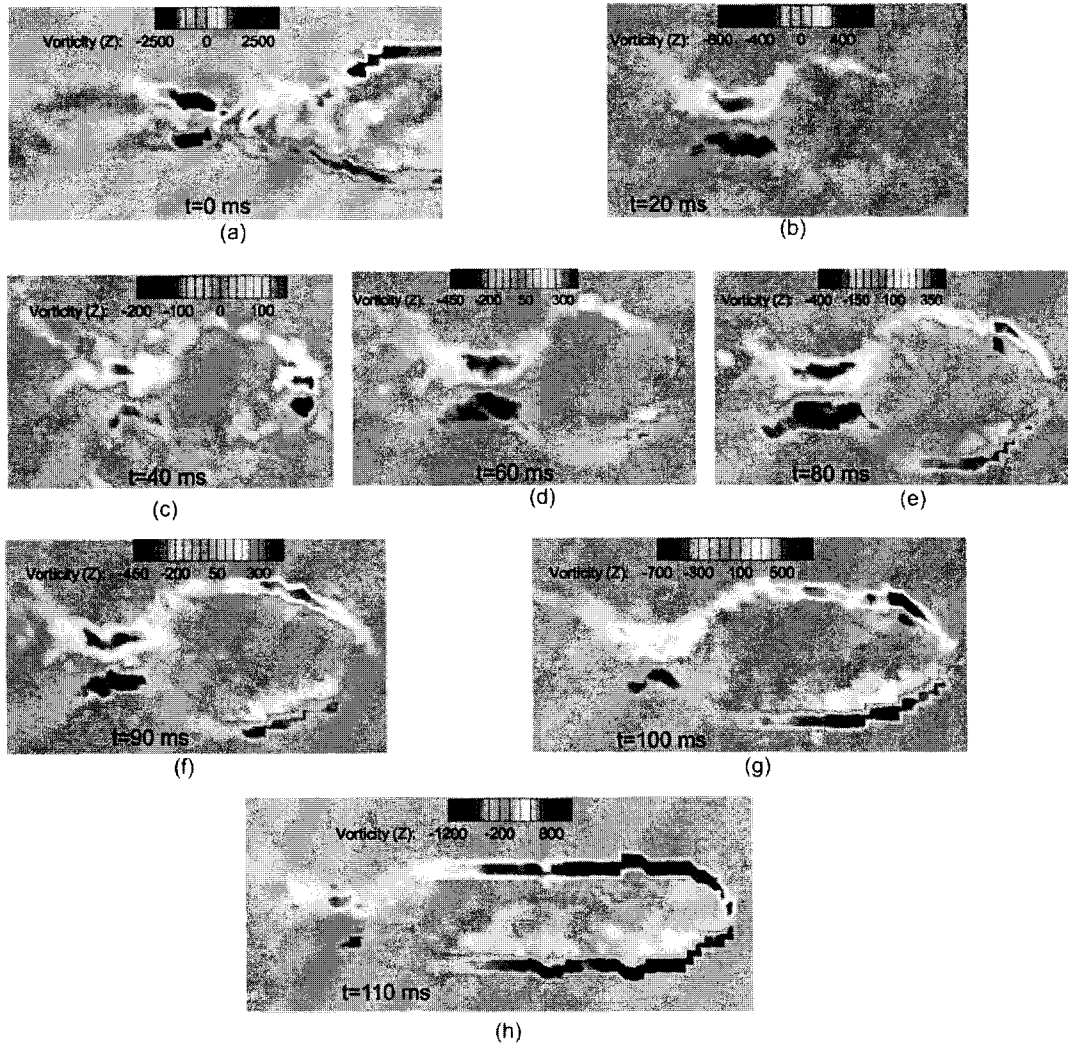


Figure 6.23 Vorticity distribution of the dispersed phase during non-Newtonian droplet formation with AC electric field in the dripping regime ($Q_{DP} : Q_{CP} = 10:80 \mu\text{L/hr}$, $V = 1 \text{ KV}$, $f = 1 \text{ KHz}$)

Figure 6.23 shows the vorticity distribution under the influence of AC electric field. The high level of vorticity is observed near the necking region and the flow front. Evidence of flow recirculation at the flow front is shown in Figure 6.23 (g) & (h). In both of the figures, vorticity at the flow front is the highest with the presence of AC field, indicating that the AC field induced Maxwell stress prompts the vorticity in the interface leading to the flow recirculation.

6.4 Summary

Non-Newtonian droplet formation in flow focusing microchannels was systematically studied by considering the combination of applied AC electric fields (voltage & frequency), flow conditions (Ca & Q_{DP}) and geometries (orifice size). The dynamics of non-Newtonian droplet formation was first addressed, where the formation of satellite droplet and evolution of filament thickness was analyzed. AC electric field induced Maxwell stress were found to be a stimulation of interfacial instability, thus prompting the formation process and leading to a smaller size of droplet. The non-Newtonian droplet size control can be achieved by the implementation of an AC electric field. More specifically, the applied voltage is more crucial as the size control can only become significant when the voltage exceed a certain value, while the frequency takes effect only under high voltages. Flow conditions and geometries, which highly influenced the hydrodynamically induced shear, plays an important role in tuning the droplet and its formation regime shifting. The combination of all the parameters provides the flow focusing microchannel with diverse formation possibilities.

The effective capacitance model for the AC field tuned non-Newtonian droplet formation was proposed based on the discovery of frequency dependent formation characteristics. The system capacitance circuit was analyzed. Comparisons between the model and the experiment are made, good matching is achieved and the power law index is analyzed for each geometry.

Finally, the high speed μ PIV measurement was conducted to quantitatively address the non-Newtonian droplet formation process. Droplet formation dynamics in the squeezing, dripping regimes were measured. The influence of the AC electric field

on non-Newtonian droplet formation was also explored. Flow fields were obtained via advanced cross correlation processing method. The indication of flow recirculation, vorticity, was also presented. Results show that flow recirculation is more significant in dripping regime than that in squeezing due to the elongated shear. The electric field generated Maxwell stress deforms the interface into a “flat” shape and strengthens the flow recirculation.

Chapter 7 Particle Free Optical Imaging of Flow Field by Liquid Crystal Polarization

7.1 Introduction

Liquid crystals (LCs) are well known for their optical properties, whose orientations can be tuned via various stimuli. In fact, LCs' orientations are sensitive to electromagnetic fields, chemical presence, surface property and hydrodynamic pressure gradient [195, 211-213]. Recent studies showed that their sensitivity to bio samples endure themselves to be bio sensor [195, 213, 214]. LCs also respond to a surface treatment, namely surface anchoring condition [121, 122, 173]. More importantly, flow field also can influence LCs' orientation, which makes a perfect condition for optofluidic research [10, 11].

Investigation on behaviors of liquid crystal under external fields has been reported for the past decades, such as electric field [124, 215-217], temperature field [200, 201, 211] and shear flow at normal scale [218]. But the LCs' flow behavior is still unexplored in modern microfluidics. The coupling of flow field with molecular reorientation at micro scale is yet to be studied so as to reveal the relation between each other. The flow confinement of LCs provided by microfluidics is ideal for research upon surface treatment, bio sensor and flow visualization due to the refined control of flow conditions. Microchannel fabricated by modern microfluidic technology has a resolution of the order of μm [132, 137]. The ease in geometry design and channel fabrication also provides benefits. Besides, nano-liter per hour flow rates can be achieved by modern syringe pump, which opens the door for exploring at a different scale. Under different flow conditions caused by varying flow rates, channel geometries or surface anchoring conditions, LCs will display different

fringe patterns illuminated by polarized light source. On one hand, all the refined controls will add to maneuver LCs' molecular orientations. Reversely, fringe patterns obtained by LCs' polarization reveal the flow condition, which achieved flow visualization. Traditional flow visualization method utilizes the seeding particles to track flow field, which is generally termed as particle image velocimetry (PIV). However, the resolution of the traditional method is strongly limited by the size & concentration of the seeding particle causing the vulnerability in micro-scale measurements. Therefore, LCs show a great potential in flow visualization under microfluidic environment.

4-Cyano-4'-pentylbiphenyl (5CB) is adopted in the investigations as it remains nematic phase under room temperature. 5CB is a type of nematic liquid crystal (NCL) called calamitics which has a rod-like molecular structure [120]. The rod-like molecular structural become observable illuminated by polarized light as it is in nematic phase. Most of the literatures have been focusing on the its' dynamic behavior under electric field [124, 215-217, 219]. Very few works have been done to study the reorientation under hydrodynamic pressure gradient at micro scale [212]. The nozzle/diffuser microchannel, also called rectifier [90, 203, 220, 221], is a well reported geometry which is utilized to show the inter connection of the flow field and 5CB molecular reorientations.

In this chapter, the dynamic responses of 5CB liquid crystal in the nozzle/diffuser microchannel under different flow rates are represented. The nozzle/diffuser design is also known for its ability to create flow recirculation [203, 220]. When 5CB flows within the geometry, the rod-like molecules are reoriented due to the flow induced shear (flow shear) and the flow recirculation created. The interconnection between the flow condition and molecular reorientation is investigated and analyzed. Three

opening angles — 15° , 30° , 45° — are designed to study the geometrical effects on the fluid field visualized by the LC polarization. The results clearly show the influence of flow condition upon reorientation of molecular structure, which in turn demonstrates 5CB's potential application in flow visualization.

7.2 Materials and method

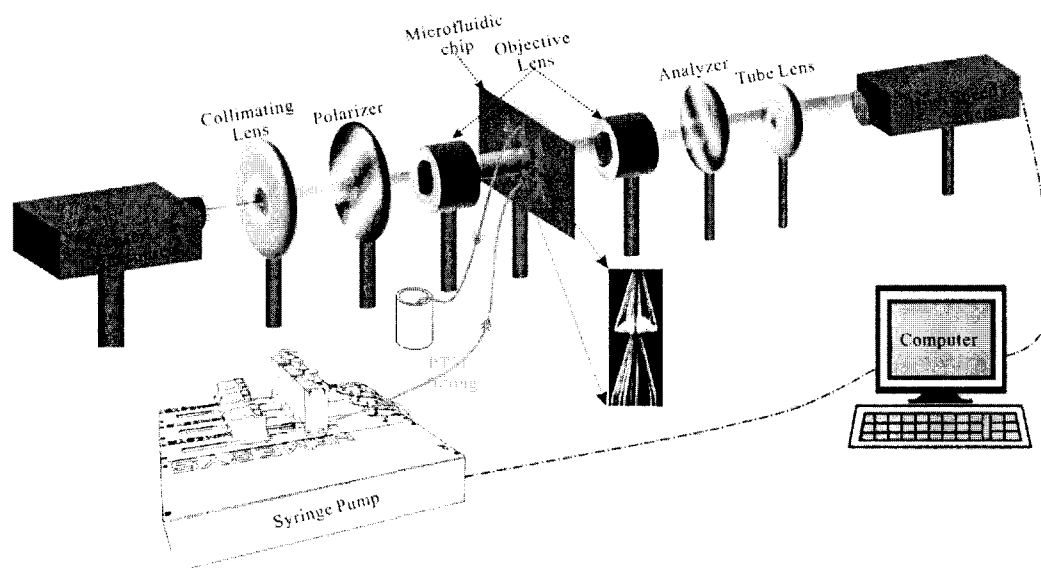


Figure 7.1 Experimental setup for visualizing single phase liquid crystal flow in nozzle-diffuser microchannels

Figure 7.1 demonstrates the overall setup configured for performing the experiments. The optical setup consists of a diode pumped solid state laser of wavelength 405 nm, a collimating lens, two objective lenses, one set of polarizer-analyzer combination, a tube lens and a high speed camera interfaced to a PC. The syringe which contains 5CB is driven by the syringe pump and connected with the nozzle-diffuser microchannels via polytetrafluoroethylene (PTFE) tubing. The camera acquires the images interfaced to the personal computer (PC). PC uses for image processing as well as syringe pump control through the controllers as shown in Figure 7.1. Further

details of the optical set up and fluidic set up configured for this study as given below.

7.2.1 Optical setup

The dynamic response of the 5CB liquid crystal in nozzle/diffuser microchannels is observed with the optical setup as shown in Figure 7.1. A Diode pumped Solid State laser (MDL 100 mW) at 404 nm wavelength is chosen for illumination. A set of polarizer and analyzer (from Thorlabs Inc.) is configured at cross polarization state for the purpose of revealing 5CB dynamic response to the flow induced shear. A microscope objective lens (Olympus 10X/0.3NA) is used to focus light into the microchannel and an infinity-corrected objective lens (Olympus 50X/0.5NA) is used for collection of images from the microchannel which is then mapped onto the high speed camera (Phantom m310) through a tube lens (Thorlabs Inc.). The high speed camera can capture 3,200 frames per second at full resolution of 1280 x 800, which has the ability of capturing the 5CB response in the nozzle/diffuser microchannel. All experimental results are recorded at the speed of 500 frames per second.

7.2.2 Fluidic setup

Centoni neMESYS high precision syringe pump and gas tight microliter syringe (Hamilton Gastight 1725) are utilized to create confined flow condition. PTFE micro tubing is chosen to connect syringe and microchannel in case of chemical corrosion.

7.2.3 Materials

The liquid crystal adopted is the single component liquid crystal 4-Cyano-4'-pentylbiphenyl (5CB), with chemical formula $C_{18}H_{19}N$, purchased from Frinton Laboratories (FR-2240). 5CB is prepared without additional treatment and it is in the

nematic phase as temperature of the microchannel is controlled at 24 °C. It is transition from nematic phase to isotropic phase occurs at temperature of 33 °C.

7.2.4 Microchannel

The nozzle/diffuser microchannel is prepared by standard soft lithographic procedure followed by polydimethylsiloxane (PDMS, Dow Corning Sylgard 184) process and plasma bonding with one slice of microscope glass spin-coated with one thin layer of PDMS to ensure uniform surface property. After exposure to the plasma, the PDMS surface becomes hydrophilic, the surface anchoring changes from homeotropic to degenerate planar [122]. It will gradually turns back to hydrophobic and homeotropic within 1-2 hours, depending on the ambient parameters such as room temperature and humidity. The microchannel was generally stored for more than one day to ensure the homeotropic surface anchoring.

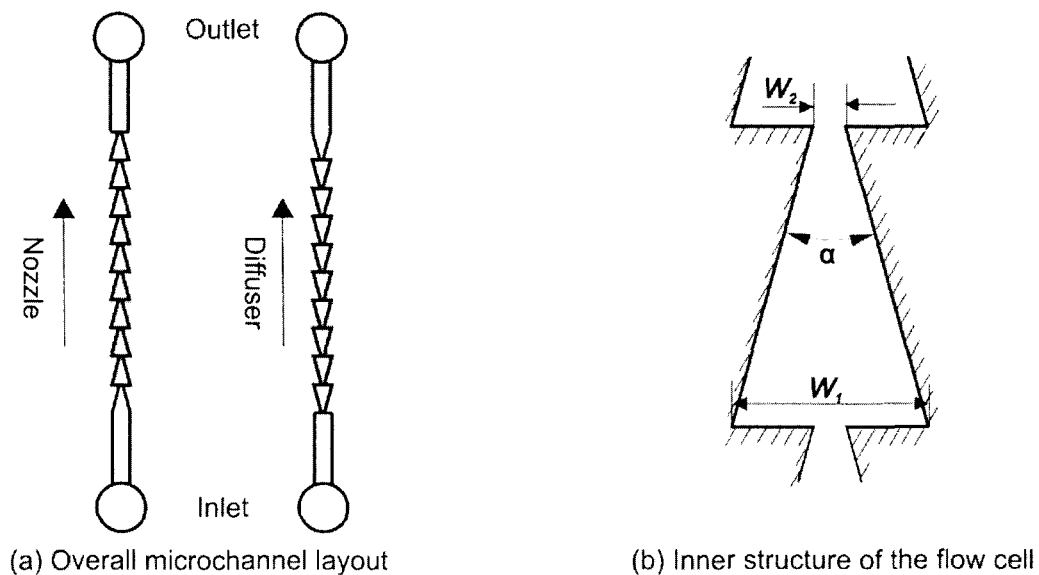


Figure 7.2 Representative diagram of the microchannel.

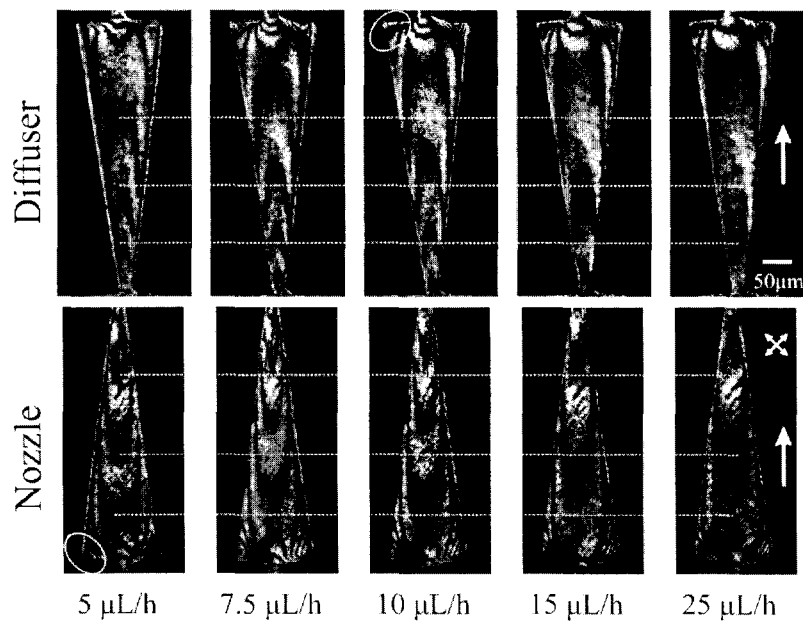
Figure 7.2 (a) shows the overall layout of the microchannel while Figure 7.2 (b) shows the flow cell of the microchannel. In total 10 flow cells built the microchannel. Both nozzle and diffuser directions are tested in the experiments. Width of the

microchannels are $W_1=150\text{ }\mu\text{m}$, $W_2=25\text{ }\mu\text{m}$ respectively with the depth $d=35\text{ }\mu\text{m}$.

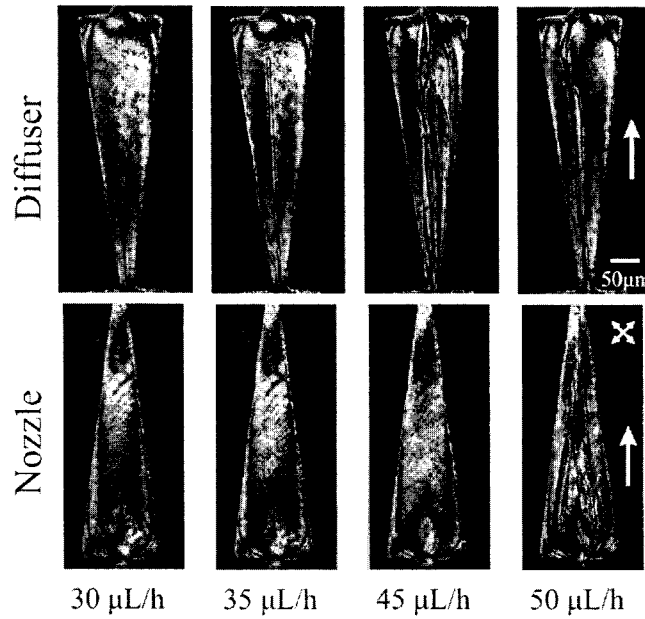
Here, ' α ' represents the opening angle of the flow cell. Microchannels with three opening angles — 15° , 30° and 45° — are designed and fabricated for investigations.

7.3 Results and discussion

7.3.1 Flow field induced fringe patterns in 15° opening angle microchannel



(a) Fringe patterns under flow rates of 5~25 microliter per hour



(b) Fringe patterns under flow rates of 30~50 microliter per hour

Figure 7.3 Fringe patterns of 15° opening angle microchannel along diffuser and nozzle directions.

Figure 7.3 shows results for 15° opening angle microchannel at different flow rates along both nozzle and diffuser directions. It is to be noted that the non-linear convection term can be ignored for flow at low Reynolds number ($Re \approx 10^{-3}$), and the governing equation becomes linear. Under this condition, flow should be reversible and insensitive to the flow direction and in this case, the fringe pattern should be identical for flows of both directions [221]. However, fringe patterns demonstrated in Figure 7.3 show a sensitive case, which is majorly due to the non-linear fluid properties. When the liquid crystal flows along the nozzle and diffuser directions, its rod like molecules experience the contraction and expansion respectively causing the flow-direction-sensitive fringe patterns.

In this work, 15° is the smallest opening angle among all microchannels. Small angle leads to less pressure variation along flow direction and thus the optical pattern varies gradually. Figure 7.3 (a) shows the results when the flow rate varies from 5 $\mu\text{L/h}$ to 25 $\mu\text{L/h}$ along both diffuser and nozzle directions. The fringes shift by 20

μm to $80\ \mu\text{m}$ along the flow direction for both directions as flow rate increases from $5\ \mu\text{L/h}$ to $7.5\ \mu\text{L/h}$, depending on the position of each fringe. Fringe pattern is directly related to the LC molecular orientation which is influenced by the flow shear. Within certain range of flow rates, larger flow rate results in a larger shear indicating more influence on the molecular orientation. Fringe pattern shifts gradually along both flow directions at 5 , 7.5 and $10\ \mu\text{L/h}$. Fringe pattern near the corner indicates the occurrence of flow recirculation. The fringes continue to shift furtherly increasing the flow rate. It shifts along the flow direction and the corner region is occupied by more recirculation patterns. The major difference between nozzle and diffuser directions is the sudden geometrical expansion of nozzle which facilitates the recirculation. That explains why flow recirculation can be seen from flow rate of $5\ \mu\text{L/h}$ along nozzle direction while it occurs only at $10\ \mu\text{L/h}$ along the diffuser direction.

The thread-like patterns, normally termed as topological defects, appear as shown in Figure 7.3 (b). When large molecular reorientation gradient applied and 5CB's molecular orientation cannot change continuously, "threads" will occur. We can conclude from Figure 7.3 (b) that the diffuser direction encourages the threads as compared to the nozzle direction. The diffuser inlet dimension is $25\ \mu\text{m}$ which is much smaller than the nozzle inlet's $150\ \mu\text{m}$. This leads to a much larger molecular reorientation gradient. No significant variation can be observed via increasing flow rates as the microchannel is covered with threads. The results in the diffuser direction shows a relatively symmetric flow structure whereas the results in the nozzle direction are asymmetric largely due to the sudden expansion geometry of the nozzle, which agrees with other reported results [221]. The flow characteristics indicated from Figure 7.3 agrees well with the literatures. The fringe pattern obtained by LC

polarization gives a clear indication of flow field and thus is capable of flow field characterization.

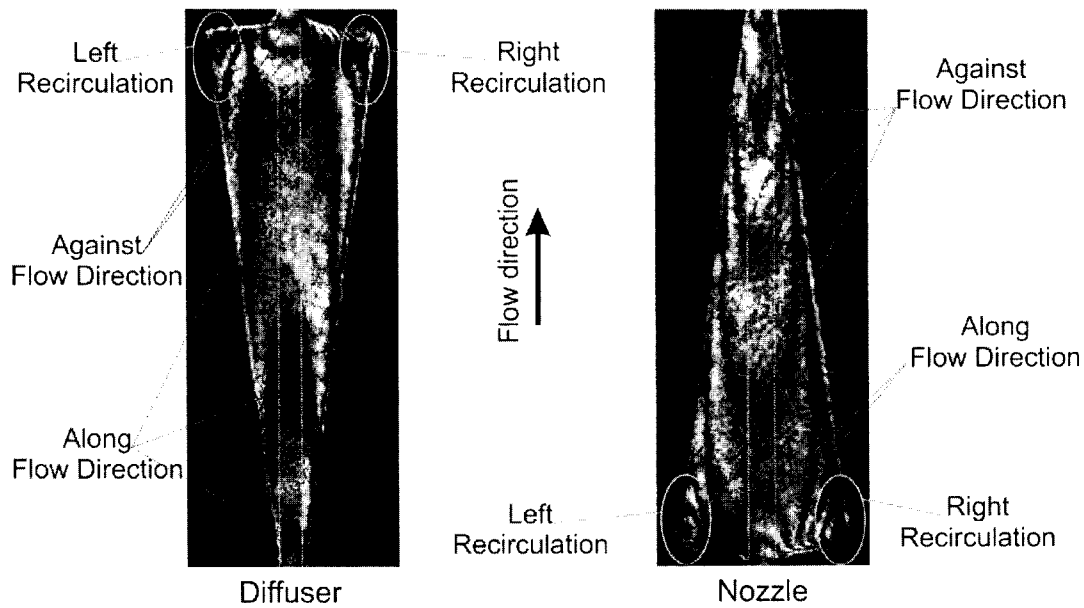


Figure 7.4 Fringe pattern characteristics along both diffuser and nozzle directions

Figure 7.4 presents the characteristics of the fringe patterns with emphasis on fringe pattern distributions. Fringe patterns can be divided into two major groups based on their locations: (1) at the central region and (2) at the corner region. With reference to the flow direction, there are two types of fringes at the central region: (1) along and (2) against flow direction. Fringes in the corner region are due to flow recirculation. We will address these types of fringes in the following sections.

7.3.2 Fringe density for different opening angles under various flow rates

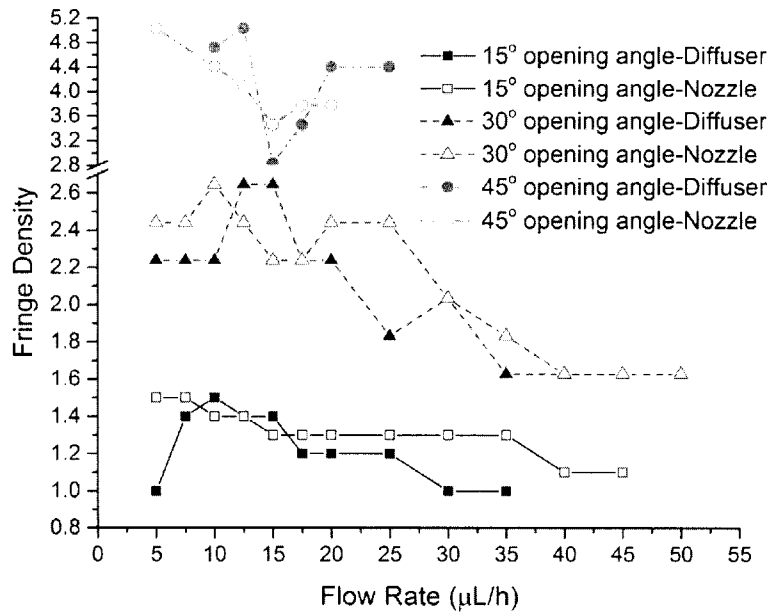


Figure 7.5 Variation in fringe density as function of flow rates for opening angles

Figure 7.5 shows that the fringe density is influenced by flow rate, opening angle and flow direction as well. Fringe density is defined as:

$$\chi^* = \frac{\chi}{\chi_{Di-15^\circ,35}} = \frac{N / A}{\chi_{Di-15^\circ,35}} \quad (7.1)$$

Where χ^* is the dimensionless fringe density, χ is the dimensional fringe density, $\chi_{Di-15^\circ,35}$ represents the fringe density of the 15° opening angle channel along the diffuser direction flowing at the rate of 35 μL/h, N is the total number of fringes and A is the area of one flow cell.

The general trend as seen in Figure 7.5 is that larger opening angles possess higher χ^* . Although χ^* has a small fluctuation at relatively low flow rates, the overall results indicates a decay in χ^* as the flow rate increases. At low flow rates, χ^* tends to have a small value due to small molecular reorientation gradient caused by

the flow shear. χ^* becomes stable when the shear is strong enough to realign the molecular orientation. χ^* turns to decay on further increasing the flow rate as the fringe number in the central part is reduced. It is seen that fringe density gradient increases significantly when adopting the 45° opening angle.

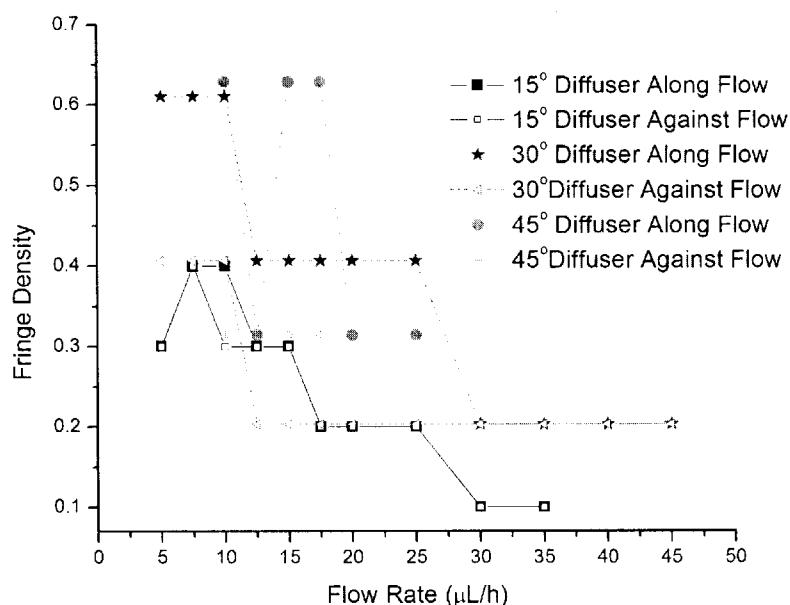


Figure 7.6 Variation in central fringe density as function of flow rate for various opening angles with flow along and against diffuser direction

Figure 7.6 analyzes the fringe pattern located at the center. The influence of flow rate on the central fringe density along diffuser direction is shown in Figure 7.6. The fringe density along the flow direction is a clear evidence of flow shear induced 5CB molecular reorientation while the one against is caused by contraction geometry. A threshold of fringe densities exists for both along and against flow directions, meaning flow field tuned fringe pattern is only sensitive under certain range of flow rate. As the flow rate increases, the flow shear applied is strong enough to realign the molecules. The threshold flow shear for the respective fringe density against flow direction can also be deduced based on this. Results in Figure 7.6 show that the opening angle is also one critical parameter. The threshold is noticeable for small

opening angles. However, for large opening angles, the central fringe density tends to stabilize due to the flow shear created by geometry.

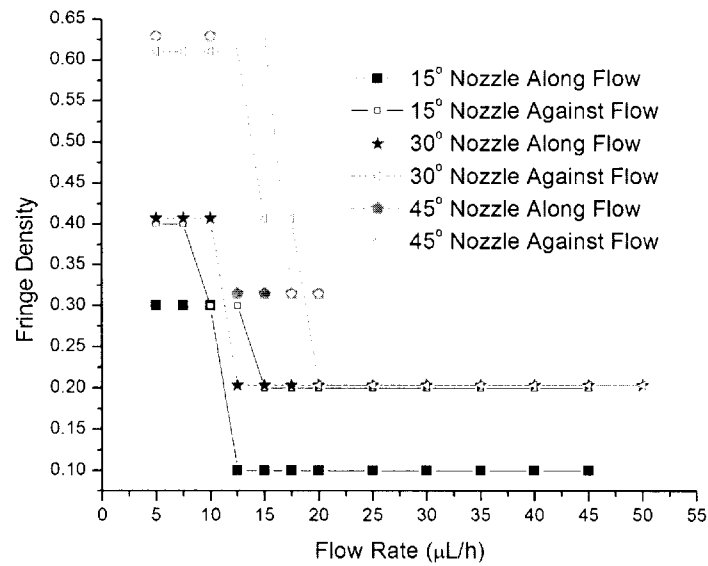


Figure 7.7 Variation in central fringe density as function of flow rate for different opening angles with flow along and against nozzle direction

Figure 7.7 analyzes the results for nozzle direction. Similar to the previous case, thresholds are observed for flow along and against nozzle directions. Both flow rate and opening angle have influence on the fringe density.

7.3.3 Flow recirculation patterns of 5CB liquid crystal for diffuser and nozzle directions

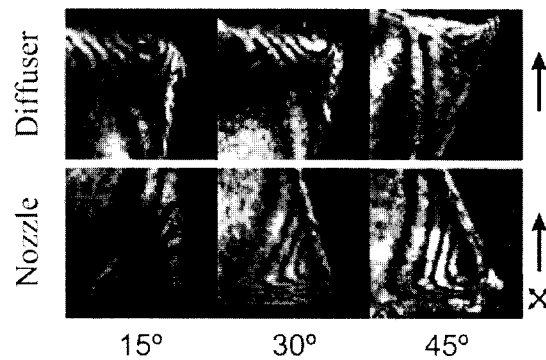


Figure 7.8 Flow recirculation fringe pattern for different opening angles

Figure 7.8 shows the fringe pattern due to flow recirculation which is one of the distinctive flow features in nozzle/diffuser microchannel. We obtained fringe patterns for diffuser/nozzle microchannels with three different opening angles: 15°, 30° and 45°. The flow recirculation is influenced by the flow rate and opening angle. So does the 5CB molecular orientation.

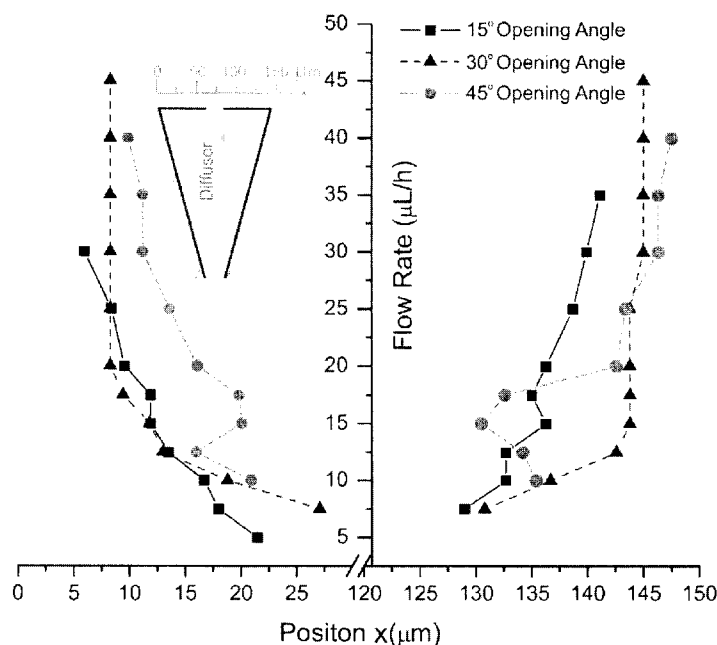


Figure 7.9 Variation of flow recirculation central positions in diffuser direction with flow rates for different opening angles

Figure 7.9 shows central positions of recirculation pattern shift with flow rate and opening angle along the diffuser direction. The position varies significantly with flow rates and opening angles along horizontal direction (x direction). However, it does not vary vertically. Therefore only the position along the x direction is presented. The central position of flow recirculation pattern is pushed to the corner when increasing the flow rate. Smaller opening angles show a good trend with relatively good symmetry. The largest opening angle, 45°, has a larger variation under flow rates from 10 to 20 μL/h. The reasonable trend of the central position of flow recirculation demonstrates the potential of flow visualization method via LC

polarization involving flow recirculation in micro-scale, which is challenging for traditional PIV measurement.

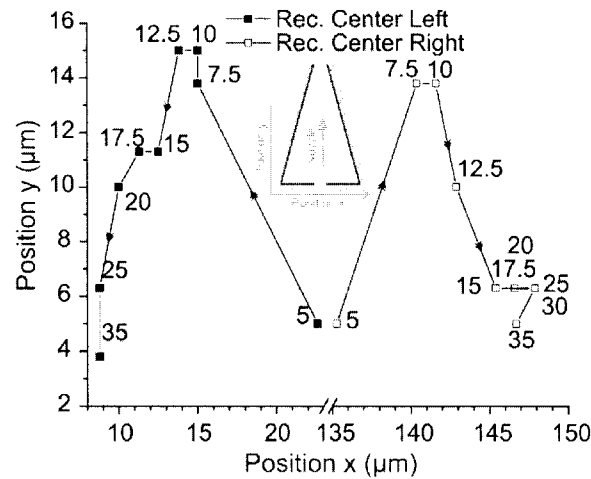


Figure 7.10 Variation of flow recirculation central positions along nozzle direction with flow rates for 15° opening angle

Figure 7.10 presents central positions of flow recirculation patterns along nozzle direction under different flow rates for 15° opening angle. The center position depends on both flow rate and opening angle and it varies in both horizontal and vertical directions (x and y directions, respectively) as shown in Figure 7.10. The center position is pushed to two corner regions on increasing the flow rate which is similar to the result in the diffuser direction. The central position in y direction rises initially with flow rates from 5 $\mu\text{L/h}$ to 7.5 $\mu\text{L/h}$ and then declines with flow rates from 12.5 $\mu\text{L/h}$ to 35 $\mu\text{L/h}$. The initial increase is due that the central position is close to the center of the microchannel and influenced by the flow. When the flow rate is larger, the center position is pushed to the corner. As the result of the flow recirculation induced flow field, the central position in y direction drops. The results obtained from the imaging of LC polarization demonstrate the characterizations of flow recirculation along nozzle direction and shows its potential in flow visualization.

7.3.4 Topological defects represented by Erikson number

Normal flow stability is characterized by *Reynolds* number Re . However, LCs flow shows instability at very low Re (typically $Re \approx 10^{-3}$). As such Erikson number should be considered for LCs flow [121]. Erikson (Er) number is defined as:

$$Er = \frac{v\mu L}{K} \quad (7.2)$$

Where v is the flow velocity, μ is the dynamic viscosity, L & K represent the characteristic length and elastic constant respectively. For 5CB, we have $\mu = 32$ cSt,

$$K = 5.5 \times 10^{-12} \text{ N}$$

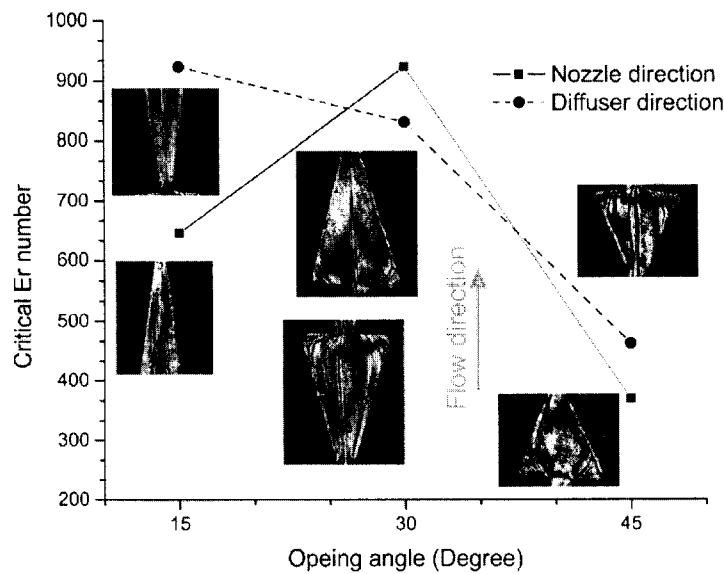


Figure 7.11 Critical Er number for different opening angles

Figure 7.11 shows the critical Er number for different opening angles. Critical Er number indicates the critical flow condition when the threads appear. We can conclude that the critical Er number drops drastically when 5CB flows in larger opening angle while difference between nozzle and diffuser direction is not significant. Large opening angle promotes the flow shear and has a relatively high

fringe density and it tends to show the thread even at low Er number. When Er number is high enough, the thread will appear and make it hard for fringe pattern observation. Therefore the critical Er number defines the range of the flow condition, within which the flow visualization via liquid crystal polarization is applicable.

7.4 Summary

In this chapter, we have investigated the flow field by analyzing the liquid crystal polarization induced fringe patterns in nozzle/diffuse microchannels. The method is implemented by imaging of the flow of the liquid crystal in microchannels under a polarization based optical interferometric configuration. The flow field is visualized and characterized by analyzing the obtained fringe patterns which indicate the flow induced shear and demonstrate the characterization of the flow recirculation. Asymmetrical flows between the nozzle and diffuser directions are proved via analyzing the associated fringe patterns. Fringe density is proposed to relate the fringe patterns to the flow induced shear. Central positions of the flow recirculation obtained from the fringe patterns characterize the flow field. The critical Er number is used to address the operational range of this method due to the occurrence of the topological defects.

The concept of particle free imaging of flow field achieved by liquid crystal polarization provides a distinctive method for flow field visualization and its related analysis. It shows great advantages over the traditional adopted PIV method in flow measurements at micro-scale.

Chapter 8 Investigations of Interfacial Dynamics of Droplet

Production via Particle Free Flow Visualization Method

8.1 Introduction

Flows within microchannels differ from that at macroscales due to the drastic drop in the inertial effects, and thus have very low Reynolds numbers [151, 220]. An interesting aspect of LC microfluidics flow is the ability to precisely control and manipulate flows [100, 105, 222]. The use of complex fluids as transport medium has paved way to the creation and study of novel phenomena, leading to varieties of applications. For example, the use of emulsions has emerged as droplet based microfluidics [92, 97, 104, 108, 110, 223]. The emerging field of topological microfluidics can control complex anisotropic interactions between molecular structures of liquid crystalline phases with geometrical constraints provided by microchannels, leading off a range of novel phenomena and potential novel applications on microfluidic platforms [10, 121, 126, 212].

With the occurrence of microfluidic based droplet and its manipulation methods, the production of liquid crystal droplet provides new opportunities on the investigation of droplet formation involving anisotropic fluids [195, 224]. Coupling with the external AC electric field, the breakup dynamics of the LC droplet become more interesting. The controlled production of LCs droplet offers applications for bio-sensors, and other tunable fluidic component [131, 214, 215, 225].

The optically revealed flow field via the LC polarization essentially achieves the flow field visualization. The widely adopted flow field visualization method via tracking the seeding particle, namely micro particle imaging velocimetry (μ PIV), is well known in flow measurement at micro scale [202, 210, 226, 227]. However, it is

vulnerable in measurements of wall /interfacial boundary dynamics due to the nature of the seeding particles. To overcome the challenges, particle free methods are to be considered. LCs, whose molecular orientation is tunable via flow field and observable via POM setup, show great potential in flow field visualization.

In this chapter, the experiment of LC droplet formation in flow focusing microchannels considering both the conditions: with and without AC electric field were conducted. The investigation of droplet formation dynamics of LC was provided. Results of experimental observation under crossed polarization setup were analyzed for illustration of its corresponding flow field. Droplet size control methods via hydrodynamic shear and AC electric field were presented. The AC electric field tuned liquid crystal droplet formation was highlighted.

8.2 Method and materials

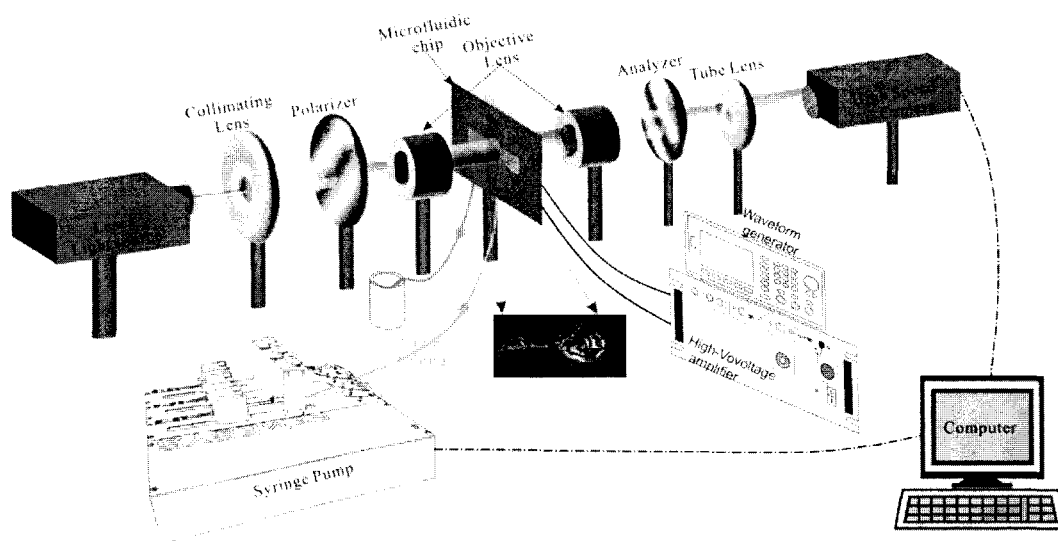


Figure 8.1 Schematic diagram of the microchannel on liquid crystal droplet generation with AC electric field

Figure 8.1 illustrates the overall experimental setup. It consists of the optical setup, microchannel, fluidic setup and the electric setup. The optical setup is utilized to

reveal the orientation of the LC within the microchannel. The microchannel is a flow focusing geometry used to produce the LC droplet. Fluidic system is meant for the refine control of flow conditions, namely the flow rates. Finally the electric system is adopted for the application of the AC electric field.

8.2.1 Optical setup

The dynamic response of LC droplet formation in microchannels is observed and recorded by the optical setup. Before the laser light (produced by A Diolde pumped Solid State laser, 405 nm, MDL 100 mW) illuminates the microchannel, it has to be collimated by the collimating lens (Thorlabs Inc.), polarized by a polarizer (Thorlabs Inc.) and then focused by a microscope objective lens (Olympus 10X/0.3). Being illuminated by the laser light, the image of the microchannel is magnified by another objective lens (Olympus 50X/0.5 NA), polarized by a analyzer, mapped by a tube lens (Thorlabs Inc.) and finally recorded by a high speed camera (Phantom m310). The high speed camera can capture 3200 frames/s at the full resolution of 1280×800 and reaches its maximum speed of 650,000 frames/s at the resolution of 64×8, which is adequate for the experimental observation.

8.2.2 Microchannel

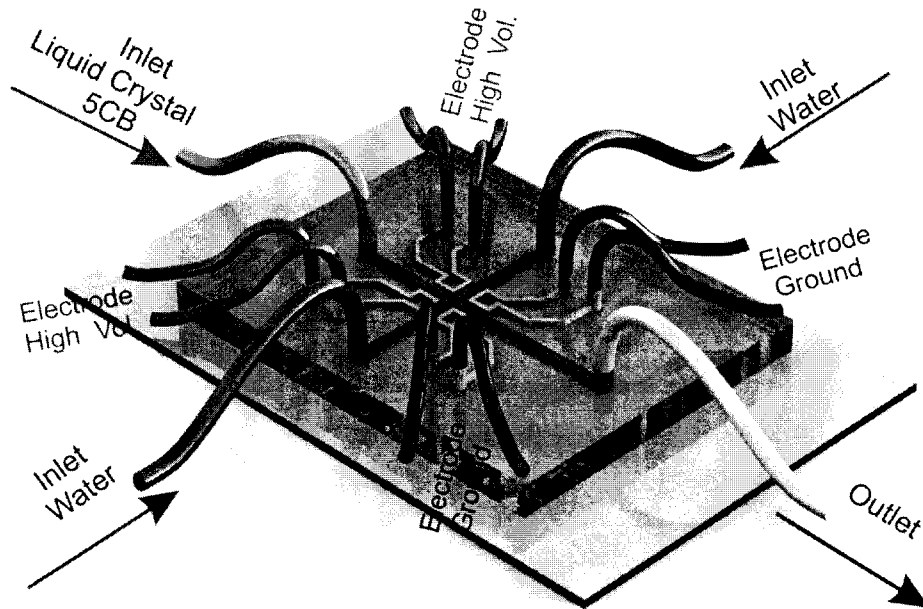


Figure 8.2 Schematic diagram of the flow focusing microchannel

Figure 8.2 shows the schematic diagram for the microchannel. The microchannel consists of two major parts: the flow focusing channel and the electrodes. The flow focusing geometry consists of three inlets and one outlet. The center inlet serves the dispersed phase (LC), while the other two inlets are symmetrically located for the continuous phase flow. Fluids from the three inlets converge in the cross junction where the LC droplet is generated.

Four electrodes are fabricated, among which two are connected to a high voltage supplier and the other two are grounded, so that the desired electric field can be achieved.

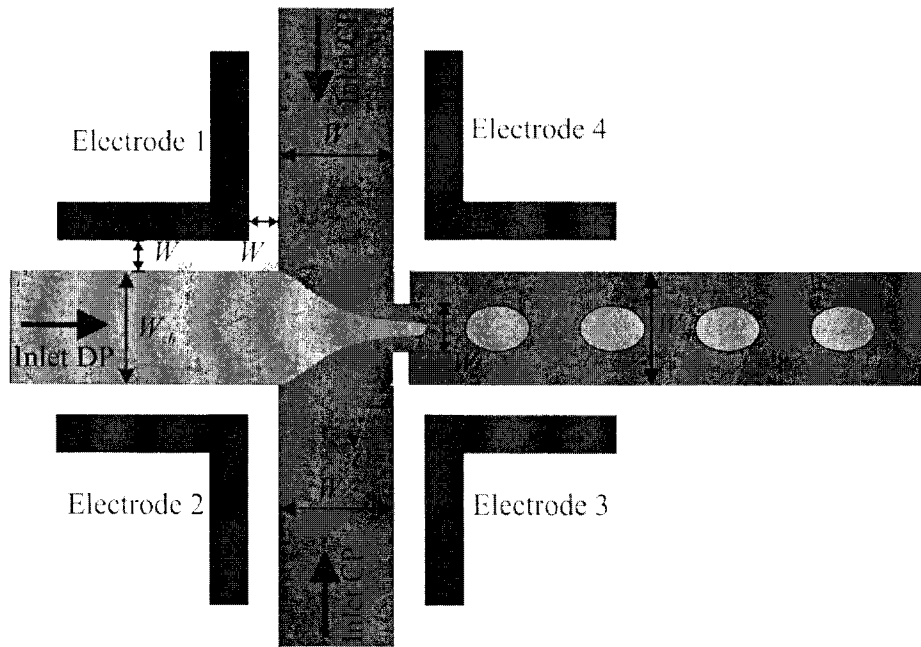


Figure 8.3 Layout and dimensions of the flow focusing microchannel with non-contact type of electrodes. DP, CP denotes the dispersed phase and continuous phase respectively.

The flow focusing microchannel is fabricated by the standard soft lithographic procedure, followed by the polydimethylsiloxane (PDMS, Dow Corning Sylgard 184) process and plasma bonding with one slice of microscope glass. After the plasma bonding procedure, the microchannel goes through the UV photoinitiated Acrylic acid procedure to modify the surface wettability from hydrophobic to hydrophilic so that the LC in water emulsion can be formed.

As shown Figure 8.3, four electrodes are designed and fabricated by melting indium alloy (Indium Corporation of America) into the electrode channel, and are then connected to the electric system via electric wires.

The major dimensions are illustrated in Figure 8.3. The microchannel width $W_{ch}=100\text{ }\mu\text{m}$, height of microchannel is fabricated to be $h=35\text{ }\mu\text{m}$ and the gap between the electrode and channel wall, W_{ga} , is designed to be $50\text{ }\mu\text{m}$. The orifice is designed

downstream of the cross junction to facility droplet formation via enhancing the viscous shear from the continuous phase. $W_{or}=50\text{ }\mu\text{m}$ is adopted in our experiments.

8.2.3 Fluidic setup

As shown in Figure 8.1, three syringes (Hamilton gas tight syringes 1725×1 & 1750×2) are utilized for storing the dispersed phase (DP) and continuous phase (CP). Then the fluids, driven by the Centoni neMESYS high precision syringe pump, flow through the polytetrafluoroethylene (PTFE) tubing and enter the microchannel. The controlling of the flow rates are achieved by the computer connected to the syringe pump.

8.2.4 Fluids

Two types of fluids, liquid crystal and water, are used in the experiment, corresponding to the dispersed phase and continuous phase respectively. The liquid crystal selected in the experiment is the single component liquid crystal of 4-Cyano-4'-pentylbiphenyl (5CB), with the chemical formula of $\text{C}_{18}\text{H}_{19}\text{N}$, purchased from Frinton Laboratories (FR-2240). 5CB is prepared without additional treatment and it stays in the nematic phase as the temperature of the microchannel is controlled at 24 °C. Its transition from nematic phase to isotropic phase occurs at temperature of 33 °C. 2% by wt. of Sodium Dodecyl Sulfate (SDS, Sigma Aldrich) is added into the DI water to assist the droplet formation and prevent the droplet coalescence.

8.2.5 Electric setup

An AC Electric field is adopted to control the liquid crystal droplet formation, as shown in Figure 8.1 and Figure 8.3. The electric field is generated by combining the Agilent 33500 B waveform generator with the Trek 5/80 high voltage amplifier.

The desired electric field is achieved by amplifying the sine wave signal generated from the waveform generator. One two-channel oscilloscope (Tektronix TDS210) is attached to the amplifier for experimental safety monitoring. The applied AC frequency varies from 500 HZ to 5 KHz with a constant voltage of 500V (p-p).

8.3 Results and discussion

8.3.1 Interfacial dynamics of LC droplet formation

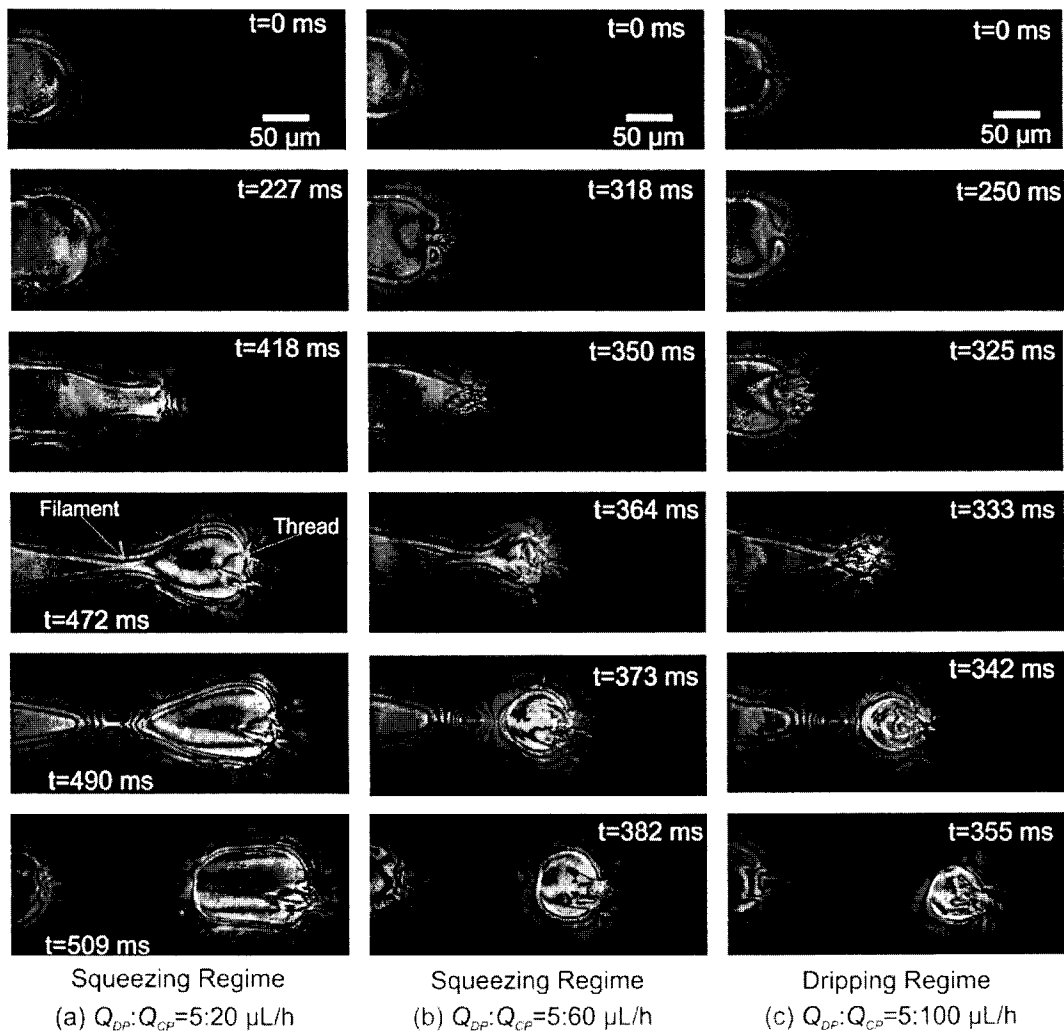


Figure 8.4 Time evolutions of the LC droplet formation

Figure 8.4 illustrates time evolutions of LC droplet formation under different flow ratios ($Q_{DP}=5 \mu\text{L/h}$). The LC droplet formation sequence, the flow front of LC dispersed phase, necking and the final break up are shown. The droplet formation in

flow focusing microchannel is controlled by the elongated flow induced shear from the continuous phase. The LC accumulates at the flow front and deformed by elongation before entering the orifice region. The droplet size shows a strong dependency on the flow rate ratio (Q_{CP} / Q_{DP}). Higher flow rate ratio of Q_{CP} / Q_{DP} produces droplets of smaller size.

The fringes within the microchannel are indications of the LC molecular orientation which is determined by the flow induced shear. Therefore, the fringe patterns generated in the droplet production elude the corresponding flow fields. Figure 8.4 (a) shows the fringe pattern produced in the LC droplet formation under low Q_{CP} . Droplet formation process starts with the advancement of the flow front the LC droplet up the orifice (from $t=0$ to $t=227$ ms). The LC filament forms and continues to fill the orifice ($t=227$ ms to $t=472$ ms). Due to the pressure and viscous stress exerted by the CP, necking occurs at $t=490$ ms and the final breakup appears at $t=509$ ms. Figure 8.4 (b) & (c) shows the LC droplet formation at higher values of Q_{CP} . The fringe patterns differ due to the higher shear caused by flow fields of the CP. The results show that the fringe patterns near the flow front indicate the occurrence of flow recirculation ((b) $t=318$ ms & (c) $t=250$ ms). The topological defects appeared as the “threads” in the LC, appear in both the necking ((b) $t=364$ ms & (c) $t=342$ ms) and breakup stages ((b) $t=382$ ms & (c) $t=355$ ms) as a result of the large hydrodynamic stress. When the hydrodynamic stress is large enough such that the molecules of the LC cannot reorient gradually, the threads appear [125, 126]. With an increasing of water flow rate, more threads appear at an early stage of droplet formation.

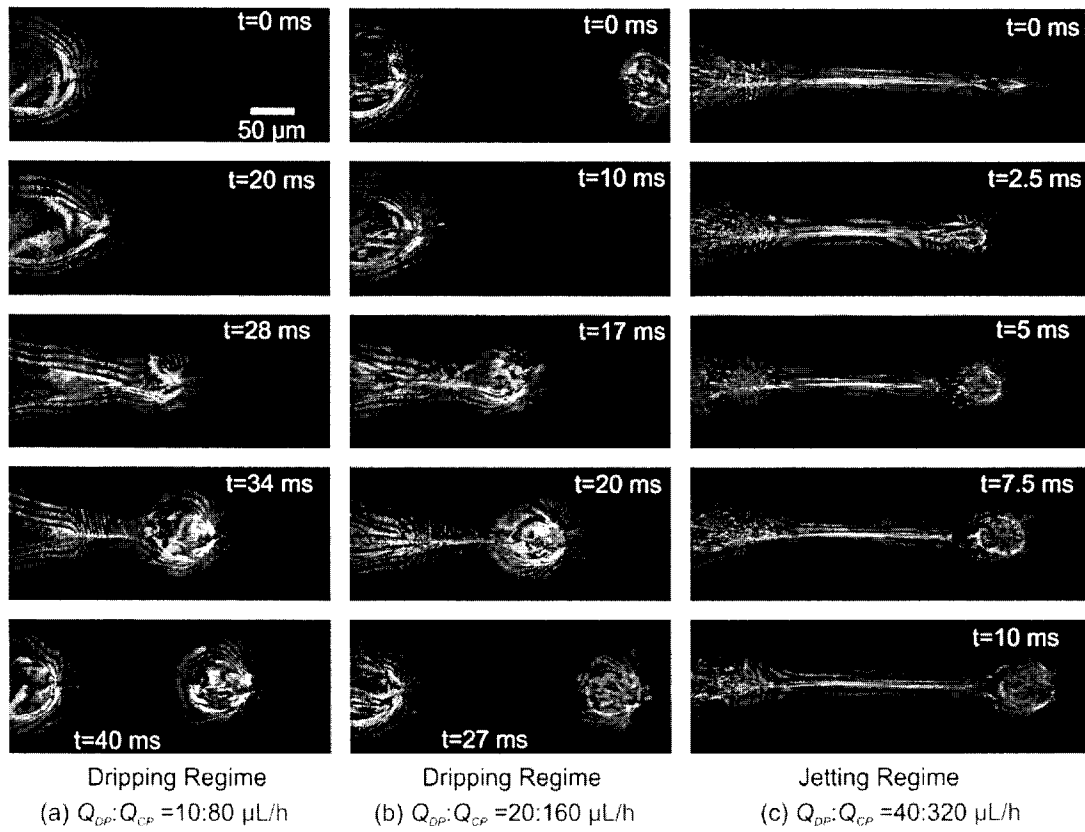


Figure 8.5 The time evolution of the LC droplet formation at higher flow rates.

Figure 8.5 shows the time evolution of the LC droplet formation at a constant $Q_{DP}/Q_{CP}=1:8$. Similar formation stages are observed in Figure 8.5 (a) & (b). As compared to those shown in Figure 8.4, the density of fringe pattern is higher due to the higher flow rates. When the flow rate is further increased (Figure 8.5 (c)), the LC droplet breakup process transits from dripping regime to jetting regime. The jetting regime occurs as a result of the large elongate shear induced by the continuous phase. The tip of the jet is pushed further downstream. The domination of the topological defects inhibits the visualization of flow field, as illustrated in Figure 8.5 (c). The occurrence of dominating “threads” defines the operational limit of this method.

8.3.2 Droplet formation and filament dynamics

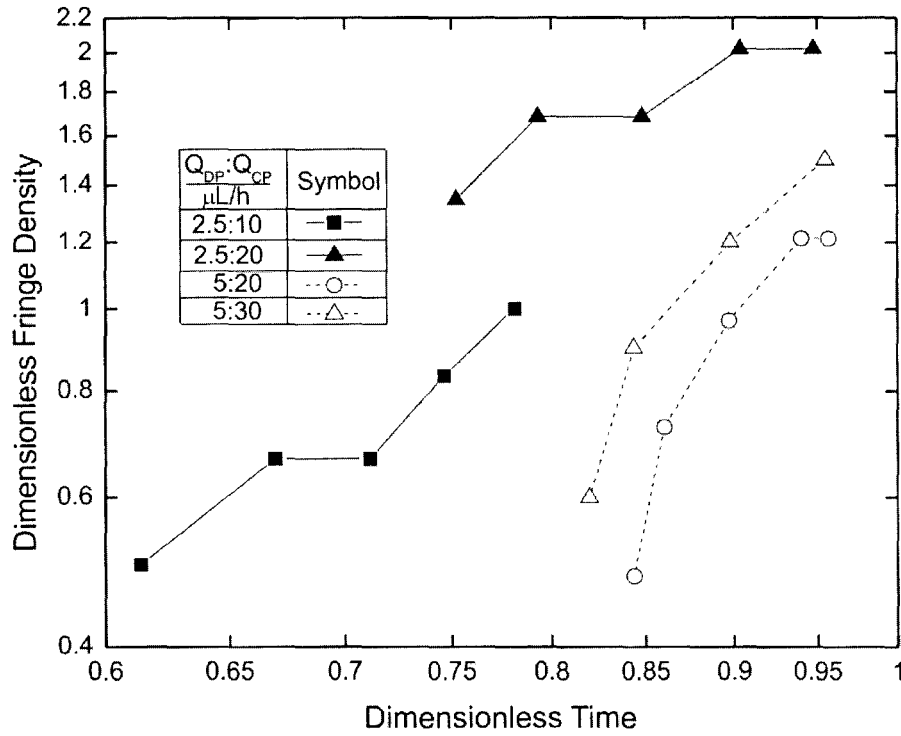


Figure 8.6 Dimensionless fringe density of the LC droplet versus dimensionless time.

Figure 8.6 shows the the dimensionless fringe density of the LC droplet increases as the dimensionless time is increased. The dimensionless fringe density of the LC droplet is defined as:

$$\chi^* = \frac{\chi}{\chi_{2.5/10}} = \frac{N/A}{\chi_{2.5/10}} \quad (8.1)$$

Where χ^* is the dimensionless fringe density, χ is the fringe density, $\chi_{2.5/10}$ depicts the fringe density of the LC droplet generated when $Q_{DP}:Q_{CP}=2.5:10 \mu L/h$, N is the total number of fringes in the droplet and A is the area of the droplet. The time begins when the last droplet breaks up and ends when the current droplet is formed and detached. The time is non-dimensioned by the total time required for each droplet formation.

$$Ca = \frac{\mu_c W_d / 2}{\sigma} \frac{\Delta U}{W_c} = \frac{\mu_c Q_{CP}}{2\sigma h} \left[\frac{1}{W_{or}} - \frac{1}{2W_{ch}} \right] \quad (8.2)$$

Where μ_c represents the viscosity of the continuous phase, $\sigma=1.7$ mN/m depicts the interfacial tension between water and liquid crystal, W_d , W_c are the channel width of the DP and CP respectively, ΔU stands for the velocity variation in the flow focusing region where the droplet formation happens, Q_{CP} is the flow rate of the CP, W_{ch} , W_{or} & h denotes the channel width, orifice width and channel height respectively as shown in Figure 8.3. The definition considers both the geometry and flow condition of the CP. Figure 8.7 shows that the fringe density increases with increasing value of Ca . The increment of Ca is caused by the higher Q_{CP} leading to a higher induced shear, which is represented by a higher fringe density.

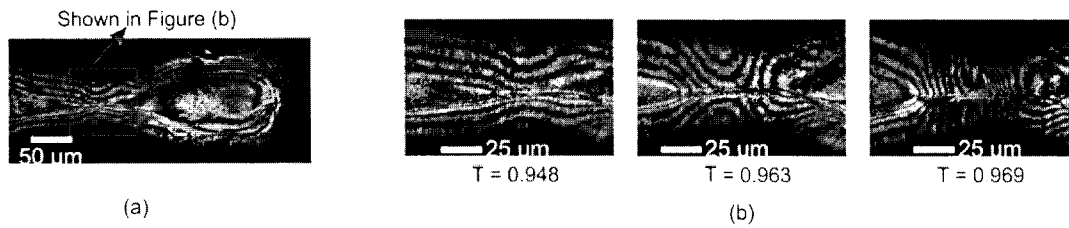


Figure 8.8 Filament evolution for $Q_{DP} : Q_{CP} = 2.5 : 10 \mu\text{L/h}$.

In Figure 8.8 (b), we show a sequence of images of the filament deformation via the LC reorientation induced fringe patterns. The fringe pattern of the filament varies with the thinning process. The fringe number increases dramatically during the thinning process and reaches a maximum value before it breaks up.

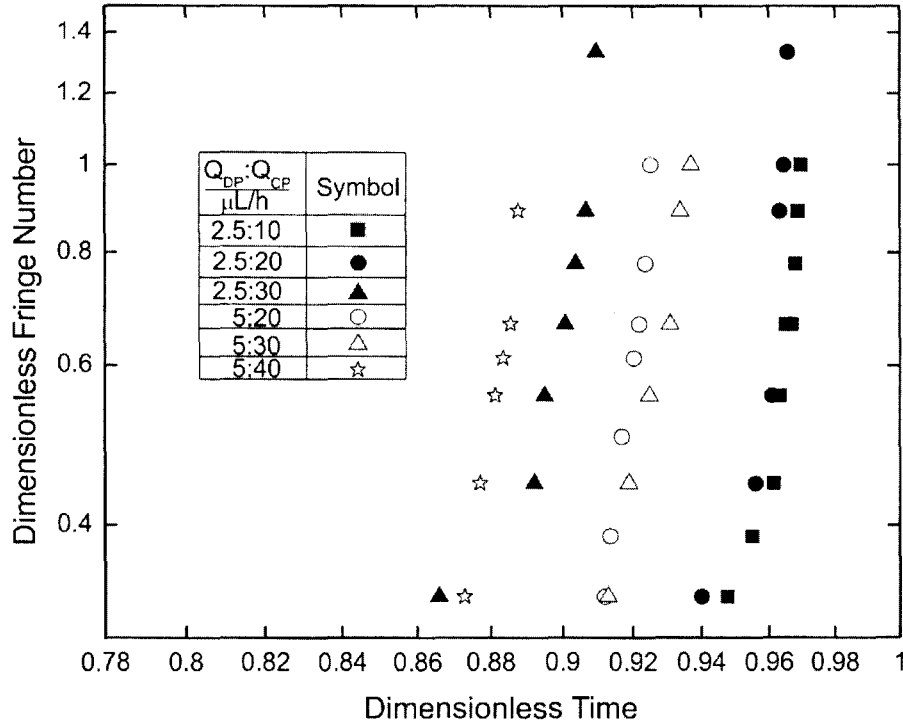


Figure 8.9 Dimensionless fringe number of the filament versus the dimensionless time

Figure 8.9 shows that the fringe number inside the filament increases with the dimensionless time. The fringe number is non-dimensioned by the maximum fringe number when $Q_{DP}:Q_{CP}=2.5:10 \mu\text{L/h}$. A rising trend is observed indicating an increasing shear during the thinning of a filament and breaking process. The filament experiences a relatively low shear at the initial stage and goes through a strong shear leading to a rapid thinning, hence the fringe number of the filament increases. The results suggest an exponential increasing of the fringe number as the function of dimensionless time in the final thinning stage.

8.3.3 LC droplet formation tuned by AC electric field

The LC droplet is reported to be functional in fields of bio-sensing and flow field visualization [126, 130]. The size control of the LC droplet is fundamental and critical. In this section we propose the controlling method of the LC droplet formation, both without and with AC electric fields in flow focusing microchannels.

LC droplet formation without electric field.

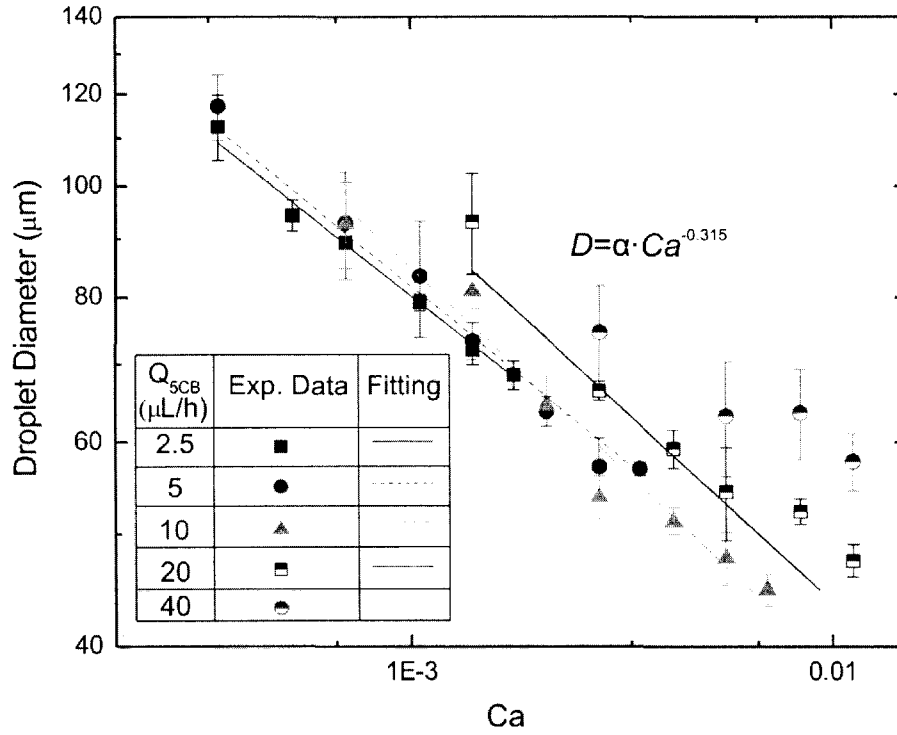


Figure 8.10 The LC droplet diameter as the function of Ca .

Figure 8.10 shows the LC droplet formation in the flow focusing microchannel via elongate flow of the continuous phase. The dependency of the LC droplet diameter on the Ca is illustrated. The decreasing tendency suggests that a stronger viscous shear generates a smaller droplet. On a log-log scale, the results show a good linear relation between the droplet diameter and Ca . The relationship between the size of the droplet and Ca is fitted by the least square method as:

$$D = \alpha Ca^{\beta} \quad (8.3)$$

The average value of the fitted exponent β corresponding to the experimental data in Figure 8.10 is -0.315, which is consistent with that reported by Anna *et al.* [108]. When $Q_{DP} = 40 \mu\text{L/h}$ and $Ca \geq 0.0084$, the droplet formation transits from the dripping to jetting regime. The exponent changes with the transition of formation regime.

LC droplet formation tuned by AC electric field.

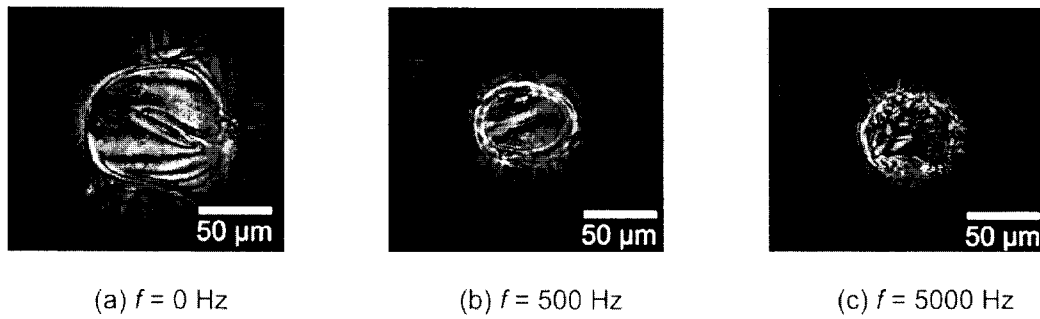


Figure 8.11 Fringe patterns of the LC droplet with diverse electric fields. Applied voltage=500 V (p-p).

When the LC droplet is generated under the influence of an electric field, electric field induced instability will change the diameter of the droplet [95, 112, 113, 228-230]. Figure 8.11 (a) shows the fringe pattern of LC droplet generated in the absence of electric field. Figure 8.11 (b) and (c) show the fringe pattern of the LC droplet generated in the presence of AC electric field with the applied frequencies of 500 Hz and 5000 Hz respectively. The droplet diameter is shrunk by the AC electric field. However, the fringe patterns are strongly interfered with the presence of AC electric field. The irregular fringe patterns cover the whole droplet at the frequency of 5000 Hz. The irregular patterns will disappear once the electric field is withdrawn.

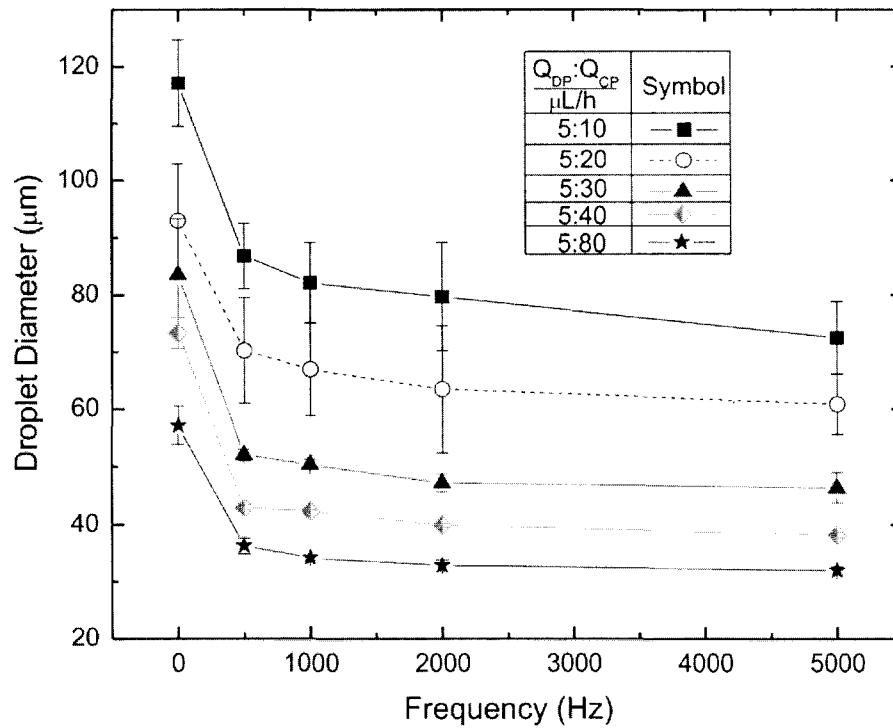


Figure 8.12 The dependency of the LC droplet diameter on the frequency of the AC electric field. The applied voltage=500 V (p-p).

As aforementioned, the droplet size drops with the presence of AC electric field. Experimental data (Figure 8.12) shows a rapid decrease in droplet size at $f=500$ Hz. The droplet size shrinks slightly and gradually when the frequency increases. This provides a method for the LC droplet size adjustment. Results in Figure 8.12 shows that the adjustment of the LC droplet diameter at the resolution of μm level is achieved via tuning the frequency of AC electric field.

8.4 Summary

The dynamics of the LC droplet formation was investigated via liquid crystal polarization, which was observed under the polarizer and analyzer set at cross position. The fringe pattern due to the LC molecular reorientation is caused by the flow field induced shear. Hence, the fringe patterns are directly related to the flow field, which achieves the flow visualization. The fringe patterns that occurred in the

droplet formation elude the shear level of the droplet. The majorly interfacial distributed fringes suggest an interfacial determined flow field in the process of droplet formation. Fringes in the droplet grow until the droplet breaks up indicating a higher level of shear during the process of necking and breaking up. The filament dynamics is revealed via LC polarization as they are difficult to be explored via means of traditional PIV system. Fringe number of the filament is found to increase exponentially before breaking up, implying a rising level of shear within the filament evolving with its thinning process.

The hydrodynamic controlled droplet diameter was achieved via altering the flow rates which influence the flow induced shear. A droplet size drop was observed via increasing the Ca . An exponential size drop with the Ca was observed. In addition to vary the flow rates, the AC electric field was applied via the electrodes fabricated in the microchannel. A rapid size reduction was gained with the presence of AC electric field. An increased frequency of AC electric field results in a slight shrinkage of droplet size. The AC electric field is capable of fine tuning the LC droplet size at μm level.

Chapter 9 Conclusions and Future work

9.1 Conclusions

The emergence of microfluidics has gained intense research focus owing to its potentials in scientific research and industrial applications. Investigations of the flow behavior of non-Newtonian fluids in microfluidic environments attract limited attention due challenges that occurred when dealing with fluids of complex rheology. Our investigations show:

- The current monitoring method is adopted as the major method in the experiment to measure the velocity of the non-Newtonian EO flow in a rectangular microchannel. The fluorescent microscopy imaging method was utilized to visualize the flow profile. The results show that the plug flow exists for a PEO solution at moderate concentration. The zeta potential was calculated through coupling a generalized Smoluchowski approach and the power-law constitutive model. The zeta potential values showed a slight variation with different PEO concentrations and the applied electric fields. A constant zeta potential is suggested, which was proven to be valid through the comparison between theoretical and experimental results. It can also be concluded that in a shear thinning fluid, the EO driven flow can be enhanced as the flow shear reduces the apparent viscosity.
- The two immiscible layers electro-osmotic driven flow model with one layer of conducting non-Newtonian fluid was proposed. The non-conducting fluid is driven by the interface shear. Both the fluid consistency coefficient m and flow behavior index n take heavily influence on the shape of the velocity profile and the volume flow rate. The results show that the shear thinning

effect improves the volume flow rate, making it ideal for both direct electro-osmotic driving and hybrid driving.

- Flow-focusing microchannels were designed and fabricated for the investigation of droplet formations of Newtonian fluid under the influence of an AC electric field. The dependency of droplet breakup regimes, and droplet sizes on the external electric fields were studied. Results show that both the electric voltage and frequency can precisely control the size of the produced droplet in flow focusing microchannels.
- Non-Newtonian droplet formation in flow focusing microchannels is systematically investigated by considering the combination of applied AC electric fields (voltage & frequency), flow conditions (Ca & Q_{DP}) and geometries (orifice size). The non-Newtonian droplet size control can be achieved by the implementation of an AC electric field. Flow conditions and geometries, which majorly determine the hydrodynamically induced shear, plays an important role in tuning the droplet and formation regime shifting. The combination of all the parameters provides the flow focusing microchannel with diverse formation possibilities. The high speed μ PIV measurement was conducted to quantitatively address the non-Newtonian droplet formation process. Results show that flow recirculation is more obvious in dripping regime than that in squeezing due to the elongated shear. The electric field generated Maxwell stress deforms the interface into a “flat” shape and strengths the flow recirculation.
- The flow fields were investigated by analyzing the liquid crystal polarization induced fringe patterns in nozzle/diffuser microchannels. Asymmetrical flows between the nozzle and diffuser directions were proven via analyzing the

associated fringe patterns. Fringe density was proposed to relate the fringe patterns to the flow induced shear. Central positions of the flow recirculation obtained from the fringe patterns characterize the flow field. The concept of particle free imaging of flow field achieved by liquid crystal polarization provides a distinctive method for flow field visualization and its related analysis.

- The dynamics of 5CB liquid crystal droplet formation were investigated via liquid crystal polarization. The majorly interfacial distributed fringes suggest an interfacial determined flow field in the process of droplet formation. The fringe number of the filament was found to increase exponentially before it broke up, implying that a rising level of shear within the filament evolved during its thinning process. An exponential droplet size decrease with increasing of the Ca was observed. A rapid size reduction is achieved with the presence of AC electric field. An increase in frequency of AC electric field results in a slight shrinkage of the droplet size. The AC electric field has been capable of fine tuning the 5CB droplet size at μm level. The novel flow visualization method via the polarization of liquid crystals proves to be feasible in visualizing flow fields of interfaces and thin filament shows great potential in flow field visualization.

9.2 Future work

Having performed the aforementioned investigations, some recommendations are listed to better understand the non-Newtonian fluids in microchannels in the future.

- The application of the EO driven flow of non-Newtonian fluids can be expanded. The transportation of bio-samples is the current focus and dynamical details of the EO driven flow of real bio-sample are required.
- The influence of surfactant on the dynamics of non-Newtonian droplet formation is to be explored. The surfactant, which influences the interfacial tension significantly, plays an important role in the dynamics. The role of surfactant in the non-Newtonian droplet formation in the presence of electric field is yet to be studied.
- The filament dynamics in the process of non-Newtonian droplet formation should be further discussed to reveal the mechanism so as to deepen the understanding of the “beads on string” phenomenon.
- The applications of the liquid crystal polarization in microfluidic environments can be considered in fields of chemical sensing. The orientation of liquid crystals is sensitive to the presence of various chemicals.

Appendix A

A.1 Plots of droplet diameter as a function of applied voltage at various frequencies

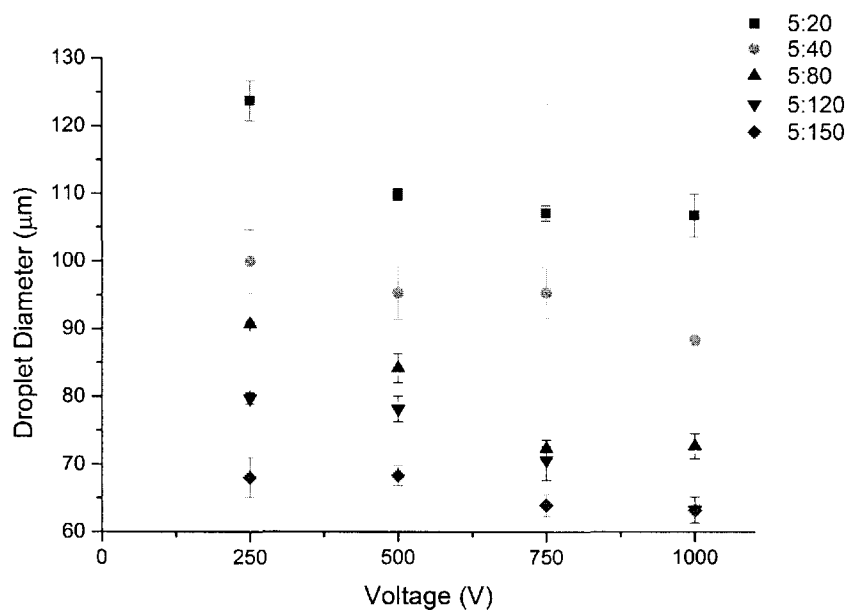


Figure A-1: Droplet diameter as a function of applied voltage at 500Hz where Q_{PEO} is $5\mu\text{l/hr}$

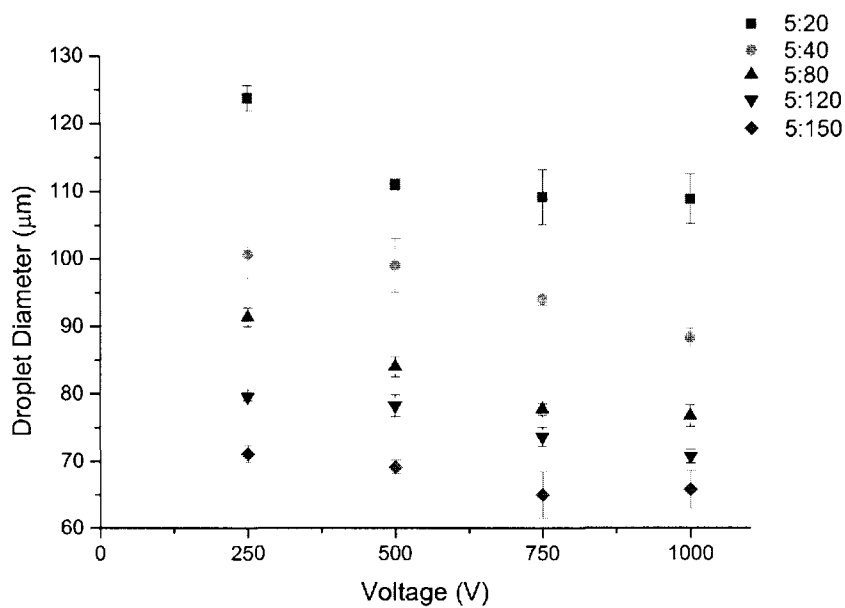


Figure A-2: Droplet diameter as a function of applied voltage at 1000Hz where Q_{PEO} is $5\mu\text{l/hr}$

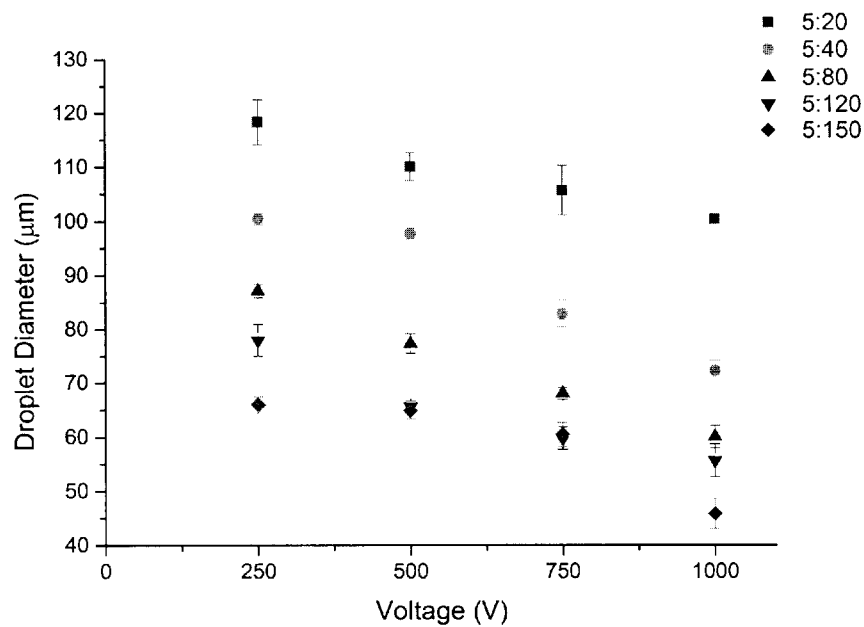


Figure A-3: Droplet diameter as a function of applied voltage at 5000Hz where Q_{PEO} is 5 $\mu\text{l/hr}$

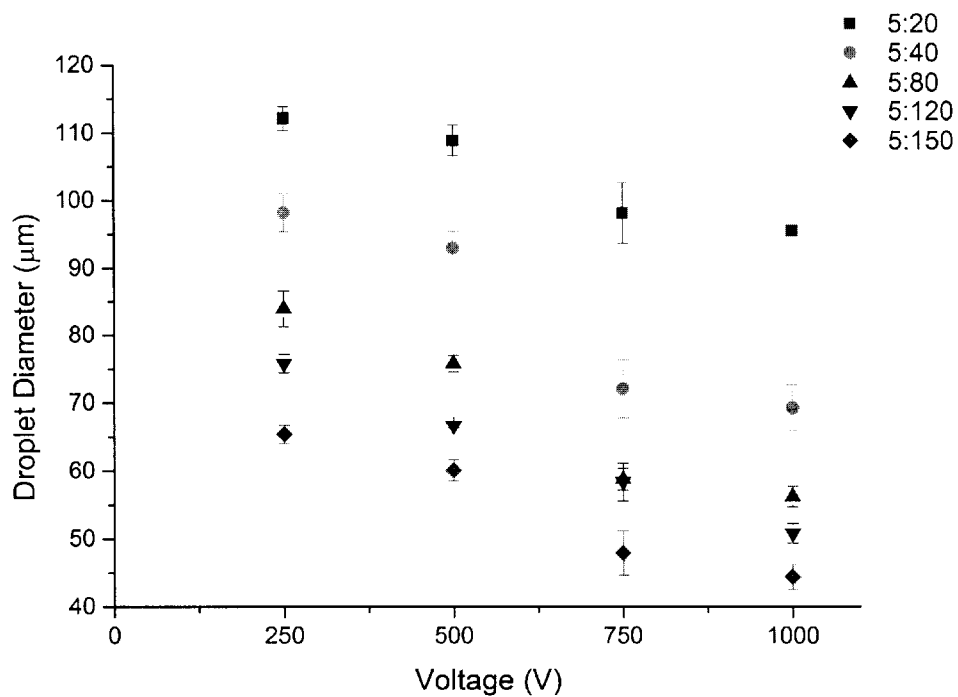


Figure A-4: Droplet diameter as a function of applied voltage at 7000Hz where Q_{PEO} is 5 $\mu\text{l/hr}$

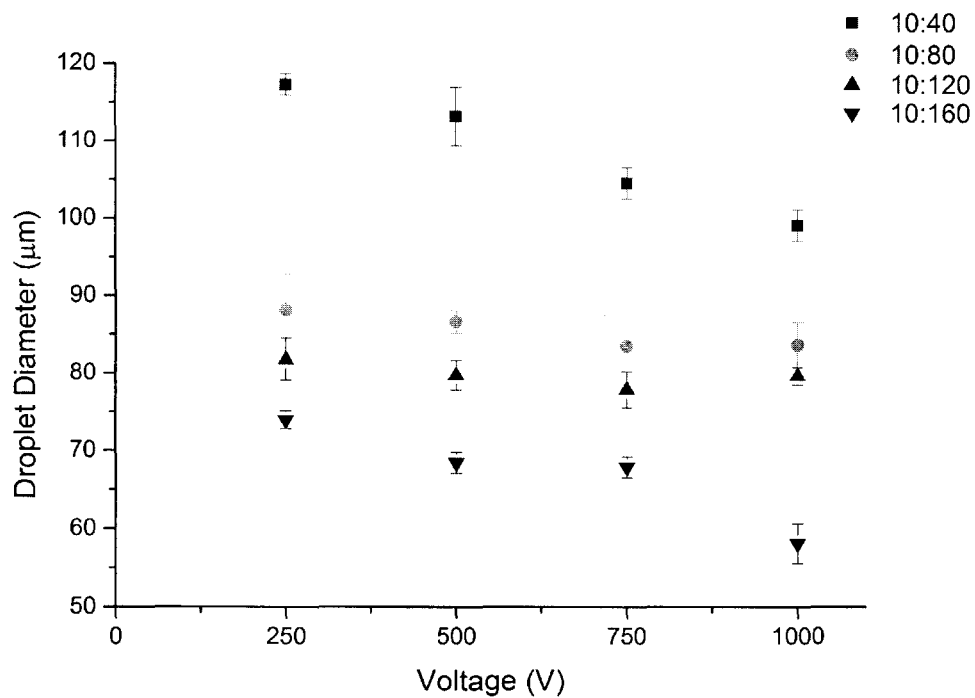


Figure A-5: Droplet diameter as a function of applied voltage at 500Hz where Q_{PEO} is 10μl/hr

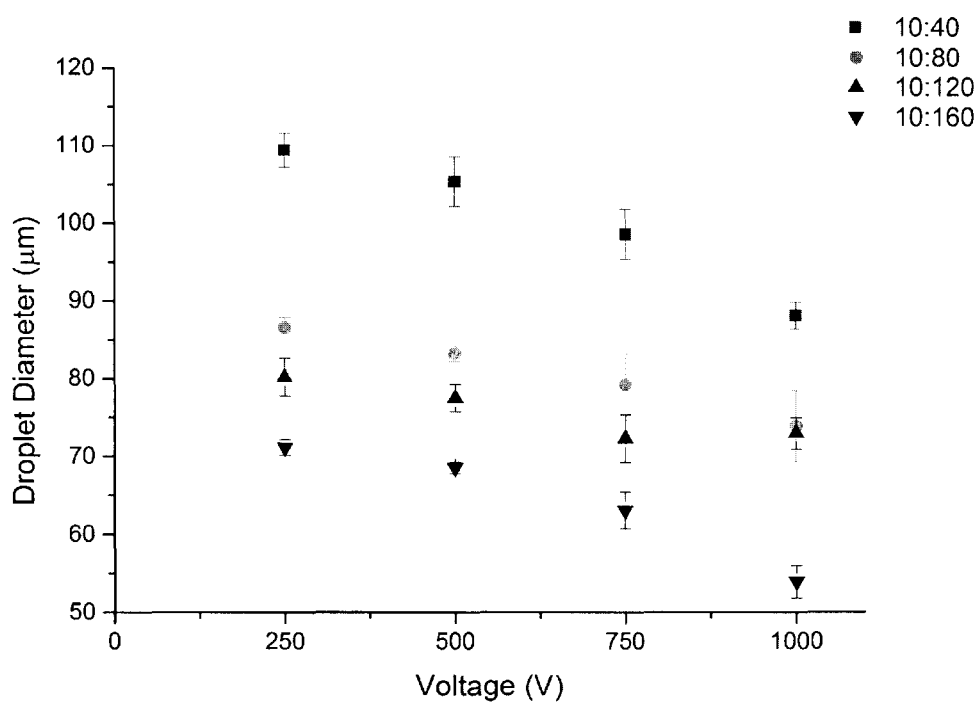


Figure A-6: Droplet diameter as a function of applied voltage at 2000Hz where Q_{PEO} is 10μl/hr

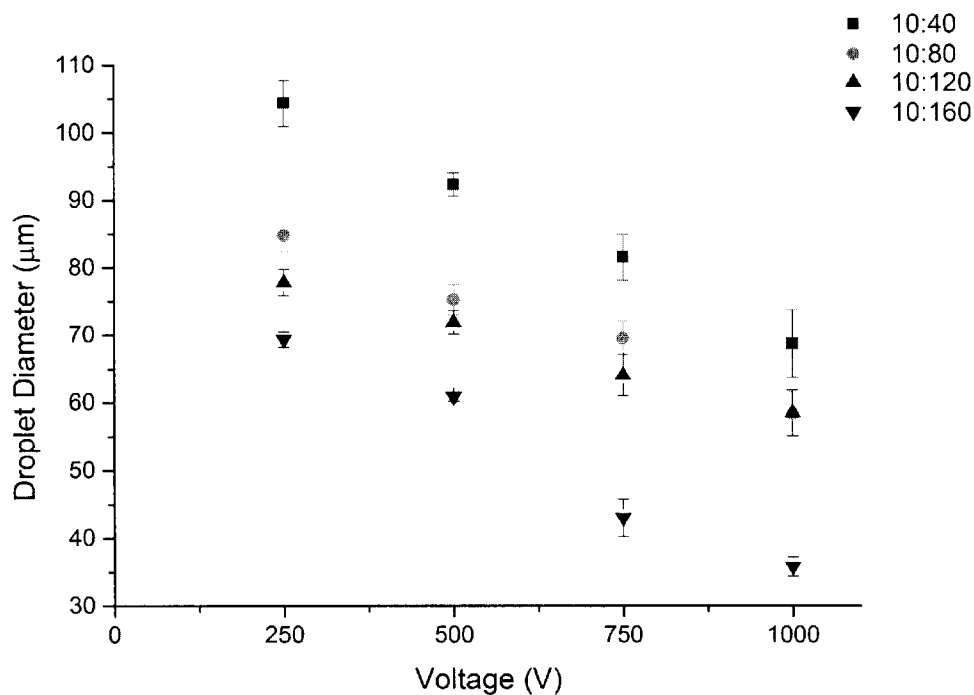


Figure A-7: Droplet diameter as a function of applied voltage at 7000Hz where Q_{PEO} is 10 μ l/hr

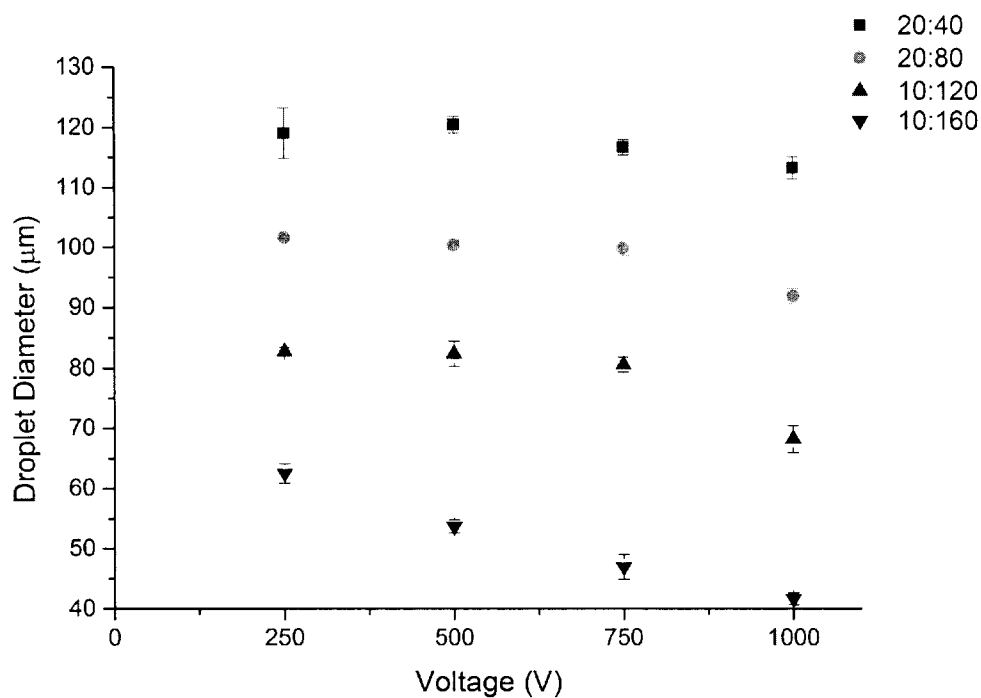


Figure A-8: Droplet diameter as a function of applied voltage at 1000Hz where Q_{PEO} is 20 μ l/hr

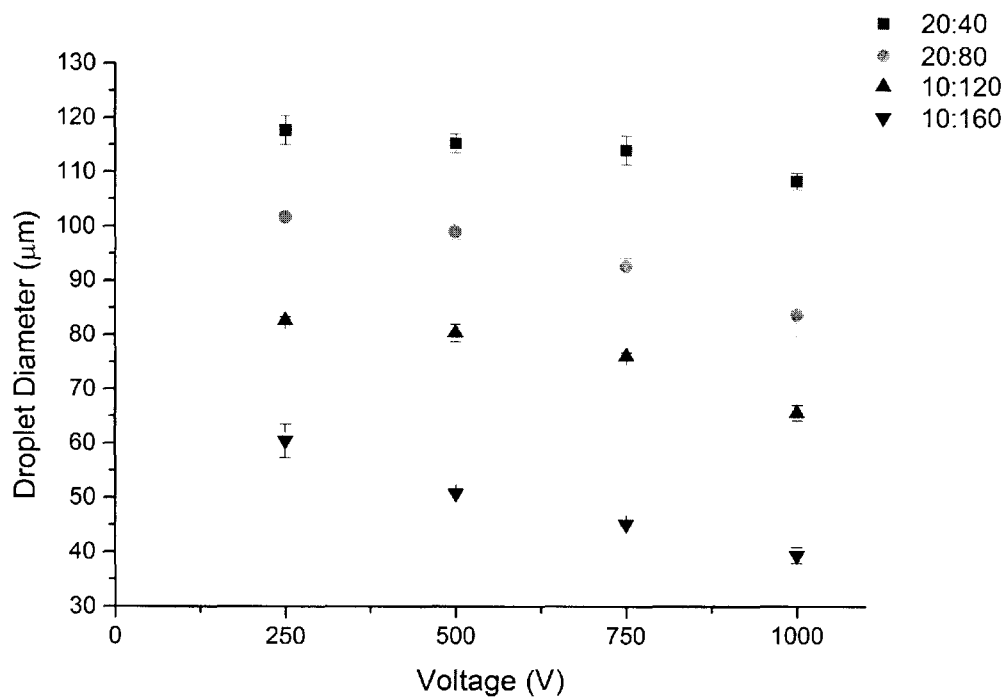


Figure A-9: Droplet diameter as a function of applied voltage at 2000Hz where Q_{PEO} is $20\mu\text{l/hr}$

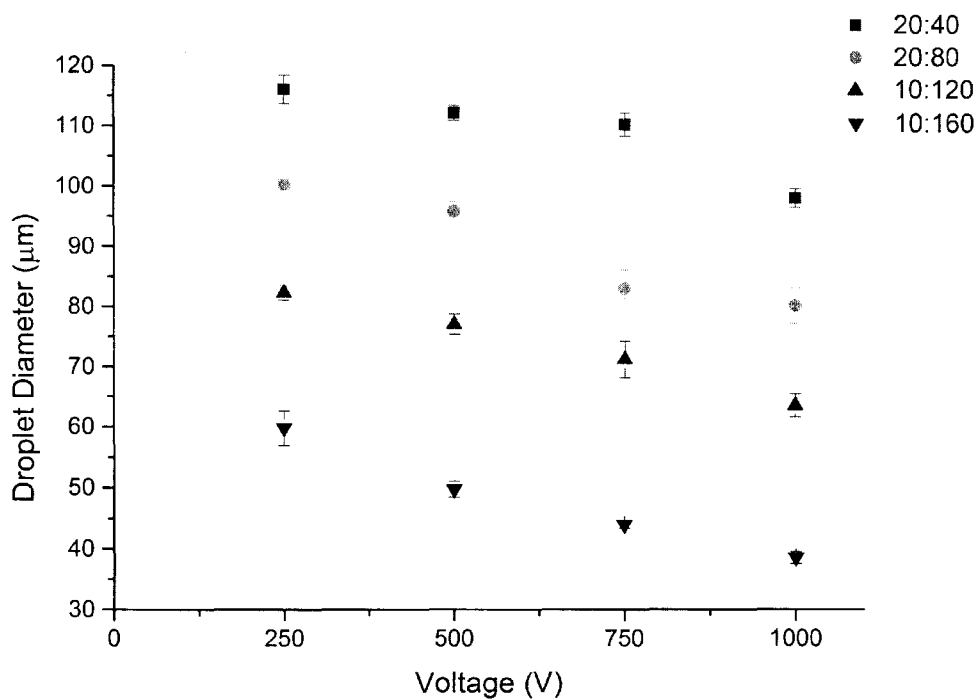


Figure A-10: Droplet diameter as a function of applied voltage at 5000Hz where Q_{PEO} is $20\mu\text{l/hr}$

A.2 Plots of droplet diameter as a function of frequency at various applied voltages

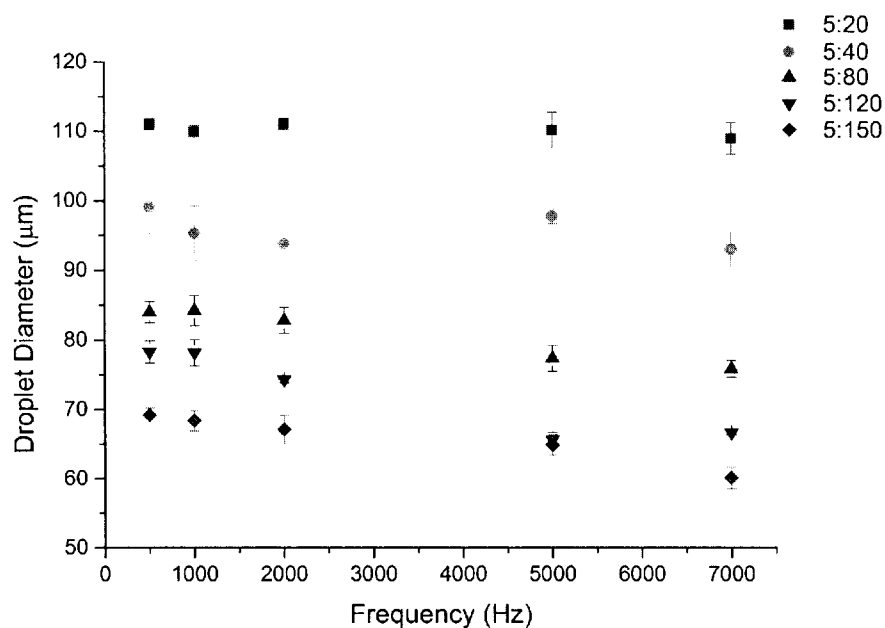


Figure A-11: Droplet diameter as a function of frequency at 500V where Q_{PEO} is 5 μ l/hr

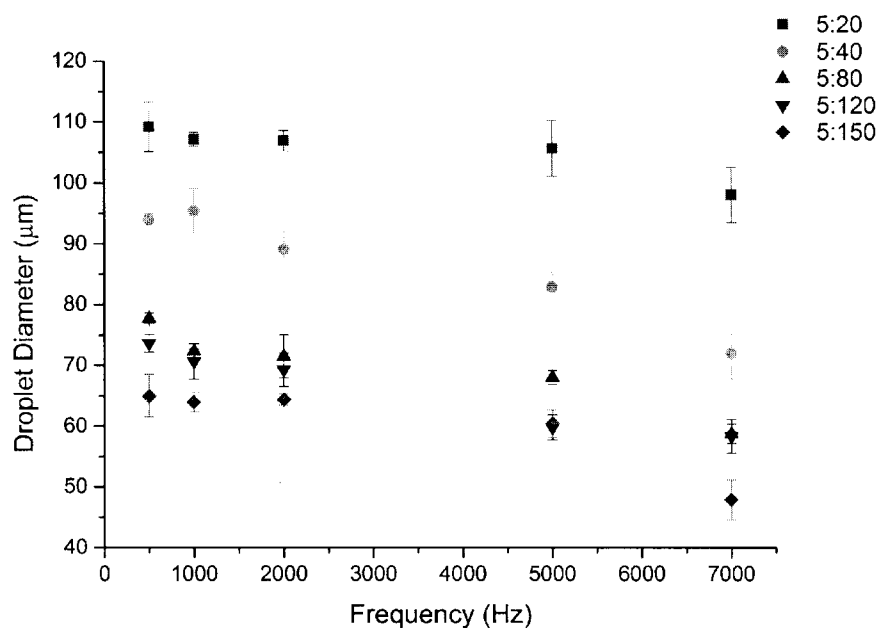


Figure A-12: Droplet diameter as a function of frequency at 750V where Q_{PEO} is 5 μ l/hr

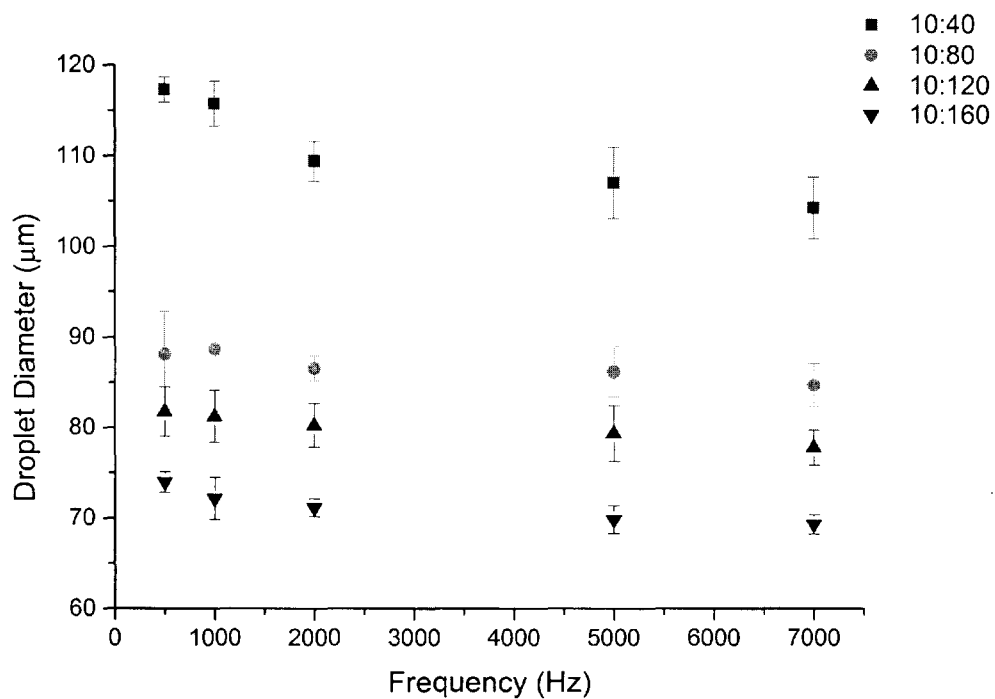


Figure A-13: Droplet diameter as a function of frequency at 250V where Q_{PEO} is $10\mu\text{l/hr}$

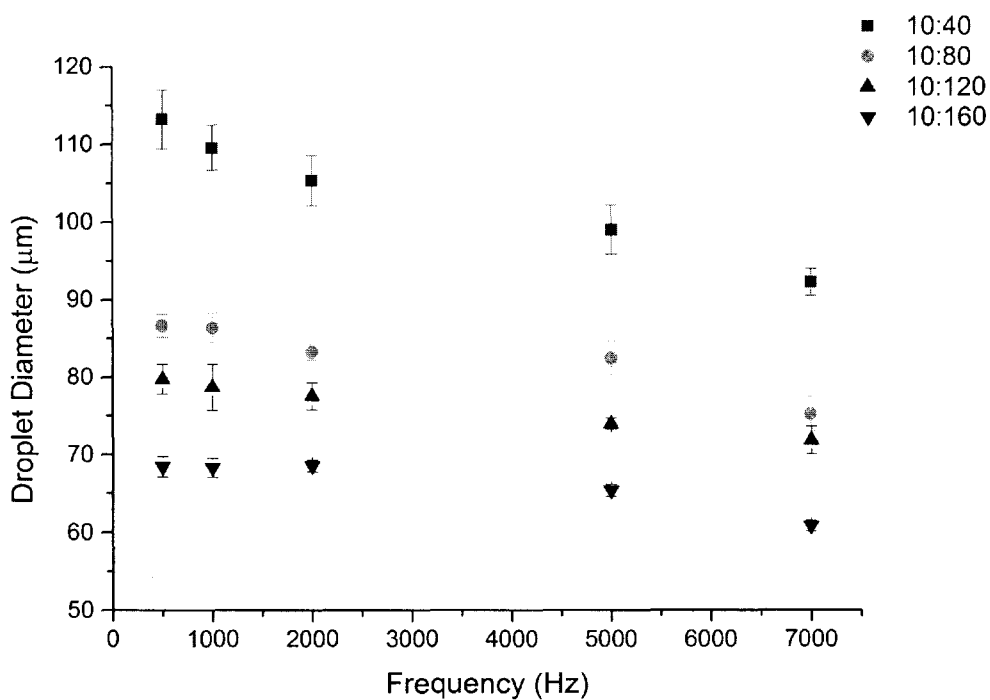


Figure A-14: Droplet diameter as a function of frequency at 500V where Q_{PEO} is $10\mu\text{l/hr}$

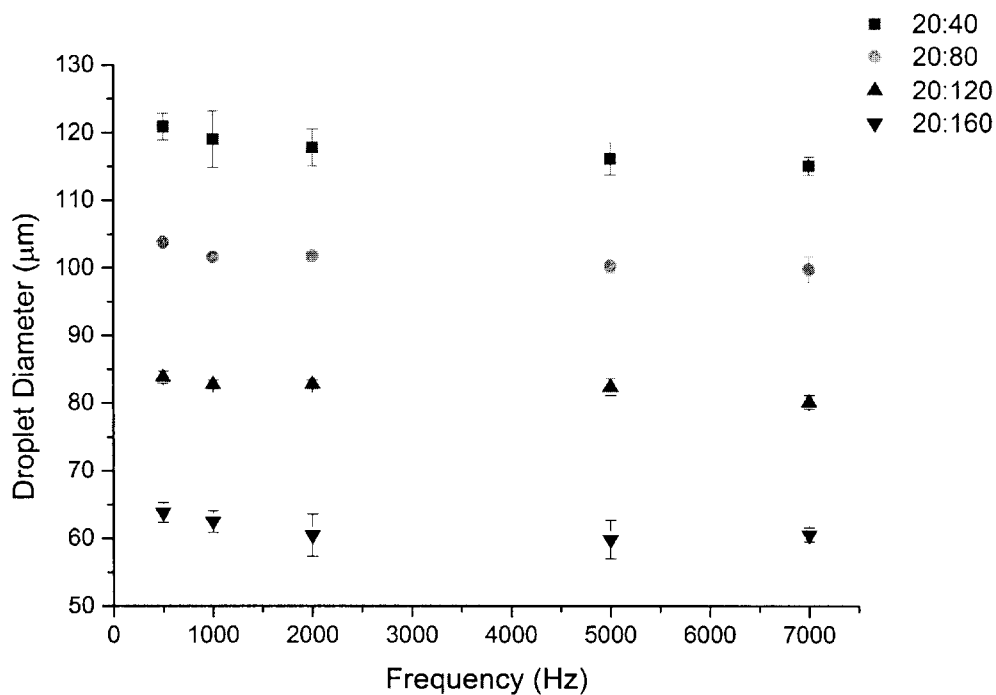


Figure A-15: Droplet diameter as a function of frequency at 250V where Q_{PEO} is 20μl/hr

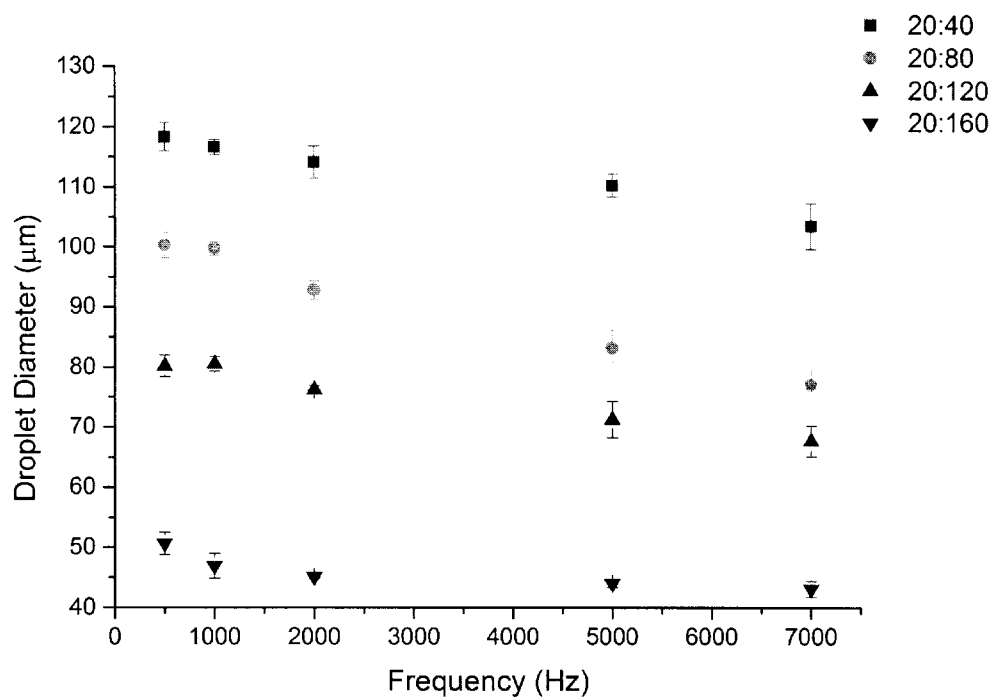


Figure A-16: Droplet diameter as a function of frequency at 750V where Q_{PEO} is 20μl/hr

A.3 Plots of droplet diameter as a function of capillary number at various applied voltages

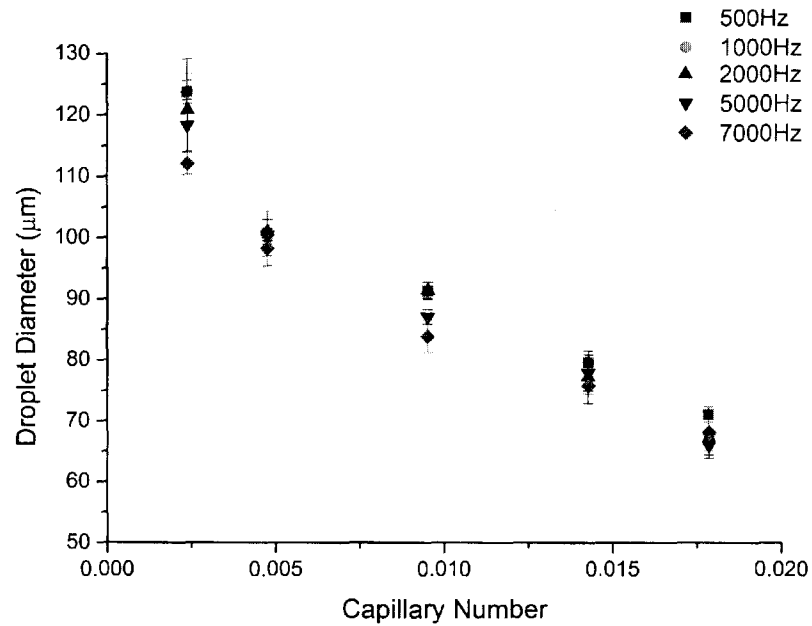


Figure A-17: Droplet diameter as a function of capillary number at 250V where Q_{PEO} is $5 \mu\text{l/hr}$

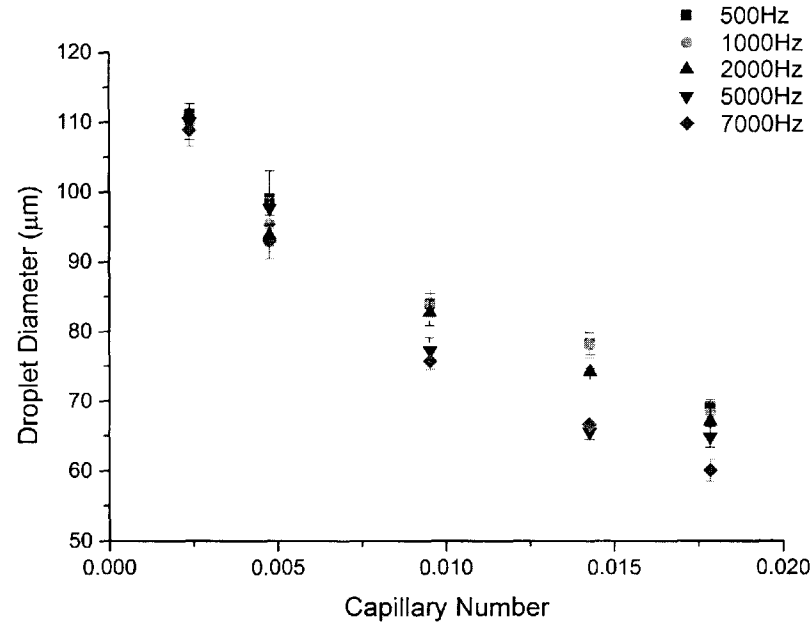


Figure A-18: Droplet diameter as a function of capillary number at 500V where Q_{PEO} is $5 \mu\text{l/hr}$

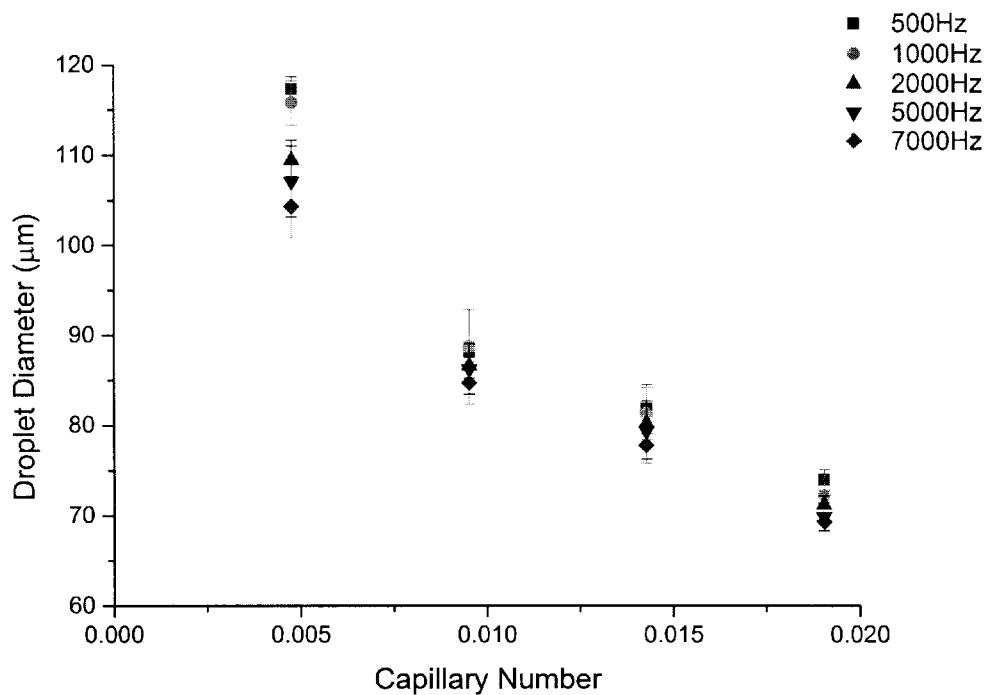


Figure A-19: Droplet diameter as a function of capillary number at 250V where Q_{PEO} is $10 \mu\text{l/hr}$

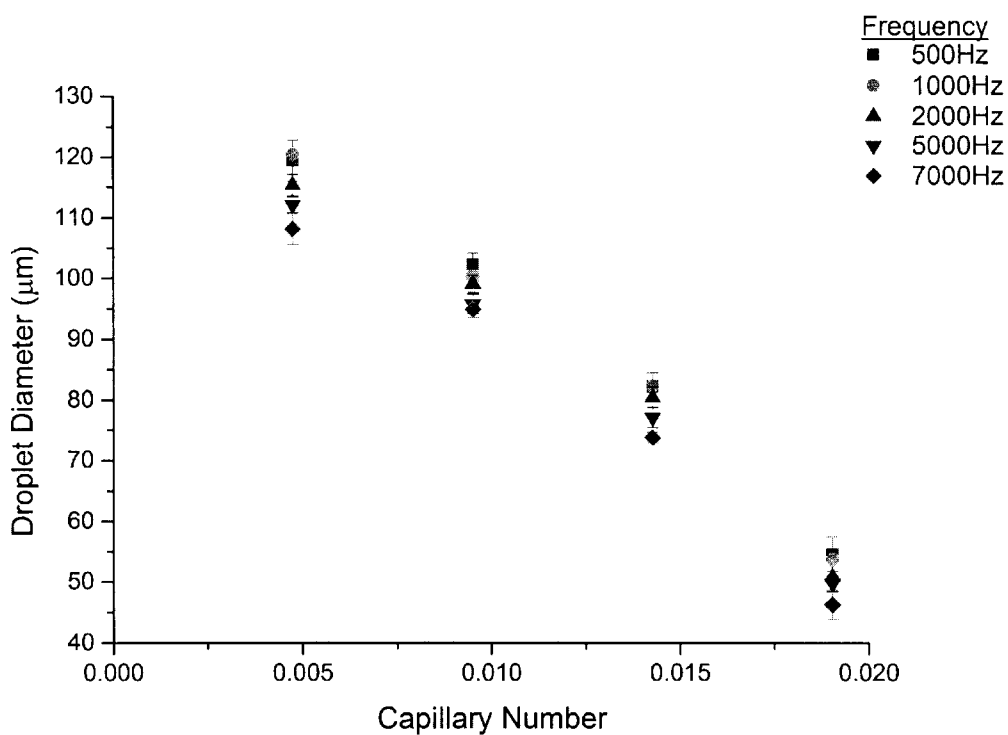


Figure A-20: Droplet diameter as a function of capillary number at 500V where Q_{PEO} is $20 \mu\text{l/hr}$

A.4 Plots of droplet diameter as a function of capillary number at various frequencies

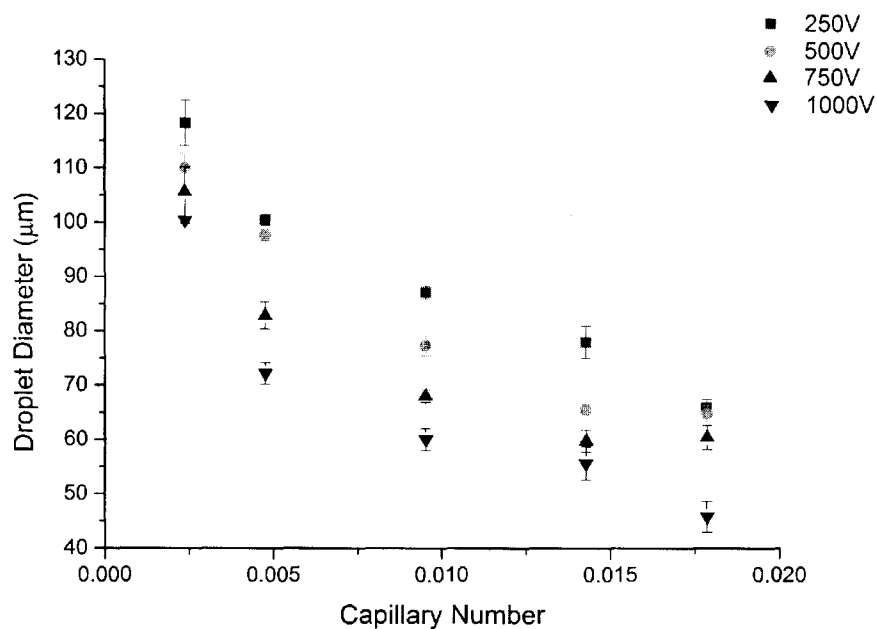


Figure A-21: Droplet diameter as a function of capillary number at 5000Hz where Q_{PEO} is $5 \mu\text{l/hr}$

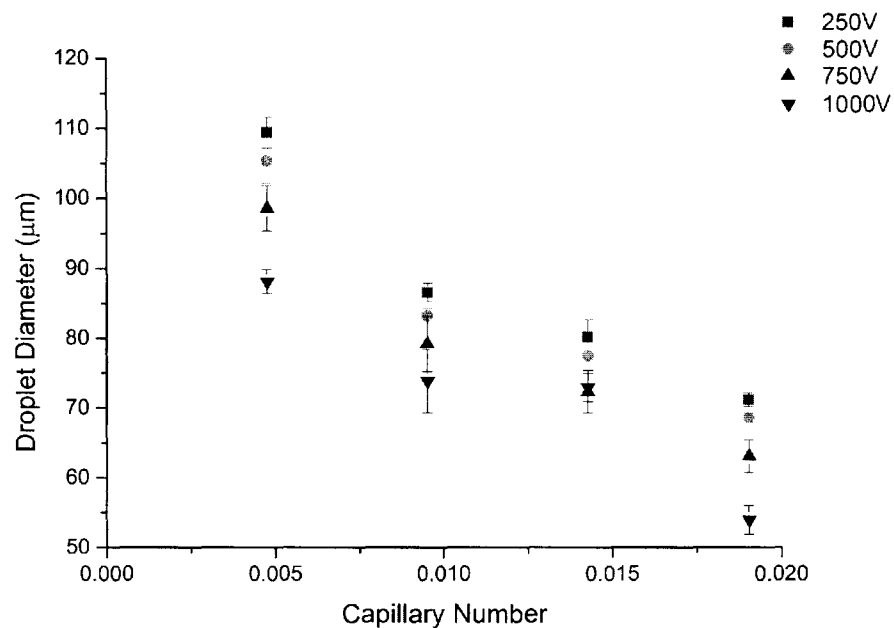


Figure A-22: Droplet diameter as a function of capillary number at 2000Hz where Q_{PEO} is $10 \mu\text{l/hr}$

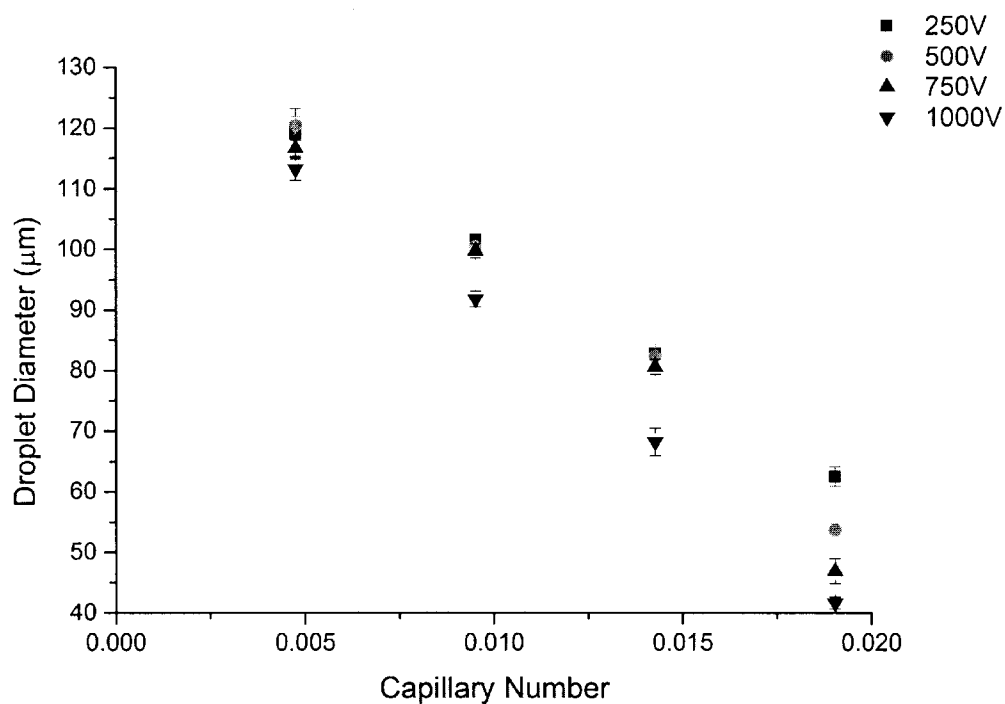


Figure A-23: Droplet diameter as a function of capillary number at 1000Hz where Q_{PEO} is 20μl/hr

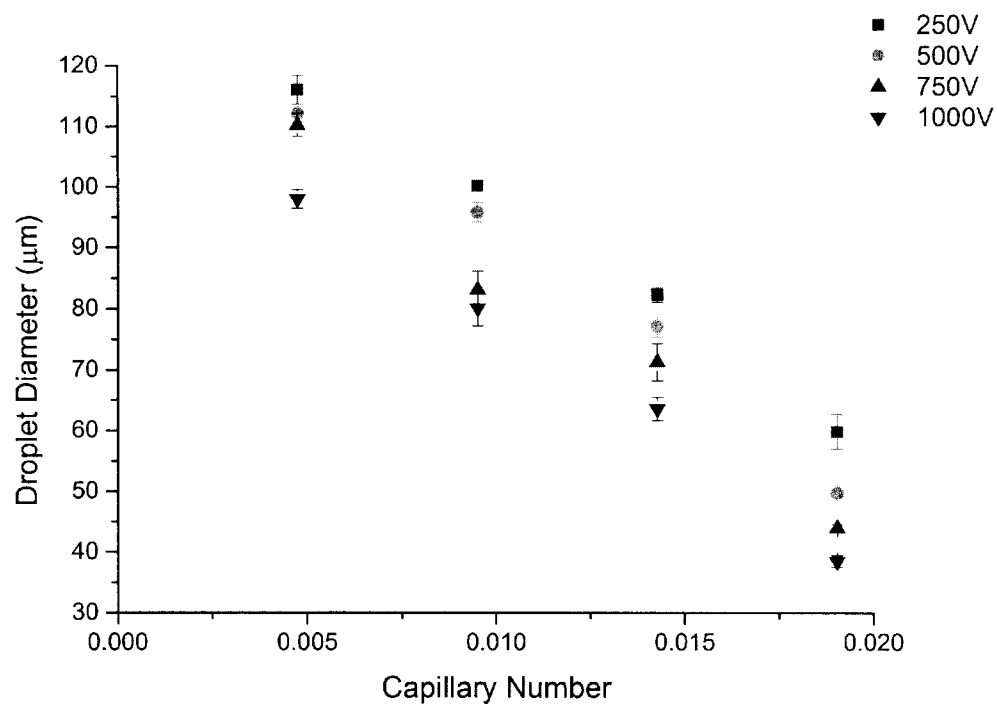


Figure A-24: Droplet diameter as a function of capillary number at 5000Hz where Q_{PEO} is 20μl/hr

A.5 Plots of droplet diameter as a function of capillary number for different orifice widths

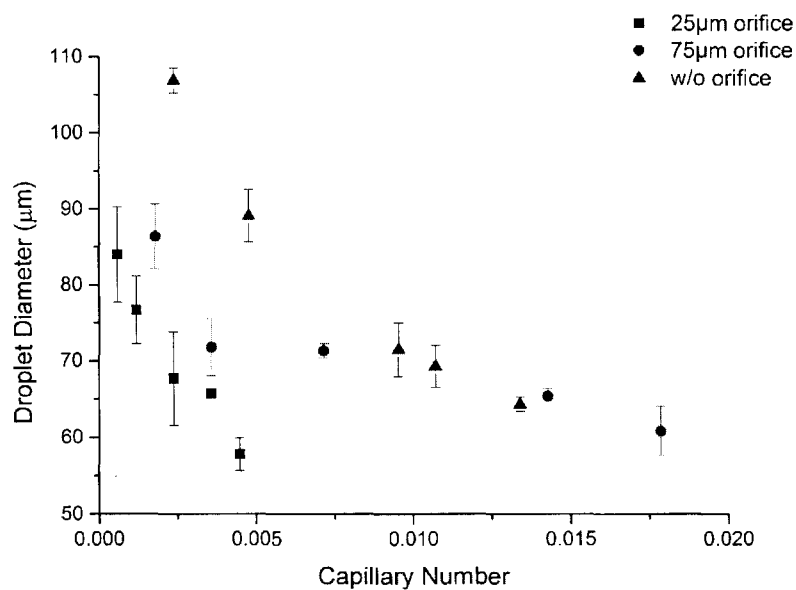


Figure A-25: Droplet diameter as a function of capillary number at 750V and 2000Hz where Q_{PEO} is 5μl/hr

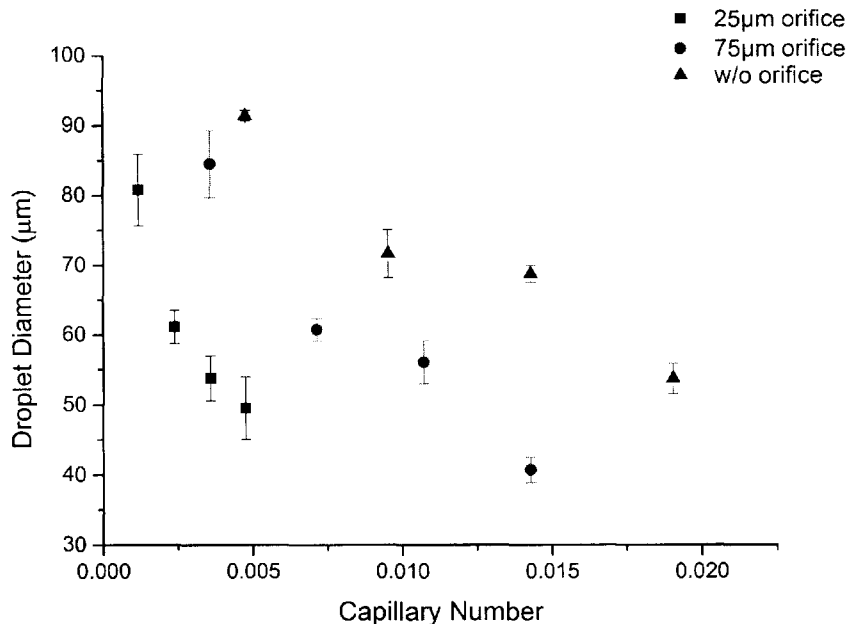
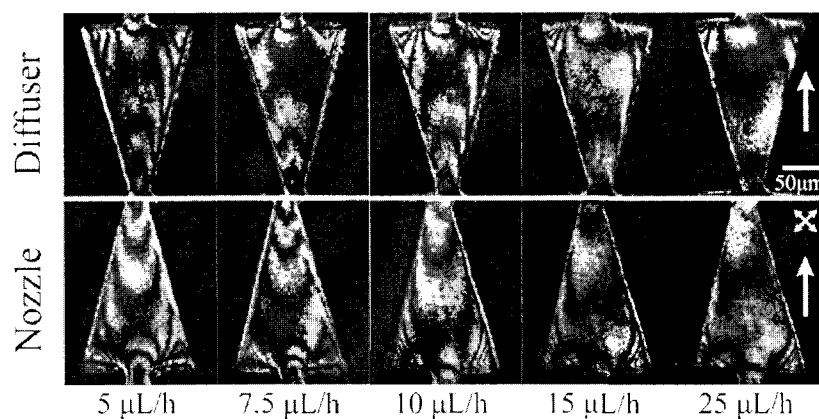
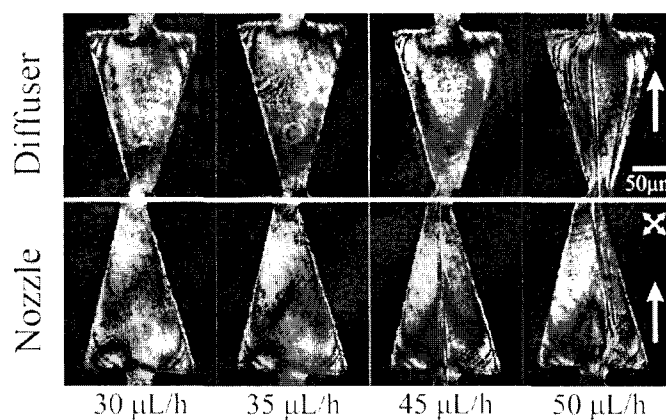


Figure A-26: Droplet diameter as a function of capillary number at 750V and 5000Hz where Q_{PEO} is 10μl/h

Appendix B



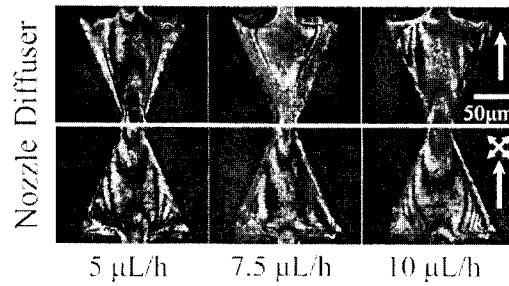
(a) Fringe patterns under relatively low flow rates



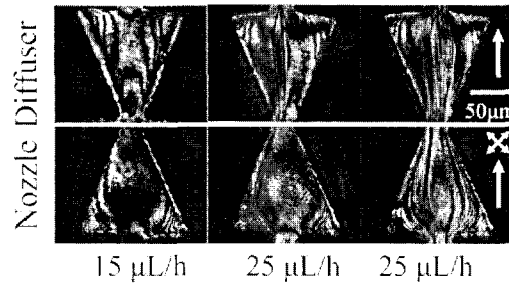
(b) Fringe patterns under relatively high flow rates

Figure B-1 Optical patterns of 30 ° opening channel for both diffuser and nozzle directions. Scale bar represents 50 μm .

The fringe patterns for 30 ° opening channel are presented in Figure B-1. Similar results are obtained that the fringe also grows with the flow rate. The recirculation pattern and asymmetric character also repeat themselves. At high flow rates, threads due to the orientation gradient are obtained. Diffuser direction induced threads are still more obvious than that of the nozzle.



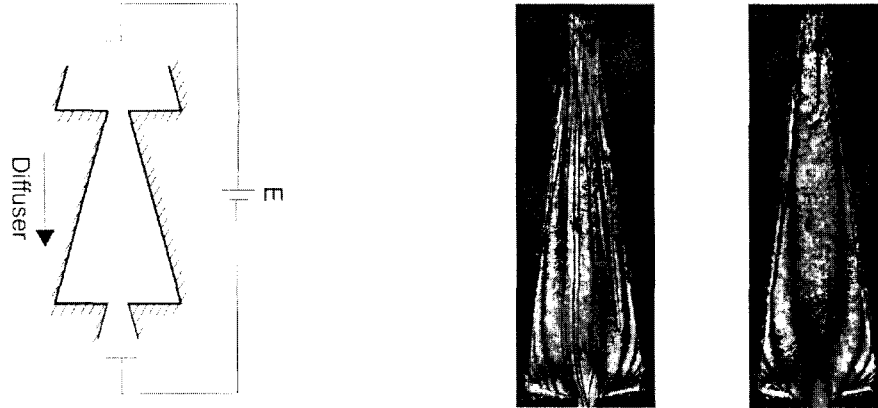
(a) Fringe patterns under relatively low flow rates



(b) Fringe patterns under relatively high flow rates

Figure B-2 Fringe patterns of 45 ° opening channel for both diffuser and nozzle directions. Scale bar represents 50 μm.

For larger angle results, as presented in Figure B-2 for 45°, the recirculation pattern becomes more interesting, which will be discussed in the next section. Optical patterns become unstable at low flow rate and the threads appear at a relatively low flow rate making the observation difficult.



(a) Schematic diagram of applying electric field (b) Without electric field (c) With electric field

Figure B-3 Optical pattern without and with the electric field coupling

Figure B-3 shows one result of applying an electric field along with the flow field. Electric field strength is 105 kV/m. The threads disappeared on the application of the electric field. The coupling of electric field and flow field are still at a very early stage and it is not the focus of this paper. We will continue the research on the coupling effect in the future.

Publications Arising from this Thesis

1. **Y. Huang**, H. Li, and T.N. Wong, *Two immiscible layers of electro-osmotic driven flow with a layer of conducting non-Newtonian fluid*. International Journal of Heat and Mass Transfer, 2014. **74**: p. 368-375.
2. **Y. Huang**, *et al.*, *Experimental and Theoretical Investigations of Non-Newtonian Electroosmotic Driven Flow in Rectangular Microchannels*, in the process of journal submission.
3. **Y. Huang**, *et al.*, *AC Electric Field Tuned Non-Newtonian Droplet Formation in Flow Focusing Microchannels*, in the process of journal submission.
4. Y. Wang, **Y. Huang**, *et al.* *An Electric Field Activated Droplet Formation in Flow-focusing Device*, in the process of journal submission.
5. **Y. Huang**, *et al.*, *Particle Free Optical Imaging of Flow Field by Liquid Crystal Polarization*, in the process of journal submission.
6. **Y. Huang**, *et al.*, *Investigations of Interfacial Dynamics of Droplet Production via Particle Free Flow Visualization Method*, in the process of journal submission.
7. **Y. Huang**, H. Li, and T.N. Wong, *Two Immiscible Layers of Electro-osmotic Driven Flow with a Layer of Conducting non-Newtonian Fluid*. 5th International conference on "Heat Transfer and Flow in Microscale", 2014.
8. **Y. Huang**, T.N. Wong and H. Li, *Two Fluids Flow of Electro-osmotic and Pressure Driven with non-Newtonian fluid*. 5th conference on Advances in Microfluidics & Nanofluidics, 2014.
9. **Y. Huang**, *et al.*, *Investigations on Non-Newtonian Electro-osmotic Driven Flow in Rectangular Microchannels*. 5th Micro/Nanoscale Heat & Mass Transfer International Conference, 2016 (Accepted).

References

1. Clemmens, J., et al., *Motor-protein "roundabouts": microtubules moving on kinesin-coated tracks through engineered networks*. Lab Chip, 2004. **4**(2): p. 83-6.
2. Kunst, B.H., A. Schots, and A.J.W.G. Visser, *Design of a confocal microfluidic particle sorter using fluorescent photon burst detection*. Review of Scientific Instruments, 2004. **75**(9): p. 2892.
3. Petersson, F., et al., *Continuous separation of lipid particles from erythrocytes by means of laminar flow and acoustic standing wave forces*. Lab Chip, 2005. **5**(1): p. 20-2.
4. Riehn, R., et al., *Restriction mapping in nanofluidic devices*. Proc Natl Acad Sci U S A, 2005. **102**(29): p. 10012-6.
5. Sia, S.K., et al., *An integrated approach to a portable and low-cost immunoassay for resource-poor settings*. Angew Chem Int Ed Engl, 2004. **43**(4): p. 498-502.
6. Skelley, A.M., et al., *Development and evaluation of a microdevice for amino acid biomarker detection and analysis on Mars*. Proc Natl Acad Sci U S A, 2005. **102**(4): p. 1041-6.
7. El Mactar, A.O., N. Aubry, and J. Batton, *Electro-hydrodynamic micro-fluidic mixer*. Lab Chip, 2003. **3**(4): p. 273-80.
8. Oddy, M.H., J.G. Santiago, and J.C. Mikkelsen, *Electrokinetic instability micromixing*. Analytical Chemistry, 2001. **73**(24): p. 5822-5832.
9. Tsouris, C., et al., *Electrohydrodynamic Mixing in Microchannels*. AIChE Journal, 2003. **49**(8): p. 2181-2186.
10. Sengupta, A., S. Herminghaus, and C. Bahr, *Opto-fluidic velocimetry using liquid crystal microfluidics*. Applied Physics Letters, 2012. **101**(16): p. 164101.
11. Khoo, I.C., et al., *Optofluidics based on liquid crystal microflows*. 2011. **8114**: p. 81140K-81140K-7.
12. Hunter, R.J., *Zeta Potential in Colloid Science: Principles and Applications*, 1981, Academic Press.
13. Probstein, R.F., *Physicochemical Hydrodynamics: An Introduction*, 1994, Wiley.
14. Chen, C.H. and J.G. Santiago, *A planar electroosmotic micropump*. Journal of Microelectromechanical Systems, 2002. **11**(6): p. 672-683.
15. Evans, D.F., *The colloidal domain : where physics, chemistry, biology, and technology meet* 1999.
16. Sinton, D., et al., *Direct and Indirect Electroosmotic Flow Velocity Measurements in Microchannels*. J Colloid Interface Sci, 2002. **254**(1): p. 184-189.
17. Mala, G.M., C. Yang, and D. Li, *Electrical double layer potential distribution in a rectangular microchannel*. Colloids and Surfaces A: Physicochemical and Engineering Aspects, 1998. **135**: p. 109-116.
18. Yang, C. and D. Li, *Analysis of electrokinetic effects on the liquid flow in rectangular microchannels*. Colloids and Surfaces A: Physicochemical and Engineering Aspects, 1998. **143**: p. 339-353.
19. Ren, L., C. Escobedo, and D. Li, *Electroosmotic Flow in a Microcapillary with One Solution Displacing Another Solution*. J Colloid Interface Sci, 2001. **242**(1): p. 264-271.
20. Burgreen, D. and F.R. Nakache, *Electrokinetic flow in ultrafine capillary slits*. Journal of Physical Chemistry, 1964. **68**(5): p. 1084-1091.
21. Yang, C., D. Li, and J.H. Masliyah, *Modeling forced liquid convection in rectangular microchannels with electrokinetic effects*. International Journal of Heat and Mass Transfer, 1998. **41**(24): p. 4229.
22. Rice, C.L. and R. Whitehead, *Electrokinetic flow in a narrow cylindrical capillary*. Journal of Physical Chemistry, 1965. **69**(11): p. 4017-4024.

23. Hildreth, D., *Electrokinetic flow in fine capillary channels*. Journal of Physical Chemistry, 1970. **74**(9): p. 2006-2015.
24. Zhang, Y., et al., *Electroosmotic flow in irregular shape microchannels*. International Journal of Engineering Science, 2005. **43**(19-20): p. 1450-1463.
25. Xuan, X. and D. Li, *Electroosmotic flow in microchannels with arbitrary geometry and arbitrary distribution of wall charge*. J Colloid Interface Sci, 2005. **289**(1): p. 291-303.
26. Arulanandam, S. and D. D. Li, *ζ potential and surface conductance by monitoring the current in electro-osmotic flow*. J. Colloid Interface Sci., 2000. **225**(2): p. 421-428.
27. Huang, X. and M.J. Gordon, *Current-monitoring method for measuring the electroosmotic flow rate in capillary zone electrophoresis*. Analytical Chemistry, 1988. **60**(17): p. 1837-1838.
28. Erickson, D. and C.W. D. Li, *An improved method of determining the ξ -potential and surface conductance*. J. Colloid Interface Sci., 2000. **231**(1): p. 186-197.
29. Wang, C., et al., *Characterization of electroosmotic flow in rectangular microchannels*. International Journal of Heat and Mass Transfer, 2007. **50**(15-16): p. 3115-3121.
30. Lindken, R., et al., *Micro-Particle Image Velocimetry (microPIV): recent developments, applications, and guidelines*. Lab Chip, 2009. **9**(17): p. 2551-67.
31. Qu, W. and D. Li, *A Model for Overlapped EDL Fields*. J Colloid Interface Sci, 2000. **224**(2): p. 397-407.
32. Sze, A., et al., *Zeta-potential measurement using the Smoluchowski equation and the slope of the current-time relationship in electroosmotic flow*. Journal of Colloid and Interface Science, 2003. **261**(2): p. 402-410.
33. Erickson, D. and D. Li, *Influence of surface heterogeneity on electrokinetically driven microfluidic mixing*. Langmuir, 2002. **18**(5): p. 1883-1892.
34. Ross, D., T.J. Johnson, and L.E. Locascio, *Imaging of electroosmotic flow in plastic microchannels*. Analytical Chemistry, 2001. **73**(11): p. 2509-2515.
35. Minerick, A.R., A.E. Ostafin, and H.C. Chang, *Electrokinetic transport of red blood cells in microcapillaries*. Electrophoresis, 2002. **23**(14): p. 2165-2173.
36. Huang, J., et al., *Temperature sensitivity and electrokinetic behavior of a N-isopropylacrylamide grafted microporous polyethylene membrane*. Desalination, 2002. **146**(1-3): p. 3864-3871.
37. Shim, Y., et al., *Effects of natural organic matter and ionic species on membrane surface charge*. Environmental Science and Technology, 2002. **36**(17): p. 3864-3871.
38. Debye, P. and E. Hückel, *Zur Theorie der Elektrolyte. I. Gefrierpunkts erniedrigung und verwandte Erscheinungen [The theory of electrolytes. I. Lowering of freezing point and related phenomena]*. Physikalische Zeitschrift 1923. **24**: p. 22.
39. Voigt, A., H. Wolf, and S. Lauckner, *Electrokinetic properties of polymer and glass surfaces in aqueous solutions: Experimental evidence for swollen surface layers*. Biomaterials, 1983. **4**(4): p. 299-304.
40. Werner, G., et al., *Extended electrokinetic characterization of flat solid surfaces*. Journal of Colloid and Interface Science, 1998. **208**(1): p. 329-346.
41. Jachowicz, J. and M.D. Berthiaume, *Heterocoagulation of silicon emulsions on keratin fibers*. Journal of Colloid and Interface Science, 1989. **133**(1): p. 118-134.
42. Zimmermann, R., S. Dukhin, and C. Werner, *Electrokinetic measurements reveal interracial charge at polymer films caused by simple electrolyte ions*. Journal of Physical Chemistry B, 2001. **105**(36): p. 8544-8549.
43. Ren, L., C. Escobedo-Canseco, and D. Li, *A new method of evaluating the average electro-osmotic velocity in microchannels*. J Colloid Interface Sci, 2002. **250**(1): p. 238-42.
44. Laser, D.J. and J.G. Santiago, *A review of micropumps*. Journal of Micromechanics and Microengineering, 2004. **14**(6): p. R35-R64.

45. Morf, W.E., O.T. Guenat, and N.F.D. Rooij, *Partial electroosmotic pumping in complex capillary systems. Part 1: Principles and general theoretical approach*. Sensors and Actuators, B: Chemical, 2001. **72**(3): p. 266-272.
46. Yao, S., et al., *Porous glass electroosmotic pumps: design and experiments*. J Colloid Interface Sci, 2003. **268**(1): p. 143-153.
47. Yao, S. and J.G. Santiago, *Porous glass electroosmotic pumps: theory*. J Colloid Interface Sci, 2003. **268**(1): p. 133-142.
48. Chen, Z., P. Wang, and H.C. Chang, *An electro-osmotic micro-pump based on monolithic silica for micro-flow analyses and electro-sprays*. Anal Bioanal Chem, 2005. **382**(3): p. 817-24.
49. Piyasena, M.E., G.P. Lopez, and D.N. Petsev, *An electrokinetic cell model for analysis and optimization of electroosmotic microfluidic pumps*. Sensors and Actuators B: Chemical, 2006. **113**(1): p. 461-467.
50. Wu, J., *Ac electro-osmotic micropump by asymmetric electrode polarization*. Journal of Applied Physics, 2008. **103**(2).
51. Debesset, S., et al., *An AC electroosmotic micropump for circular chromatographic applications*. Lab on a Chip - Miniaturisation for Chemistry and Biology, 2004. **4**(4): p. 396-400.
52. Mpholo, M., C.G. Smith, and A.B.D. Brown, *Low voltage plug flow pumping using anisotropic electrode arrays*. Sensors and Actuators B: Chemical, 2003. **92**(3): p. 262-268.
53. Brask, A., G. Goranovic, and H. Bruus, *Electroosmotic pumping of nonconducting liquids by viscous drag from a secondary conducting liquid*. 2003 Nanotechnology Conference and Trade Show - Nanotech 2003, 2003: p. 190-193.
54. Brask, A., et al., *A novel electro-osmotic pump design for nonconducting liquids: theoretical analysis of flow rate-pressure characteristics and stability*. Journal of Micromechanics and Microengineering, 2005. **15**(4): p. 883-891.
55. Gao, Y., et al., *Two-fluid electroosmotic flow in microchannels*. J Colloid Interface Sci, 2005. **284**(1): p. 306-14.
56. Gao, Y., et al., *Transient two-liquid electroosmotic flow with electric charges at the interface*. Colloids and Surfaces A: Physicochemical and Engineering Aspects, 2005. **266**(1-3): p. 117-128.
57. Haiwang, L., T.N. Wong, and N.-T. Nguyen, *Analytical model of mixed electroosmotic/pressure driven three immiscible fluids in a rectangular microchannel*. International Journal of Heat and Mass Transfer, 2009. **52**(19-20): p. 4459-4469.
58. Haiwang, L., T.N. Wong, and N.-T. Nguyen, *Time-dependent model of mixed electroosmotic/pressure-driven three immiscible fluids in a rectangular microchannel*. International Journal of Heat and Mass Transfer, 2010. **53**(4): p. 772-785.
59. Wang, C., et al., *Interface control of pressure-driven two-fluid flow in microchannels using electroosmosis*. Journal of Micromechanics and Microengineering, 2005. **15**(12): p. 2289-2297.
60. Lee, J.S.H., et al., *Electrokinetic flow in a free surface-guided microchannel*. J. Appl. Phys, 2006. **99**(5).
61. Pan, Y.-J., C.-M. Ren, and R.-J. Yang, *Electrokinetic flow focusing and valveless switching integrated with electrokinetic instability for mixing enhancement*. Journal of Micromechanics and Microengineering, 2007. **17**(4): p. 820-827.
62. Chhabra, R.P. and J.F. Richardson, *Non-Newtonian flow and applied rheology* 2008.
63. R.B.Bird, *Useful non-Newtonian models*. Annu. Rev. Fluid Mech, 1976. **8**: p. 13.
64. B.Bird, R. and J. M.Wiest, *Constitutive-Equations for Polymeric Liquids*. Annual Review of Fluid Mechanics, 1995. **27**(1): p. 169-193.
65. R.B.Bird, R.C.Armstrong, and O.Hassager, *Dynamics of Polymeric Liquids*. Fluid Dynamics, ed. 2nd. Vol. 1. 1987, New York: Wiley.

66. P.J.Carreau, D.Dekee, and R.P. Chhabra, *Rheology of Polymeric Systems: Principles and Applications* 1997, Munich: Hanser.
67. P.J.Carreau, *Rheological Equations from Molecular Network Theories* Trans. Soc. Rheol., 1972. **16**: p. 99.
68. W.H.Boersma, J.Levan, and H.N.Stein, *AIChE J*, 1990. **36**: p. 321.
69. Berli, C.L., *Electrokinetic energy conversion in microchannels using polymer solutions*. *J Colloid Interface Sci*, 2010. **349**(1): p. 446-8.
70. Berli, C.L. and M.L. Olivares, *Electrokinetic flow of non-Newtonian fluids in microchannels*. *J Colloid Interface Sci*, 2008. **320**(2): p. 582-9.
71. Das, S. and S. Chakraborty, *Analytical solutions for velocity, temperature and concentration distribution in electroosmotic microchannel flows of a non-Newtonian bio-fluid*. *Analytica Chimica Acta*, 2006. **559**(1): p. 15-24.
72. Zhao, C. and C. Yang, *An exact solution for electroosmosis of non-Newtonian fluids in microchannels*. *Journal of Non-Newtonian Fluid Mechanics*, 2011. **166**(17-18): p. 1076-1079.
73. Zhao, C., et al., *Analysis of electroosmotic flow of power-law fluids in a slit microchannel*. *J Colloid Interface Sci*, 2008. **326**(2): p. 503-10.
74. Zhao, C. and C. Yang, *Electro-osmotic mobility of non-Newtonian fluids*. *Biomicrofluidics*, 2011. **5**: p. 14110.
75. Vasu, N. and S. De, *Electroosmotic flow of power-law fluids at high zeta potentials*. *Colloids and Surfaces A: Physicochemical and Engineering Aspects*, 2010. **368**(1-3): p. 44-52.
76. Berli, C.L.A., *Output pressure and efficiency of electrokinetic pumping of non-Newtonian fluids*. *Microfluidics and Nanofluidics*, 2009. **8**(2): p. 197-207.
77. Khair, A., D. Posluszny, and L. Walker, *Coupling electrokinetics and rheology: Electrophoresis in non-Newtonian fluids*. *Physical Review E*, 2012. **85**(1).
78. Li, J., P.S. Sheeran, and C. Kleinstreuer, *Analysis of Multi-Layer Immiscible Fluid Flow in a Microchannel*. *Journal of Fluids Engineering*, 2011. **133**(11): p. 111202.
79. Afonso, A.M., M.A. Alves, and F.T. Pinho, *Analytical solution of mixed electro-osmotic/pressure driven flows of viscoelastic fluids in microchannels*. *Journal of Non-Newtonian Fluid Mechanics*, 2009. **159**(1-3): p. 50-63.
80. Dhinakaran, S., et al., *Steady viscoelastic fluid flow between parallel plates under electro-osmotic forces: Phan-Thien-Tanner model*. *J Colloid Interface Sci*, 2010. **344**(2): p. 513-20.
81. Ahmed, M.E.S., *Numerical solution of power law fluids flow and heat transfer with a magnetic field in a rectangular duct*. *International Communications in Heat and Mass Transfer*, 2006. **33**(9): p. 1165-1176.
82. Cho, C.-C., C.-L. Chen, and C.-K. Chen, *Electrokinetically-driven non-Newtonian fluid flow in rough microchannel with complex-wavy surface*. *Journal of Non-Newtonian Fluid Mechanics*, 2012. **173-174**: p. 13-20.
83. Craven, T.J., J.M. Rees, and W.B. Zimmerman, *Pressure sensor positioning in an electrokinetic microrheometer device: simulations of shear-thinning liquid flows*. *Microfluidics and Nanofluidics*, 2010. **9**(2-3): p. 559-571.
84. Hadigol, M., et al., *Numerical study of electroosmotic micromixing of non-Newtonian fluids*. *Journal of Non-Newtonian Fluid Mechanics*, 2011. **166**(17-18): p. 965-971.
85. Wang, C.-H. and J.-R. Ho, *A lattice Boltzmann approach for the non-Newtonian effect in the blood flow*. *Computers & Mathematics with Applications*, 2011. **62**(1): p. 75-86.
86. Zimmerman, W.B., J.M. Rees, and T.J. Craven, *Rheometry of non-Newtonian electrokinetic flow in a microchannel T-junction*. *Microfluidics and Nanofluidics*, 2006. **2**(6): p. 481-492.
87. Pipe, C.J. and G.H. McKinley, *Microfluidic rheometry*. *Mechanics Research Communications*, 2009. **36**(1): p. 110-120.

88. Juang, Y.J., et al., *Dynamics of Single Polymers in a Stagnation Flow Induced by Electrokinetics*. Physical Review Letters, 2004. **93**(26).
89. Steinhaus, B., A.Q. Shen, and R. Sureshkumar, *Dynamics of viscoelastic fluid filaments in microfluidic devices*. Physics of Fluids, 2007. **19**(7): p. 073103.
90. Sousa, P.C., et al., *Efficient microfluidic rectifiers for viscoelastic fluid flow*. Journal of Non-Newtonian Fluid Mechanics, 2010. **165**(11-12): p. 652-671.
91. Zeng, H. and Y. Zhao, *Rheological analysis of non-Newtonian blood flow using a microfluidic device*. Sensors and Actuators A: Physical, 2011. **166**(2): p. 207-213.
92. Christopher, G.F. and S.L. Anna, *Microfluidic methods for generating continuous droplet streams*. Journal of Physics D: Applied Physics, 2007. **40**(19): p. R319-R336.
93. Guo, M.T., et al., *Droplet microfluidics for high-throughput biological assays*. Lab Chip, 2012. **12**(12): p. 2146-55.
94. Gupta, A., S.M.S. Murshed, and R. Kumar, *Droplet formation and stability of flows in a microfluidic T-junction*. Applied Physics Letters, 2009. **94**(16): p. 164107.
95. Ozen, O., et al., *Monodisperse Drop Formation in Square Microchannels*. Physical Review Letters, 2006. **96**(14).
96. Atencia, J. and D.J. Beebe, *Controlled microfluidic interfaces*. Nature, 2005. **437**(7059): p. 648-55.
97. Casadevall i Solvas, X. and A. deMello, *Droplet microfluidics: recent developments and future applications*. Chem Commun (Camb), 2011. **47**(7): p. 1936-42.
98. Garstecki, P., H.A. Stone, and G.M. Whitesides, *Mechanism for Flow-Rate Controlled Breakup in Confined Geometries: A Route to Monodisperse Emulsions*. Physical Review Letters, 2005. **94**(16).
99. Teh, S.Y., et al., *Droplet microfluidics*. Lab Chip, 2008. **8**(2): p. 198-220.
100. Garstecki, P., et al., *Formation of droplets and bubbles in a microfluidic T-junction-scaling and mechanism of break-up*. Lab Chip, 2006. **6**(3): p. 437-46.
101. Tan, S.H. and N.-T. Nguyen, *Generation and manipulation of monodispersed ferrofluid emulsions: The effect of a uniform magnetic field in flow-focusing and T-junction configurations*. Physical Review E, 2011. **84**(3).
102. van Steijn, V., M.T. Kreutzer, and C.R. Kleijn, *-PIV study of the formation of segmented flow in microfluidic T-junctions*. Chemical Engineering Science, 2007. **62**(24): p. 7505-7514.
103. De Menech, M., et al., *Transition from squeezing to dripping in a microfluidic T-shaped junction*. Journal of Fluid Mechanics, 2008. **595**.
104. Anna, S.L. and H.C. Mayer, *Microscale tipstreaming in a microfluidic flow focusing device*. Physics of Fluids, 2006. **18**(12): p. 121512.
105. Ward, T., et al., *Microfluidic flow focusing: drop size and scaling in pressure versus flow-rate-driven pumping*. Electrophoresis, 2005. **26**(19): p. 3716-24.
106. Utada, A.S., et al., *Dripping to Jetting Transitions in Coflowing Liquid Streams*. Physical Review Letters, 2007. **99**(9).
107. Link, D.R., et al., *Geometrically Mediated Breakup of Drops in Microfluidic Devices*. Physical Review Letters, 2004. **92**(5).
108. Lee, W., L.M. Walker, and S.L. Anna, *Role of geometry and fluid properties in droplet and thread formation processes in planar flow focusing*. Physics of Fluids, 2009. **21**(3): p. 032103.
109. Gu, H., M.H. Duits, and F. Mugele, *Droplets formation and merging in two-phase flow microfluidics*. Int J Mol Sci, 2011. **12**(4): p. 2572-97.
110. Chen, J.M., M.-C. Kuo, and C.-P. Liu, *Control of Droplet Generation in Flow-Focusing Microfluidic Device with a Converging-Diverging Nozzle-Shaped Section*. Japanese Journal of Applied Physics, 2011. **50**(10): p. 107301.
111. Seemann, R., et al., *Droplet based microfluidics*. Rep Prog Phys, 2012. **75**(1): p. 016601.
112. Link, D.R., et al., *Electric control of droplets in microfluidic devices*. Angew Chem Int Ed Engl, 2006. **45**(16): p. 2556-60.

113. Tan, S.H., B. Semin, and J.C. Baret, *Microfluidic flow-focusing in ac electric fields*. Lab Chip, 2014. **14**(6): p. 1099-106.
114. Nguyen, N.-T., et al., *Thermally mediated droplet formation in microchannels*. Applied Physics Letters, 2007. **91**(8): p. 084102.
115. Husny, J. and J.J. Cooper-White, *The effect of elasticity on drop creation in T-shaped microchannels*. Journal of Non-Newtonian Fluid Mechanics, 2006. **137**(1-3): p. 121-136.
116. Christopher, G.F. and S.L. Anna, *Passive breakup of viscoelastic droplets and filament self-thinning at a microfluidic T-junction*. Journal of Rheology, 2009. **53**(3): p. 663.
117. Arratia, P.E., J.P. Gollub, and D.J. Durian, *Polymeric filament thinning and breakup in microchannels*. Physical Review E, 2008. **77**(3).
118. Arratia, P.E., et al., *The effects of polymer molecular weight on filament thinning and drop breakup in microchannels*. New Journal of Physics, 2009. **11**(11): p. 115006.
119. Feng, X., *Structures and Self-Organization at Liquid Crystal Interfaces: Surface Ordering and Anchoring*, G.-A.U. Go ttingen, Editor 2013, Diss.
120. Kralj, S., S. Žumer, and D. Allender, *Nematic-isotropic phase transition in a liquid-crystal droplet*. Physical Review A, 1991. **43**(6): p. 2943-2952.
121. Sengupta, A., et al., *Functionalization of microfluidic devices for investigation of liquid crystal flows*. Microfluidics and Nanofluidics, 2012. **13**(6): p. 941-955.
122. Sengupta, A., U. Tkalec, and C. Bahr, *Nematic textures in microfluidic environment*. Soft Matter, 2011. **7**(14): p. 6542.
123. Ranjini, R., M.V. Matham, and N.-T. Nguyen, *Analysis on the birefringence property of lyotropic liquid crystals below Krafft temperature*. Optical Materials, 2011. **33**(8): p. 1338-1341.
124. Ranjini, R., M.V. Matham, and N.T. Nguyen, *Conoscopic analysis of electric field driven planar aligned nematic liquid crystal*. Appl Opt, 2014. **53**(13): p. 2773-6.
125. Sengupta, A., *Topological Microfluidics Nematic Liquid Crystals and Nematic Colloids in Microfluidic Environment*, in *Max Planck Institute for Dynamics and Self-Organization* 2013, University of Göttingen: Göttingen, Germany.
126. Sengupta, A., et al., *Liquid Crystal Microfluidics for Tunable Flow Shaping*. Physical Review Letters, 2013. **110**(4).
127. Dierking, I., *Polarizing Microscopy*, in *Textures of Liquid Crystals* 2004, Wiley: VCH Verlag GmbH & Co. KGaA. p. 33-42.
128. Acharya, B.R., et al., *In-line liquid-crystal microcell polarimeter for high-speed polarization analysis*. Opt. Lett., 2003. **28**: p. 3.
129. Coleman, D.A., et al., *Polarization-Modulated Smectic Liquid Crystal Phases*. Science, 2003. **301**(5637): p. 1204-1211.
130. Brake, J.M., et al., *Biomolecular Interactions at Phospholipid-Decorated Surfaces of Liquid Crystals*. Science, 2003. **302**(5653): p. 2094-2097.
131. Lin, I.-H., et al., *Endotoxin-Induced Structural Transformations in Liquid Crystalline Droplets*. Science, 2011. **332**(6035): p. 1297-1300.
132. Wereley, N.-T.N.s.T., *Fundamentals and applications of microfluidics* 2002, Boston, MA: Artech House.
133. Lee, C.-Y., et al., *Electrokinetically driven active micro-mixers utilizing zeta potential variation induced by field effect*. Journal of Micromechanics and Microengineering, 2004. **14**(10): p. 1390-1398.
134. Dreyfus, R., P. Tabeling, and H. Willaime, *Ordered and Disordered Patterns in Two-Phase Flows in Microchannels*. Physical Review Letters, 2003. **90**(14).
135. Thorsen, T., et al., *Dynamic Pattern Formation in a Vesicle-Generating Microfluidic Device*. Physical Review Letters, 2001. **86**(18): p. 4163-4166.
136. *Microfluidics roadmap: The trend to use low-cost technologies and microfluidics platforms* 2004, Bremen, Germany.

137. S.Brittain, K.P., X.M.Zhao, and G.Whitesides, *Softlithography and microfabrication*. Physics World, 1998. **11**(5): p. 31-36.
138. Ichikawa, N., K. Hosokawa, and R. Maeda, *Interface motion of capillary-driven flow in rectangular microchannel*. J. Colloid Interface Sci., 2004. **280**(1): p. 155-164.
139. Kim, B.J., Y.Z. Liu, and H.J. Sung, *Micro PIV measurement of two-fluid flow with different refractive indices*. Meas. Sci. Technol., 2004. **15**(6): p. 1097-1103.
140. Sato, Y., et al., *Visualization of convective mixing in microchannel by fluorescence imaging*. Meas. Sci. Technol., 2003. **14**(1): p. 114-121.
141. Dutta, P., A. Beskok, and T.C. Warburton, *Electroosmotic flow control in complex microgeometries*. JOURNAL OF MICROELECTROMECHANICAL SYSTEMS, 2002. **11**(1): p. 36-44.
142. Zhao, C. and C. Yang, *Electrokinetics of non-Newtonian fluids: a review*. Adv Colloid Interface Sci, 2013. **201-202**: p. 94-108.
143. González, A., A. Ramos, and A. Castellanos, *Pumping of electrolytes using travelling-wave electro-osmosis: a weakly nonlinear analysis*. Microfluidics and Nanofluidics, 2008. **5**(4): p. 507-515.
144. Chakraborty, S., *Dynamics of capillary flow of blood into a microfluidic channel*. Lab Chip, 2005. **5**(4): p. 421-30.
145. Huang, Y., H. Li, and T.N. Wong, *Two immiscible layers of electro-osmotic driven flow with a layer of conducting non-Newtonian fluid*. International Journal of Heat and Mass Transfer, 2014. **74**: p. 368-375.
146. Chakraborty, S., *Electroosmotically driven capillary transport of typical non-Newtonian biofluids in rectangular microchannels*. Anal Chim Acta, 2007. **605**(2): p. 175-84.
147. Olivares, M.L., L. Vera-Candioti, and C.L. Berli, *The EOF of polymer solutions*. Electrophoresis, 2009. **30**(5): p. 921-9.
148. Duval, M., *Monitoring of Cluster Formation and Elimination in PEO Solutions*. Macromolecules, 2000. **33**: p. 7862-7867.
149. Ebagninin, K.W., A. Benchabane, and K. Bekkour, *Rheological characterization of poly(ethylene oxide) solutions of different molecular weights*. J Colloid Interface Sci, 2009. **336**(1): p. 360-7.
150. Lin, Y.W. and H.T. Chang, *Analysis of double-stranded DNA by capillary electrophoresis using poly(ethylene oxide) in the presence of hexadecyltrimethylammonium bromide*. J Chromatogr A, 2006. **1130**(2): p. 206-11.
151. Stone, H.A., A.D. Stroock, and A. Ajdari, *Engineering Flows in Small Devices*. Annual Review of Fluid Mechanics, 2004. **36**(1): p. 381-411.
152. Schoch, R., J. Han, and P. Renaud, *Transport phenomena in nanofluidics*. Reviews of Modern Physics, 2008. **80**(3): p. 839-883.
153. Mostofi, M., et al., *Analytical Solution of Electrokinetic Flow in a Nanotube with Complex Fluids*. 2011: p. 399-404.
154. Tang, G.Y., et al., *Joule heating effect on electroosmotic flow and mass species transport in a microcapillary*. International Journal of Heat and Mass Transfer, 2004. **47**(2): p. 215-227.
155. Hiemenz, P.C., *Principles of colloid and surface chemistry*, ed. second 1986, New York: Marcel Dekker.
156. Song, H., D.L. Chen, and R.F. Ismagilov, *Reactions in droplets in microfluidic channels*. Angewandte chemie international edition, 2006. **45**(44): p. 7336-7356.
157. Casadevall i Solvas, X. and A. deMello, *Droplet microfluidics: recent developments and future applications*. Chemical Communications, 2011. **47**(7): p. 1936-1942.
158. Anna, S.L., N. Bontoux, and H.A. Stone, *Formation of dispersions using "flow focusing" in microchannels*. Applied Physics Letters, 2003. **82**(3): p. 364-366.
159. Christopher, G. and S. Anna, *Microfluidic methods for generating continuous droplet streams*. Journal of Physics D: Applied Physics, 2007. **40**(19): p. R319.
160. Bejan, A. and D. Gobin, *Constructal theory of droplet impact geometry*. International Journal of Heat and Mass Transfer, 2006. **49**(15-16): p. 2412-2419.

161. Seemann, R., et al., *Droplet based microfluidics*. Reports on progress in physics, 2012. **75**(1): p. 016601.
162. Jullien, M.-C., et al., *Droplet breakup in microfluidic T-junctions at small capillary numbers*. Physics of Fluids (1994-present), 2009. **21**(7): p. 072001.
163. Garstecki, P., et al., *Formation of droplets and bubbles in a microfluidic T-junction—scaling and mechanism of break-up*. Lab on a Chip, 2006. **6**(3): p. 437-446.
164. Tan, S.H. and N.-T. Nguyen, *Generation and manipulation of monodispersed ferrofluid emulsions: The effect of a uniform magnetic field in flow-focusing and T-junction configurations*. Physical Review E, 2011. **84**(3): p. 036317.
165. Shi, Y., G. Tang, and H. Xia, *Lattice Boltzmann simulation of droplet formation in T-junction and flow focusing devices*. Computers & Fluids, 2014. **90**: p. 155-163.
166. Cheung, Y.N. and H. Qiu, *Dynamics of Droplet Pinch-off in Acoustically Actuated Flow Focusing Devices*.
167. Martín - Banderas, L., et al., *Flow Focusing: A Versatile Technology to Produce Size - Controlled and Specific - Morphology Microparticles*. Small, 2005. **1**(7): p. 688-692.
168. Tan, S.H., B. Semin, and J.-C. Baret, *Microfluidic flow focusing in ac electric field*. Lab Chip, 2014. **14**: p. 1099-1106.
169. Ward, T., et al., *Microfluidic flow focusing: Drop size and scaling in pressure versus flow - rate - driven pumping*. Electrophoresis, 2005. **26**(19): p. 3716-3724.
170. Anna, S.L. and H.C. Mayer, *Microscale tipstreaming in a microfluidic flow focusing device*. Physics of Fluids (1994-present), 2006. **18**(12): p. 121512.
171. Thorsen, T., et al., *Dynamic pattern formation in a vesicle-generating microfluidic device*. Physical review letters, 2001. **86**(18): p. 4163.
172. Si, T., et al., *Modes in flow focusing and instability of coaxial liquid-gas jets*. Journal of Fluid Mechanics, 2009. **629**: p. 1-23.
173. Shojaei-Zadeh, S. and S.L. Anna, *Role of surface anchoring and geometric confinement on focal conic textures in smectic-A Liquid Crystal*. Langmuir, 2006. **22**: p. 9986-9993.
174. Bejan, A. and S. Lorente, *Constructal theory of generation of configuration in nature and engineering*. Journal of Applied Physics, 2006. **100**(4): p. 041301.
175. Bejan, A., *Why humans build fires shaped the same way*. Sci. Rep., 2015. **5**.
176. Bejan, A. and S. Lorente, *The constructal law and the evolution of design in nature*. Phys Life Rev, 2011. **8**(3): p. 209-40.
177. Bejan, A. and S. Lorente, *Constructal law of design and evolution: Physics, biology, technology, and society*. Journal of Applied Physics, 2013. **113**(15): p. 151301.
178. Kim, H., et al., *Controlled production of emulsion drops using an electric field in a flow-focusing microfluidic device*. Applied Physics Letters, 2007. **91**(13): p. 133106.
179. He, P., et al., *Low-frequency ac electro-flow-focusing microfluidic emulsification*. Applied Physics Letters, 2010. **96**(17): p. 174103.
180. Link, D.R., et al., *Electric control of droplets in microfluidic devices*. Angewandte chemie international edition, 2006. **45**(16): p. 2556-2560.
181. Malloggi, F., et al., *Electrowetting-controlled droplet generation in a microfluidic flow-focusing device*. Journal of Physics: Condensed Matter, 2007. **19**(46): p. 462101.
182. Gu, H., et al., *Electrowetting-enhanced microfluidic device for drop generation*. Applied Physics Letters, 2008. **93**(18): p. 183507.
183. Hohman, M.M., et al., *Electrospinning and electrically forced jets. I. Stability theory*. Physics of Fluids (1994-present), 2001. **13**(8): p. 2201-2220.
184. Whitesides, G.M., et al., *Soft lithography in biology and biochemistry*. Annual review of biomedical engineering, 2001. **3**(1): p. 335-373.

185. Siegel, A.C., et al., *Microsolidics: Fabrication of Three - Dimensional Metallic Microstructures in Poly (dimethylsiloxane)*. *Advanced Materials*, 2007. **19**(5): p. 727-733.
186. Gañán-Calvo, A.M., *Generation of steady liquid microthreads and micron-sized monodisperse sprays in gas streams*. *Physical review letters*, 1998. **80**(2): p. 285.
187. Stone, H.A., *Dynamics of drop deformation and breakup in viscous fluids*. *Annual Review of Fluid Mechanics*, 1994. **26**(1): p. 65-102.
188. Whitesides, G.M., *The origins and the future of microfluidics*. *Nature*, 2006. **442**(7101): p. 368-73.
189. Cheung, Y.N. and H. Qiu, *Characterization of acoustic droplet formation in a microfluidic flow-focusing device*. *Physical Review E*, 2011. **84**(6).
190. Hagedorn, J.G., N.S. Martys, and J.F. Douglas, *Breakup of a fluid thread in a confined geometry: droplet-plug transition, perturbation sensitivity, and kinetic stabilization with confinement*. *Physical Review E*, 2004. **69**(5).
191. Li, Y., et al., *Control of the breakup process of viscous droplets by an external electric field inside a microfluidic device*. *Soft Matter*, 2015. **11**: p. 16.
192. Okushima, S., et al., *Controlled Production of Monodisperse Double Emulsions by Two-Step Droplet Breakup in Microfluidic Devices*. *Langmuir*, 2004. **20**: p. 4.
193. Barbier, V., et al., *Producing droplets in parallel microfluidic systems*. *Physical Review E*, 2006. **74**(4).
194. Niu, X., et al., *Pillar-induced droplet merging in microfluidic circuits*. *Lab Chip*, 2008. **8**(11): p. 1837-41.
195. Priest, C., et al., *Microfluidic polymer multilayer adsorption on liquid crystal droplets for microcapsule synthesis*. *Lab on a Chip*, 2008. **8**(12): p. 2182-7.
196. Elvira, K.S., et al., *The past, present and potential for microfluidic reactor technology in chemical synthesis*. *Nat Chem*, 2013. **5**(11): p. 905-15.
197. Bayraktar, T. and S.B. Pidugu, *Characterization of liquid flows in microfluidic systems*. *International Journal of Heat and Mass Transfer*, 2006. **49**(5-6): p. 815-824.
198. Jeong, W.C., et al., *Controlled generation of submicron emulsion droplets via highly stable tip-streaming mode in microfluidic devices*. *Lab Chip*, 2012. **12**(8): p. 1446-53.
199. Nie, Z., et al., *Emulsification in a microfluidic flow-focusing device: effect of the viscosities of the liquids*. *Microfluidics and Nanofluidics*, 2008. **5**(5): p. 585-594.
200. Cui, M. and J.R. Kelly, *Temperature Dependence of Visco-Elastic Properties of 5CB*. *Molecular Crystals and Liquid Crystals Science and Technology. Section A. Molecular Crystals and Liquid Crystals*, 1999. **331**(1): p. 49-57.
201. Porter, D., et al., *Temperature dependence of droplet breakup in 8CB and 5CB liquid crystals*. *Physical Review E*, 2012. **85**(4).
202. Cheung, Y.N. and H. Qiu, *Acoustic microstreaming for droplet breakup in a microflow-focusing device*. *Applied Physics Letters*, 2010. **97**(13): p. 133111.
203. Nguyen, N.T., et al., *Improvement of rectification effects in diffuser/nozzle structures with viscoelastic fluids*. *Biomicrofluidics*, 2008. **2**(3): p. 34101.
204. Weigl, B.H., et al., *Lab-on-a-chip sample preparation using laminar fluid diffusion interfaces computational fluid dynamics model results and fluidic verification experiments*. *Analytical and Bioanalytical Chemistry*, 2001. **371**(2): p. 97-105.
205. Yue, P., et al., *Elastic encapsulation in bicomponent stratified flow of viscoelastic fluids*. *Journal of Rheology*, 2008. **52**(4): p. 1027.
206. Aytouna, M., et al., *Drop Formation in Non-Newtonian Fluids*. *Physical Review Letters*, 2013. **110**(3).
207. Kinoshita, H., et al., *Three-dimensional measurement and visualization of internal flow of a moving droplet using confocal micro-PIV*. *Lab Chip*, 2007. **7**(3): p. 338-46.
208. Lima, R., et al., *Confocal micro-PIV measurements of three-dimensional profiles of cell suspension flow in a square microchannel*. *Measurement Science and Technology*, 2006. **17**(4): p. 797-808.
209. Lu, H.W., et al., *A study of EWOD-driven droplets by PIV investigation*. *Lab Chip*, 2008. **8**(3): p. 456-61.

210. Shinohara, K., et al., *High-speed micro-PIV measurements of transient flow in microfluidic devices*. Measurement Science and Technology, 2004. **15**(10): p. 1965-1970.
211. Kim, Y.K., B. Senyuk, and O.D. Lavrentovich, *Molecular reorientation of a nematic liquid crystal by thermal expansion*. Nat Commun, 2012. **3**: p. 1133.
212. Sengupta, A., *Tuning fluidic resistance via liquid crystal microfluidics*. Int J Mol Sci, 2013. **14**(11): p. 22826-44.
213. Tjipto, E., et al., *Tailoring the Interfaces between nematic Liquid crystal Emulsions and Aqueous Phase via Layer-by-layer Assembly*. NANO LETTERS, 2006. **6**(10).
214. Bera, T. and J. Fang, *Interaction of Surfactants and Polyelectrolyte-Coated Liquid Crystal Droplets*. Journal of Materials Science and Chemical Engineering, 2014. **02**(11): p. 1-7.
215. Aguirre, L.E., et al., *Regular structures in 5CB liquid crystals under the joint action of ac and dc voltages*. Physical Review E, 2012. **85**(4).
216. Bondar, V.G., D. Lavrentovich, and V.M. Pergamenschchik, *Threshold of structural hedgehog-ring transition in drops of a nematic in an alternating electric field*. Sov. Phys. JETP, 1992. **74**(1): p. 60-67.
217. de Oliveira, B.F., et al., *Nematic liquid crystal dynamics under applied electric fields*. Physical Review E, 2010. **82**(4).
218. Faetti, S., L. Fronzoni, and P.A. Rolla, *Static and dynamic behavior of the vortex-electrohydrodynamic instability in freely suspended layers of nematic liquid crystals*. The Journal of Chemical Physics, 1983. **79**(10): p. 5054.
219. Zhang, X., et al., *Anti-electroviscous effect of near-surface 5CB liquid crystal and its boundary lubrication property*. Rheologica Acta, 2011. **51**(3): p. 267-277.
220. Squires, T.M. and S.R. Quake, *Microfluidics: Fluid physics at the nanoliter scale*. Reviews of Modern Physics, 2005. **77**(3): p. 977-1026.
221. Groisman, A. and S. Quake, *A Microfluidic Rectifier: Anisotropic Flow Resistance at Low Reynolds Numbers*. Physical Review Letters, 2004. **92**(9).
222. Utada, A.S., et al., *Monodisperse Double Emulsions generated from a microcapillary device*. Science, 2005. **308**: p. 5.
223. Abate, A.R., et al., *Synthesis of monodisperse microparticles from non-Newtonian polymer solutions with microfluidic devices*. Adv Mater, 2011. **23**(15): p. 1757-60.
224. Khan, M. and S.-Y. Park, *General Liquid-crystal droplets produced by microfluidics for urea detection*. Sensors and Actuators B: Chemical, 2014. **202**: p. 516-522.
225. Kim, Y.-K., et al., *Domain walls and anchoring transitions mimicking nematic biaxiality in the oxadiazole bent-core liquid crystal C7*. Soft Matter, 2015. **11**(20): p. 3963-3970.
226. Ninomiya, N. and K. Yasuda, *Visualization and PIV Measurement of the Flow around and inside of a Falling Droplet*. Journal of Visualization, 2006. **9**(3): p. 8.
227. Oishi, M., et al., *Confocal micro-PIV measurement of droplet formation in a T-shaped micro-junction*. Journal of Physics: Conference Series, 2009. **147**: p. 012061.
228. Ahn, K., et al., *Dielectrophoretic manipulation of drops for high-speed microfluidic sorting devices*. Applied Physics Letters, 2006. **88**(2): p. 024104.
229. Paik, P., et al., *Electrowetting-based droplet mixers for microfluidic systems*. Lab Chip, 2003. **3**(1): p. 28-33.
230. Zagnoni, M. and J.M. Cooper, *On-chip electrocoalescence of microdroplets as a function of voltage, frequency and droplet size*. Lab Chip, 2009. **9**(18): p. 2652-8.